INFORMATION TO USERS

This manuscript has been reproduced from the microfilm master. UMI films the text directly from the original or copy submitted. Thus, some thesis and dissertation copies are in typewriter face, while others may be from any type of computer printer.

The quality of this reproduction is dependent upon the quality of the copy submitted. Broken or indistinct print, colored or poor quality illustrations and photographs, print bleedthrough, substandard margins, and improper alignment can adversely affect reproduction.

In the unlikely event that the author did not send UMI a complete manuscript and there are missing pages, these will be noted. Also, if unauthorized copyright material had to be removed, a note will indicate the deletion.

Oversize materials (e.g., maps, drawings, charts) are reproduced by sectioning the original, beginning at the upper left-hand corner and continuing from left to right in equal sections with small overlaps.

Photographs included in the original manuscript have been reproduced xerographically in this copy. Higher quality 6" x 9" black and white photographic prints are available for any photographs or illustrations appearing in this copy for an additional charge. Contact UMI directly to order.

Bell & Howell Information and Learning
300 North Zeeb Road, Ann Arbor, MI 48106-1346 USA
800-521-0600

DETERMINATION OF THE STRUCTURE AND DYNAMICS OF SALIVARY STATHERIN AND N-TERMINAL FRAGMENTS BOUND TO HYDROXYAPATITE USING SOLID STATE NMR

by

Wendy Jane Shaw

A dissertation submitted in partial fulfillment of
the requirements for the degree of

Doctor of Philosophy

University of Washington

2000

Program Authorized to Offer Degree: Department of Chemistry

Bell & Howell Information and Learning Company
300 North Zeeb Road
P.O. Box 1346
Ann Arbor, MI 48106-1346

Doctoral Dissertation

In presenting this dissertation in partial fulfillment of the requirements for the Doctoral degree at the University of Washington, I agree that the Library shall make its copies freely available for inspection. I further agree that extensive copying of this dissertation is allowable only for scholarly purposes, consistent with "fair use" as prescribed in the U.S. Copyright Law. Requests for copying or reproduction of this dissertation may be referred to Bell and Howell Information and Learning, 300 North Zeeb Road, Ann Arbor, MI 48106-1346, to whom the author has granted "the right to reproduce and sell (a) copies of the manuscript in microform and/or (b) printed copies of the manuscript made from microform."

Signature Lindy J. Shaw

Date 05/23/00

University of Washington
Graduate School

This is to certify that I have examined this copy of a doctoral dissertation by

Wendy Jane Shaw

and have found that it is complete and satisfactory in all respects,
and that any and all revisions required by the final
examining committee have been made.

Chair of Supervisory Committee:

Gary P. Drobny

Reading Committee:

Charles T. Campbell

Patrick S. Stayton

Date: 05/23/00

University of Washington

Abstract

DETERMINATION OF THE STRUCTURE AND DYNAMICS OF SALIVARY STATHERIN AND N-TERMINAL FRAGMENTS BOUND TO HYDROXYAPATITE USING SOLID STATE NMR

Wendy Jane Shaw

Chairperson of the Supervisory Committee: Professor Gary P. Drobny

Department of Chemistry

This dissertation contains solid-state NMR studies of the structure and dynamics of the biomineralization protein, salivary statherin, adsorbed onto its relevant biomineral surface, hydroxyapatite. The structure of statherin and the N-terminal 15 residue peptide were studied using both homonculear and heteronuclear dipolar recoupling techniques. ^{13}C-^{13}C DRAWS experiments were employed to determine the backbone torsion angle φ for samples isotopically labeled at the backbone carbonyl positions at the following residues: pS_2pS_3, F_7L_8 and $I_{11}G_{12}$, in both the peptide and the full protein. These measurements indicate that the peptide is disordered at the pS_2pS_3 region with the remaining residues adopting a helical conformation. In contrast, the full protein, studied under hydrated conditions, was found to adopt a well-defined helix throughout most of the pentadecyl domain. The heteronuclear recoupling technique, REDOR, was used to confirm the helical content by measuring the distance between the backbone ^{13}C=O and $H^{15}N$ participating in the hydrogen bond of the α-helix. The peptide was labeled at L_8G_{12}

and was found to be helical both on and off the surface. The full protein was labeled throughout the pentadecyl region at pS_3F_7 and L_8G_{12}, and agreed with the DRAWS results, supporting a largely helical N-terminus.

The dynamics of the peptide and protein under hydrated conditions were studied using $T_{1\rho}$ relaxation measurements and line shape analysis. In both cases the pS_2pS_3 region was found to be very immobile, thus interacting very strongly with the hydroxyapatite surface. The F_7L_8 region was slightly more mobile in the peptide and even more so in the protein. The $I_{11}G_{12}$ region experienced a great deal of high frequency and large amplitude motion in the peptide, but had more constrained mobility in the protein. These findings indicate that the highly charged region of the N-terminus is strongly interacting with the surface of hydroxyapatite, indicating the importance of the N-terminal pentapeptide in the binding of statherin, while the remainder of the domain is only weakly interacting with the surface.

TABLE OF CONTENTS

LIST OF FIGURES

LIST OF TABLES

Acknowledgements

I would like to thank my advisors, Gary Drobny and Pat Stayton for their support, encouragement and enthusiasm as well as Dr. Joanna Long and Dr. John Stringer whose mentorship at different times in my research was very valuable. I would also like to thank Dr. Myriam Cotten and soon-to-be Dr. Nathan Oyler who provided many stimulating and thoughtful discussions, and the rest of the Drobny group who offered encouragement, feedback and generally made graduate school an enjoyable experience. Dr. Jim Franz gave me the opportunity to pursue a graduate career and has been constantly interested and supportive of my research endeavors. Most importantly, I would like to extend my deepest gratitude to my friends, family and husband who have always given me endless support (and tolerance!) no matter which road I have chosen to travel.

CHAPTER 1:

INTRODUCTION

1.1 Proteins

Peptides and proteins are critical in defining the properties of any biological system by expressing the information that is encoded in genes.[1] Protein functions are very broad in scope, including catalytic functions in enzymes, preventing foreign objects from making us sick, conversion of chemical energy to mechanical energy, and storage and transport of electrons and molecules, to name a few. Suprisingly, with the multitude of different functions, proteins are all chemically very similar, being composed of polymer chains of amino acids. The properties that define a protein's unique function are its structure and dynamics.

Protein structure is broken into four parts: primary, secondary, tertiary and quaternary structure. Proteins are composed of a chain of amino acid residues, defined from the N-terminus to the C-terminus as shown in Figure 1.1 and the number, identity and order of amino acid residues is referred to as the primary structure. There are 20 naturally occurring amino acids that could contribute to the primary structure, with over 200 variant amino acid residues, modified post-translationally, that are observed to varying degrees. Each amino acid consists of a basic structure shown in the inset of Figure 1.1, with the sidechain, R, defining each amino acid uniquely. Amino acids can be grouped into the following four categories: acidic, basic, polar uncharged and uncharged and are shown in Table 1.1.

Each of the bond angles in an amino acid has a range in conformational space that it can adopt. When combined with another amino acid, the torsion angles also have a range of conformations. These angles are defined as the torsion angles, ω, φ, and ψ (Figure 1.2). ω is restricted by the partial double bond character of the C-N bond, and is usually locked at 180°. Thus the combination of φ and ψ are the only variables contributing to the protein secondary structure. Theoretically, each torsion angle would have 360° of phase space available to it, but steric hindrance within the molecule reduces the number of possible conformations. A plot of φ vs. ψ (called a Ramachandran plot) is shown in Figure 1.3, where the darkened areas indicate "allowed" combinations of φ vs. ψ. Also indicated are commonly observed secondary structures.

Two of the most common secondary structures are the α-helix and β-sheet, both of which are particularly important in this thesis work. Figure 1.4a shows a representation of an α-helix. Based on Pauling and Corey's work in 1951 [2], the α-helix is defined as having 3.6 amino acids per turn, which involve 13 residues from the O to the H in the hydrogen bond.[1] The pitch of an α-helix is 5.4 Å per turn, and the diameter, ignoring sidechains, is about 6 Å. Each of the carbonyl groups is hydrogen bonded to the N-H group 4 residues down the chain (referred to as i i+4), thus requiring at least 4 amino acids to define a helix, and each of the hydrogen bonds is parallel with the helix axis. Of particular importance for later discussion is that each of the carbonyl groups is pointing in the same direction relative to the helix axis, and each of the nitrogen groups is pointing in the opposite direction. Torsion angles for α-helices are classically defined as

$\varphi = -57°$ and $\psi = -47°$. Careful analysis of secondary structure data available in the protein data bank[3] indicates that less rigid definitions are appropriate, with angles of $\varphi = -65 \pm 13$ and $\psi = -39 \pm 12$. An α-helix defined with the classical angles are indicated on the Ramachandran plot. The β–sheet is a second very common secondary structure. A representation shown in Figure 1.4b and can be imagined as a piece of paper folded into a series of pleats. The hydrogen bonding occurs intermolecularly between adjacent strands and the side chains point normal to the sheet plane, both into and out of the plane. The classically defined β-sheet is shown on the Ramachandran plot (with torsion angles of $\varphi = -119°$ and $\psi = 113°$), but it also has less rigidly defined backbone torsion angles of $\varphi = -112.6 \pm 41$ and $\psi = 123 \pm 60$.

The secondary structure of a protein is very critical in determining function, but to completely understand the mechanisms controlling the function of a protein, the 3 dimensional structure has to be determined. The tertiary structure is the 3-dimensional folding of a protein, or the packing of the secondary structural elements and is perhaps the most critical part in the function of the protein. In fact, site directed mutagenesis is often used on one or two residues for various reasons and has been shown in many instances not to alter protein function, indicating the importance of the secondary and tertiary structure.

Quaternary structure or protein-protein interaction is also very crucial in some cases, where proteins exist as dimers or aggregates to perform their function. Dynamics light scattering (DLS) has been used successfully to determine the extent of aggregation.[4]

It has become quite common to determine complete secondary and tertiary structures of proteins[1] using a combination of techniques such as liquid state NMR and X-ray crystallography. There are many instances, however, when such techniques are not applicable, such as for very large proteins, for proteins that will not crystallize or for the surface immobilized proteins of focus in this work.

1.2 Biomineralization proteins

In the last few decades, a group of proteins which govern the formation of hard tissues such as bone, teeth and shells has received much attention. To overcome the inherent brittleness of the inorganic phase, organisms that are seen to utilize minerals for structural support or protection have accomplished this with the assistance of proteins. These proteins are utilized throughout the plant and animal kingdom, and interact with inorganic crystals to control crystal growth and morphology. They are known as biomineralization proteins, and the resulting materials, biominerals. Although the amount of protein in the resulting crystal structure is often significantly less than 10%, biomineralization proteins have been found experimentally to be critical in the proper formation and function of biological minerals. Proteins identified to participate in the biomineralization processes are generally found to be highly acidic, in many cases containing 50% or more aspartic acid, glutamic acid and post-translationally modified charged residues, such as phosphoserine, phosphotyrosine and carboxyglutamic acid. Due to the very unique crystal structures resulting from interactions of growing crystals with different macromolecular components, the protein-crystal interactions are thought to be very specific[5], even though the mechanisms for regulation are thought to vary widely.

Protein-crystal interactions are being probed by scientists in fields ranging from medicine to materials, in an effort to elucidate the mechanisms driving biomineralization.[6-12]

1.3 Mineral Systems

Inorganic crystals utilized by nature in biominerals include calcium phosphates, such as bone, dentin and enamel, calcium carbonates including calcite, aragonite and amorphous calcium carbonate found in marine creatures and calcium oxalates found in kidney and gall stones.[13,14] Protein crystal regulation is also observed in silica-based plants and organisms[7] as well as iron materials[13] and ice[15].

Because of the relevance to human systems, understanding calcium phosphate biomineralization is of particular interest. Hydroxyapatite (HAP) ($Ca_2(PO_4)_6(OH)_2$) is the principle calcium phosphate phase involved in biomineralization, with octacalcium phosphate having been identified in a small number of cases.[16,17] Most of the proteins involved in calcium phosphate biomineralization have been identified and isolated, making structure-function studies possible, but the small and irregular shape of the HAP crystals offers a continual challenge, making the crystal growth process less well understood than for larger, more ordered crystals. Some of the proteins controlling calcium phosphate mineralization include osteocalcin, osteonectin, bone sialoprotein and osteopontin from bone tissues[9,10,12], amelogenins and enamelins found in enamel[18] and the proline-rich acidic proteins and statherin found in salivary fluids. These proteins are typically very acidic proteins and phosphoproteins, with interaction thought to occur primarily between the carboxylate and phosphate sidechains and the surface calcium

ions.[17,19-21] Bone and dentin formation both occur in the presence of highly acidic proteins, with bone having a final biomineral phase consisting of 30% organic matrix, 10% cells and fluid and only 60% mineral by weight.[22] In contrast, enamel formation utilizes an extracellular matrix consisting largely of non-acidic proteins,[18] which are proteolytically removed during enamel formation so that the resulting matrix is 99.9% inorganic hydroxyapatite.[16]

Similarly remarkable crystal engineering properties have been documented in marine organisms, where soluble proteins have been shown to control crystal phase switching and to regulate the growth of specific crystal faces in calcium carbonates.[5,23-30] Because of the large, ordered crystals formed by calcium carbonates, they are the most thoroughly studied of all biominerals. In contrast to calcium phosphates, few of the proteins controlling biomineralization have been identified or isolated. Examples of protein controlled calcium carbonate growth include proteins found in oyster shells[31], abalone shells[30] and sea urchin exoskeletons[25]. The beautiful crystals that form have a large diversity in shape and size. A few particularly striking examples are shown in Figure 1.5[26], comparing the crystal structure of a sea urchin spine with that of a sponge and several other calcite crystals. Both of these are composed of calcite, one form of calcium carbonate, but clearly, have very different crystal sizes and shapes, demonstrating the incredible sophistication of the biomineralization process.

A final well-studied biomineralization system is that of the antifreeze proteins.[15,32-35] A great deal of effort has been put into studying these proteins that

function to prevent arctic fish from freezing in the icy waters by modifying ice crystal morphology. They are mentioned here because of their highly ordered secondary structure and the proposed correlation between highly structured proteins and biomineral formation (see Section 1.5). They are composed of a rigid amphipathic alpha-helix and are believed to block ice crystal growth by interacting specifically with the $20\bar{2}1$ face to cause hexaganol bipyramids rather than hexaganol plates to grow, ultimately preventing the growth of ice crystals.[29] This series of proteins has prompted more in depth study of designing proteins to control crystal morphology.[29]

1.4 Applications of Protein-Crystal Interaction

An in-depth understanding of the interactions of biomineralization proteins with biologically relevant minerals is desired. This knowledge would ultimately be used for very specific applications. Interest in understanding the mechanisms by which crystal regulation occurs ranges from the medical community to the semiconductor industry to the Navy. Both promoting and preventing biomineralization is sought, depending on the application. Promotion of biomineralization is desired in the case of bone implants[36], where the focus is to encourage "healing" of the implant, rather then encapsulation or rejection.[37] Often, though, the preventing of biomineralization is the main goal. Examples include biosensors, artificial organs or any other foreign object that needs to be placed in the human body. The body has remarkable defenses against objects it does not recognize. Preventing this response in select cases could reduce costly secondary operations and inaccurate equipment readings. Other areas of research focused at

prevention of biomineralization include the formation of kidney and gall stones, as well as the deposits of calcium phosphates in the salivary glands, which are due to a deficiency in a protein designed to prevent precipitation.

Less severe to human health, but still very important biomineralization processes are found throughout science and industry. The attachment of molluscs to ship hulls or the calcification of heat exchangers are major areas of concern to industry.[7] Studies in the area of geobiomineralization focus on how microbes contribute to geological formations and weathering.[38] By mimicking nature, ceramics and semiconductors are examples of materials that could be improved to develop new products with unique properties. Understanding the basic interaction mechanisms of proteins and inorganic crystals is a critical stepping stone in approaching these specific problems.

1.5 Crystal Regulation

There are a broad number of mechanisms by which biominerals are thought to form, and while they are still not well understood, based on the resulting crystals, there are clearly different formation mechanisms. For instance, in sea urchins, proteins are occluded into the calcium carbonate crystal, directly causing changes in crystal shape and morphology[25], whereas in saliva, proline rich proteins are seen to bind strictly to exposed surfaces to inhibit mineralization.[39] In enamel, the very hydrophobic protein, amelogenin, is thought to function as a spacer between crystals, to allow crystal elongation to occur before lateral fusion takes place.[18]

It has been shown that proteins can regulate both crystal size and shape[26,29,30], which is ultimately accomplished by controlling two processes: primary and/or secondary crystallization. Primary crystallization is the process of spontaneous nucleation of crystals from solution, and some proteins are designed to promote or inhibit nucleation. Secondary crystallization is the continued growth of an already present crystal. Growth inhibition is thought to occur by the protein binding to and covering the nucleation sites. Binding could occur on all faces of the crystal, preventing all crystal growth, or may only interact with one or a few of the crystal faces, preventing growth on the interaction face, and as a result promoting growth in a different direction. An additional influence on crystal growth is whether the protein binds to the crystal ridges and steps or directly on the face. The combination of these factors and potentially others results in the unique crystal structures of biominerals.

Several models have been proposed for protein and peptide interactions with biomineral surfaces, two of which are shown in Figure 1.6. Of particular importance in addressing protein-crystal interactions is the question of protein structure on and off the mineral surface, as well as the question of which side-chains interact with the crystal surface and which are exposed to the solvent environment. The lattice-matching model emphasizes specific interactions of side chains with a surface site or ion, for example the side-chain carboxylate of glutamic acid with Ca^{2+}. In this model, secondary structural motifs such as the α-helix or β-sheet, which may be present in solution or induced upon adsorption to the surface, position the interacting side-chains with a periodicity or

registry that matches ions in the crystal lattice, as is more specifically shown in Figure 1.7.[23,29] A second model, electrostatic interaction theory, considers the overall charge of the peptide and the interaction of that charge with the potential of the biomineral surface.[15,29] An amphipathic helix could be oriented in this manner with the surface. Hydrogen bonding between -OH sidechain groups such as serine or tyrosine and surface oxygens is another important interaction mechanism, although from experimental evidence,[40] it probably plays a secondary stabilizing role, rather then a primary binding role. Lastly, chelation of the calcium ions into the protein sidechains might be observed for amino acids like phosphoserine or carboxyglutamic acid, as shown in Figure 1.7.

1.6 Protein Secondary structure in Biomineralization

Ordered secondary structure has been postulated as a necessary contribution to ordered crystal growth.[10,20,29] Both β-sheet and α-helix secondary structures are observed commonly in biomineralization proteins and are thought to contribute to promote specific protein crystal interaction by one of the mechanisms mentioned above (see Figure 1.6 and 1.7). Protein secondary structure is widely believed to be a primary influence in biomineral crystal structure, however the many techniques that have been used to study protein function have met with little success in correlating this to the secondary structure of the surface bound protein. Most evidence supporting the role of protein secondary structure has been postulated from data taken of the proteins in the liquid state using circular dichroism (CD) solution characterization or theoretical secondary structure predictions.[10] A few techniques have been utilized in an attempt to

quantify secondary structure of surface adsorbed proteins. These include IR, CD, HPLC and chemical shifts in solid state NMR and will be discussed below.

1.6.1 Circular Dichroism (CD)

CD is a commonly used technique for extracting secondary structure in solution, but because of the need for a transparent surface, few studies have utilized this technique for surface bound proteins. One study by DeGrado et al[41], involved immobilizing proteins on glass slides. This study utilized model proteins designed to be amphipathic helices based on the repeat spacing of charged residues. In dilute solution they were found by CD to be random coil, but by immobilizing the peptides onto glass slides, they discovered an ordered secondary structure.

This study utilized CD well to observe the general properties of a surface bound peptide and, provided insight into the mechanism of surface induced secondary structure. Unfortunately, for most systems there are several problems with CD, perhaps the most important being that very few surfaces can be used since they are not transparent. Additionally, interpretation of CD absorption spectra can be difficult if more than one conformational species is present. This is due to the overlapping of absorption curves for different secondary structural motifs. Separation of contributions is accomplished by fitting linear combinations of "known" curves. Relatedly, CD, at best, can only determine a percentage of secondary structure, but does not determine which part of the protein experiences that secondary structure. All of these problems limit CD to the study of model systems with well-defined secondary structure.

1.6.2 Fourier Transform Infrared Spectroscopy (FT-IR)

FT-IR is well established in being sensitive to secondary structure.[42] The real advantage of using FTIR to probe biomineralization systems is that proteins bound to many types of surfaces can be studied. Additionally, both solution and solid samples can be probed, and the multitude of studies done with FT-IR shows its possibilities.[19,42-46] The limitations to FT-IR are similar to CD in that multiple conformations can overlap, making determinations of secondary structure very difficult. Specifically, the amide I band frequencies observed for α-helical structure are very difficult to separate from random coil structure, resulting in inconclusive studies.[42] As with CD, the lack of correspondence of a particular secondary structure to a specific region of the protein is limiting, leaving the final data interpretation up to predictions made from molecular modeling programs. A very thorough review of the advantages and disadvantages in using FTIR for surface adsorbed proteins is recommended.[42]

1.6.3 Reverse Phase High Pressure Liquid Chromatography (RP-HPLC)

A suprising amount of work has been done in the area of RP-HPLC to determine protein secondary structures. The premise behind using HPLC is that proteins with different secondary structures will bind with different affinities to a column, and based on that retention time, the secondary structure and range of conformations can be observed. While statements about a change in structure may be possible based on retention time, defining absolute conformations is best done in combination with FTIR or CD,[47,48] thus the same problems remain.

These techniques have provided some insight into the conformation of immobilized proteins, but as indicated there are often questions of data interpretation, especially when considering anything more complicated than model systems with well-defined structures. The initial studies of secondary structure of surface bound proteins are promising, but more quantitative information is desired, particularly on real biomineralization systems.

Questions still to be answered or issues still to be addressed include a more quantitative determination of secondary structure, particularly with emphasis on isolating the secondary structure to a particular region in the protein. Determining if secondary structure is present in solution or induced upon adsorption and which sidechains are interacting with the surface and where are also fundamental questions in need of elucidation. Dynamics of the surface bound protein would also provide insight into the function of the surface bound protein.

1.7 Solid State Nuclear Magnetic Resonance (SSNMR)

SSNMR is ideally suited for studying the secondary structure[49], orientation[50] and dynamics[49] of peptides immobilized onto surfaces. Few other techniques can provide structural and dynamic information and none of them with the high resolution found in SSNMR. SSNMR is capable of utilizing many sample conditions, including amorphous samples, hydrated samples and samples involving very small crystals. [49-55] These are conditions that often preclude other biomineralization techniques, such as AFM and secondary structure techniques such as X-ray crystallography. Recent developments

in the area of dipolar recoupling have been successful in extracting distance and angular information inaccessible to other techniques.[53,55-61]

Until very recently, secondary structure of immobilized proteins using solid state NMR has been minimal and restricted to chemical shift studies.[49] Chemical shifts are very sensitive to changes in the electronic environment and thus to changes in secondary structure.[62-66] Fernandez et al[49] incorporated the use of chemical shift measurements and relaxation measurements to determine secondary structure and dynamics of polyglutamic acid and polylysine proteins bound to both silica and hydroxyapatite surfaces. While isotropic chemical shifts have been shown to be very sensitive to changes in secondary structure[66], the high dielectric of the hydroxyapatite surface might interfere with a straightforward determination.

Dipolar recoupling techniques very quantitatively measure the distance between two nuclei, and this can be directly correlate this to secondary structure. This has been demostrated in many instances[52,53,56,67-70] and very recently was applied to a surface bound peptide.[57,58] SSNMR is also unique in its ability to provide site specific dynamic information.[49,71-73] Isotopic labeling allows extraction of relaxation parameters for individual positions in the molecule, resulting in a very detailed picture of molecular motions as a function of temperature, hydration and solution conditions. Directly correlating site-specific structure and dynamic information with known protein function can provide insight into the mechanisms of biomineralization proteins.

1.8 Salivary Statherin

The work presented in this thesis focuses on the biomineralization protein salivary statherin, found in saliva. Saliva is supersaturated with respect to calcium and phosphate salts in order to maintain and recalcify enamel.[74] Typically salts will crystallize out of supersaturated solutions, but neither primary nor secondary crystallization is observed in the mouth. This has been attributed to several macromolecules, such as the proline rich proteins, histatins, cystatins and statherin, which are thought to stabilize the supersaturated state.[39]

Statherin is a 43 residue salivary protein that is proline and tyrosine-rich (see sequence, Table 1.2)[75,76], with a PI of 4.2, representative of the large number of acidic residues of the molecule. Statherin contributes to the stabilization of the supersaturated solution conditions found in saliva by controlling both primary and secondary hydroxyapatite (HAP) crystallization.[77,78] Statherin also functions as a boundary lubricant and a bacterial binding protein.

The primary structure of statherin is very charge assymetric, highlighted by a very acidic N-terminus.[79] All but one of the charged residues occurs within the first third of the molecule, as seen in Table 1.2. The only other charged residue is a glutamic acid at position 26, amidst a large number of proline, tyrosine and glutamine residues (7 each), resulting in a very hydrophobic C-terminus. Also of interest is that there is no alanine, which is generally ubiquitous in proteins.

1.8.1 Functions

Extensive studies of statherin and statherin fragments have been performed in an effort to identify functional portions of the protein.[40,74,78] Table 1.2 shows the fragments that have been studied along with the full-length statherin sequence.

The N-terminal domain of statherin has a high affinity for calcium phosphates such as hydroxyapatite, which is typically the inorganic crystal used as a simulant for enamel.[74] The negatively charged residues at the N-terminus, including an aspartic acid, two phosphoserines, and two glutamic acids likely mediate this interaction.[79] It is assumed that binding to, and thus blocking nucleation sites prohibits secondary crystallization. Consequently, much time and effort has been focused on understanding the adsorption isotherms and kinetics of statherin binding to HAP.

Experimental adsorption isotherms show that the adsorption of statherin to hydroxyapatite can be described by a Langmuir isotherm.[80,81] Because the adsorption is not reversible, it is not accurately described in this manner,[74,80,81] however information can be extracted from adsorption isotherms much more easily when compared to a model, so authors have utilized it for this purpose. Although this is not something that directly effects this work, careful consideration of the adsorption phenomena does become important when considering thermodynamic arguments to describe binding events, since equilibrium thermodynamic equations cannot be used. Thermodynamic studies have been undertaken and interpreted using these equilibrium equations[82,83], but in light of the above statements, the interpretations need to be handled very carefully.

SN15 was found to have the highest adsorption onto HAP of all fragments and full length statherin studied by Raj et al.[74] It was found to bind approximately 4 times more than statherin, but using the Langmuir equation[80]

$$\frac{C}{Q} = \frac{1}{KN} + \frac{C}{N} \qquad [1.1]$$

where C is the equilibrium concentration, Q is the adsorption, K is the affinity coefficient and N is the number of sites), this was found to be almost completely due to the larger number of sites available to the smaller sized peptide. The middle and C-terminal fragments had 8% or less adsorption under similar conditions, indicating that the N-terminus of statherin is primarily responsible for binding the protein to HAP. The observed binding for the SC15 and SC25 had half the number of binding sites as statherin, possibly indicating a different binding mechanism. It is likely that the polar, uncharged residues in the C-terminus are interacting with the surface via hydrogen bonding, but based on the low binding affinity, this is clearly not a major interaction mechanism for this protein.

The SN15 analogs that were studied also revealed very interesting results. SN_A15, which replaced the phosphoserines in SN15 with aspartic acids, had almost the same adsorption. However, SN_S15, which was made with serines instead of phosphoserines, saw significant reductions in binding. These two results suggest that the charged groups at positions 2 and 3 are critical to binding, but that phosphoserine itself is not required. Based on this, chelation is probably not a key mechanism for the phosphoserine binding motif, but is more consistent with an electrostatic mechanism.

Constant composition kinetics (CCK) revealed that statherin is a potent inhibitor of calcium phosphate mineralization[74]. Consistent with the idea that higher adsorption means higher crystal growth inhibition, Raj et al found that SN15 has the highest growth inhibition properties. It was nearly identical to the inhibition properties exhibited by statherin, providing support that the N-terminus is responsible for secondary nucleation inhibition, while the C-terminus has other functional properties. Generally true of all of the fragments, lower binding parameters were equated with less crystal growth inhibition. Statherin, SN15, SN_A15 and SN_S15 exhibited similar inhibition, SN11, SC15 and SC25 were grouped together, exhibiting lower inhibition than the statherin group and SM15 had almost no inhibition. The one inconsistency was SN_S15, in that it too inhibited crystal growth almost as well as SN15, even though binding was more on the order of the SN11 group. The authors do not propose a theory for this observation. It is possible that SN_S15 is binding to different sites than that for SN15, thus growth inhibition is occurring by a different mechanism, but without further experimental evidence, many proposed mechanisms could be valid.

While the C-terminus did not play a significant role in inhibiting secondary crystallization, it was found to be critical in preventing primary precipitation. Studies by Schwartz[78] revealed that the removal of only 10 C-terminal residues ($Peptide_{(1-32/37)}$) reduced the primary inhibition by 75%. Shorter fragments ($Peptide_{(1-9)}$ and $Peptide_{(1-6)}$) showed approximately the same inhibition as ($Peptide_{(1-32/37)}$), isolating the primary crystallization function to the highly glutamine and proline rich C-terminus. Interestingly, the N-terminus does contribute to the inhibition of primary crystallization,

inhibiting nucleation about 25% as well as statherin. Although the exact mechanism has yet to be determined, soluble statherin could remove calcium ions by chelating them with the phosphoserine groups (even though this doesn't appear to be a binding mechanism, it could contribute in the solution phase). Two ^{31}P-solution NMR studies agree with this result, indicating a strong interaction between the phosphoserine groups and calcium ions.[84,85] This is potentially a contribution of the N-terminus in preventing primary precipitation, but the real active site is the C-terminus.

The function of statherin as a boundary lubricant prevents wear of the enamel during mastication. This is thought to occur by the formation of statherin into an oriented film on the surface of HAP, as inferred by comparison to SDS and Gramicidin S with lubricity experiments.[40] The authors postulated that the N-terminus is affixed very strongly to HAP so it is not easily removed during the normal grinding processes of teeth. They proposed that the hydrophobic C-terminus provides lubrication by stabilizing an oriented film through hydrogen bonding interactions, forming an extended structure on the surface of HAP. Interestingly, studies have shown that none of the fragments (SN15, SM15 and SC25) exhibit lubricity behavior and that the full molecule is necessary for boundary lubrication.[40]

Statherin also serves as a bacterial binding site for many bacteria, including *P. Gingivalis*[86] and *A. viscosus*[87]. These are found to bind to statherin, only when statherin is immobilized onto HAP, and not to solubilized statherin, suggesting that there is a conformational change that reveals a hidden binding site when statherin adsorbs to HAP.

A secondary structure change upon binding was also proposed as a mechanism allowing statherin to act as a boundary lubricant (see above), but is unsubstantiated with direct experimental evidence.

1.8.2 Secondary and Tertiary Structure

The secondary structure of statherin has been found to "deviate significantly from random coil structure" and to be remarkably stable across a range of pH's from 1.9-9.4 as well as in a variety of denaturing solvents as determined by liquid state NMR.[85] Circular dichroism (CD) and secondary structure prediction have also been used to determine the secondary structure of statherin and its fragments in solution.[40,74,84,88] In solution under physiological conditions, CD characterization indicates that the N-terminus contains 16-18% α-helical structure[40,84,88]. Secondary structure prediction supports this finding in that residues 5-15 are predicted to form an amphipathic helix, and the N-terminal fragment, SN15 is also found to be helical via CD.[74] The middle portion (residues 15-38) is found to consist of a long poly-proline helix as determined by CD and secondary structure prediction, with the possibility of a turn or two in this region. The C-terminal 5 residues are postulated to form a 3_{10}-helix.[84]

There has been much less success experimentally determining the tertiary structure of statherin, but several hypotheses have been put forth. Specifically, a turn is predicted at residues Gly-17 and Tyr-18, where an unusual *S. aureous* protease cleavage site was seen to occur.[79] A turn at these residues would be consistent with findings by Elgavish, et al,[85] suggesting that Ile-11 and Val-24 are interacting with aromatic

residues. These residues would only be in the proximity of each other if a fold was present in the protein. They also observed that the three phenylalanine residues are well resolved from each other, indicating unique environments. Ramasubbu et al[87] combined this finding with their molecular modeling predictions to place Phe-7 nearby in space to a proline and oriented such that Phe-14 was interacting with Tyr-18.

There has also been speculation that statherin exists primarily as a dimer in solution, although there is some inconsistency within the literature as to which part of the molecule would dimerize. Some feel it would be the highly charged N-terminal regions that would interlock[85], while others have predicted that the C-terminus would stabilize a dimer through hydrogen bonding interactions[87].

1.8.3 Structure and Function

Correlating structure and function to particular regions of a protein can be challenging, even for a small protein such as statherin. Raj et al have attempted this by studying the series of fragments shown in the upper section of Table 1.2.[74] N-terminal fragments were found to inhibit HAP crystal growth at least as strongly as the parent protein. As noted above, CD and secondary structure predictions have found this region to be largely helical also. The α-helix has been proposed to play a role in the recognition of HAP by statherin[88], as has been similarly proposed for protein/crystal interactions in other biological settings[15,29,89] (see Figure 1.6 and 1.7). The spacing between the phosphoserine sidechains is between 4.2 Å and 6.4Å[74], which correlates well with the distance of 5.4 Å between Ca^{2+} ions in the 001 face of the hydroxyapatite crystal lattice[89]

suggesting that lattice matching between the helix and calcium ions may be the mode for interaction. Replacement of the phosphoserines by aspartic acids had nearly identical binding affinities and growth inhibition, however, which might suggest that an electrostatic mechanism is responsible for the binding of HAP. The correlation between structure and function for this segment was the basis for focusing initially at the N-terminal 15-residue peptide and then progressing to studies of the same segment in the complete protein.

1.9 The Importance of Statherin

The importance of determining the structure of a surface adsorbed salivary protein may not be obvious, when there are so many other proteins that perform critical regulatory and life-dependent functions. There are many advantages to studying statherin. Statherin has been extensively studied in solution in terms of biological function and to some extent, secondary structure. In addition to determining the biological function of statherin, these studies have shown that is has very high binding coefficients, which yield high NMR sensitivity at monolayer coverages. Because of its small size, it can be synthesized using an automated peptide synthesizer, rather than recombinantly, which allows very large yields as well as being completely flexible in isotopic label incorporation.

While statherin is interesting as a biomineralization protein in its own right, it also serves as a model protein for the other calcium phosphate biomineralization proteins. Statherin is an acidic phosphoprotein, which is typical of most calcium phosphate biomineralization proteins. It is in a more simple biological setting than other calcium

phosphate proteins, so *in vitro* experiments more closely model *in vivo* processes yielding more straightforward results. From a biomineralization standpoint, statherin is very interesting in that there are residues present which could potentially involve each one of the binding motifs discussed in Section 1.4. There is an alpha helix for lattice matching, phosphoserines for chelation, a highly charged portion for electrostatic interactions and a long chain of polar, uncharged residues that could hydrogen bond.

Lastly, hydroxyapatite is a calcium phosphate ($Ca_{10}(PO_4)_6(OH)_2$), and thus has no NMR background for the carbon based experiments done here. HAP also typically consists of very small crystals with very high surface areas (from 20 m^2/g up to 200 m2/g), resulting in a larger amount of protein adsorbed per monolayer, as compared to lower surface area minerals. Additionally, ^{31}P is an NMR active nuclei and can be utilized with recoupling techniques to orient the protein with the crystal surface. Fluoroapatite, which is commonly found in enamel, has ^{19}F within its matrix that can also be used for NMR experiments. All of these factors make statherin an ideal protein with which to begin correlating secondary structure to function.

1.10 Goal of Dissertation

The focus of this research has been to determine the secondary structure and dynamics of surface immobilized proteins, with specific focus on the protein salivary statherin. Dipolar recoupling techniques (DRAWS and REDOR) were used to quantitatively measure the secondary structure of surface bound salivary statherin. Double isotopically labeled carbonyl carbons were incorporated into identical sites in the backbone of both SN15 and the N-terminus of full statherin for DRAWS analysis and

single labeled ^{13}C, ^{15}N samples for REDOR. An investigation of peptide dynamics at these positions was conducted on hydrated samples to provide further information on the SN15-HAP and statherin-HAP recognition mechanisms. Solid state NMR was used to extract site specific mobility by determining chemical shift anisotropy (CSA) tensor values[90], which are very sensitive to molecular dynamics and electronic structure[72]. $T_{1\rho}$ relaxation measurements were also made to elucidate the dynamic modes occurring in the surface bound N15 peptide.

Chapter 2 will introduce the fundamental interactions in solid state NMR. Dipolar recoupling and relaxation techniques will then be discussed in detail. Experimental methods will be presented in Chapter 3, discussing in detail both sample preparation and NMR experiments and simulations. Chapters 4-7 will present experimental results. Results and discussion of the structural and dynamic findings of the N-terminal peptide, SN15, will be presented in Chapters 4 and 5. Chapters 6 and 7 will discuss the structure and dynamics, respectively, of the N-terminus of the full protein, statherin.

1.11 Notes to Chapter 1

1. Creighton, T. E. *Proteins, Structures and Molecular Properties,* (W.H. Freeman and Company, New York, 1993).

2. Pauling, L. & al, e. The Structure of Proteins: Two Hydrogen-bonded Helical Configurations of the Polypeptide Chain. *Proceedings of the National Acadamy of Science USA* **37**, 205-211 (1951).

3. Smith, L. J. *et al.* Analysis of Main Chain Torsion Angles in Proteins: Prediction of NMR Coupling Constants for Native and Random Coil Conformations. *Journal of Molecular Biology* **255**, 494-506 (1996).

4. Moradian-Oldak, J., Leung, W. & Fincham, A. G. Temperature and pH-Dependent Supramolecular Self-Assembly of Amelogenin Molecules: A Dynamic Light-Scattering Analysis. *Journal of Structural Biology* **122**, 320-327 (1998).

5. Aizenberg, J., Hanson, J., Koetzle, T. F., Weiner, S. & Addadi, L. Control of Macromolecule Distribution within Synthetic and Biogenic Single Calcite Crystals. *Journal Of The American Chemical Society* **119**, 881-886 (1997).

6. Kestell, M. F. & et al. A Calcium-binding Protein in Bile and Gallstones. *Hepatology* **16**, 1315-1321 (1992).

7. Stupp, S. I. & Braun, P. V. Molecular Manipulation of Microstructures: Biomaterials, Ceramics, and Semiconductors. *Science* **277**, 1242-1248 (1997).

8. George, A., Sabsay, B., Simonian, P. A. & Veis, A. Charcterization of a Novel Dentin Matrix Acidic Phosphoprotein--Implications for Induction of Biomineralization. *Journal Of Biological Chemistry* **268**, 12624-12630 (1993).

9. Goldberg, H. A., Warner, K. J., Stillman, M. J. & Hunter, G. K. Determination of the Hydroxypatite Nucleating Region of Bone Sialoprotein. *Connective Tissue Research* **35**, 439-446 (1996).

10. Hunter, G. K. & Goldberg, H. A. Modulation of Crystal Formation by Bone Phosphoproteins: Role of Glutamic Acid-Rich Seuqences in the Nucleation of Hydroxyapatite by Bone Sialoprotein. *Biochemical Journal* **302**, 175-9 (1994).

11. Hunter, G. K., Hauschka, P. V., Poole, A. R., Rosenberg, L. C. & Goldberg, H. A. Nucleation and Inhibition of Hydroxyapatite Formation by Mineralized Tissue Proteins. *Biochemical Journal* **317**, 59-64 (1996).

12. Fujisawa, R., Wada, Y., Nodasaka, Y. & Kuboki, Y. Acidic Amino Acid-Rich Sequences as Binding Sites of Osteonectin to Hydroxyapatite Crystals. *Biochimica Et Biophysica Acta* **1292**, 53-60 (1996).

13. Weiner, S. & Addadi, L. Design Strategies in Mineralized Biological Materials. *Journal of Materials Chemistry* **7**, 689-702 (1997).

14. Lowenstam, H. A. & Weiner, S. *On Biomineralization* (Oxford University Press, New York, 1989).

15. Sicheri, f. & Yang, D. S. C. Ice-binding Structure and Mechanism of an Antifreeze Protein from Winter Flounder. *Nature* **375**, 427-431 (1995).

16. Diekwisch, T. G. H., Berman, B. J., Gentner, S. & Slavkin, H. C. Initial Enamel Crystals are not Spatially Associated with Mineralized Dentine. *Cell and Tissue Research* **279**, 149-167 (1995).

17. Hunter, G. K. Interfacial Aspects of Biomineralization. *Current Opinion in Solid State and Materials Science* **1**, 430-435 (1996).

18. Fincham, A. G., Moradian-Oldak, J. & Simmer, J. P. The Structural Biology of the Developing Dental Enamel Matrix. *Journal of Strucutral Biology* **136**, 270-299 (1999).

19. Garcia-Ramos, J. V., Carmona, P. & Hidalgo, A. The Adsorption of Acidic Amino Acids and Homopolypeptides on Hydroxyapatite. *Journal of Colloid and Interface Science* **83**, 479-484 (1981).

20. Addadi, L. & Weiner, S. Interactions Between Acidic Proteins and Crystals: Sterochemical Requirements in Biomineralization. *Proceedings of the National Academy of Science* **82**, 4110-4114 (1985).

21. Gorski, J. P. Acidic Phophoproteins from Bone Matrix: A Structural Rationalization of Their Role in Biomineralization. *Calcified Tissue International* **50**, 391-396 (1992).

22. Hauska, P. V. & Frank H. Wians, J. Osteocalcin-Hydroxyapatite Interaction in the Extracellular Organic Matrix of Bone. *The Anatomical Record* **224**, 180-188 (1989).

23. Johnsson, M., Levine, M. J. & Nancollas, G. H. Hydroxyapatite Binding Domains in Salivary Proteins. *Critical Reviews In Oral Biology and Medicine* **4**, 371-8 (1993).

24. Belcher, A. M. *et al.* Control of Crystal Phase Switching and Orientation by Soluble Mollusc-Shell Proteins. *Nature* **381**, 56-58 (1996).

25. Berman, A., Addadi, L. & Weiner, S. Interactions of Sea-Urchin Skeleton Macromolecules with Growing Calcite Crystals--a Study of Intracrystalline Proteins. *Nature* **331**, 546-548 (1988).

26. Berman, A. *et al.* Biological Control of Crystal Texture: A Widespread Strategy for Adapting Crystal Properties to Function. *Science* **259**, 776-779 (1993).

27. Falini, G., Albeck, S., Weiner, S. & Addadi, L. Control of Aragonite or Calcite Polymorphism by Mollusk Shell Macromolecules. *Science* **271**, 67-69 (1996).

28. Hanein, D., Geiger, B. & Addadi, L. Differential Adhesion of Cells to Enantiomorphous Crystal Surfaces. *Science* **263**, 1413-6 (1994).

29. DeOliviera, D. B., Laursen, R. A. & . Control of Calcite Crystal Morphology by a Peptide Designed to Bind to a Specific Surface. *Journal of the American Chemical Society* **119**, 10627- 10631 (1997).

30. Walters, D. A. *et al.* Modification of Calcite Crystal Growth by Abalone Shell Proteins: An Atomic Force Microscope Study. *Biophysical Journal* **72**, 1425-1433 (1997).

31. Wierzbicki, A., Sikes, C. S., Madura, J. D. & Drake, B. Atomic Force Microscopy and Molecular Modeling of Proetin and peptide Binding to Calcite. *Calcified Tissue International* **54**, 133-141 (1994).

32. Wen, D. & Laursen, R. A. Structure-Function Relationships in an Antifreeze Polypeptide. *The Journal of Biological Chemistry* **267**, 14102-14108 (1992).

33. Knight, C. A., Cheng, C. C. & DeVries, A. L. Adsorption of α-Helical Antifreeze Peptides on Specific Ice Crystal Surface Planes. *Biophysical Journal* **59**, 409-418 (1991).

34. Chakrabartty, A., Yang, D. S. C. & Hew, C. L. Structure-Function Relationship in a Winter Flounder Antifreeze Polypeptide II. *The Journal of Biological Chemistry* **264**, 11313-11316 (1989).

35. Chakrabartty, A., Yang, D. S. C. & Hew, C. L. Structure-Function Relationship in a Winter Flounder Antifreeze Polypeptide I. *The Journal of Biological Chemistry* **264**, 11307-11312 (1989).

36. Davies, J. E. In Vitro Modeling of the Bone/Implant Interface. *The Anatomical Record* **245**, 426-445 (1996).

37. Ratner, B. D., Horbett, T. A., Shuttleworth, D. & Thomas, H. R. Analysis of the Organization of Protein Films on solid Surfaces by ESCA. *Journal Of Colloid and Interface Science* **83** (1981).

38. Barker, W. W., Welch, S. A. & Banfield, J. F. Experimental Observations on the Effects of Microorganisms on Silicate Weathering. *American Mineralogist* **83**, 1551-1563 (1998).

39. Lamkin, M. S. & Oppenheim, F. G. Structural Features of Salivary Function. *Critical Reviews in Oral Biology and Medicine* **4**, 251-259 (1993).

40. Douglas, W. H. & et al. Statherin: A Major Boundary Lubricant of Human Saliva. *Biochemical and Biophysical Research Communications* **180**, 91-97 (1991).

41. DeGrado, W. F. & Lear, J. D. Induction of Peptide Conformation at Apolar/Water Interfaces. 1. A study with Model Peptides of Defined Hydrophobic Periodicity. *Journal of the American Chemical Society* **107**, 7684-7689 (1985).

42. Chittur, K. K. FTIR/ATR for protein Adsorption to Biomaterial Surfaces. *Biomaterials* **19**, 357-369 (1998).

43. Strong, A. E. & Moore, B. D. Self-assembling Chiral Monolayers of Helical Peptides Bound to Gold via Side-chain Thioethers. *Chemical Communications*, 473-474 (1998).

44. Kim, H. S., Hartgerink, J. D. & Ghadiri, M. R. Oriented Self-Assembly of Cyclic Peptide Nanotubes in Lipid Membranes. *Journal of the American Chemical Society* **120**, 4417-4424 (1998).

45. Boncheva, M. & Vogel, H. Formation of Stable Polypeptide Monolayers at Interfaces: Controlling Molecular Conformation and Orientation. *Biophysical Journal* **73**, 1056-1072 (1997).

46. Narita, M., Tomotake, Y., Isokawa, S., Matsuzawa, T. & Miyauchi, T. Syntheses and Properties of Resin-Bound Oligopeptides. 2. Infrared Spectroscopic Conformational Analysis of Cross-Linked Polystrene Resin Bound Oligoleucines in the Swollen State. *Macromolecules* **17**, 1903-1906 (1984).

47. Steer, D. L., Thompson, P. E., Blondelle, S. E., Houghten, R. A. & Aguilar, M.-I. Comparison of the Binding of α-helical and β-sheet Peptides to a Hydrophobic Surface. *Journal of Peptide Research* **51**, 401-412 (1998).

48. Lee, T.-H., Thompson, P. E., Hearn, M. T. W. & Aguilar, M.-I. Conformational Stability of a Type II' β-turn Motif in Human Growth Hormone [6-13] Peptide Analogues at Hydrophobic Surfaces. *Journal Peptide Research* **49** (1997).

49. Fernandez, V. L., Reimer, J. A. & Denn, M. M. Magnetic Resonance Studies of Polypeptides Adsorbed on Silica and Hydroxyapatite Surfaces. *Journal of the American Chemical Society* **114**, 9634-9642 (1992).

50. Simmons, A. H., Michal, C. A. & Jelinski, L. W. Molecular Orientation and Two-Component Nature of the Crystalline Fraction of Spider Dragline Silk. *Science* **271** (1996).

51. Asakura, T. & et al. . NMR Study of Silk I Structure of *Bombyx mori* Silk Fibroin with ^{15}N-and ^{13}C-NMR Chemical Shift Contour Plots. *Biopolymers* **41**, 193-203 (1997).

52. Heller, J. *et al.* Solid-State NMR Studies of the Prion Protein H1 Fragment. *Protein Science* **5**, 1655-1661 (1996).

53. Klug, C. A., Burzio, L. A., Waite, J. H. & Schaefer, J. *In Situ* Analysis of Peptidyl DOPA in Mussel Byssus Using Rotational-Echo Double-Resonance NMR. *Archives Of Biochemistry And Biophysics* **333**, 221-224 (1996).

54. Lansbury, P. T. & et al. Structural Model for the β-Amyloid Fibril Based on Interstrand Alignment of an Antiparallel-Sheet Comprising a C-terminal Peptide. *Nature Structural Biology* **2**, 990-998 (1995).

55. Merritt, M. E., Christensen, A. M., Kramer, K. J., Hopkins, T. L. & Schaefer, J. Detection of Intercatechol Cross-Links in Insect Cuticle by Solid-State Carbon-13 and Nitrogen-15 NMR. *Journal Of the American Chemical Society* **118**, 11278-11282 (1996).

56. Gregory, D. M. *et al.* Dipolar Recoupling NMR of Biomolecular Self-Assemblies: Determining Inter- and Intrastrand Distances in Fibrilized Alzheimer's β-Amyloid Peptide. *Solid State Magnetic Resonance* **13**, 149-166 (1998).

57. Long, J. R. *et al.* A Peptide That Inhibits Hydroxyapatite Growth is in an Extended Conformation on the Crystal Surface. *Proceedings of the National Academy of Science* **95**, 12083-12087 (1998).

58. Shaw, W. J. *et al.* Determination of Statherin N-Terminal Peptide Conformation on Hydroxyapatite Crystals. *Journal of the American Chemical Society* **122**, 1709-1716 (2000).

59. Mehta, M. A. *et al.* Distance Measurements in Nucleic Acids Using Windowless Dipolar Recoupling Solid State NMR. *Solid State Nuclear Magnetic Resonance* **7**, 211-228 (1996).

60. Gregory, D. M., Mehta, M. A., Shiels, J. C. & Drobny, G. P. Determination of Local Structure in Solid Nucleic Acids Using Double Quantum Nuclear Magnetic Resonance Spectroscopy. *Journal of Chemical Physics* **107**, 28 (1997).

61. Gregory, D. M. *et al.* Windowless Dipolar Recoupling: The Detection of Weak Dipolar Couplings Between Spin 1/2 Nuclei With Large Chemical Shift Anisotropies. *Chemical Physics Letters* **246**, 654-663 (1995).

62. Asakawa, N. *et al.* Hydrogen-Bonding Effect on ^{13}C NMR Chemical Shifts of L-alanine Residue Carbonyl Carbons of Peptides in the Solid State. *Journal of the American Chemical Society* **114**, 3261 (1992).

63. Asakawa, N., Kurosu, H. & Ando, I. Structural Study of Peptides Containing L-alanine Residues by *ab initio* Chemical Shielding Calculation. *Journal of Molecular Structure* **323**, 279 (1994).

64. Wishart, D. S. & Sykes, B. D. The ^{13}C Chemical-Shift Index: A Simple Method for the Identification of Protein Secondary Structure Using ^{13}C Chemical-Shift Data. *Journal of Biomolecular NMR* **4**, 171 (1994).

65. Fuijisawa, R. & Kuboki, Y. Conformation of Dentin Phophophoryn Adsorbed on Hydroxyapatite Crystals. *European Journal or Oral Sciences* **106**, 249-253 (1998).

66. Spera & Bax, A. Emperical Correlation Between Protein Backbone Conformation and C_α and C_β ^{13}C Nuclear Magnetic Resonance Chemical Shifts. *Journal of the American Chemical Society* **113**, 5490 (1991).

67. Bennett, A. E., Weliky, D. P. & Tycko, R. Quantitative Conformational Measurements in Solid State NMR by Constant-Time Homonuclear Dipolar Recoupling. *Journal of the American Chemical Society* **120**, 4897-4898 (1998).

68. Jarvie, T. P. & Went, G. T. Simultaneous Multiple Distance Measurements in Peptides via Solid-State NMR. *Journal of the American Chemical Society* **118**, 5330-5331 (1996).

69. Peersen, O. B., Groesbeek, M., Aimoto, S. & Smith, S. O. Analysis of Rotational Resonance Magnetization Exchange Curves from Crystalline Peptides. *Journal of the American Chemical Society* **117**, 7228-7237 (1995).

70. Bower, P. V. *et al.* Determination of Torsion Angles in Proteins and Peptides Using Solid State NMR, Journal of the American Chemical Society. *Journal of the American Chemical Society* **121**, 8373-8375 (1999).

71. Geheagin, K., Meints, G. A., Hatcher, M. E. & Drobny, G. P. The Dynamic Impact of CpG Methylation in DNA. *Biochemistry* (2000).

72. Ruocco, J. J., Siminovitch, D. J., Long, J. R., Das Gupta, S. K. & Griffen, R. G. ^{2}H and ^{13}C Nuclear Magnetic Resonance Study of N-Palmitoylgalactosylsphingosine (Cerebroside)/Cholesterol Bilayers. *Biophysical Journal* **71**, 1776-1788 (1996).

73. Long, J. R., Sun, B. Q., Bowen, A. & Griffin, R. Molecular Dynamics and Magic Angle Spinning NMR. *Journal of the American Chemical Society* **116**, 11950-11956 (1994).

74. Raj, P. A., Johnsson, M., Levine, M. J. & Nancollas, G. H. Dependence on Sequence, Charge, Hydrogen Bonding Potency, and Helical Conformation for Adsorption to Hydroxyapatite and Inhibition of Mineralization. *Journal Biological Chemistry* **267**, 5968-5976 (1992).

75. Moreno, E. C., Varughese, K. & Hay, D. I. Effect of Human Salivary Proteins on the Precipitation Kinetics of Calcium Phosphate. *Calcified Tissue International* **28**, 7-16 (1979).

76. Hay, D. I., Smith, D. J., Schluckebier, S. K. & Moreno, E. C. Relationship Between Concentration of Human Salivary Statherin and Inhibition of Calcium Phosphate Precipitation in Stimulated Human Parotid Saliva. *Journal of Dental Research* **63**, 857-863 (1984).

77. Wikiel, K., Burke, E. M., Perich, J. W., Reynolds, E. C. & Nancollas, G. H. Hydroxyapaptite Mineralization and Demineralization in the Presence of Synthetic Phosphorylated Pentapeptides. *Archives Of Oral Biology* **39**, 715-21 (1994).

78. Schwartz, S. S., Hay, D. I. & Schluckebier, S. K. Inhibition of Calcium Phosphate Precipitation by Human Salivary Statherin: Structure-Activiy Relationships. *Calcified Tissue International* **50**, 511-517 (1992).

79. Schlesinger, D. H. & Hay, D. I. Complete Covalent Structure of Statherin, a Tyrosine-rich Acidic Peptide Which Inhibits Calcium Phosphate Precipitation from Human Parotid Saliva. *Journal of Biological Chemistry* **252**, 1689-1695 (1977).

80. Kresak, M., Moreno, E. C., Zahradnik, R. T. & Hay, D. I. Adsorption of Amino Acids onto Hydroxyapatite. *Journal of Colloid and Interface Science* **59**, 283-292 (1977).

81. Moreno, E. C., Kresak, M. & Hay, D. I. Adsorption of Two Human Parotid Salivary Macromolecules on Hydroxy-,Fluorhydroxy- and Fluorapatites. *Archives of Oral Biology* **23**, 525-533 (1978).

82. Moreno, E. C., Kresak, M. & Hay, D. I. Adsorption Thermodynamics of Acidic Proline-Rich Human Salivary Proteins onto Calcium Apatites. *The Journal of Biological Chemistry* **257**, 2981-2989 (1982).

83. Moreno, E. C., Kresak, M. & Hay, D. I. Adsorption of Molecules of Biological Interest onto Hydroxyapatite. *Calcified Tissue International* **36**, 48-59 (1984).

84. Naganagowda, G. A., Gururaja, T. L. & Levine, M. J. Delineation of Conformational Preferences in Human Salivary Statherin by ^{1}H- ^{31}P- NMR and CD Studies: Sequential Assignment and Structure-Function Correlations. *Biomolecular Structure & Dynamics* **16**, 91-107 (1998).

85. Elgavish, G. A., Hay, D. I. & Schlesinger, D. H. ^{1}H and ^{31}P Nuclear Magnetic Resonance Studies of Human Salivary Statherin. *International Journal of Peptide and Protein Research* **23**, 230-234 (1984).

86. Amano, A., Kataoka, K., Raj, P. A., Genco, R. J. & Shizukuishi, S. Binding Sites of Salivary Statherin for *porphyromonas gingivalis* Recombinant Fimbrillan. *Infection and Immunity* **64**, 4249-4254 (1996).

87. Ramasubbu, N., Thomas, L. M., Bhandary, K. K. & Levine, M. J. Structural Characteristics of Human Salivary Statherin: A Model for Boundary Lubrication at the Enamel Surface. *Critical Reviews in Oral Biology and Medicine* **4**, 363-370 (1993).

88. Gururaja, T. L. & Levine, M. J. Solid-Phase Synthesis and Characterization of Human Salivary Statherin: A Tyrosine-Rich Phosphoprotein Inhibitor of Calcium Phosphate Precipitation. *Peptide Research* **9**, 283-289 (1996).

89. Hauschka, P. V. & Carr, S. A. Calcium-Dependent α-Helical Structure in Osteocalcin. *Biochemistry* **21**, 2538-2547 (1982).

90. Herzfeld, J. & Berger, A. E. Sideband Intesities in NMR Spectra of Samples Spinning at the Magic Angle. *Journal of Physical Chemistry* **73**, 6021-6030 (1980).

Table 1.1 The 20 naturally occurring amino acids arranged according to their charge classification. Phosphoserine is post translationally modified but is included as it is very important to this work.

Charge Classification	Amino acid	Sidechain
Acidic	Glutamic Acid	$-CH_2CH_2COOH$
	Aspartic Acid	$-CH_2COOH$
	Phosphoserine	$-CH_2OPO_3$
Basic	Arginine	$-CH_2CH_2CH_2NHC(NH_2)_2$
	Lysine	$-CH_2CH_2CH_2CH_2NH_3$
	Histidine	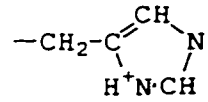
Polar, uncharged	Serine	$-CH_2OH$
	Tyrosine	$-CH_2(C_6H_5OH)$
	Threonine	$-CH(OH)CH_3$
	Cysteine	$-CH_2SH$
	Glycine	$-H$
	Glutamine	$-CH_2CH_2CONH_2$
	Asparagine	$-CH_2CONH_2$
Hydrophobic	Alanine	$-CH_3$
	Valine	$-CH(CH_3)_2$
	Leucine	$-CH_2CH(CH_3)_2$
	Isoleucine	$-CH(CH_3)CH_2CH_3$
	Proline	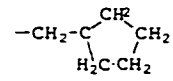
	Methionine	$-CH_2CH_2SCH_3$
	Phenylalanine	$-CH_2(C_6H_5)$
	Tryptophan	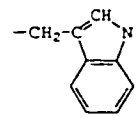

Table 1.2 The primary sequence of full statherin is shown on the top row. The other sequences are statherin peptide fragments that have been studied in some detail in the literature. The sequences in the top portion were studied by Raj, et al[74], and the sequences on the bottom, by Schwartz[78].

	5 10 15 20 25 30 35 40
Statherin	DpSpSEEKFLRRIGRFGYGYGPYQPVPEQPLYPQPYQPQYQQYTF
SN15(1-15)	DpSpSEEKFLRRIGRFG
SN_S15 (1-15, no pS)	D S SEEKFLRRIGRFG
SN_A15 (1-15, pS replaced with D)	D D DEEKFLRRIGRFG
SN11 (5-15)	EKFLRRIGRFG
SM15 (15-29)	GYGYGPYQPVPEQPL
SC15 (29-43)	LYPQPYQPQYQQYTF
SC25 (19-43)	GPYQPVPEQPLYPQPYQPQYQQYTF

$Peptide_{(1-6)}$	DpSpSEEK
$Peptide_{(1-9)}$	DpSpSEEKFLR
$Peptide_{(1-32/37)}$	DpSpSEEKFLRRIGRFGYGYGPYQPVPEQPLYPQPYQPQ

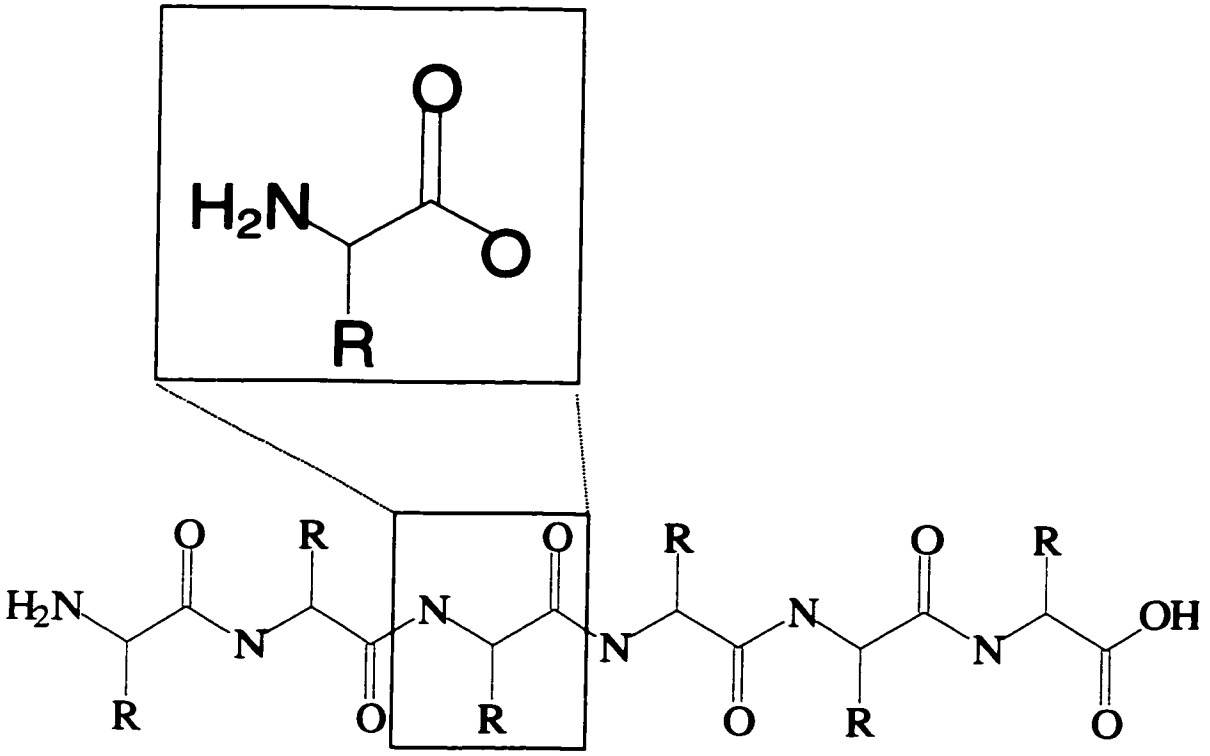

Figure 1.1 The basic protein primary structure is shown. A single amino acid residue is shown in the inset before incorporation into the polymer-like chain. See Table 1.1 for R definitions.

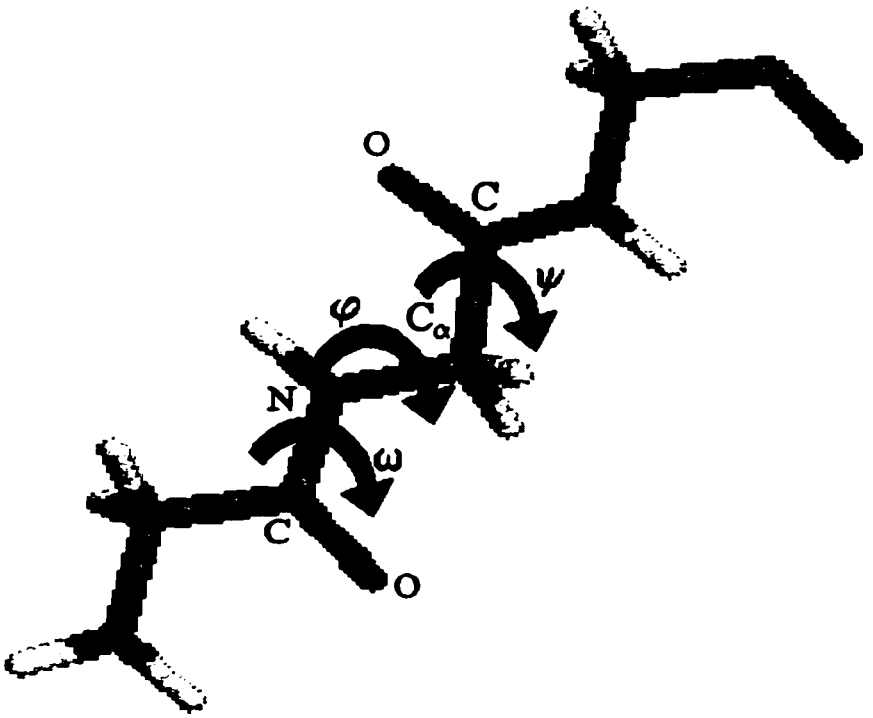

Figure 1.2 The torsion angles of a peptide fragment are shown for definition. In most cases, ω is restricted to 180° due to the delocalized electron density of the O=C-N bond, leaving φ and ψ as the only variables in determining the secondary structure of the protein.

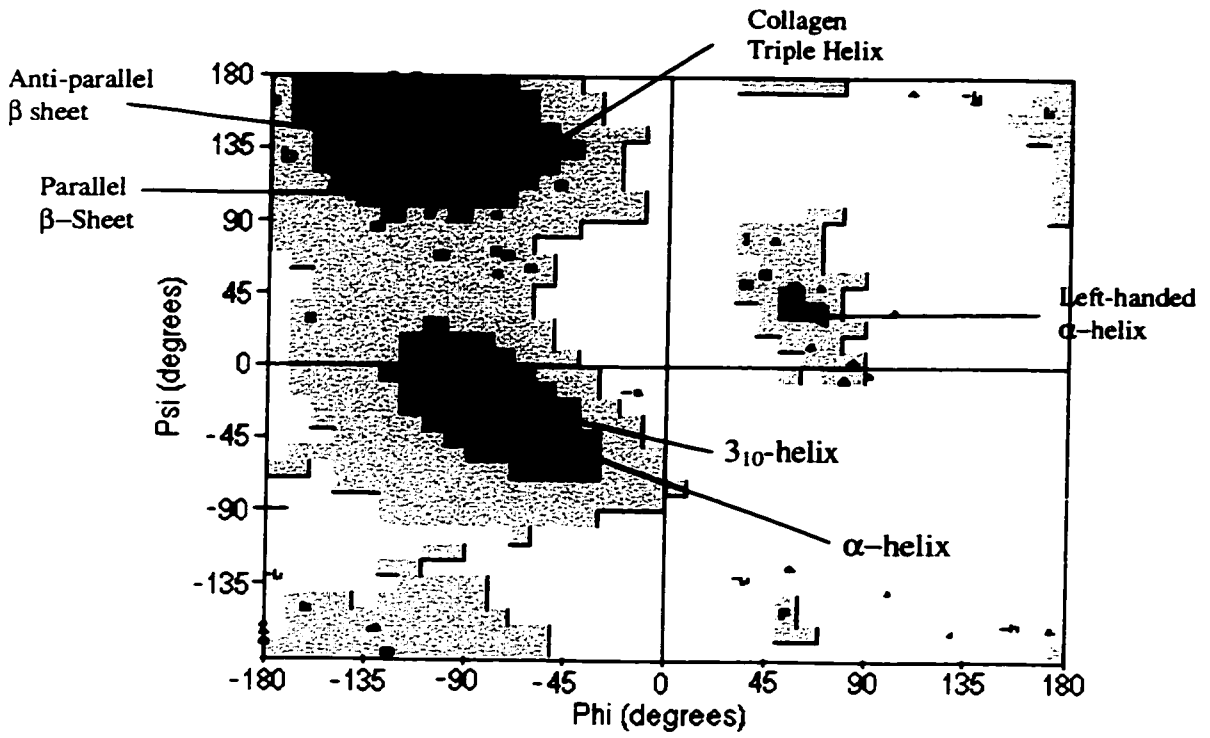

Figure 1.3 The Ramachandran plot maps φ and ψ combinations, illustrating the energetically favored conformations for peptide bonds. The dark gray areas are the most energetically favored, the light gray, less so and the white areas are energetically not allowed. The black markers represent experimentally determined φ and ψ angles, clustered in the dark gray regions. The special secondary structures (α-helix, β-sheet (parallel and anti-parallel), and the collagen triple helix) have also been indicated, according to their classically defined values.

A)

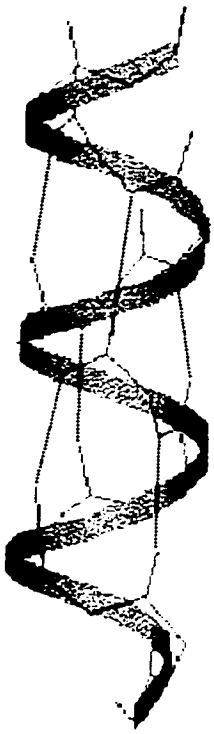

B)

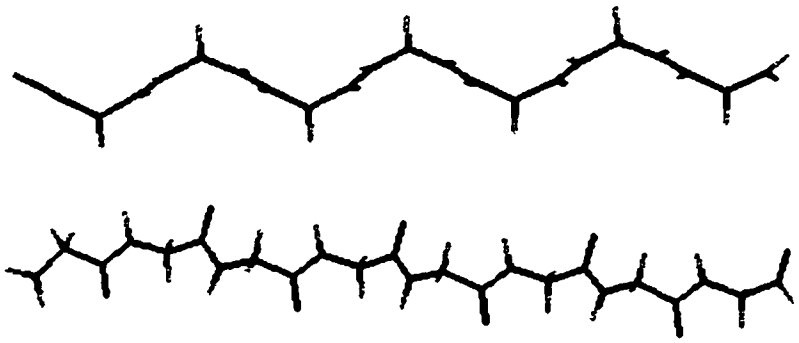

Figure 1.4. Two common secondary structures are shown. A) α-helix. Note the hydrogen bonding between the carbonyl oxygen and the NH hydrogen four residues removed, and the unidirectional orientation of the carbonyl groups (shown in red) with respect to the helix axis. B) β-sheet. The top portion shows the pleats that are formed in the β-sheet. The bottom portrayal shows the carbonyl orientation oscillating up and down, perpendicular to the peptide plane, indicating how hydrogen bonding might best be taken advantage of intermolecularly.

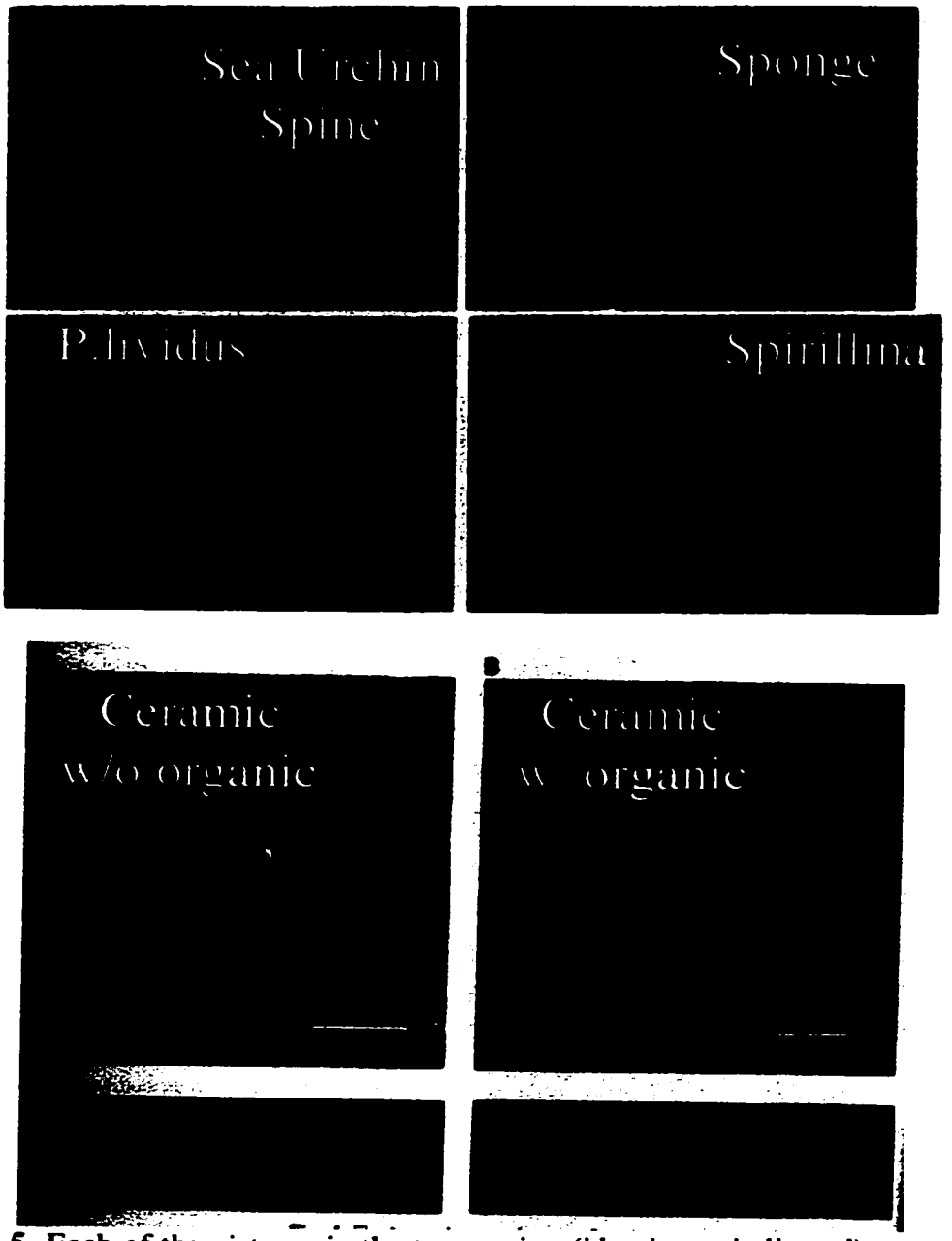

Figure 1.5 Each of the pictures in the top portion (identity as indicated) are crystals of calcium carbonate, specifically calcite. Their uniquely different structures are determined by the proteins present during formation. This picture, taken from Berman et al., 1993, shows the complexity and diversity of structure that inorganic minerals can form in nature and really exemplifies the impact of biomineralization proteins. The bottom pictures (Stupp and Braun, 1997) demonstrate the change that takes place in ceramics formation when a small amount of organic is present during formation.

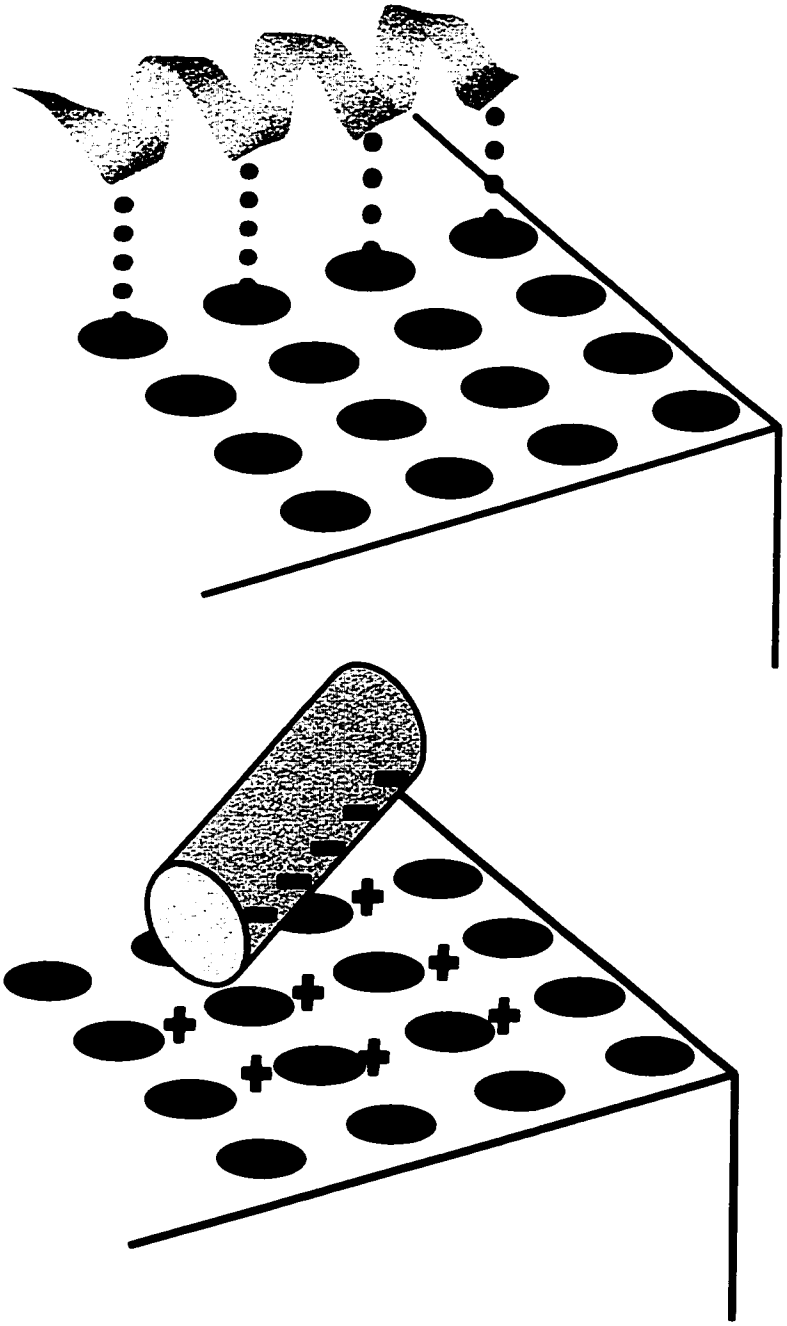

Figure 1.6 Two of the possible interaction models are shown. Above, the lattice matching mechanism is demonstrated with the charged sidechains of an α-helix repeating at such a frequency to match with the oppositely charged crystal lattice spacing. On the bottom, an electrostatic interaction is demonstrated by an amphipathic helix interacting with the total surface charge.

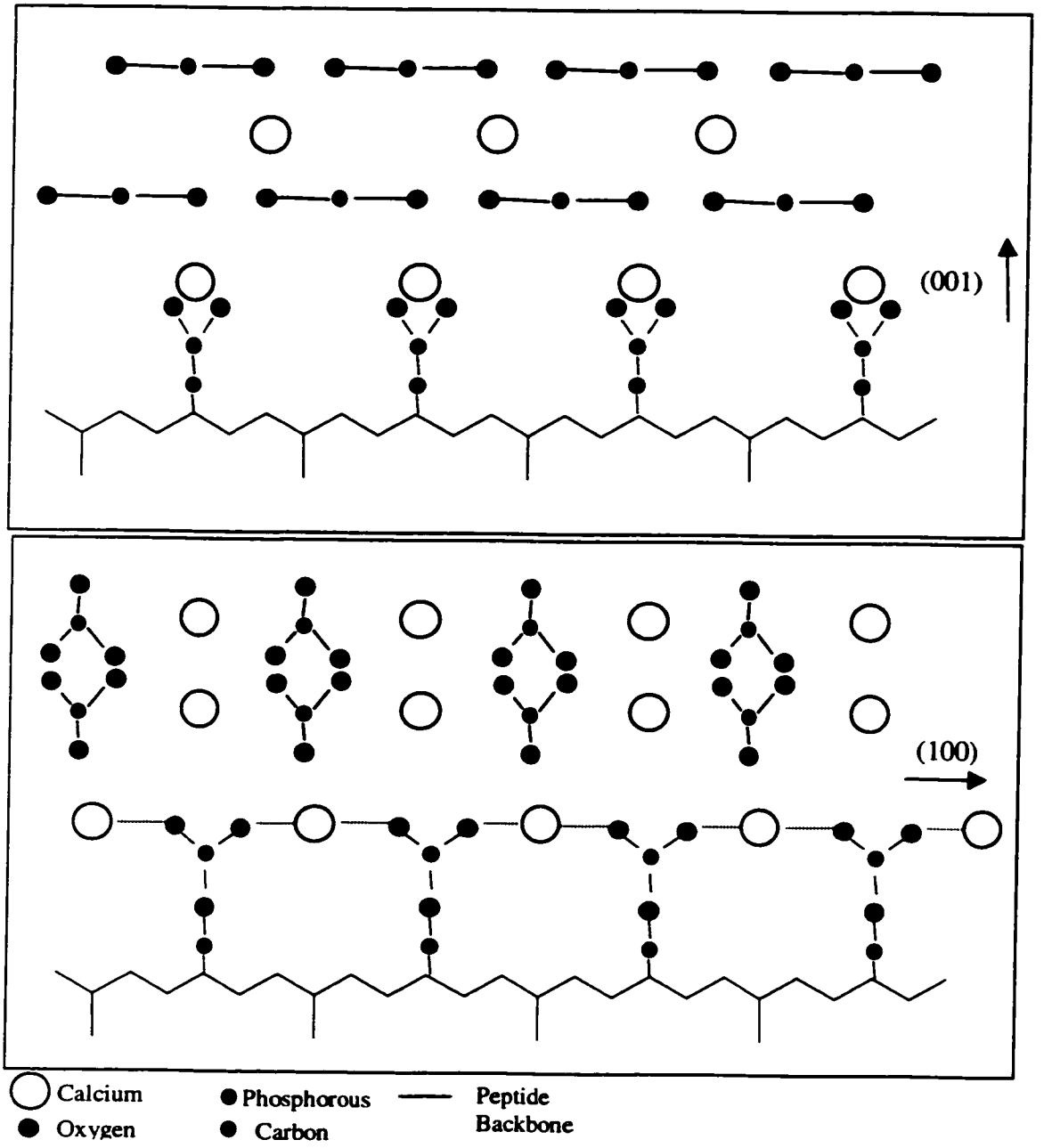

Figure 1.7 Modified from Hunter[17], the upper figure shows the interaction of aspartic acid sidechains in a β-sheet conformation head-on with the calcium ions in the 001 face of calcium carbonate or could also be thought of as a chelation interaction. In the lower figure, the intercalation shown is representative of how phosphoserines might interact with the 100 face and is another example of lattice matching. The arrow indicates the direction of the c axis.

CHAPTER 2:

BASIC NMR THEORY AND EXPERIMENTAL METHODS

Nuclear magnetic resonance (NMR) has grown faster than any other spectroscopic technique due to the broad range of applications across many different fields. NMR can be extended to all of the different chemical phases, as well as operating well at low and high temperatures and pressures, quantitatively determining chemical identity, composition, kinetics, individual structure and macroscopic order. NMR has been shown to be particularly valuable in biological studies, providing indisputable evidence of secondary and tertiary structures and dynamics in both the liquid and solid states. Within the last 20 years, high-resolution solid state NMR has become common place and this chapter will discuss the interactions that are observed in static solid state NMR experiments, the removal of these interactions to obtain high resolution spectra and the selective reintroduction of these interactions to obtain valuable structural information.

2.1 Interactions

NMR exploits a property of that some nuclei have called spin. When placed in a magnetic field, nuclei have a magnetic moment that causes them to line up with or against the applied field. The difference in population between these two energy states can be manipulated with an applied r.f. pulse to result in the NMR spectrum. The quantum mechanical description of the spin system is described briefly below from the

viewpoint of solid state NMR and the reader is referred to the many excellent texts that have been written describing the fundamental processes occurring in NMR.[1-3]

The Hamiltonian that describes the evolution of the spin system as a function of time can be separated into two parts, an internal Hamiltonian and an external Hamiltonian.

$$H_{tot} = H_{Ext} + H_{Int} \qquad [2.1]$$

The external Hamiltonian describes the interaction of the nuclei with the static magnetic field and the applied radio frequency field:

$$H_{Ext} = H_{Zeeman} + H_{Radio\ Frequency} \qquad [2.2]$$

The internal Hamiltonian describes the interactions of the nuclei with fields generated within the sample.[1,3,4]

$$H_{Int} = H_{Quadrupolar} + H_{Dipole\text{-}Dipole} + H_{Chemical\ Shift} + H_{J\text{-}coupling} \qquad [2.3]$$

For this work, only spin ½ nuclei are considered, thus the internal Hamiltonian can be further simplified, since $H_{Quadrupole}$, which exists only for spins > ½, will not contribute. Also, the J-coupling interaction in solid state NMR is much smaller than the other interactions (1-2 Hz) and can be neglected. This leaves a total truncated Hamiltonian of

$$H_{tot} = H_Z + H_{RF} + H_{DD} + H_{CS} \qquad [2.4]$$

H_Z is the largest interaction (on the order of 10-1000 MHz) and each of the other contributions can be considered a small perturbation. In comparison, H_{RF} is on the order of 10-150 kHz, H_{DD} is on the order of 120 kHz for H-H couplings, 20-30 kHz for H-C couplings and100-2000 Hz for C-C couplings and H_{CS} is approximately 15-20 kHz for

the carbonyl carbons discussed here. Each of these contributions will be discussed below (Refer to texts by Mehring[2], Slichter[3], Stejskal[4] and Haeberlen[1] for further discussion).

2.2 Zeeman Hamiltonian

When a nucleus with spin quantum number (I) of ½ is placed in a static magnetic field, it aligns with the magnetic field. The interaction of the nucleus with the field is defined as

$$H_z = -i\hbar\gamma \boldsymbol{I} \bullet \boldsymbol{B_0} \qquad [2.5]$$

where γ is the gyromagnetic ratio for that particular nucleus, $\boldsymbol{I}$ is the total spin angular momentum operator vector and $\boldsymbol{B_0}$ is the static field vector. The magnetic moment for a single dipole is defined as $\mu = \gamma\hbar\boldsymbol{I}$.

Traditionally, the direction of the external magnetic field is defined along the z-axis, simplifying the above equation to

$$H_z = -\hbar\gamma I_z B_0 \qquad [2.6]$$

where I_z = ½ or -½. In the static experiment, approximately half of the nuclei align with the field and half against the field, with energy levels of $E = \pm\ \gamma B_0/2$.

The above discussion has considered the behavior of a single spin in a magnetic field. An NMR sample, however, consists of many nuclei precessing about the z-axis at the Larmor frequency as shown in Figure 2.1. This is treated classically by collapsing all of the individuals vectors into one vector aligned on the z-axis called the magnetization vector, $\boldsymbol{M} = \sum\mu$. This description works very well to visualize the movement of the spin vector as a function of time, however, it does break down in some cases and density

matrix theory more adequately describes the spin ensemble.[3] The density matrix will be introduced in later sections and was used exclusively for dipolar recoupling simulations in this thesis.

2.3 RF Hamiltonian

Each nucleus precesses about the magnetic field at a frequency, $\omega_0 = \gamma B_0$ called the Larmor frequency. To perturb the nuclei from equilibrium, a second field must be applied at this frequency. The applied field is linearly polarized and can be split into right and left polarized contributions. Only the portion applied in the same direction as the Larmor frequency will contribute and this time dependent field is described by

$$H_{RF} = -\hbar \gamma_I B_1 (\boldsymbol{i} \cos\omega t + \boldsymbol{j} \cos\omega t) \bullet \boldsymbol{I} \qquad [2.7]$$

where B_1 is the field induced by the RF pulse.

2.4 Rotation Matrices and Coordinate Frames

The two significant contributions from the internal Hamiltonian for spin ½ systems are H_{DD} and H_{CS}, dipolar coupling and chemical shift, respectively, which both transform as second rank tensors. Interactions are often expressed in Cartesian coordinates, however with the many rotation transformations that are performed in a typical multiple pulse experiment, spherical coordinates are often easier to manipulate. The Rose convention is typically used, and the rotation in Cartesian coordinates is shown:

$$\boldsymbol{R}(\alpha,\beta,\gamma) = \begin{pmatrix} \cos\alpha\cos\beta\cos\gamma - \sin\alpha\sin\gamma & \sin\alpha\cos\beta\cos\gamma + \cos\alpha\sin\gamma & -\sin\beta\cos\gamma \\ -\cos\alpha\cos\beta\sin\gamma - \sin\alpha\cos\gamma & -\sin\alpha\cos\beta\sin\gamma + \cos\alpha\cos\gamma & \sin\beta\sin\gamma \\ \cos\alpha\sin\beta & \sin\alpha\sin\beta & \cos\beta \end{pmatrix}$$

[2.8]

where α, β and γ are performed sequentially and α is the rotation about the z-axis, β is the rotation about the new axis y axis, y' and γ is the rotation about the new z-axis, z'.

The general relationship between cartesian and spherical tensors is shown here. A general interaction, H_I is shown in Cartesian coordinates, where I and S are either spatial or spin components, depending on the interaction, and A_{ij} is a Cartesian second rank tensor representing the spatial interaction between I and S.

$$H_I = \begin{pmatrix} I_x & I_y & I_z \end{pmatrix} \begin{pmatrix} A_{xx} & A_{xy} & A_{xz} \\ A_{yx} & A_{yy} & A_{yz} \\ A_{zx} & A_{zy} & A_{zz} \end{pmatrix} \begin{pmatrix} S_x \\ S_y \\ S_z \end{pmatrix} \qquad [2.9]$$

The general form of a Hamiltonian in spherical coordinates is:

$$H = \sum_{k=0}^{2} \sum_{q=-k}^{+k} (-1)^q A_{kq} T_{k-q} \qquad [2.10]$$

where A_{kq} and T_{kq} are spherical tensors of rank k that contain the spatial variables and spin variables, respectively. The Hamiltonian above expressed in Cartesian coordinates can be transformed into spherical coordinates by using the relations, $I_+ = I_x + iI_y$ and $I_- = I_x - iI_y$ to give:

$$\begin{aligned} H_I &= A_{00}T_{00} + A_{10}T_{10} - (A_{11}T_{1-1} + A_{1-1}T_{11}) \\ &+ A_{20}T_{20} - (A_{21}T_{2-1} + A_{2-1}T_{21}) + A_{22}T_{2-2} + A_{2-2}T_{22} \end{aligned} \qquad [2.11]$$

Each of the spatial (A_{kq}) and spin (T_{kq}) terms to aid in the transformation are defined in Mehring.[2]

In the case that $H_0 >> H_I$, the only contributions from H_I to H_{tot} are those that commute with H_0, as seen by perturbation theory. These components are time

independent and are referred to as secular. This leads to great simplification to first order, and the remaining Hamiltonians will be presented using this simplification as appropriate.

2.5 Dipolar Coupling Hamiltonian

The dipolar interaction is most commonly shown in spherical coordinates, and simplifications referred to later on are most easily seen in this coordinate frame.

$$H_{DD} = -\frac{\hbar\gamma_I\gamma_S}{r^3}(1-3\cos^2\theta)(3I_ZS_Z - \boldsymbol{I}\bullet\boldsymbol{S}) \qquad [2.12]$$

for the case where $I = S$ (the homonuclear case), and

$$H_{DD} = -\frac{\hbar\gamma_I\gamma_S}{r^3}(1-3\cos^2\theta)I_ZS_Z \qquad [2.13]$$

when $I \neq S$ (i.e., for heteronuclei).

H_{DD} describes the magnetic interaction between the two nuclei where $\boldsymbol{r}$ is the vector orienting the two dipoles, and θ is the angle between $\boldsymbol{r}$ and the magnetic field. As shown in the equation above, the dipolar coupling is proportional to $1/r^3$. Thus, by measuring the dipolar interaction, molecular distances can be determined. The simplification of the Hamiltonian in the case of heteronuclear coupling is due to the fact that the larmor frequencies of the spins are very different, causing a fast averaging of the heteronuclear dipole-dipole interaction. This can also be thought of by recalling the fact that we are only considering the secular or time-independent contributions to the Hamiltonian, thus only contributions that commute with I_Z should be included. In the case of heteronuclei, I·S does not commute with I_Z, and thus should be dropped.[5]

2.6 Chemical Shift Hamiltonian

The chemical shift Hamiltonian is generally thought of in cartesian coordinates, shown for a particular nucleus

$$H_{CS} = -\hbar\gamma_I \boldsymbol{I} \bullet \sigma \bullet \boldsymbol{B} \qquad [2.14]$$

where σ is a second rank tensor, describing the effect of electrons surrounding a particular nucleus and its interaction with the external magnetic field, B_0. This is more explicity shown below:

$$\boldsymbol{H}_{CS} = -\hbar\gamma_I \begin{pmatrix} \boldsymbol{I}_x & \boldsymbol{I}_y & \boldsymbol{I}_z \end{pmatrix} \begin{pmatrix} \sigma_{11} & \sigma_{12} & \sigma_{13} \\ \sigma_{21} & \sigma_{22} & \sigma_{23} \\ \sigma_{31} & \sigma_{32} & \sigma_{33} \end{pmatrix} \begin{pmatrix} \boldsymbol{B}_x \\ \boldsymbol{B}_y \\ \boldsymbol{B}_z \end{pmatrix} \qquad [2.15]$$

Rotation of the chemical shift tensor, σ, into its principal axis system (PAS) results in a diagonal tensor. These three diagonal elements, σ_{11}, σ_{22}, and σ_{33}, completely define the anisotropic electronic environment of the nucleus, and Figure 2.2 shows two powder patterns whose shape is defined by the PAS tensor values as indicated. Changes in these values as a function of temperatures or solvent conditions are very sensitive to molecular dyanmics and will be explored more in Section 2.11 and Chapters 5 and 7.

The spherical coordinate description of the chemical shift Hamiltonian is shown below, and will be useful for later reference.

$$\boldsymbol{H}_{CS} = \omega_0 \boldsymbol{I}_z \left[(\sigma_{iso}) + (\tfrac{1}{2})(3\cos^2\theta - 1)(\sigma_{33} - \sigma_{iso}) \right] \qquad [2.16]$$

The first term corresponds to the isotropic chemical shift and the additional term is due to the anisotropic interactions with the field, where θ is the angle of the sample with respect

to the magnetic field, σ_ι is the isotropic chemical shift ($\sigma_{iso} = (\sigma_{11}+\sigma_{22}+\sigma_{33})/3$), $\sigma_{3'3'}$ is σ_{33} in the rotating frame and ω_0 is the larmor frequency.

2.7 Rotating Frame

Because the spins are precessing about the *z*-axis at their Larmor frequency, it is often convenient to describe events in the frame of the spins, rather than the laboratory frame. This frame of reference is called the rotating frame. To visualize the rotating frame, imagine drawing a white arrow from the center of a record to the edge of the record and placing it on the turn-table. As it begins to turn, the white arrow would turn, or precess, around the *z*-axis. Now imagine if you could get on the turntable and lay on the white arrow. The white arrow, or magnetization, would no longer be moving. This coordination transformation allows a great deal of simplification in many of the following manipulations. One important thing to note is that the field is no longer defined by B_0. It is now defined by B_{eff}:

$$B_{eff} = \left[\left(B_0 - \omega/\gamma\right)^2 + \left(B_1^2\right)\right]^{1/2} \qquad [2.17]$$

which is nearly just the B_1 field at resonance.

2.8 Density Matrix and Propagators

In order to predict the effect of a pulse or series of pulses on a spin ensemble, the ensemble is propagated as a function of time. To describe the distribution of an ensemble of spins quantum mechanically, the density matrix is used.[6] The time dependent density matrix is defined as:

$$\hat{\rho}(t) = \rho_{jk}|j,t\rangle\langle k,t| \qquad [2.18]$$

The spin ensemble at equilibrium can be described by a Boltzman distribution expressed in terms of the density matrix.

$$\rho = \frac{\exp(-H/kT)}{Tr\{\exp(-H/kT)\}} \qquad [2.19]$$

H represents the effective Hamiltonian ($H_0 + H_1$ transformed into the rotating frame), k is the Boltzman constant and T is the spin temperature. In the high temperature limit at equilibrium, $\rho = I_z$.

Simulations are performed by applying propagators to the initial density matrix according to the following equation:

$$\rho(t) = U\rho(0)U^{-1} \qquad [2.20]$$

where U, the propagator, is defined as

$$U = \exp(-i2\pi Ht) \qquad [2.21]$$

This assumes that the time range of interest is small enough that the Hamiltonian is time-independent over that range, leaving the time dependence in the density matrix. Discussions in more detail are found in Mehring[2] and Farrar and Harriman[6].

2.9 Cross Polarization with Magic Angle Spinning

Without the random tumbling motion provided by a solvent, the resulting spectrum of a powdered solid sample is a very inhomogeneous, broad powder pattern due to the magnitude of the chemical shift anisotropy and dipolar coupling (Figure 2.2). Cross polarization was introduced by Hartman and Hahn[7] in an effort to remove these

interactions (Figure 2.3). Cross polarization (CP) is the process of transferring the polarization of a large population of spins (typically protons), to a small population of spins (often carbon), thereby increasing the magnetization vector, **M**, ($\mathbf{M} = \sum\mu$) of the smaller population. CP can enhance signal by a factor proportional to (γ_I/γ_S), which is approximately a factor of 4 in the case of $^1H/^{13}C$ CP. In addition to the signal enhancement, the relaxation time is shortened to that of the common spins (^1H). In the case of ^{13}C, this added benefit yields a potential increase in repetition rate, and thus signal-to-noise, of 10^3, although real yields are probably more on the order of 10^2.[7,8]

Even with the signal enhancement from cross polarization, the lines observed are still very broad due to the dipolar coupling and CSA interactions (Figure 2.4-bottom). Tilting the sample axis to 54.7° causes the dependence on $(3\cos^2\theta - 1)$ to be removed for a single crystal, and for this reason is known as the magic angle. For a polycrystalline or lyophilized sample, rapid rotation of the sample about this axis, called magic angle spinning (MAS), removes broadening due to weak dipolar interactions (<500 Hz) and chemical shift anisotropy (Figure 2.4-middle). By spinning faster than the interactions, both the CSA and dipolar coupling will be completely averaged, leaving only a narrow isotropic line approaching a liquid state spectrum (Figure 2.4-top. A very slow spinning rate would completely remove the smaller dipolar interactions (≤ 2000 Hz), but CSA's are often on the order of 15-20 kHz or more. Although spinning at these rates is technologically possible, there are other limitations making these spinning speeds unrealistic for many experiments. At spinning rates slower than the CSA interaction, the

signal intensity is reduced from a broad powder pattern to one isotropic line and an array of spinning sidebands, so named because their repeat unit is equivalent to the spinning frequency (Figure 2.4-middle).[4,9] High field proton decoupling is combined with CPMAS to remove the remaining dipolar interactions, resulting in a high resolution solid state NMR spectra.

Because CP depends upon spinlocking to transfer magnetization, molecular motion can be inferred due to a loss in CP efficiency.[2,10] Motions on all timescales could potentially disturb the spinlock. If motion was present on the timescale of the spinlock, then the spinlock would be difficult to maintain because the motion of the spins would compete with the applied RF field. If the motion was fast or slow with respect to the spinlock the maximum cross polarization rate would take longer to achieve, and at some point, the rate of relaxation ($T_{1\rho}$) will be faster than the rate of cross polarization, so the maximum signal will never be attained.

2.10 MAS Line Shape Analysis

The chemical shift tensor defined above completely describes the electronic environment surrounding a particular nucleus. While the individual tensor elements are lost in a liquid state experiment due to random isotropic tumbling, they are retained in the solid state and provide a great deal of information regarding the local environment. Each nucleus has a principal axis system that diaganolizes the chemical shift tensor, leaving only 3 components, σ_{11}, σ_{22} and σ_{33}, to describe the electronic environment. Determining these three values is thus very important in understanding the electronic surrounding of a

nucleus. Figure 2.2 demonstrates how these 3 values map out onto a spectrum and can be determined by inspection from a powder pattern. There are several parameters that help to describe the lineshape[11] and in the following definitions, σ_{11} is the least shielded tensor element, σ_{33} the most shielded and σ_{22} corresponds to the powder pattern maximum. The span is defined as

$$\Omega = |\sigma_{11} - \sigma_{33}| \qquad [2.22]$$

which describes the width of the anisotropy. A closely related parameter and more often used is

$$\delta=(\sigma_{33}-\sigma_{iso}) \qquad [2.23]$$

which is effectively half of the span and is referred to as the anisotropy, and

$$\eta=|(\sigma_{22} - \sigma_{11})/(\sigma_{33}-\sigma_{iso})| \qquad [2.24]$$

is known as the assymetry parameter and defines the deviation of the lineshape from axial symmetry[12].

Changes in the lineshape are very sensitive to molecular dynamics and electronic structure and thus can be indicative of motion.[2,13-15] As the chemical shift tensor experiences mobility, the tensor will become averaged. As mobility increases, the powder pattern will decrease in overall width as well as changing shape to reflect the axis about which averaging is occurring. The extreme mobility limit is a solubilized sample, where the tensor is averaged to its isotropic values, and no anisotropy remains.

The resolution of the powder pattern by MAS into spinning sidebands retains the shape of the powder pattern allowing fitting the manifold of sidebands[16] to determine the

principle values of the CSA tensor, provided the spinning speed is slow relative to the CSA interaction. Once the principle values of the rigid molecule are known, changes in the CSA as a result of molecular motion due to hydration can be determined.

The dependence of the CSA on molecular motion can be seen directly in the Hamiltonian describing the interaction of the CSA of a rigid system with an external magnetic field

$$\boldsymbol{H} = \mathbf{I} \bullet \boldsymbol{\sigma} \bullet \mathbf{B}_0 \qquad [2.25]$$

as compared to the equation for a molecule undergoing motion

$$\boldsymbol{H} = \mathbf{I} \bullet \bar{\boldsymbol{\sigma}} \bullet \mathbf{B}_0 \qquad [2.26]$$

The relative comparison of rigid samples to samples exhibiting molecular motion provides a qualitative measure of motional averaging. This is best explained pictorially in Figure 2.5, where simulations were performed by changing the tensor values to maintain η and Ω. It is important to note that these simulations did not specifically address motion in the simulation code, but approached it from the point of view of what the CSA would look like if different values of η and Ω were used. In order to quantify the observed motion, a motional model must be applied. Thesis work by Dave Wemmer[10] and Joe Dumais[17] provide examples of simulations performed with motional models included. In systems that have at least one axis with restricted motional freedom, lineshape can be combined with relaxation measurements to yield very quantitative dynamic information.

2.11 Relaxation

When an NMR active nucleus is perturbed from equilibrium in a static magnetic field, an NMR signal is observed. Eventually the nuclei return back to equilibrium. Two relaxation phenomena, T_1 and T_2, describe the decay mechanism. T_1 is the longitudinal relaxation describing the relaxation of the spin with the lattice, or surrounding environment. T_2 is the transverse relaxation describing the spin-spin relaxation. The change in magnetization, **M**, with respect to time is[4,6]:

$$d\vec{M}/dt = \gamma\vec{M} \times \vec{B} - \frac{M_{\perp}}{T_2} + \frac{\left(M_0 - M_{\parallel}\right)}{T_1} \qquad [2.27]$$

where $M_\perp$ is the magnetization perpendicular to the magnetic field, M_0 is the initial magnetization and M is the magnetization parallel to the magnetic field. This can be separated into vectorial components as follows:

$$dM_x/dt = \gamma(M_y B_z - M_x B_y) \qquad [2.28]$$

$$dM_y/dt = \gamma(M_z B_x - M_x B_z) \qquad [2.29]$$

$$dM_z/dt = \gamma(M_x B_y - M_y B_x) \qquad [2.30]$$

Equation 27 can be solved for M_x, M_y and M_z and expressed in terms of a relaxation parameter, T_1 or T_2, yielding the following expressions:

$$M_z(t) = M_0\left[1 - \exp(-t/T_1)\right] \qquad [2.31]$$

$$M_x(t) = M_y(t) = M_0\left[\exp(-t/T_2)\right] \qquad [2.32]$$

By comparing equations 28-30 with 31 and 32, M_z is effected only by B_y and B_z, thus B_z has no effect on T_1. However, M_x and M_y are dependent on both B_x, B_y and B_z, and thus T_2 is dependent on all three vectorial components. This is an important distinction between T_1 and T_2 and explains why they are rarely, if ever, the same. It is also important in defining the rate of dynamic processes contributing to the two. B_z is not moving very quickly in the laboratory frame since the rotation is about the z-axis. B_x and B_y however are moving on the order of the Larmor frequency. Thus T_1 has contributions only from the fast B_x and B_y components, and thus is sensitive to dynamics on the Megahertz timescale. T_2 on the other hand is sensitive to both slow and fast frequencies.

Another related relaxation is $T_{1\rho}$. $T_{1\rho}$ is applicable only during spin-locking, when a 90° pulse places the magnetization into the xy-plane and another pulse is applied 90° out of phase to effectively lock the magnetization in the xy-plane. In this case, B_{eff} (eq. 2.9) becomes the magnetic field the sample sees and is very nearly described by the B_1 field. Thus, in an analogous description to that above for T_1, $T_{1\rho}$ is sensitive to dynamics on the timescale of the B_1 field, usually on the order of 20-150 kHz. This will be discussed in more detail in section 2.12. The equation describing this relaxation is

$$M_Z(t) = M_0\left[\exp(-t/T_{1\rho})\right] \qquad [2.33]$$

2.12 $T_{1\rho}$

Relaxation measurements are a common way to extract dynamic information about a sample in NMR. T_1 measurements give dynamic information on the timescale of the larmor frequency. T_2 measurements contain information on both slow and fast frequency motions. $T_{1\rho}$ relaxation measurements yield information on the timescale of 10^3 to 10^5 Hz, the timescale of the spin-locking field. Two types of $T_{1\rho}$ are commonly measured: that of the abundant spin and that of the rare spin. As seen in Figure 2.6, two different pulse sequences define the different experiments. The top figure is the pulse sequence for the proton $T_{1\rho}$, and measures the degree of mobility of the proton bath. This is possible because during spinlocking, the decay of the carbon signal is a mirror of the decay of the proton signal, so observing the rare spin yields insight into the abundant spin[4] (see Figure 2.6). By incrementally increasing the length of the spinlocking pulse, the decay of the proton bath is observed.

The ^{1}H $T_{1\rho}$ provides information on the overall motion of the system, which can be the desired information in some instances. Site specific dynamic information is also of interest and this can be obtained with ^{13}C $T_{1\rho}$ (or rare spin $T_{1\rho}$). ^{13}C $T_{1\rho}$ is measured by turning off the ^{1}H spinlocking field while leaving the carbon spinlocking field on, as shown in the bottom portion of Figure 2.6.

While the ^{13}C $T_{1\rho}$ can be measured and compared to similar samples in a relative manner, relating it to a correlation time is very difficult. This is due to the contribution of both the chemical shift anisotropy and the dipolar coupling, which are both on the order of the relaxation measurement. Although this means that $T_{1\rho}$ is more difficult to quantitate, it can be used qualitatively to compare a given sample's relaxation under different conditions. A great deal of work in this area has been undertaken by Schaefer in the field of polymers[9,18] and the reading of the publications are highly recommended to understand the nature of the experiment as well as some of the difficulties in interpreting $T_{1\rho}$ measurements.

2.13 Dipolar Recoupling

Dipolar coupling can be observed in a non-spinning solid, provided the coupling is strong enough. The development of CPMAS provides high-resolution spectra, but at the cost of removing the dipolar couplings due to the averaging effects of magic angle spinning. In order to regain this information, radio frequency pulses can be used to remove the averaging effects of MAS and recover dipolar coupling and structural information with dipolar recoupling pulse sequences. Recoupling techniques exist for both heteronuclear and homonuclear couplings, as discussed in section 2.5, and the techniques utilized in this work are presented here.

2.13.1 REDOR

REDOR, or Rotational Echo DOuble Resonance, was developed in the Schaefer lab to measure dipolar couplings between heteronuclei[19]. It is a technique that has

proven to be very successfully applied to biological systems, particularly in the study of proteins and peptides.[20-22]

REDOR is a rotor synchronized technique and is perhaps best explained by taking a step back to a more simple experiment, SEDOR (Spin Echo DOuble Resonance), which is the non-spinning equivalent to REDOR. SEDOR is based on one of the more simple relaxation experiments, the Hahn spin echo, which consists of generating magnetization along x, then waiting a time τ and applying 180° pulses at increments of time τ. This generates a series of spin echoes, which result from the magnetization being refocused onto the x-axis. In the absence of any relaxation mechanisms, the intensity of each spin echo would be the same height. Other relaxation mechanisms as discussed in section 2.11-2.12 are present, however, so a steady decrease in intensity is observed as a function of the spin echo. The pulse sequence is shown in Figure 2.7 (A). In part B, the pulse sequence SEDOR is shown. If the SEDOR experiment was performed by applying only the pulses to the *S* spin channel, and not the *I* spins, then it would be identical to the Hahn spin echo experiment and the entire signal would be regained. This is a result of the *S* spin pulse refocusing both the dipolar coupling and chemical shift anisotropy. By adding the pulse on the *I* spins, the dipolar coupling is affected, and is no longer refocused, as can be seen by comparing the dipolar and chemical shift Hamiltonians. The dipolar hamiltonian is proportional to $I_Z S_Z$ ($H_{DD} \propto I_Z S_Z$) but the chemical shift of S is proportional only to S_Z ($H_{CS} \propto S_Z$) thus pulses on the *I* spins effect the dipolar coupling portion of the Hamiltonian, but not the chemical shift Hamiltonian. The result is that any

spins that are dipolar coupled to *I* spins will not be refocused, yielding a decreased signal intensity.

Adding spinning adds a phenomenon similar to spin echoes called rotational echoes. For Hamiltonians that transform as second rank tensors such as dipolar couplings and chemical shift interactions, MAS introduces time dependence with a time average that is zero over one rotor period, resulting in the full recovery of the signal, analogous to the spin echo sequence. Introducing π pulses on the *I* spins interferes with the dipolar coupling Hamiltonian as described above, causing a loss in signal for any *S* spins coupled to *I* spins. This is more easily seen by mapping out the magnetization as a function of rotor period, Figure 2.8, that is described by the following equation:

$$\phi(\alpha,\beta;t)=\int_0^{t_2}\frac{D}{4\omega_r}(\sin^2\beta[\sin 2(\alpha+\omega_r t_2)-\sin 2\alpha]-2\sqrt{2}\sin 2\beta[\sin 2(\alpha+\omega_r t_2)-\sin\alpha] \quad [2.34]$$

where α is the azimuthal angle and β is the polar angle defined by the internuclear vector in a coordinate system defined with the z-axis parallel to the rotor axis. Figure 2.7C shows the more commonly used REDOR pulse sequence, utilizing the XY8 phase cycling to reduce effects from chemical shift offset and pulse imperfections. This version of REDOR was used exclusively for the work presented in this thesis.

REDOR has been particularly applicable for studying secondary structure in proteins, as demonstrated.[21,22] The utility of REDOR for the work presented here is in determining the presence of α-helices vs. any other secondary structure. This can be seen in Figure 2.9 which shows a distance of 4.2 Å between the backbone carbonyl carbon and

the backbone amide involved in a hydrogen bond for an α-helix (residues i i+4). Also shown are the distances between the same residues for a 3_{10} helix (5.8 Å) and a β-sheet (10.6 Å) secondary structure. This clear distinction between secondary structures is reflected in the REDOR dephasing curves, allowing straightforward interpretation of results. The drawback to REDOR is that it is useful only for helical secondary structure, since distance for other secondary structures utilizing the same labeling scheme are too long to be measured with this technique. REDOR can also be applied to help define tertiary structures, but without some understanding of the folding a prior, much time and money could be invested in vain.

2.13.2 DRAWS

Measuring protein structure without any previous knowledge of the secondary structure can best be accomplished by taking advantage of homonuclear recoupling techniques. φ is characteristic of secondary structure and by measuring the distance between adjacent backbone carbonyl carbons, can be determined independent of the other torsion angles as seen in Figure 2.10, where common secondary structures are indicated. In this figure, the distance is mapped out as a function of φ over a range from 2.7 Å to 3.7 Å, couplings easily measurable using one of many homonuclear techniques (177 Hz – 486 Hz). This measurement results in the direct measure of any secondary structure.

There are many homonuclear recoupling techniques including R^{2}[23], SEDRA[24], RFDR[25], DRAMA[26], MELODRAMA[27], HORROR[28], C7[29], DRAWS[30] and DQDRAWS[31]. While these pulse sequences have been reviewed in the literature[32],

understanding the utility of DRAWS, specifically for protein systems, requires an understanding of the drawbacks of other techniques, so a brief review is presented here.

R^2 (Rotational Resonance) was introduced in 1990[23]. It takes advantage of the fact that when a multiple of the spinning frequency matches the chemical shift difference between two nuclei (a condition called rotational resonance), magnetization transfer is enhanced.[23] When it was developed, it was one of the few techniques that could accurately (within 0.2 Å) measure 5 Å distances. The advantage of this technique above others available at the time was based on the fact that the experiment is performed in the longitudinal plane, not the transverse. Since longitudinal magnetization depends on T_1, which is often quite long in solids, it was much more successful at measuring small dipolar couplings than previous transverse experiments that are dependent upon short T_2's. While it was a major step forward, there are still some severe limitations with this technique. The major drawbacks are: 1) It requires the isolated spin pair to be chemically shifted from each other by 2000-15000 Hz—these values represent practical spinning limits for signal to noise as well as spinning technology. 2) Accurate simulations depend heavily on the principal values of the chemical shift anisotropy at both sites, the isotropic J-coupling between the sites, the relative orientation of the two shielding tensors with respect to one another and a parameter called T_2^{ZQ} which describes the coupling of the spin pair with the environment. Knowing the relative orientation between the two spins is a very significant drawback since many compounds do not have available crystal structures, and simulations showed that it became very dependent at distances of 4-5 Å. 3) Because of the incorporation of chemically shifted species, the samples are often very

expensive, cost limiting or unavailable for protein samples and would also have a dependence on both φ and ψ, making modeling a significant portion of the fitting process.

RFDR (Rotor Frequency-driven Dipolar Recoupling) is another longitudinal homonuclear recoupling experiment that was an improvement over SEDRA (Simple Excitation for the Dephasing of Rotational-echo Amplitudes) which applied a single π pulse and observed the dipolar coupling through the disappearance of the transverse magnetization. An advantage of RFDR over other techniques is that it does not depend strongly on CSA. Its major drawback is that it works best for nuclei that are significantly chemically shifted. DRAMA (Dipolar Recoupling at the Magic Angle) is a transverse technique that recouples the dipolar coupling with 2 $\pi/2$ pulses placed at ¼ and ¾ of the rotor period. It was found to be work very well for nuclei with little or no chemical shift difference, but is highly dependent on CSA. MELODRAMA was an improvement that corrected well for CSA when the field strength is appropriately matched to the spinning speed, but had reduced recoupling efficiency in some cases.[32]

All of these techniques have one of two problems: either they are not dependent on CSA, but are dependent on a chemical shift difference, or they are not dependent on a chemical shift difference, but dependent on CSA. DRAWS was developed in the Drobny lab to allow determination of dipolar couplings independent of CSA, chemical shift offset, relative orientation of the CSA tensors, and RF pulse imperfection. Simulations have shown that effects from each of these contributions using DRAWS are minimized

and experimental results have confirmed the finding.[30,33] DRAWS utilizes a windowless pulse sequence shown in Figure 2.11, and thus is called Dipolar Recoupling with A Windowless Sequence (DRAWS).[30] This pulse sequence was an improvement on the pulse sequence DRAMA, which consisted of two 90° pulses, located at ¼ and ¾ of the rotor period. These pulses reverse the sign of the dipolar Hamiltonian at specific intervals in the rotor period so that the dipolar coupling is not averaged to zero (Figure 2.12). DRAMA, however, does not compensate well for chemical shift anisotropy and offset effects. The 360-degree pulses incorporated into DRAWS are present to suppress both of these effects. The average dipolar Hamiltonian after one application of R in Figure 2.11 is:

$$\bar{H}_D^{(0)} = \frac{d}{17\pi}[c_{xx} - c_{yy}(I_x S_x - I_y S_y) + c_{zz}(3I_z S_z - \boldsymbol{I} \bullet \boldsymbol{S})] \qquad [2.35]$$

where $d = \gamma^2/r^3$ and c_{xx}, c_{yy} and c_{zz} are functions of the Euler angles, α, β and γ and are given explicitly by Gregory et al.[30] Supercycling the basic sequence 4 times further removes the chemical shift offset dependence, resulting in a pulse sequence independent of chemical shift effects to zeroeth order. Experimentally, ^{13}C-^{13}C distances of 5-6 Å have been measured with DRAWS to an accuracy of 0.1 Å.[33,34]

DRAWS is well suited for studying peptide systems. The suppression of the chemical shift anisotropies allows the observation of homonuclear dipolar couplings even when they are much smaller than the CSA's of the observed nuclei, as is the case with carbonyl carbons in the peptide bonds. Being independent of chemical shift differences allows the use of chemically unresolved resonances such as carbonyl carbons, which

directly yields the torsion angle phi (φ) in the peptide backbone as shown above in Figure 1.2. It is significant that most secondary structures will have φ values on the linear portion of the curve allowing differentiation of distances as small as 0.1 Å. This is shown in Figure 2.13, where several DRAWS dephasing curves for distances experienced between peptide backbone carbonyl carbons are shown.

As discussed above, the technique does not depend strongly on the isotropic chemical shift difference.[33] It has been well documented that differences in chemical shift correspond directly to secondary structure in peptides and proteins.[35-37] Thus DRAWS has the potential to distinguish conformational heterogeneity since the dipolar recoupling efficiency is independent of any correlation between the chemical shifts and the peptide structure in a given sample. Figure 2.13 shows simulations of a fixed distance and the same distance with several different conformational distributions, indicating the dependence of longer times in the dephasing curve on the presence of multiple structures.

As mentioned in the beginning of this section, this technique determines the torsion angle φ. ψ is also critical in defining secondary structure, so even though a φ angle may be consistent with a particular secondary structure, this cannot be absolutely determined until ψ is known. DRAWS techniques are also able to measure ψ using one of two techniques, ^{15}N-^{15}N DRAWS, or double quantum DRAWS. ^{15}N-^{15}N DRAWS is exactly analogous to ^{13}C-^{13}C DRAWS, except that it measures the dipolar coupling between the backbone amides, yielding the torsion angle ψ. The disadvantage with this

technique is that either two samples have to be made or 4 labels have to be incorporated into one sample, increasing cost. There are also concerns of sensitivity, since the γ is 40% that of ^{13}C, but this is partially outweighed by the slower T_2 of ^{15}N.

Double quantum DRAWS measures the relative orientation between the two carbonyl CSA's which results in ψ, given that φ was measured using DRAWS. This technique has the particular advantage of needing only one sample for both techniques and also shows a clearly different sideband pattern for α-helices, 3_{10}-helices and β-sheet.[38] The disadvantage is the loss of signal during DQ filtering. This loss is so significant (70%--check number), that for the inherently low signal surface bound protein samples, one experiment would take about 2 weeks to a month to finish and then would need to be repeated in triplicate! For the work done here, the helical secondary structure allowed the use of the more sensitive REDOR experiment. This experiment also has the advantage of determining global secondary structure, rather than isolated secondary structure, allowing fewer samples to be made for a complete view of the secondary structure of the protein.

2.14 Notes to Chapter 2

1. Haeberlen, U. *High Resolution NMR in Solids Selective Averaging* (ed. Waugh, J. S.) (Academic Press, New York, 1976).

2. Mehring, M. *Principles of High Resolution NMR in Solids* (Springer-Verlag, New York, 1983).

3. Slichter, C. P. *Principles of Magnetic Resonance* (ed. Fulde, P.) (Springer-Verlag, Berlin, 1990).

4. Stejskal, E. O. & Memory, J. D. *High Resolution NMR in the Solid State* (Oxford University Press, New York, 1994).

5. Abragam, A. *Principles of Nulcear Magnetism* (Oxford University Press, New York, 1961).

6. Farrrar, T. C. & Harriman, J. E. *Density Matrix Theory and Its Applications in NMR Spectroscopy* (The Farragut Press, Madison, WI, 1998).

7. Hartmann, S. R. & Hahn, E. L. Nuclear Double Resonance in the Rotating Frame. *Physical Review* **128**, 2042-2053 (1962).

8. Pines, A., Gibby, M. G. & Waugh, J. S. Proton-Enhanced NMR of Dilute Spins in Solids. *Journal of Chemical Physics* **59**, 569-590 (1973).

9. Schaefer, J. & Stejskal, E. O. Carbon-13 Nuclear Magnetic Resonance of Polymers Spinning at the Magic Angle. *Journal of the American Chemical Society* **98**, 1031 (1976).

10. Wemmer, D. E. in *Lawrence Livermore Berkeley, Laboratory Materials and Molecular Research Division* 288 (University of California, Berkeley, Berkeley, 1978).

11. Duncan, T. M. *Principal Components of Chemical Shift Tensors: A Compilation; 2nd Ed.* (The Farragut Press, Madison, 1997).

12. Spiess, H. W. *Rotation of Molecules and Nuclear Spin Relaxation* (eds. Diehl, P. & Kosfeld, E. F. R.) (Springer, Berlin, 1978).

13. Ruocco, J. J., Siminovitch, D. J., Long, J. R., Das Gupta, S. K. & Griffen, R. G. ^{2}H and ^{13}C Nuclear Magnetic Resonance Study of N-

Palmitoylgalactosylsphingosine (Cerebroside)/Cholesterol Bilayers. *Biophysical Journal* **71**, 1776-1788 (1996).

14. Geheagin, K., Meints, G. A., Hatcher, M. E. & Drobny, G. P. The Dynamic Impact of CpG Methylation in DNA. *Biochemistry* (2000).

15. Long, J. R., Sun, B. Q., Bowen, A. & Griffin, R. Molecular Dynamics and Magic Angle Spinning NMR. *Journal of the American Chemical Society* **116**, 11950-11956 (1994).

16. Herzfeld, J. & Berger, A. E. Sideband Intesities in NMR Spectra of Samples Spinning at the Magic Angle. *Journal of Physical Chemistry* **73**, 6021-6030 (1980).

17. Dumais, J. J. in *Chemistry Department* 199 (University of Washington, Seattle,).
18. Schaefer, J., Stejskal, E. O. & Buchdahl, R. Magic-Angle 13C NMR Analysis of Motion in Solid Glassy Polymers. *Macromolecules* **10**, 384-405 (1977).

19. Gullion, T. & Schaefer, J. Rotational-Echo Double-Resonance NMR. *Advances in Magnetic Resonance* **13**, 57 (1989).

20. Merritt, M. E., Christensen, A. M., Kramer, K. J., Hopkins, T. L. & Schaefer, J. Detection of Intercatechol Cross-Links in Insect Cuticle by Solid-State Carbon-13 and Nitrogen-15 NMR. *Journal Of the American Chemical Society* **118**, 11278-11282 (1996).

21. Marshall, G. R. *et al.* Determination of Precise Interatomic Distance in a Helical Peptide by REDOR NMR. *Journal of the American Chemical Society* **112**, 963 (1990).

22. Klug, C. A., Burzio, L. A., Waite, J. H. & Schaefer, J. *In Situ* Analysis of Peptidyl DOPA in Mussel Byssus Using Rotational-Echo Double-Resonance NMR. *Archives Of Biochemistry And Biophysics* **333**, 221-224 (1996).

23. Levitt, M. H., Raleigh, D. P., Creuzet, F. & Griffin, R. G. Theory and Simulations of Homonuclear Spin Pair Systems in Rotating Solids. *Journal of Chemical Physics* **92**, 6347 (1990).

24. Gullion, T. & Vega, S. A Simple Magic Angle Spinning NMR Experiment for the Dephasing of Rotational Echoes of Dipolar Coupled Homonuclear Spin Pairs. *Chemical Physics Letters* **194**, 423 (1992).

25. Bennett, A. E., Ok, J. H., Griffin, R. G. & Vega, S. Chemical Shift Correlation Spectroscopy in Rotating Solids: Radio Frequency-Driven Dipolar Recoupling and Longitudinal Exchange. *Journal of Chemical Physics* **96**, 8624-8627 (1992).

26. Tycko, R. & Dabbagh, G. Measurement of Nuclear Magnetic Dipole-Dipole Coupling in Magic Angle Spinning NMR. *Chemical Physics Letters* **173**, 461-465 (1990).

27. Sun, B. Q., Costa, P. R., Kocisko, D., Lansbury, P. T. & Griffen, R. G. Internuclear Distance measurements in Solid State Nuclear Magnetic Resonance: Dipolar Recoupling via Rotor Synchronized Spin Locking. *Journal of Chemical Physics* **102**, 702-707 (1995).

28. Nielsen, N. C., Bildsoe, H., Jakobsen, H. J. & Levitt, M. H. Double-Quantum Homonuclear Rotary Resonance--Efficient Dipolar Recovery in Magic-Angle Spinning Nuclear-Magnetic-Resonance. *Journal of Chemical Physics* **101**, 1805-1812 (1994).

29. Lee, Y. K. *et al.* Efficient Dipolar Recoupling in the NMR of Rotating Solids. A Sevenfold Symmetric Radiofrequency Pulse Sequence. *Chemical Physics Letters* **242**, 304-309 (1995).

30. Gregory, D. M. *et al.* Windowless Dipolar Recoupling: The Detection of Weak Dipolar Couplings Between Spin 1/2 Nuclei With Large Chemical Shift Anisotropies. *Chemical Physics Letters* **246**, 654-663 (1995).

31. Gregory, D. M., Wolfe, G. M., Jarvie, T. P., Sheils, J. C. & Drobny, G. P. Double-Quantum Filtering in Magic-Angle-Spinning NMR Spectroscopy Applied to DNA Oligomers. *Molecular Physics* **89**, 1835-1849 (1996).

32. Baldus, M., Geurts, D. G. & Meier, B. H. Broadband Dipolar Recoupling in Rotating Solids: A Numerical Comparison of some Pulse Schemes. *Solid State Nuclear Magnetic Resonance* **11**, 157-168 (1998).

33. Mehta, M. A. *et al.* Distance Measurements in Nucleic Acids Using Windowless Dipolar Recoupling Solid State NMR. *Solid State Nuclear Magnetic Resonance* **7**, 211-228 (1996).

34. Gregory, D. M. *et al.* Dipolar Recoupling NMR of Biomolecular Self-Assemblies: Determining Inter- and Intrastrand Distances in Fibrilized Alzheimer's β-Amyloid Peptide. *Solid State Magnetic Resonance* **13**, 149-166 (1998).

35. Asakawa, N. *et al.* Hydrogen-Bonding Effect on ^{13}C NMR Chemical Shifts of L-alanine Residue Carbonyl Carbons of Peptides in the Solid State. *Journal of the American Chemical Society* **114**, 3261 (1992).

36. Asakawa, N., Kurosu, H. & Ando, I. Structural Study of Peptides Containing L-alanine Residues by *ab initio* Chemical Shielding Calculation. *Journal of Molecular Structure* **323**, 279 (1994).

37. Spera & Bax, A. Emperical Correlation Between Protein Backbone Conformation and C_α and C_β ^{13}C Nuclear Magnetic Resonance Chemical Shifts. *Journal of the American Chemical Society* **113**, 5490 (1991).

38. Bower, P. V. *et al.* Determination of Torsion Angles in Proteins and Peptides Using Solid State NMR, Journal of the American Chemical Society. *Journal of the American Chemical Society* **121**, 8373-8375 (1999).

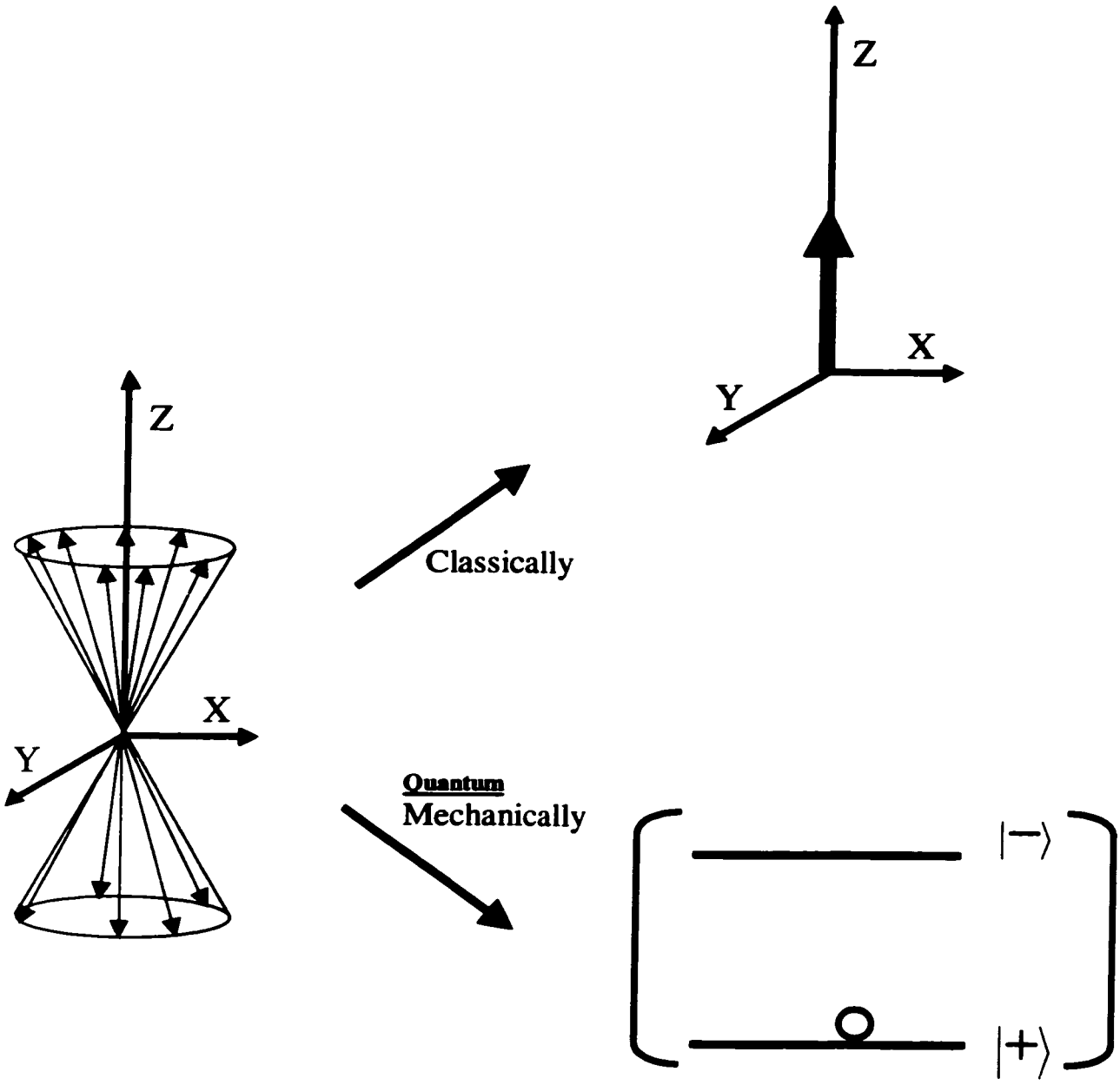

Figure 2.1. The individual spins are shown to precess about the main magnetic field at the larmor frequency, ω. This can be thought of classically as one vectorial contribution along the z-axis or quantum mechanically as the wavefunction, ψ, being completely described by the lower energy state, $|+\rangle$.

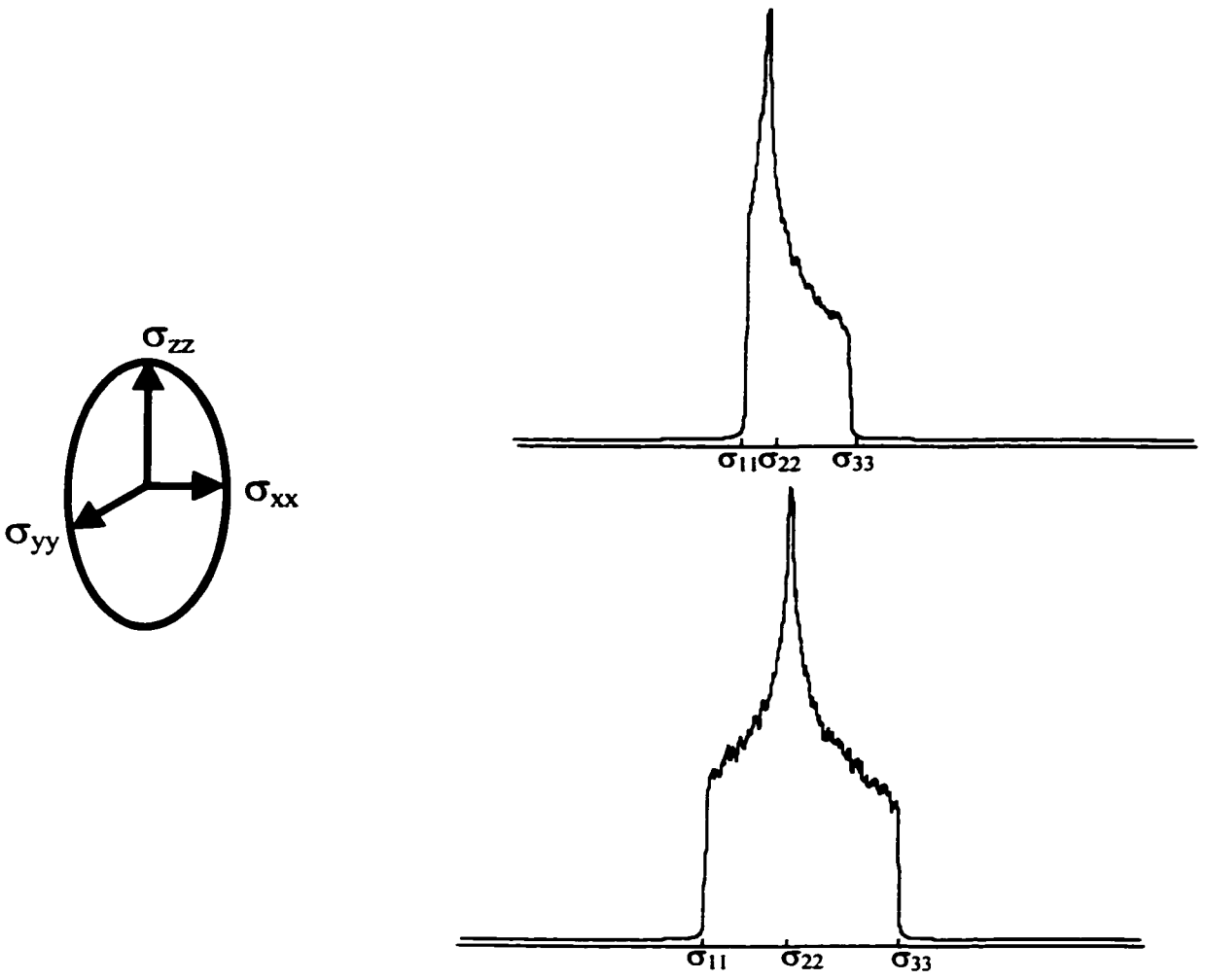

Figure 2.2. The chemical shift tensor values are shown for an arbitrary tensor, defining σ_{11}, σ_{22}, and σ_{33}. On the right, the contributions of the tensors to the spectrum are indicated in two different cases. The top has an η of almost 0, indicating nearly axial symmetry, and the bottom has an $\eta = 1$.

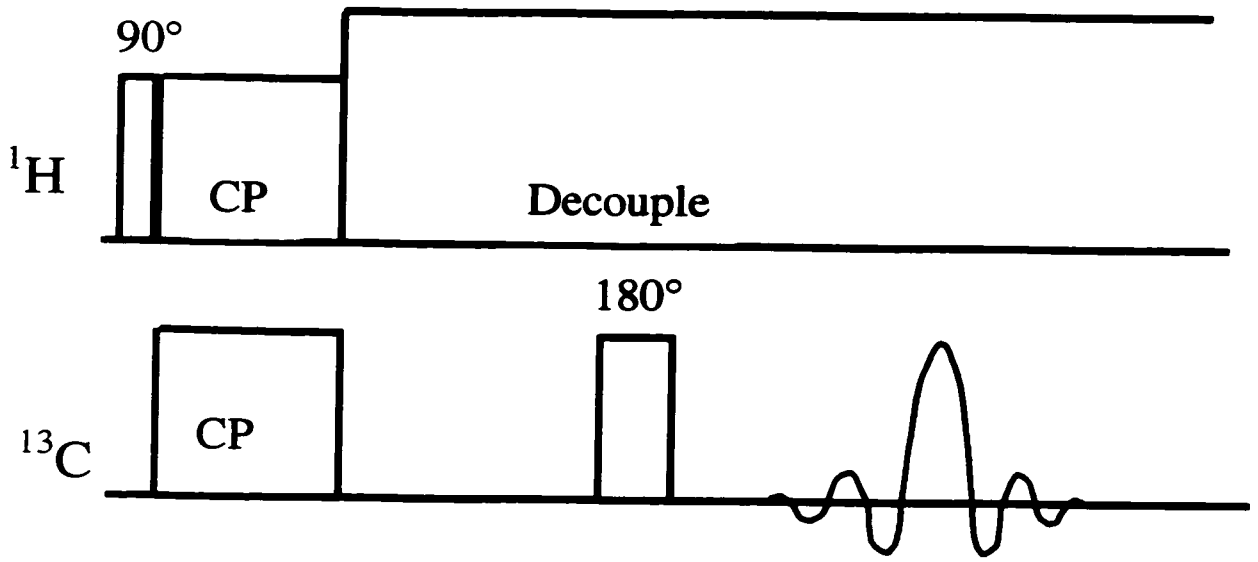

Figure 2.3. A 90° pulse on the proton channel is followed by a spinlocking pulse to generate cross polarization from the abundant spins to the rare spins. The cross polarization sequence here is shown followed by a spin echo and acquisition.

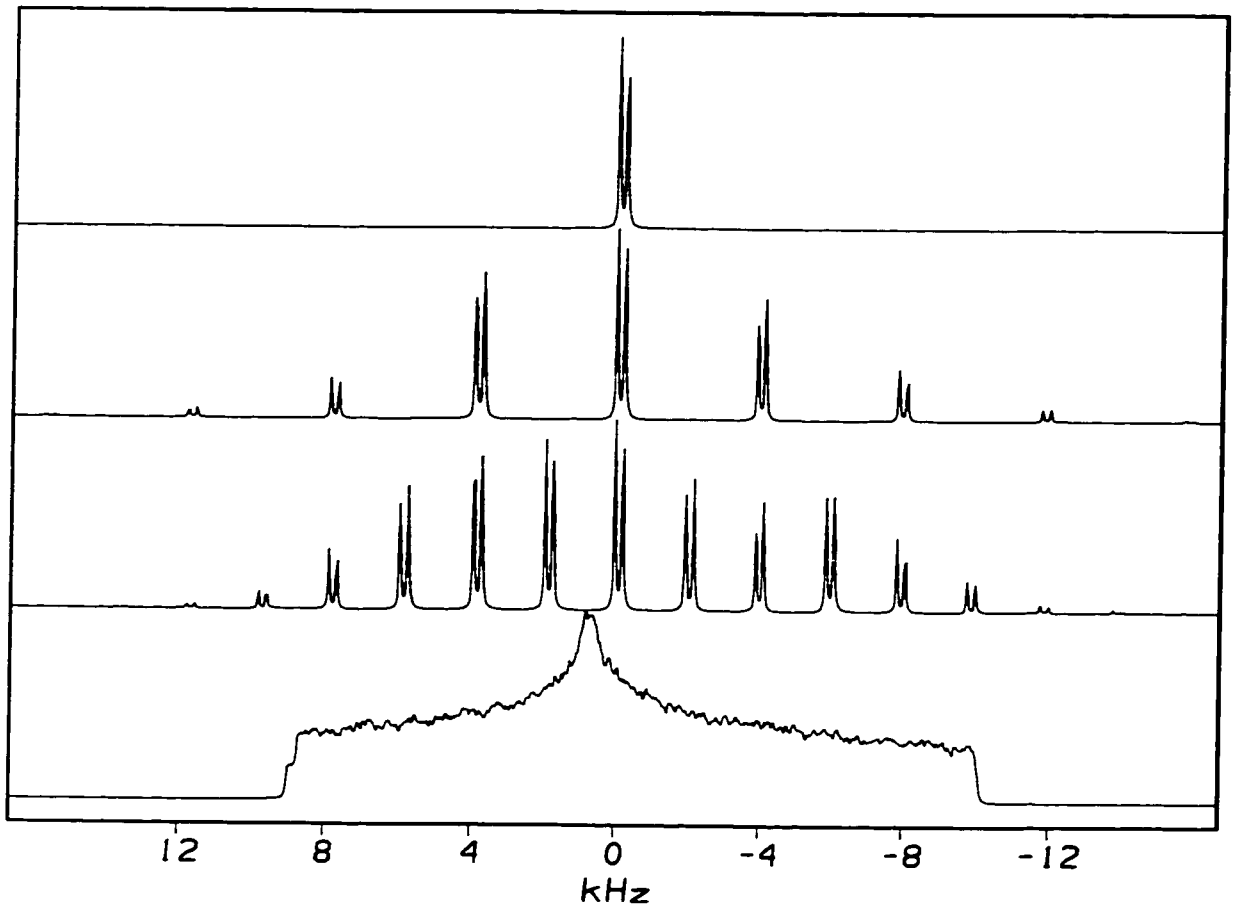

Figure 2.4. Simulations of a peptide, labeled at two carbonyl carbons, are shown as a function of spinning speed. The bottom most spectrum is a static sample, with each subsequent simulation at a spinning speed of 2000 Hz, 4000 Hz, and 20000 Hz. As the spinning speed surpasses the size of the interaction, the interaction is completely averaged, leaving a liquid like spectrum.

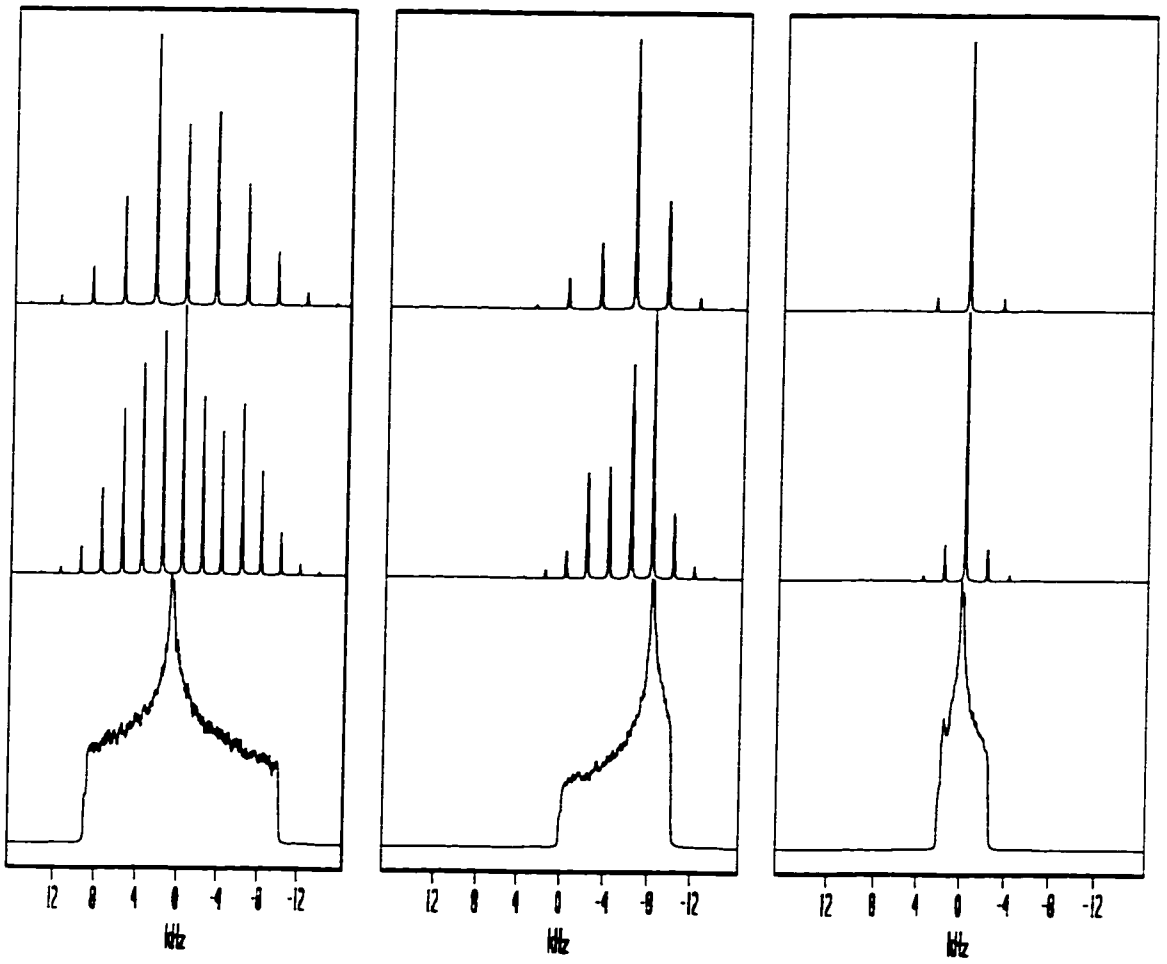

η=0.81
Ω=160 ppm

η=0.81
Ω=80 ppm

η=0.81
Ω=40 ppm

Figure 2.5. Simulations of a carbonyl carbon showing the effects of motion on the chemical shift anisotropy. On the left, the rigid powder pattern is shown on the bottom, along with changes as a function of spinning. In the middle, the narrowing could be observed by either a fast rate, mid-angle motion or a large angle, mid-rate motion. On the right is a very averaged powder pattern that could result from high frequency, multiaxial motion. These simulations were generated by changing the chemical shift tensor values, not by simulating a specific motion, so any motion implied is based on the knowledge of motional averaging on the chemical shift tensor and not on a direct simulation of motion.

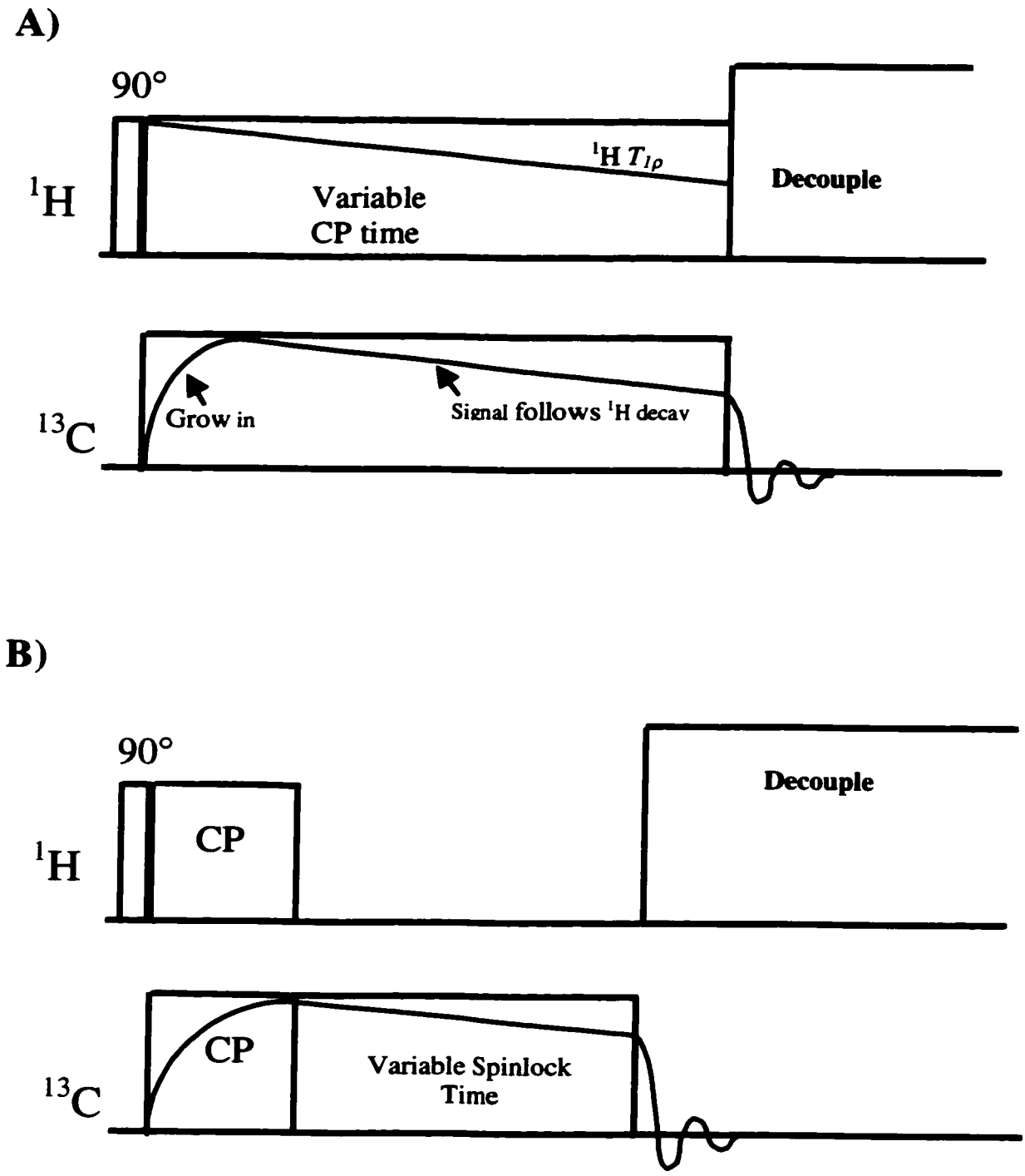

Figure 2.6. A) ^{1}H $T_{1\rho}$ pulse sequence used to determine the overall motion of a sample. B) The ^{13}C $T_{1\rho}$ pulse sequence allows determination of site specific motion. The magnetization is shown as a function of time to emphasize the different mechanisms present in each experiment.

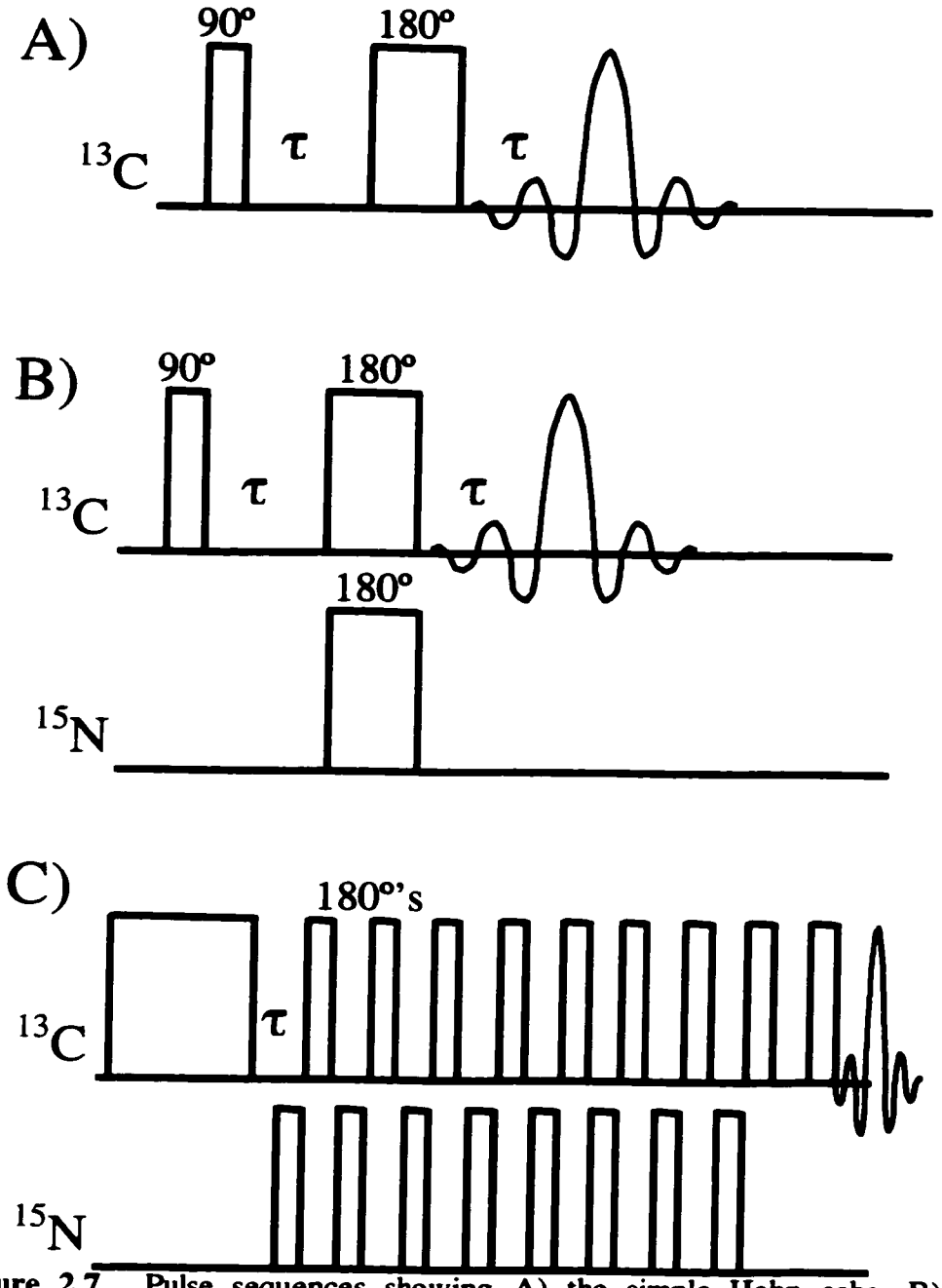

Figure 2.7. Pulse sequences showing A) the simple Hahn echo, B) the SEDOR experiment, which is equivalent to the REDOR experiment when spinning is added, and C) the REDOR experiment used for this work, incorporating XY8 phase cycling on both channels to minimize off resonance and finite pulse effects. In the XY8 REDOR experiment, the 180° pulses are evenly spaced on the rotor period (^{13}C) and the ½ rotor period (^{15}N), and were kept to less than 10% of the rotor period to avoid finite pulse effects. The FID was collected on an additional echo pulse.

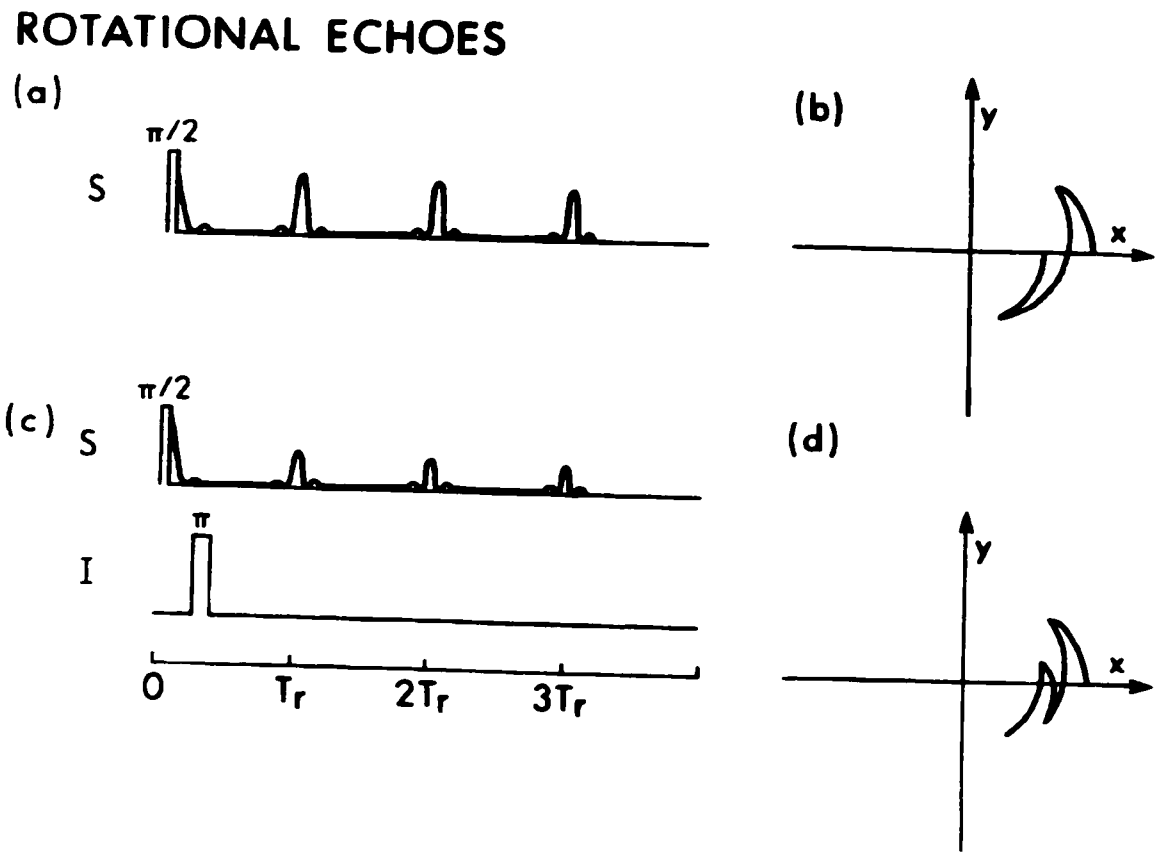

Figure 2.8. Magnetization as a function of time under rotational echoes without I spin pulses and with I spin pulses, showing that the dipolar coupling is not averaged when a pulse is applied to the I spins.

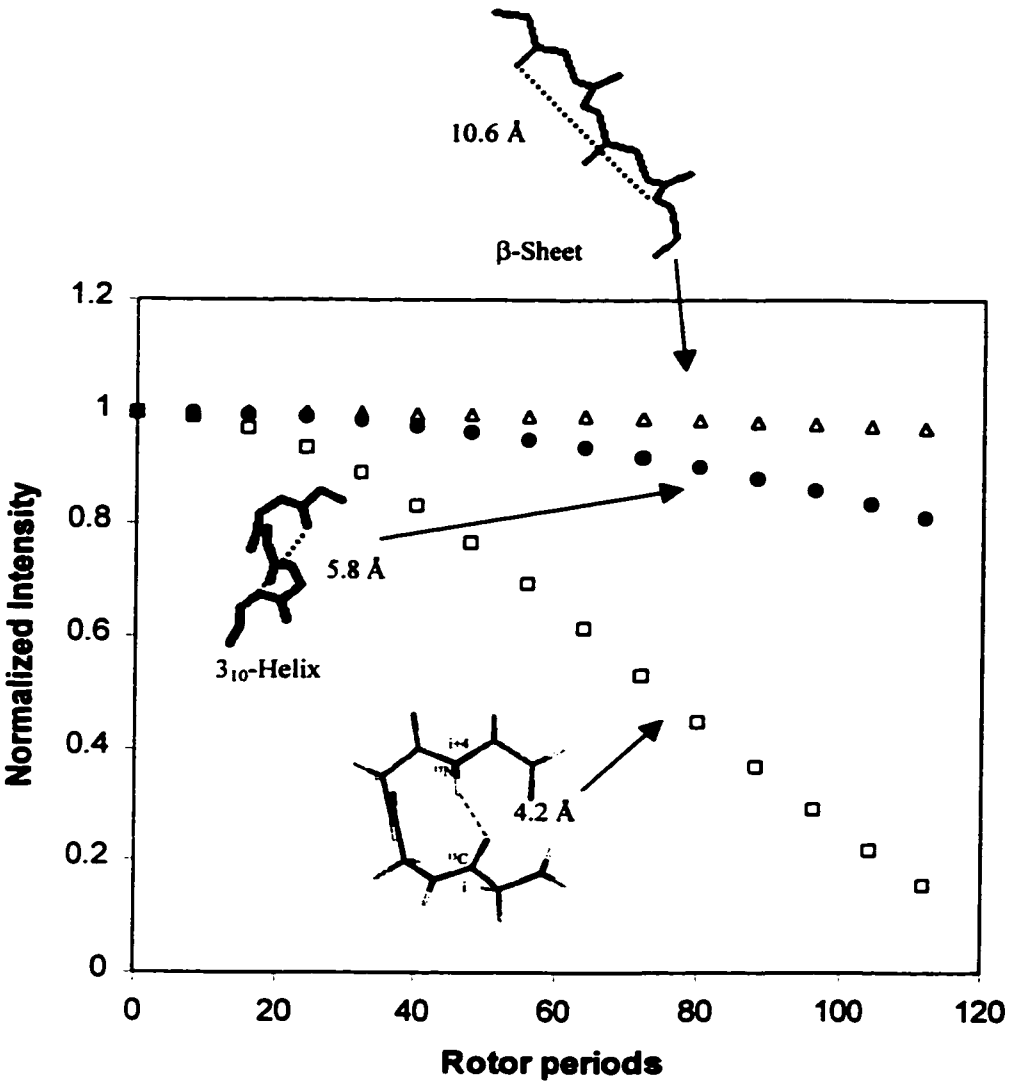

Figure 2.9. REDOR dephasing curves are shown as a function of secondary structure for the (i i+4) labeled ^{13}C-^{15}N spin pair. The distance across the hydrogen bond in the α-helix is easily measured, whereas the same labeling scheme in the β-sheet is not measurable by REDOR.

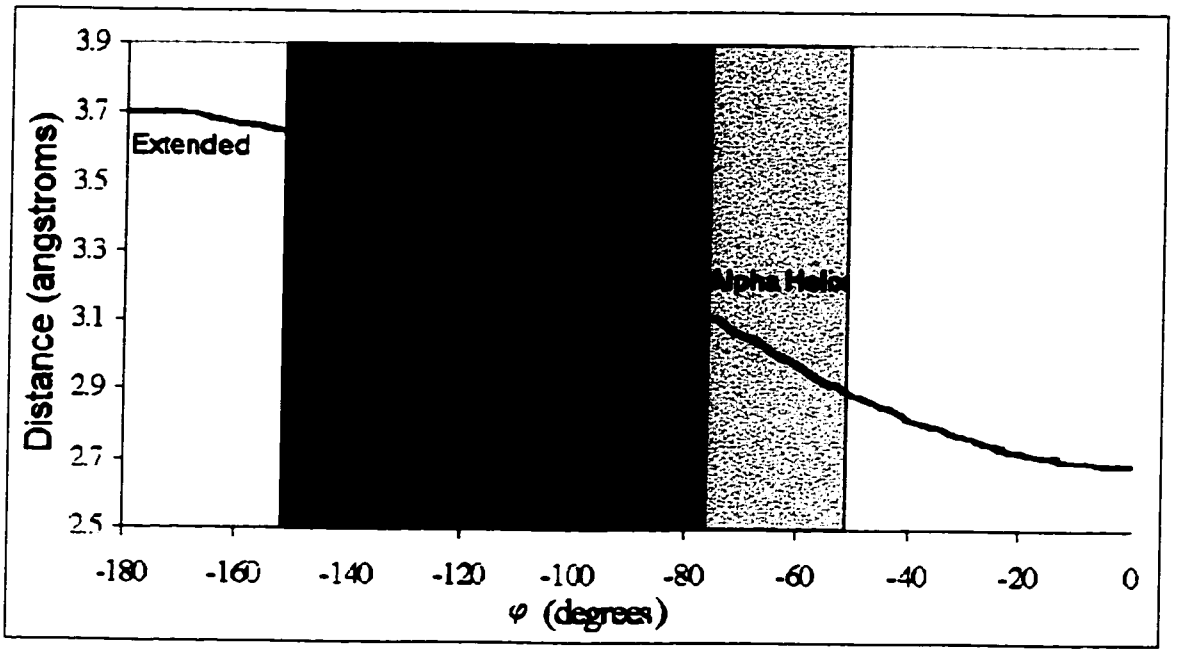

Figure 2.10. Labeling two adjacent backbone carbonyl carbons determines the torsion angle φ. This maps out onto distance as shown above, with the common secondary structures indicated, based on work done by Smith, et al, 1996.

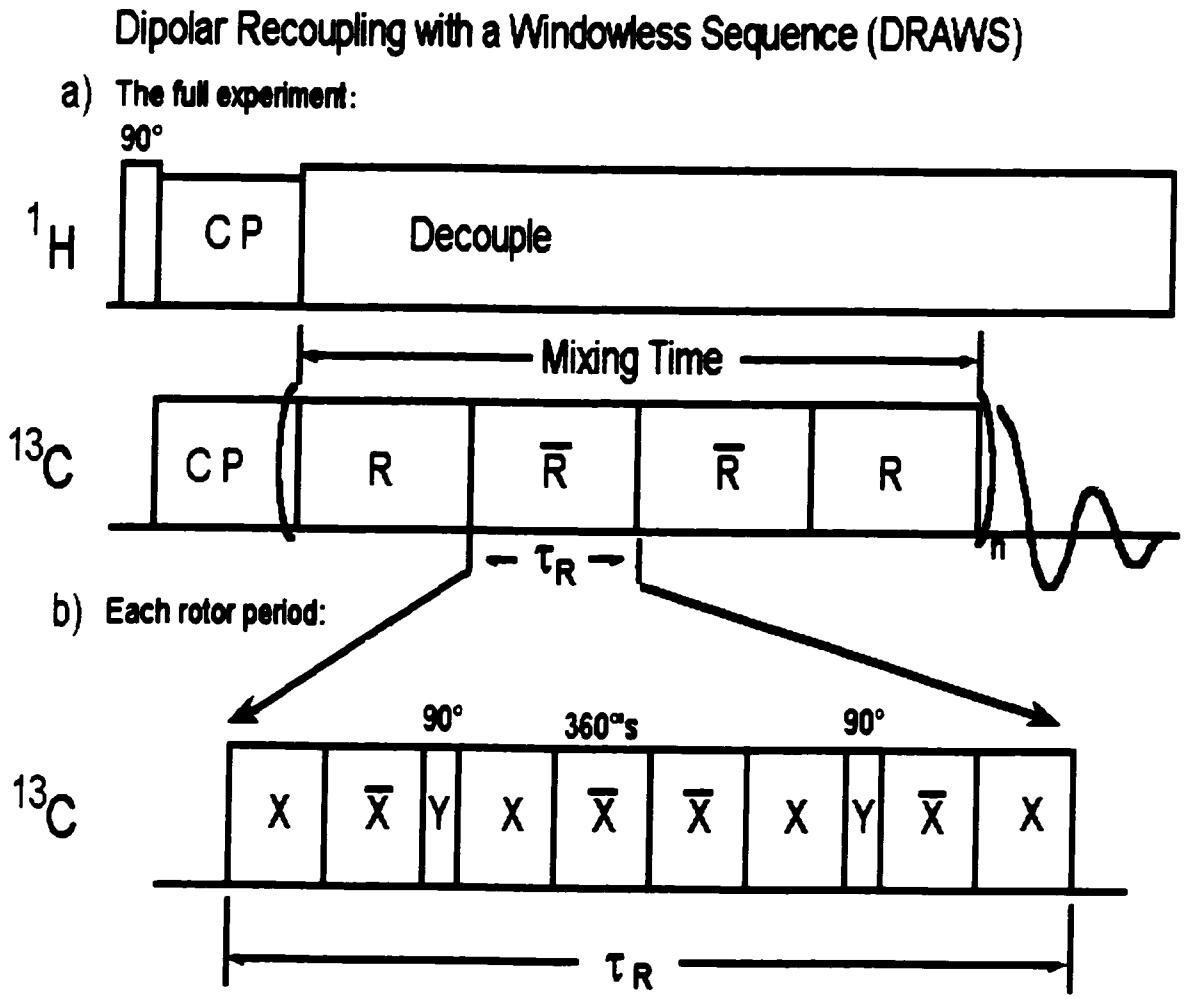

Figure 2.11. Dipolar Recoupling using A Windowless Sequence (DRAWS). The complete sequence with a 4-rotor supercycle is shown in (a). In (b) the basic sequence over one rotor cycle is shown. The more simplified DRAMA sequence is shown in (c) for comparison.

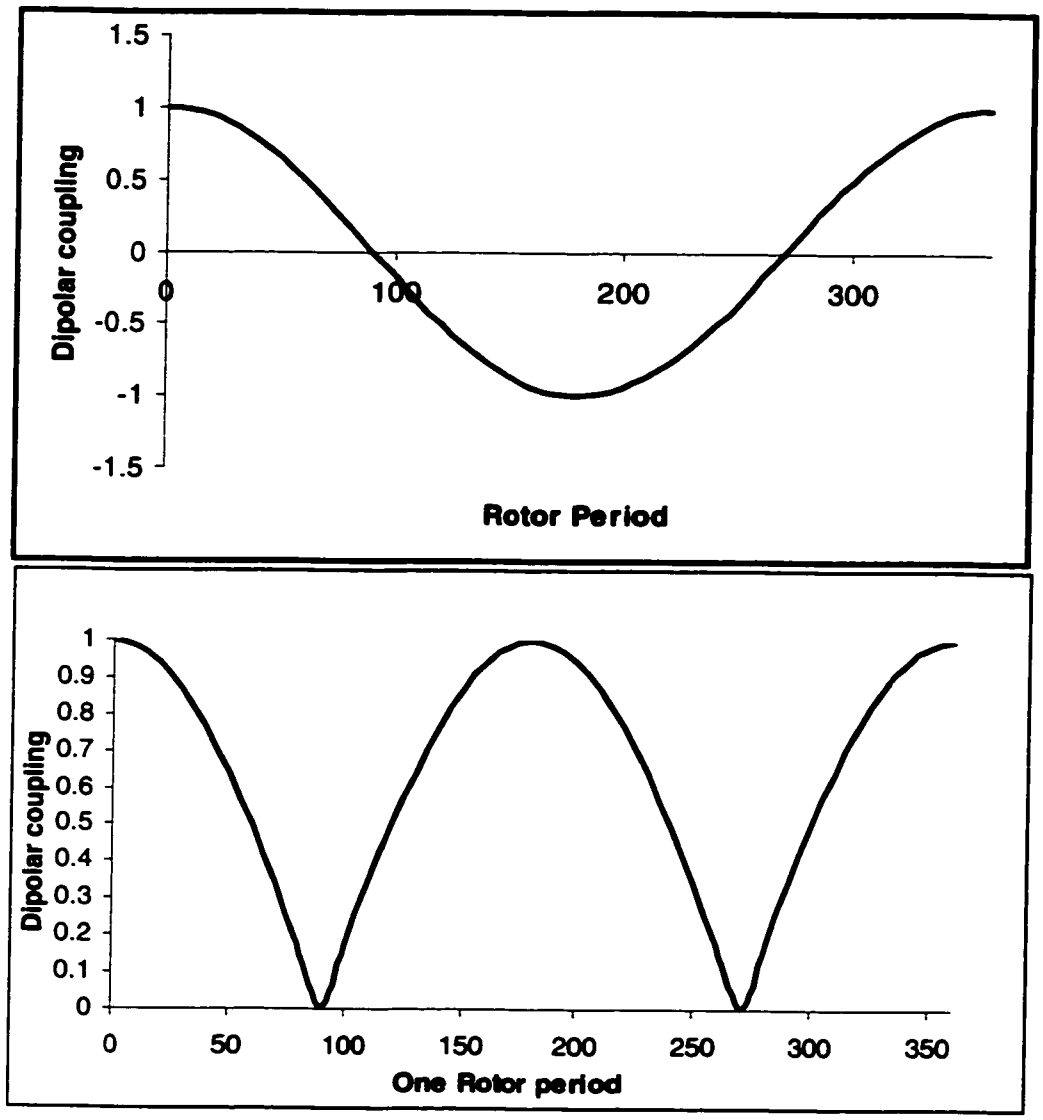

Figure 2.12. A pictorial representation of how the 90° pulses prevent the averaging of the dipolar couplings during DRAWS.

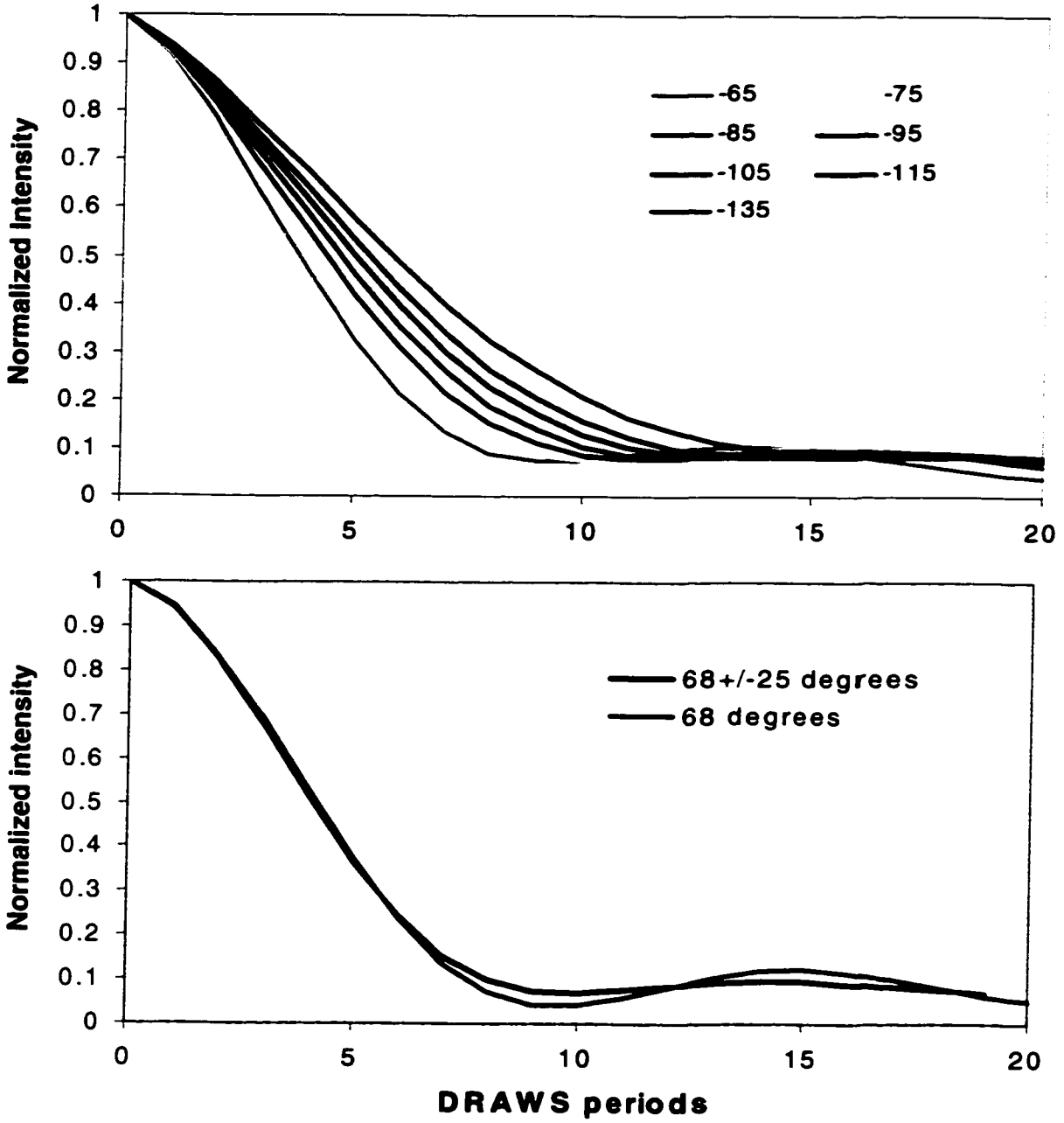

Figure 2.13. A) DRAWS curves as a function of distance, showing the distinguishability between curves for every 10° in the dihedral angle, φ, which corresponds to a distance of 0.1 Å. B) These two curves show the sensitivity of the endpoints in DRAWS to conformational distributions, specifically with the loss of oscillation when a distribution is present. Also of significance is the independence of the first 7 msec on a distribution, thus the average measured distance can be determined carefully in spite of a distribution.

CHAPTER 3:

MATERIALS AND METHODS

3.1 Materials

Protected amino acids and preloaded resins were purchased from Novabiochem (San Diego, CA) and Advanced Chemtech (Louisville, KY). Carbonyl ^{13}C- and ^{15}N - labeled alanine, serine, phenylalanine, leucine, isoleucine, and glycine were purchased from Cambridge Isotope Laboratories (Andover, MA).

SN15-LG, SN15-pSF, SN15-G, Stath-SS, Stath-pSF, Stath-FL, Stath-LG, Stath-IG, Stath-Q and R-Stath-IG were purchased in crude form from United Biochemical Research, Inc. (Seattle, WA).

Materials used in the design of a 3-channel probe were purchased at the following locations: vespel, Kel-F, brass tubing, phenolic rod and copper tubing were purchased from Small Parts, Inc (Miami Lakes, Fl). Finger stock was purchased from Instrument Specialties (Placentia, CA). Aluminum tubing for the body was obtained at LMJ (Seattle, WA). Fixed capacitors were purchased at and variable capacitors were purchases at Voltronics. Microstock (West Point, PA) supplied all semi-rigid coax and N-type, SMA and BNC connectors. The spin rate detector was purchased and installed by the University of Washington, Department of Chemistry Electronics Shop. All other items were obtained and fabricated in the University of Washington, Department of Chemistry Machine Shop.

3.2 FMOC Protection of Labeled Amino Acids

FMOC protection of labeled amino acids was accomplished using a standard procedure modified from Carpino and Han.[1] 3.8 mmole of labeled amino acid was placed in a 100 mL round bottom flask with 15 mL of warm 10% Na_2CO_3, with excess added as necessary until the amino acid was dissolved. 4.07 mmole Fmoc-OSu (9-Fluorenylmethyloxycarbonyl-N-hydroxysuccinimide) was dissolved into 10 mL dioxane and added to the amino acid solution. This was stirred for 24 hrs, another 150 mg of Fmoc-OSu was added and stirred for an additional 24 hours. To clean up, the solution was diluted with 50 mL of water and washed 3 times with 20 mL diethyl ether. Ethyl acetate (50 mL) was added and the pH was brought to 2 with concentrated HCl (~5 mL). The ethyl acetate layer was washed 2 times with 1N HCl, 2 times with water, dried over MgSO4 and rotovapped. Purity was checked by TLC with 10:1 toluene:acetic acid, and typically used without further purification. Yields were >95%.

3.3 Peptide Synthesis and Characterization

The peptides were synthesized with standard solid phase synthetic techniques using FastMoc[2,3] chemistry on an automated Applied Biosystems 433A peptide synthesizer starting with Fmoc-Gly-Wang or Fmoc-Gly-Novasyn-TGA preloaded resin (substitution 0.4 mmol/g and 0.13mmol/g, respectively). To introduce isotopically labeled phosphoserine, the unphosphorylated peptide was synthesized with labeled serine and subsequently phosphorylated using di-tert-butyl-N,N-diisopropylphosphoramidite followed by oxidation with 5-6M t-butylhydroperoxide to yield the t-butyl protected phosphate moiety (see below for procedure). In all other cases, phosphoserine was

incorporated during peptide synthesis using commercially available Fmoc-Ser[PO(OBzl)OH]-OH. Capping with acetic anhydride and double coupling were used in most cases to improve the yield and purity.

The peptides were cleaved from the resin using King's reagent (10-15 mL volume per gram of peptidyl resin, 82.5% TFA, 5% water, 5% thioanisole, 5% phenol and 2.5% ethane dithiol). After cleavage, the resin was filtered and the TFA removed under vacuum, taking care to neutralize the volatile TFA with an inline trap of saturated sodium bicarbonate solution. The concentrated peptide/scavenger solution was added dropwise to 50 mL of 0°C t-butyl methyl ether, immediately precipitating the peptide as a white solid. This was spun down and the peptide was washed 2 additional times with 0°C t-butyl methyl ether, rinsing the reaction flask with TFA and adding to the cold t-butyl ether as necessary. After the final rinse, the peptide was dried under N_2, brought up in water and lyophilized.

Purification was carried out on a Rainin HPLC C-18 reverse phase column using a water/acetonitrile solvent system with 0.1% TFA. Flow rates of 15-20 mL/minute were used with a gradient of 20-40% acetonitrile at 1% per minute and detecting at 222 nm. In the case of a single component, 2 mL injections with concentrations of 10-20 mg/mL were used, and the peptide collected at 32-35% acetonitrile. If closely retained impurities were present, lower concentrations were used as necessary. Peptide fractions were lyophilized and analyzed by MALDI (matrix assisted laser desorption/ ionization) mass spectrometry to establish composition and purity.

3.4 Protein Synthesis and Characterization

Statherin-$I_{11}G_{12}$ (Stath-IG) was chemically synthesized using the same procedures as for SN15 with FMOC-Phe-Novasyn TGA resin at a substitution level of 0.16 mmole/g. Capping was used after each coupling procedure and double coupling was incorporated for Asp-1 to Leu-29. The other statherin samples were synthesized by United Biochemical Research, Inc. using similar procedures, with the exception that no capping or double coupling was incorporated, replacing those chemistries with 4 hour coupling times. 0.63 mmole/g substituted resin was used. One exception to this was R-Stath-IG, which had all of the pS, R and isotopic labels double coupled and used 0.16 mmole/g substituted resin.

All post phosphorylation utilized the procedure that follows. Cleavage was carried out in the same manner with a larger volume as indicated (15 mL volume per gram of peptidyl resin, 82.5% TFA, 5% water, 5% thioanisole, 5% phenol and 2.5% ethane dithiol). The solution ranged from green to dark brown during cleavage. After precipitating statherin from t-butyl methyl ether, the protein was purified with HPLC, detecting at 275 nm, with the pure statherin peak coming off at approximately 40% acetonitrile. Analysis for molecular weight and purity was done using either MALDI or electrospray mass spec.

3.5 Post-phosphorylation

Introduction of isotopically labeled phosphoserine was accomplished by synthesizing the unphosphorylated peptide with a TFA cleavable Boc terminal protecting group on the N-terminus. Before cleaving the peptide, the following phosphorylation

procedure was utilized (the numbers listed here take into account 2 phosphoserine groups). 14 mmole 1-H-tetrazole was placed in a 25 mL round bottom and purged with argon. 15 mL of DMF (freshly distilled from calcium oxide after drying over potassium hydroxide) was added under argon. 5.71 mmole dibenzyl diisopropyl phosphoramidite was added to the DMF/tetrazole mixture under argon and the entire solution was transferred to ~0.1 mmole dried peptide + resin, and allowed to stir for 1 hour under argon. The peptide was filtered and washed quickly with DMF, transferred into a clean dry flask and covered with DMF. 7.5 mL t-butyl hydroperoxide in decane was added and stirred for 30 minutes, then filtered, the resin washed with DMF, methanol and ether and dried under vacuum overnight before cleaving. Yields varied widely from 50-90%, but impurities were easily separated on the HPLC.

3.6 Model Peptides and Model Compounds

Doubly labeled carbonyl peptides utilized for DRAWS setup were prepared as follows. Purified ***AG***G was prepared by Peter Bower and diluted to 10% with natural abundance AGG to remove intermolecular dipolar couplings, where the italicized bold residues are labeled at the backbone carbonyl carbon position. The peptide was then crystallized from water and analyzed using X-ray diffraction to verify a structure agreeing with published results.[4] ***FL***R, prepared by Manish Mehta, was diluted to 20% with natural abundance FLR and lyophilized for study.

^{13}C=O, ^{15}N glycine was diluted to 10% with natural abundance glycine and recrystallized from water:ethanol by evaporation and used for REDOR setup. Chemical shift spectra confirmed a single conformation.

3.7 Hydroxyapatite (HAP) Preparation

The HAP crystals were prepared at Pacific Northwest National Labs by the following procedure. Dropwise addition of 40 mL of a solution containing 0.25M $(NH_4)_2HPO_4$ and 2.7% NH_4OH, to 0.9L of boiling 0.20M $Ca(NO_3)_2$ was done over a 3 hour period. The slurry was then refluxed for 15 additional minutes. The product was filtered, dried at 110°C and calcined at 900°C for 24 hours. HAP was characterized by X-ray powder diffraction to confirm the absence of other calcium phosphate phases. Crystal specific surface area was determined to be 17 m^2/g using N_2 BET measurements, and was used for initial peptide binding. For protein samples and some of the N15 samples, HAP was prepared as above, but the product was allowed to remain in solution until ready for use and had a specific surface area of 77 m^2/g.

3.8 Phosphate Buffer

pH 7.4 phosphate buffer was prepared with the following concentrations: 100 mM NaCl, 40 mM KCl, 4.3 mM Na_2HPO_4, and 1.4 mM KH_2PO_4. This was modified from standard PBS buffer in that the K^+/Na^+ ratio was increased to minimize pH changes upon freezing.[5]

3.9 Dissolution of Statherin for Binding

The tendency for statherin to aggregate in aqueous solutions required special conditions for dissolution. Typically, 40 mg of statherin was placed in a solution of 25% acetonitrile/water solution at pH=2 (with HCl) at a concentration of 10 mg/mL (approximately 2 mM). This concentrated solution was added to 50 mL PBS and 150 mL

water and brought to pH 7.4. The acetonitrile was then removed under vacuum and the volume brought back up to 200 mL with water to make a solution of 3.7×10^{-5} M statherin. The solution was then added to HAP crystals as described below. After binding, the supernatant was kept frozen and reused for additional binding experiments. 10-15 mg of protein dissolved in approximately 5 mL 25% acetonitrile/water at pH=2 was added to the supernatant to replace what had been removed before another binding was undertaken (as estimated by the amount of protein removed from solution to cover a monolayer of 100 mg of 77 m2/g HAP crystals, weighted to the amount of surface area accessible to the protein). After adding additional protein, the pH was again brought to 7.4, the acetonitrile removed, and the final volume brought back to 200 mL, as before.

3.10 Preparation of Lyophilized Peptide

Typically, solutions of 1.5-3 mM purified peptide in PBS were frozen with liquid nitrogen and lyophilized. They were stored in the freezer until ready for use. A few experiments were done using a "quick-freezing" procedure to prevent loss of structure from slow freezing.[6] A bath was made consisting of a falcon tube containing isopentane, nested in a lyophilizing jar containing isopentane, nesting in a liquid nitrogen dewar (shown in Figure 3.1), keeping the isopentane in the lyophilizing jar between –80° and –100° C. The peptide/buffer solution to be lyophilized was sprayed (small sprayed droplets are preferable to a stream to allow for more rapid freezing) into the falcon tube containing isopentane using a 100-500 μL syringe, allowing time between additions of

solution to let the isopentane recool. Once the entire solution has been added, quickly (using gloves!) centrifuge and decant the isopentane from the falcon tube and lyophilize.

3.11 Peptide Adsorption to HAP

The phosphorylated peptides were adsorbed to HAP by adding a solution of 1.5-3 mM peptide in phosphate buffer to 100 mg of HAP crystallites (previously sonicated for 20 minutes and washed 3x with phosphate buffer) and adjusting to pH 7.4 with HCl or NaOH, as necessary. The mixture was shaken vigorously for 5 minutes, then allowed to equilibrate with periodic mixing. After 2-4 hours, the HAP crystallites were separated from the peptide in solution via centrifugation and washed repeatedly with buffer solution. The peptide adsorbed to HAP was frozen and lyophilized in preparation for SSNMR experiments.

For preparation of hydrated samples, the sample was not lyophilized, but was placed in the freezer after the last buffer wash until ready for use.

3.11.1 Quantitating Peptide adsorption

Fluorescence measurements were made on some of the peptide samples to quantitate the extent of peptide binding. Samples were taken from the supernatant before adding hydroxyapatite, after the hydroxyapatite was removed and of each of the buffer washes. 10 μL of sample was added to 1 mL of fluoraldehyde. Fluoraldehyde attacks primary amine groups, producing a fluorescent species that can be quantified. Since all N-terminal amines are attacked, arginine and lysine sidechains are subject to reaction and could result in incorrect concentration measurements. This was taken into account by generating a calibration curve using known concentrations of N15-RGD

(DpSpSEEKFLRRIGRFGPGRGDS), very similar to SN15. The calibration curve was generated by Michele Gilbert and gave the following equation relating fluorescense and concentration: Fl = 1.198e7[X] + 7.143e1. The curve was based on 100 μL of sample in 1 mL fluoraldehyde, so a dilution factor of 10 was taken into account.

Each sample measurement was made in triplicate, and the contributing background subtracted before calculating the peptide concentration. Instrumental parameters for the fluorometer were Ex/Em slit 5.0 nm, 240 scans/min, PMT setting = 700, response = 2 seconds and shutter control = on. The excitation wavelength was 360 nm and the emission spectrum was obtained from 400-500 nm. The fluorescence measurement was taken at 445 nm.

3.12 Samples for Dynamics Studies

The HAP/buffer slurry was transferred to a rotor and packed by repeatedly spinning the sample and removing excess solution, leaving the final surface adsorbed peptide in the bulk hydrated state. To facilitate direct comparisons between hydrated and lyophilized samples, the hydrated spectra were characterized first, with the same sample being subsequently frozen and lyophilized in the rotor prior to acquisition of the lyophilized spectra.

3.13 SSNMR Studies

3.13.1 CPMAS for SN15

Chemical shift spectra utilized cross polarization with magic angle spinning (CPMAS) on a homebuilt spectrometer operating at a ^{13}C frequency of 125.74 MHz using a home-built, triply resonant MAS probe. These experiments employed a ^{1}H 90°

pulsewidth of 5 μsec followed by a contact time of 2 msec. FID acquisition was collected after a 180° echo pulse in synchrony with spinning speeds of 3000 and 5000 Hz. 512 scans were taken for the samples off the surface. The samples on the surface were signal-averaged for 5120 scans (SN15-FL) or 10240 scans (SN15-IG and SN15-pSpS). The chemical shifts were referenced externally to crystalline 1,4-^{13}C succinic acid and converted to a tetramethylsilane reference by the addition of 180.8 ppm.

3.13.2 CPMAS for Statherin

Statherin CPMAS spectra were taken on two different 500 MHz narrowbore magnet, one with a homebuilt console and triple resonance probe, the other with a Chemagnetics Infinity spectrometer and Chemagnetics 2-channel probe. The chemical shift spectra used for CP efficiency were taken on the homebuilt spectrometer, with identical parameters as listed for the SN15 peptide. The spectra for the CSA and linewidth measurements for the hydrated surface bound samples were taken on samples prepared seperately on the Chemagnetics spectrometer. A 7.5 μsec 90° pulse was used, followed by a 1.5 msec CP spinlock and immediate acquisition, with about 60 kHz decoupling at a spinning speed of 3 kHz. The lyophilized CSA measurements and linewidths were made on a Chemagnetics spectrometer operating at 300 MHz proton frequency, using a 6.0 μsec 90° pulse, a 1.5 msec CP pulse, with approximately 80 kHz decoupling and a spinning speed of 1800 Hz.

3.13.3 Relaxation Measurements for SN15

^{13}C $T_{1\rho}$ relaxation measurements for SN15 were taken for peptides under three conditions: 1) lyophilized from buffer, 2) bound to the surface and 3) lyophilized, and bound to the surface and hydrated. The measurements were taken on a 2 channel Chemagnetics probe using a Chemagnetics Infinity spectrometer operating at a proton frequency of 300 MHz. Cross polarization was maintained for 1.5 msec at 42 kHz field, followed by a lock time varying from 0.05 to 4.55 msec, followed immediately by acquisition with a decoupling frequency of 70 kHz. 2048 scans were taken per data point and three repetitive sets were taken for error analysis.

^{1}H $T_{1\rho}$ measurements were taken on a 500 MHz proton frequency homebuilt spectrometer and a 3-channel homebuilt probe. A 90° pulse of 5 μsec was used, followed by a cross polarization length varying from 0.5 msec to 5 msec. The FID was collected with 110 kHz decoupling.

3.13.4 Relaxation Measurements for Statherin

^{13}C $T_{1\rho}$ measurements for statherin were performed using a Chemagnetics 2-channel probe and Chemagnetics Infinity console with an operating proton frequency of 500 MHz. The spinning speed was either 5000 Hz or 7000 Hz, the cross polarization and spinlock fields were 35 kHz, the lock time was varied from 0.05 to 4.55 msec and the decoupling field was 60 kHz.

The $T_{1\rho}$ relaxation measurements for surface bound statherin were repeated under identical conditions as listed above for SN15, specifically, at 300 MHz proton frequency, with a 42 kHz B_1 field.

3.13.5 DRAWS experiments

DRAWS experiments were carried out on a homebuilt spectrometer operating at a ^{13}C NMR frequency of 100.7 MHz using a Doty Scientific triply resonant magic angle spinning probe or a 2-channel homebuilt probe. DRAWS is very sensitive to the instrument setup and as such, the following procedure was used. Phase transients were optimized as described elsewhere.[7,8] Cross polarization was optimized and generally employed a 6–7 μsec ^1H 90° pulse followed by a 2 msec mixing time. The DRAWS pulse sequence consists of a windowless pulse train applied in synchrony with the rotor cycle.[9] The transverse magnetization is then observed stroboscopically every four rotor cycles and normalized with respect to the magnetization observed without any DRAWS dephasing.

The exact 90° and 360° utilized in the DRAWS pulse sequence were determined by using the series of pulse sequences shown in Figure 3.2. The setup was usually checked on the model compound ***AG***G. A typical fit is shown in Figure 3.3, accounting for natural abundance by subtracting 20.6% (measured experimentally by comparison to the natural abundance glycine carbonyl) and renormalized. A natural abundance AGG sample was also run to determine the single quantum relaxation (T_2^{SQ}). The natural abundance curve typically fit well to 60 to 100 Hz, and was directly dependent on the

decoupling field used, under the condition that the remaining set up was okay as determined by a correctly fitting distance. The spinning speed was then calculated using the equation: Rotor period = 2*(90° pulse time) + 8*(360° pulse time). It is important to note that due to field inhomogeneities, the 360° pulse time was not necessarily exactly 4x the 90° pulse time. Typical values for the ^{13}C r.f. field used during the DRAWS mixing period were 33-35 kHz, corresponding to 7-7.5 μsec π/2 pulse, respectively, with proton decoupling of >110 kHz applied throughout the DRAWS and acquisition periods. The samples were spun at approximately 4000 Hz, matched carefully with the DRAWS cycle time. Each DRAWS experiment was run at least 3 times, but more typically 5 times, using between 512 and 2048 scans per spectrum and a repetition time of 4 sec. Adsorbed samples consisted of approximately 2-10 mg of phosphopeptide adsorbed to 100 mg of HAP packed into a 5 mm rotor. The Simulated DRAWS decay curves were calculated using numerical methods that incorporated the observed relaxation times from singly-labeled peptides, chemical shift anisotropy's and experimental parameters.

3.13.6 REDOR for SN15 and Statherin

REDOR experiments utilized a Chemagnetics spectrometer operating at 300 MHz proton frequency. A triply-resonant Chemagnetics probe was used, with a ^{13}C r.f field of 43 kHz (11.6 μsec π pulse), an ^{15}N field of 45 kHz (11.1 μsec π pulse) and a decoupling field of 70 kHz throughout, at a spinning speed of 4 kHz. XY8 phase cycling was used on both channels to minimize pulse imperfections and offset effects, with the dephasing pulses on the ½ rotor period and the observe pulses on the rotor period. 1024 scans were

taken for the peptide off the surface and 2560 scans for the adsorbed peptide, every 8 rotor cycles, out to 104 rotor periods for both samples, using a 3 second pulse delay for room temperature experiments and a 1 second pulse delay at low temperatures. Simulated REDOR decay curves were calculated using numerical methods that incorporated chemical shift anisotropy's and experimental parameters and accounted for finite pulse effects.

The REDOR setup was done using two samples. An uncut, 1 bond distance $^{13}C_{\alpha}$-^{15}N very small volume alanine sample was used to set the 180° times for both nuclei, using the pulse programs shown in Figure 3.2. The REDOR curve was run on this using a single pulse REDOR experiment (shown in Figure 2.8B), rather than XY8, so the early time data could be observed. The experimental spectra as a function of rotor cycles are shown in Figure 3.4 (top). The integrated intensities fit well to a 1.5-1.55 Å distance (895 Hz), as shown in Figure 3.4 (bottom). Once the setup was optimized so the one bond distance alanine sample fit to the correct distance, a 2 bond distance, ^{13}C=O, ^{15}N glycine was measured. A very small volume was used for the initial setup, but was increased to the maximum volume, determined to be just under the point where the dephasing curve becomes affected by the field inhomogeneity. This sample fit well to a distance of 2.5 Å (193 Hz) with an 8.3% subtraction to account for the natural abundance contribution. Experimental spectra and simulated dephasing curves are shown in Figure 3.5 (top and bottom). During the first instrument setup, a 4.2 Å distance helical sample was checked to confirm the setup at a known longer distance. The peptide, prepared by Peter Bower, with the primary sequence Ac-LKK*L(^{13}C)*LKL*L(^{15}N)*KKLLKL was

designed and experimentally determined with DRAWS and DQDRAWS to be helical. It fit to the expected distance of 4.15-4.2 Å, as seen in Figure 3.6.

All REDOR samples were prepared with a single carbonyl label and a single 15N label. An initial attempt was made to measure a REDOR distance on the doubly carbonyl labeled DRAWS sample, that had a ^{15}N included in the synthesis for the purpose of measuring the i i+4 distance (specifically, ...***F(^{13}C)L(^{13}C)***RRI***G(^{15}N)***....). The S_o curve was found to dephase much too quickly, so that by 104 rotor periods, the S_o signal was down to 10% of the original signal, leaving almost no signal to discriminate S/S_o values. Additionally, the natural abundance background increases to 50% due to the second carbonyl, making accurate results in the face of poor signal to noise very difficult. Experimental spectra are shown as a function of the rotor period for the doubly carbonyl labeled sample and the singly carbonyl labeled sample in Figure 3.7, clearly showing the impact of the nearby carbonyl on the dephasing curve.

Setup for low temperature experiments was done at room temperature and rechecked on model compounds at low temperature. The probe was fitted with a cold temperature stack to transfer in temperature controlled liquid nitrogen blow off. The temperature in the sample rotor was determined using $Pb(NO_3)_2$, whose chemical shift is sensitive to the temperature according to the following equation, assuming room temperature is 25° C:

$$T = \frac{\delta(\pm)}{0.753 ppm/°C} + 25°C \qquad [3.1]$$

Hydrated samples were run at –25° C, experimentally determined to freeze out motion on the timescale of the REDOR experiment.

3.14 Background Subtractions

To remove the contribution from natural abundance decay in the dephasing curves, the background contribution for each peptide or protein had to be taken into account. For SN15, 9% carbonyl natural abundance subtraction was used for DRAWS (double carbonyl label) and a 16% carbonyl natural abundance subtraction for REDOR (single carbonyl label).

The full protein background subtraction was more complicated, due to the larger number of contributing species. For the DRAWS dephasing curves, 52 carbonyls contribute to the natural abundance signal, 41 of which are backbone carbonyl carbons, and the remaining 11 from the sidechains of 7 tyrosines, 3 glutamic acids, and 1 aspartic acid. Additionally accounted for is the dephasing due to the overlapping aromatic peaks from the tyrosine and phenylalanine, which contribute 60 carbons. The isotropic peak overlaps with the 1^{st} sideband on the right, but the most intense peak is in the 2^{nd} aromatic sideband which overlaps with the isotropic carbonyl peak (Figure 3.8). In total, about 70% of the aromatic intensity contributes to the 3 integrated carbonyl peaks. When both of these sources of background are taken into account, the carbonyl background is 19% and the aromatic background is 15.3%. The SQ dephasing of the carbonyl background was determined during each setup with a model compound. The aromatic subtraction was based on the dephasing curve measured from the aromatic peaks observed in the model compound, GFF (Figure 3.8).

For REDOR, the natural abundance subtractions included only the carbonyl contributions. Faster relative spinning was used, and typically only the center band was integrated, thus the contribution would be significantly reduced as compared to DRAWS. Additionally, an So curve was taken for every S curve, so the total correction curve contains both the carbonyl and aromatic decay. Estimates using a 21% contribution from the total aromatic intensity make a change of less than 0.1 Å for a 4.2 Å distance by simply adding a larger contribution to the total background. A more careful estimate on a 5.2 Å distance was made by estimating what the natural abundance dephasing would be for aromatics, based on the difference between the So curve for SN15 and statherin, which should correspond to the dephasing from the aromatics. Subtractions were then made using 34% contribution from the carbonyl dephasing curve and 8% from aromatic dephasing curve. In this more careful estimate, the distance fit to 5.1 Å (as compared to 5.2 Å), but was not statistically different than the 5.2 Å distance. Based on the small contribution, the estimates that are made to fit the distance likely contain as much error as the aromatic contribution itself, so it was left out of the equations, leaving a background correction of 37.3% due to the carbonyl carbons. Also taken into account was the contribution from couplings of the natural abundance carbons to the labeled nitrogen, including both a one and two bond distance. This contribution did not have a noticeable effect on the dephasing curves.

3.15 Simulations

Simulations were performed using code developed by Nathan Oyler (PhD thesis, to be published). DRAWS and REDOR dephasing curves were calculated using

numerical methods and to first order take into account the relative CSA orientations, chemical shift offset, the observed relaxation times measured with singly labeled peptides, and finite pulse effects. Chemical shift anisotropy, as well as spinning speeds and RF fields are also included in the simulations.

DRAWS simulations of experimental data were done in the following manner to take into account conformational distributions. The model compound AGG was fit by fixing the T_2^{SQ} to the value experimentally determined by the natural abundance sample, and letting the distance and T_2^{DQ} float until optimized using a reduced chi squared routine. The experimentally determined T_2^{SQ} and the fitting parameter T_2^{DQ} determined by fitting were then utilized to generate simulations ranging from $\varphi = 0° - 180°$, or 2.7-3.7 Å. The experimental data for SN15 and statherin were then fit to these simulations, and distributions of these simulations. This procedure was repeated for every setup, taking into account the new relaxation parameters.

REDOR curves were simulated for distances in the region of the observed dephasing. Since the S/So curve is used, relaxation is taken into account, so no fitting parameters are needed. Experimental values are reported as a range, and were not fit using a reduced chi squared routine.

3.16 Analysis of Conformational Distributions

Simulated DRAWS dephasing curves representing Gaussian distributions were generated by summing simulations using an increment of 0.5 standard deviations (σ) and weighting them according to their Gaussian probabilities out to 3 standard deviations (3σ). For each set of experimental data, a χ^2 analysis was performed for a series of

distributions about the average value determined by the first 5-8 msec of dephasing. The single conformation, Gaussian distribution models with standard deviations of ± 10°, ± 20°, ± 30°, and an average distribution of ± 50° were analyzed. The latter distribution was used, rather than a Gaussian distribution with a standard deviation of ± 50°, due to the inherent torsional constraints of the peptide bond. Lastly, weighted distributions representing φ angle populations observed in random coil, α-helix or 3_{10} helix protein secondary structures were simulated (see Figure 3.9). These weighted distributions are based on the observed torsion angles in secondary structures of 85 proteins, yielding distributions that are more representative of the torsion angles that are typically sampled for given secondary structures.[10]

The reduced χ^2 (χ_ν^2) values in Tables 2 and 3 were generated using the following equations[11,12]:

$$\chi^2 = \sum_i \frac{(E_i - S_i)^2}{\sigma^2} \qquad [3.2]$$

where E_i is the experimental value for data point i, S_i is the simulated value for data point i, σ is the standard deviation of the experimental data, and

$$\chi_\nu^2 = \frac{\chi^2}{\nu} \qquad [3.3]$$

where ν is the number of degrees of freedom. The relative probabilities were calculated using

$$\frac{P_1}{P_2} = \exp[-(\chi_1^2 - \chi_2^2)/2] \qquad [3.4]$$

where χ_1^2 is calculated for the simulation of a single conformation and χ_2^2 corresponds to the simulation of a given distribution. Therefore, a relative probability less than one ($P_2 > P_1$) indicates the experimental data is best described by the simulated distribution rather than a single conformation, and a relative probability greater than 1 ($P_2 < P_1$) indicates that a single conformation best describes the data. A relative probability between 0.51 to 1.95 (within a standard deviation) indicates the difference between the two simulations is statistically insignificant.

3.17 Notes to Chapter 3

1. Carpino, L. A. & Han, G. Y. The 9-Fluorenylmethoxy carbonyl Amino-Protecting Group. *Journal of Organic Chemistry* **37**, 3404-3409 (1972).

2. Fields, C. G., Lloyd, D. H., Macdonald, R. L., Ottesen, K. M. & Noble, R. L. *Peptide Research* **4**, 95-101 (1990).

3. *433A Peptide Synthesizer User's Manual* (Applied Biosystems Inc, 1993).

4. Lalitha, V., Subramanian, E. & Bordner, J. Structure and Conformation of Linear Peptides.4. Crystal Structure of L-alanyl-glycyl-glycine Monohydrate. *Indian Journal of Pure and Applied Physics* **23**, 506 (1985).

5. van den Berg, L. & Rose, D. Effect of Freezing on the pH and Composition of Sodium and Potassium Phosphate Solutions: the Reciprocal System KH2PO4-Na2HPO4-H2O. *Archives of Biochemistry and Biophysics* **81**, 349 (1959).

6. Christensen, A. M. & Schaefer, J. Solid-State NMR Determination of Intra- and Intermolecular 31P-13C Distances for Shikimate 3-Phosphate and [1-13C]Glyphosate Bound to Enolpyruvylshikimate-3-phosphate Synthase. *Biochemistry* **32**, 2868-2873 (1993).

7. Burum, D. P., Linder, M. & Ernst, R. R. A New "Tune-Up" NMR Pulse Cyclo for Minimizing and Characterizing Phase Transients. *Journal of Magnetic Resonance* **43**, 463-471 (1981).

8. Stringer, J. in *Chemistry Department* (University of Washington, Seattle, 1998).
9. Gregory, D. M. *et al.* Windowless Dipolar Recoupling: The Detection of Weak Dipolar Couplings Between Spin 1/2 Nuclei With Large Chemical Shift Anisotropies. *Chemical Physics Letters* **246**, 654-663 (1995).

10. Smith, L. J. *et al.* Analysis of Main Chain Torsion Angles in Proteins: Prediction of NMR Coupling Constants for Native and Random Coil Conformations. *Journal of Molecular Biology* **255**, 494-506 (1996).

11. Bevington, P. R. & Robinson, D. K. *Data Reduction and Error Analysis for the Physical Sciences* (WCB/McGraw-Hill, Boston, 1992).

12. Gebe, J. A., Allison, S. A., Clendenning, J. B. & Schurr, J. M. Monte Carlo Simulations of Supercoiling Free Energies for Unknotted and Trefoil Knotted DNAs. *Biophysical Journal* **68**, 619-633 (1995).

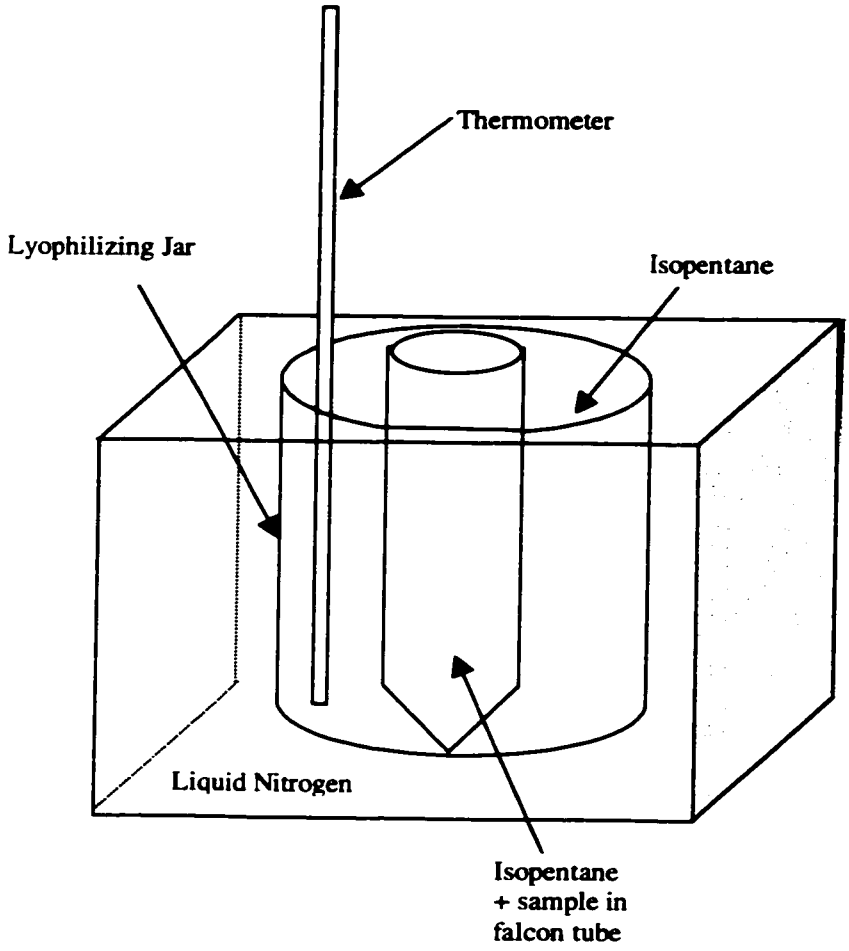

Figure 3.1. Quick-freeze apparatus. A falcon tube is nested inside a lyophilizing jar, which is in a dewar of liquid nitrogen. The lyophilizing jar and the falcon tube both contain isopentane. The isopentane is kept at -100°C to facilitate the instant freezing of the sample sprayed into the falcon tube.

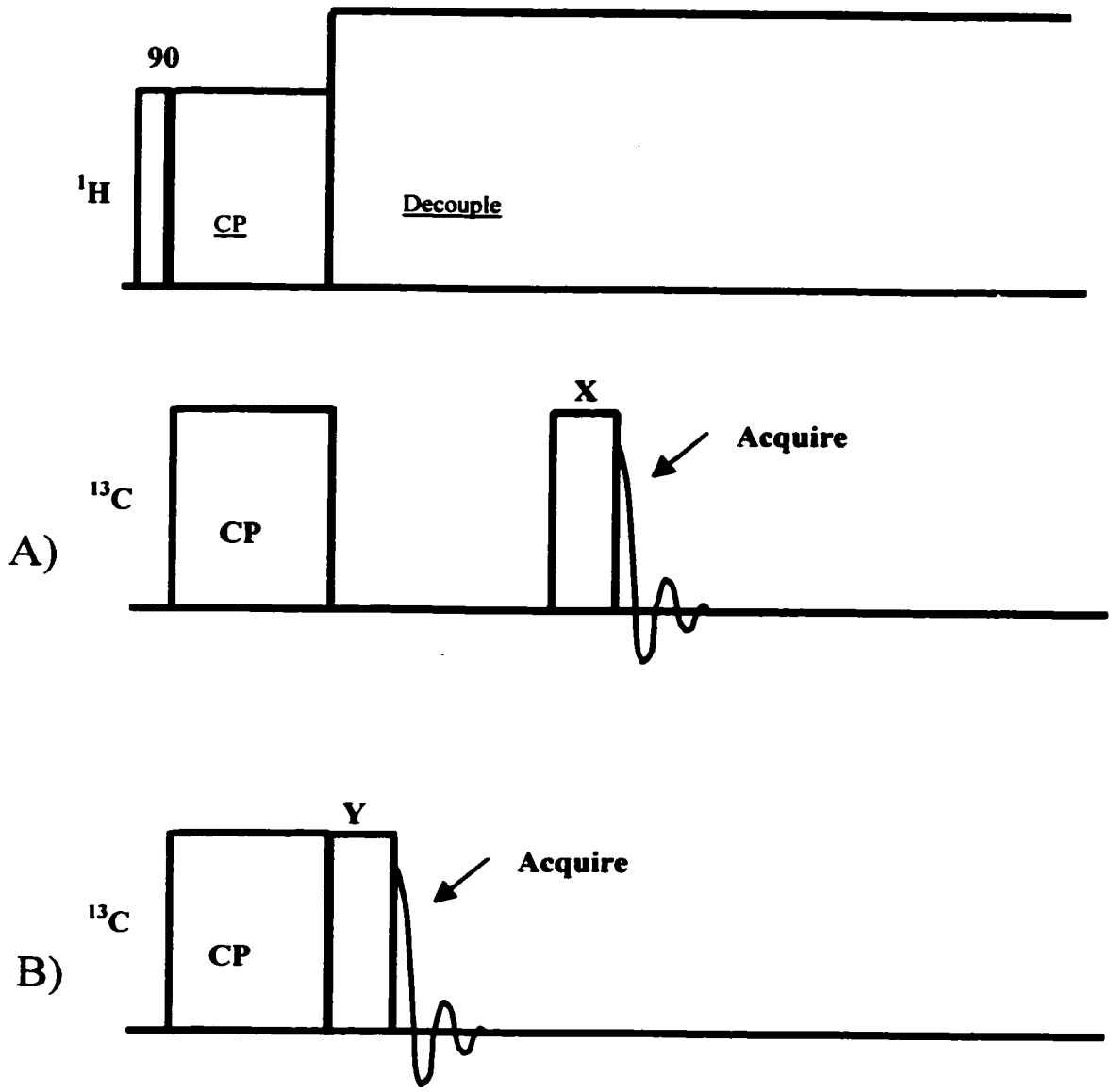

Figure 3.2 Pulse sequences used for setting up DRAWS and REDOR experiments. Sequence A was used for determining free standing pulse lengths. Sequence B was used to determine continuous RF pulse lengths. X and Y were made successively longer, varying from slightly less than a 90° pulse to slightly longer than a 360° pulse. The integrated intensities were then compared and could be analyzed visually (as was done for REDOR), or fitted using a MATLAB routine (as for DRAWS) to accurately determine the pulse length.

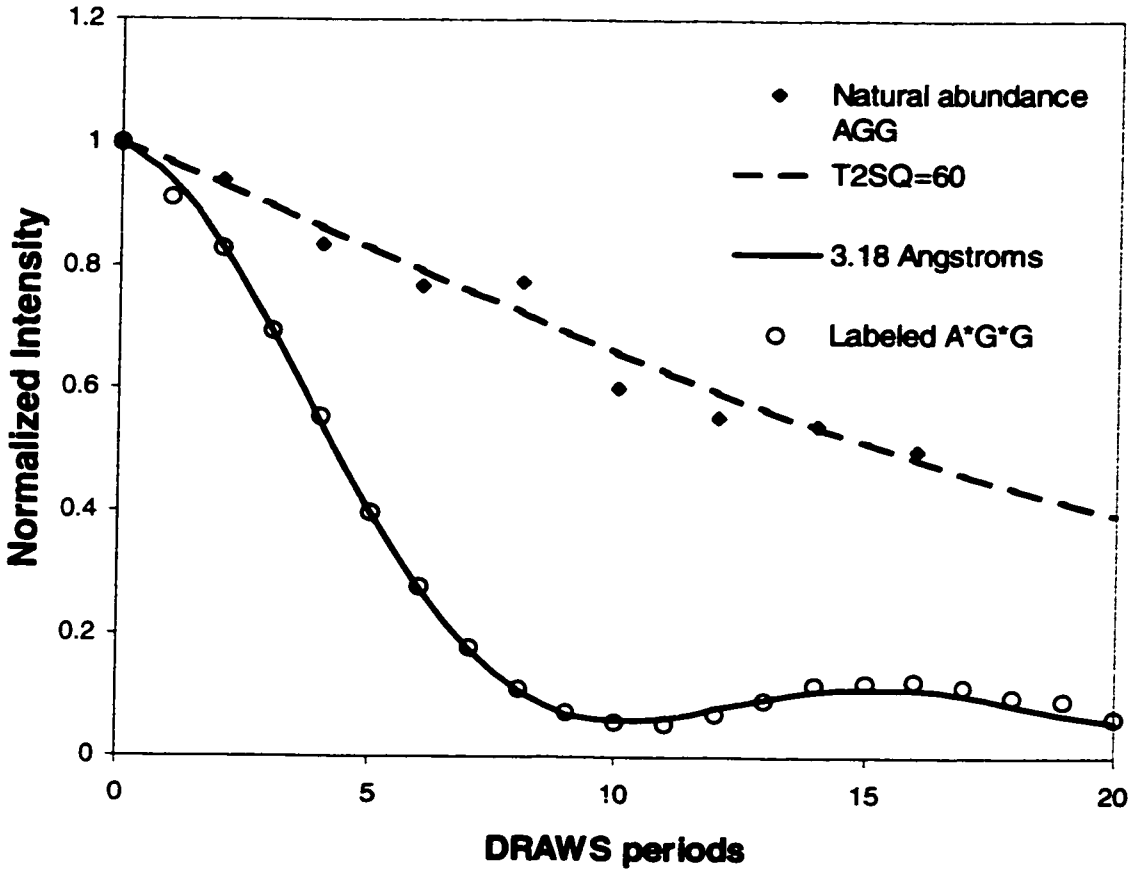

Figure 3.3. Experimental DRAWS dephasing curve for the model compound, A*G*G. The simulated curve agrees with the crystallographic distance of 3.18 Å (φ = -83°). Experimental data for natural abundance AGG is also shown, fitting well to a T_2^{SQ} of 60 Hz.

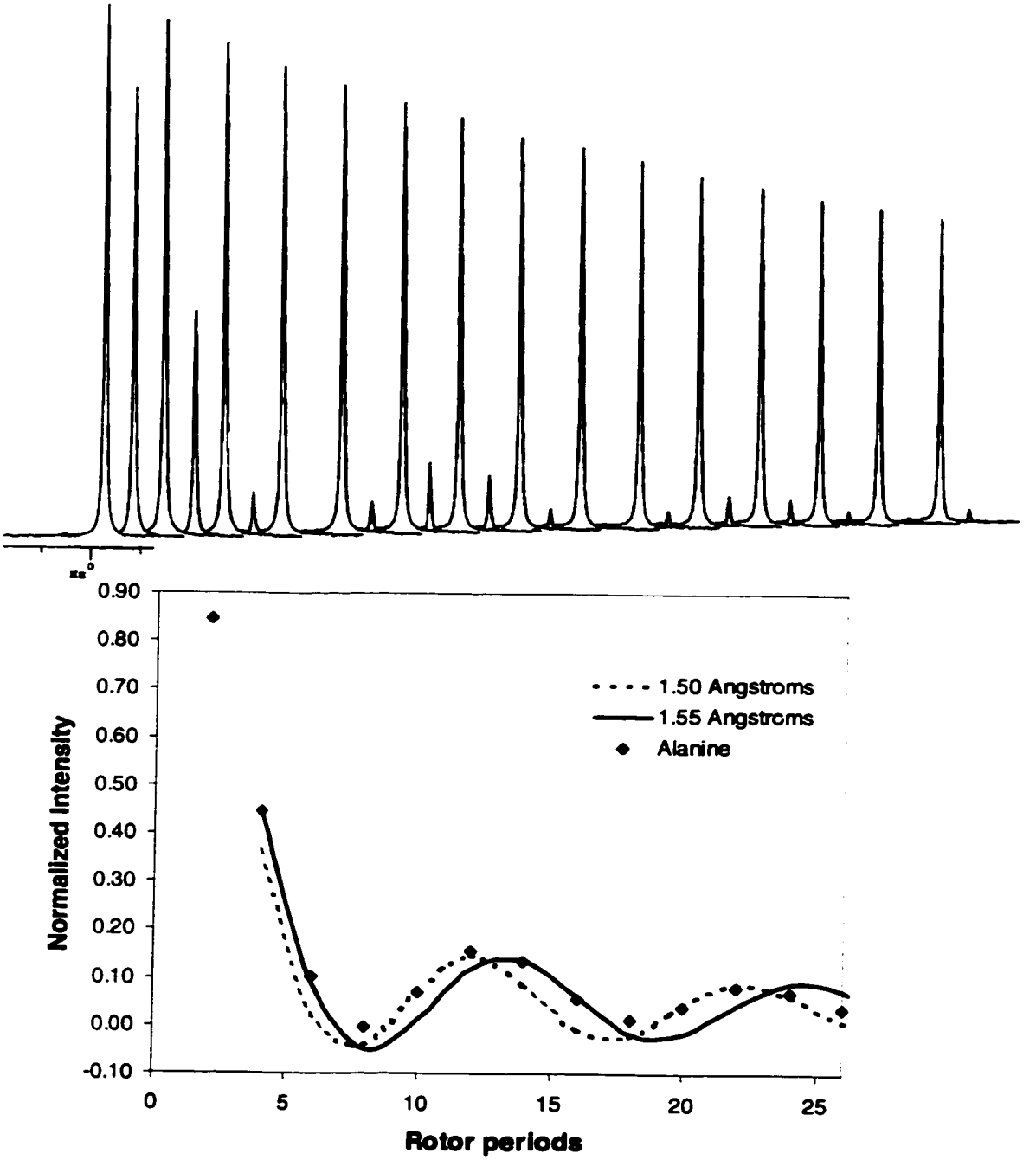

Figure 3.4. Experimental REDOR spectra alternating between S and S_o for uncut C_α, N labeled alanine, and the corresponding dephasing curve (diamonds) with simulations of 1.5 Å and 1.55 Å, as indicated.

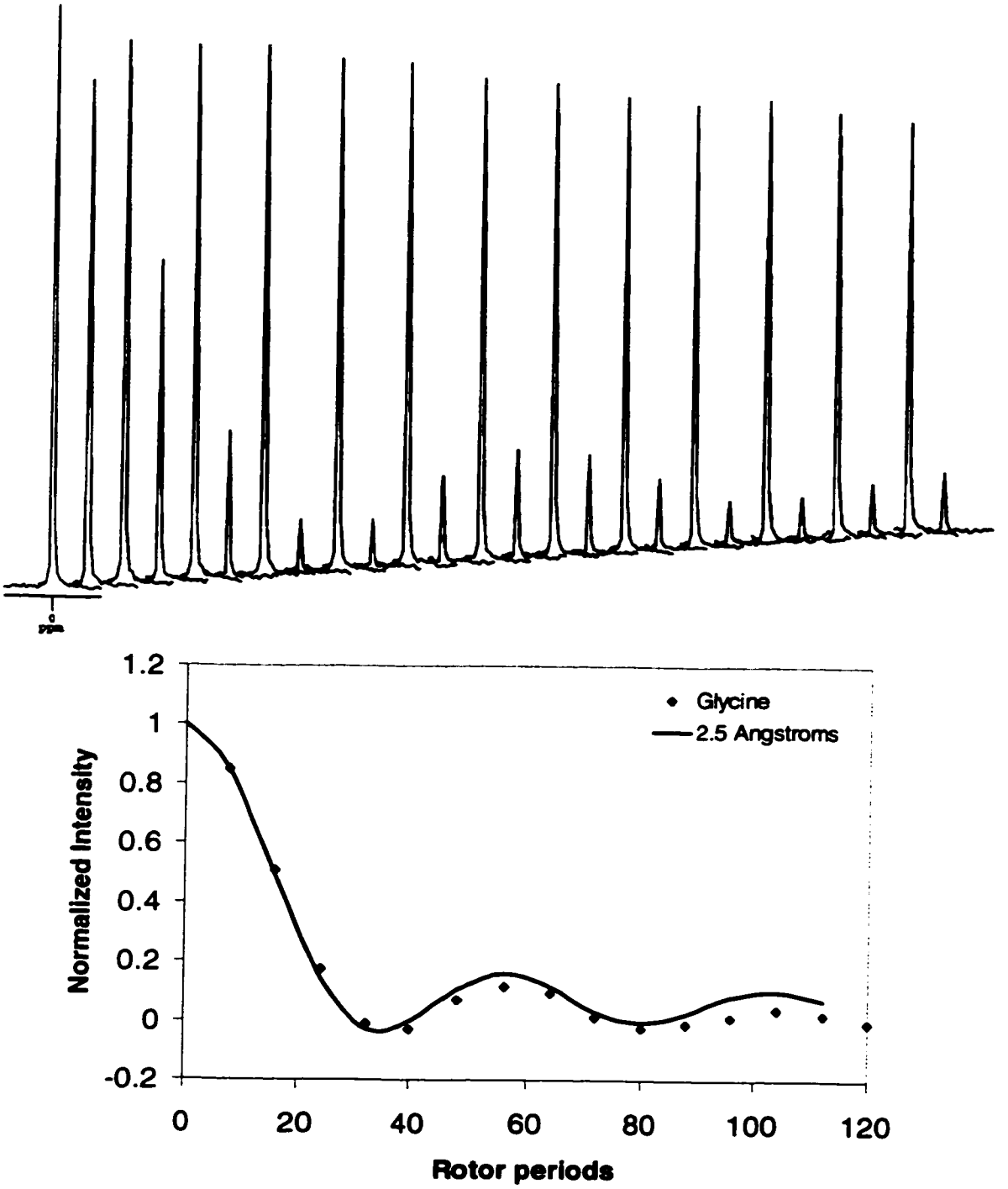

Figure 3.5. Experimental REDOR spectra for $^{13}C{=}O$, ^{15}N glycine (diamonds), cut to 10% with natural abundance glycine. Simulations are fit well by a 2.5 Å distance, consistent with the expected distance.

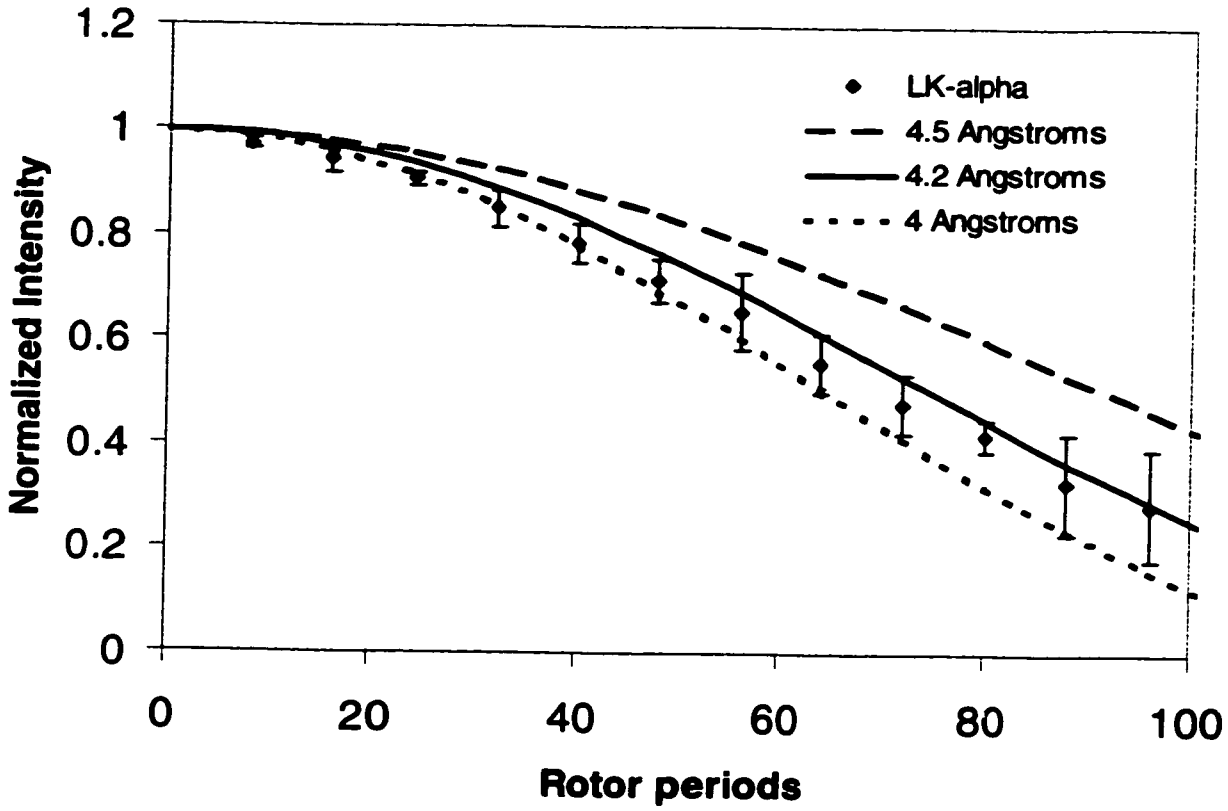

Figure 3.6. REDOR dephasing curves of the helical peptide, LKα (Ac-LKK*L*LKL*L*KKLLKL), fit to the expected distance for a classical α-helix, 4.2 Å.

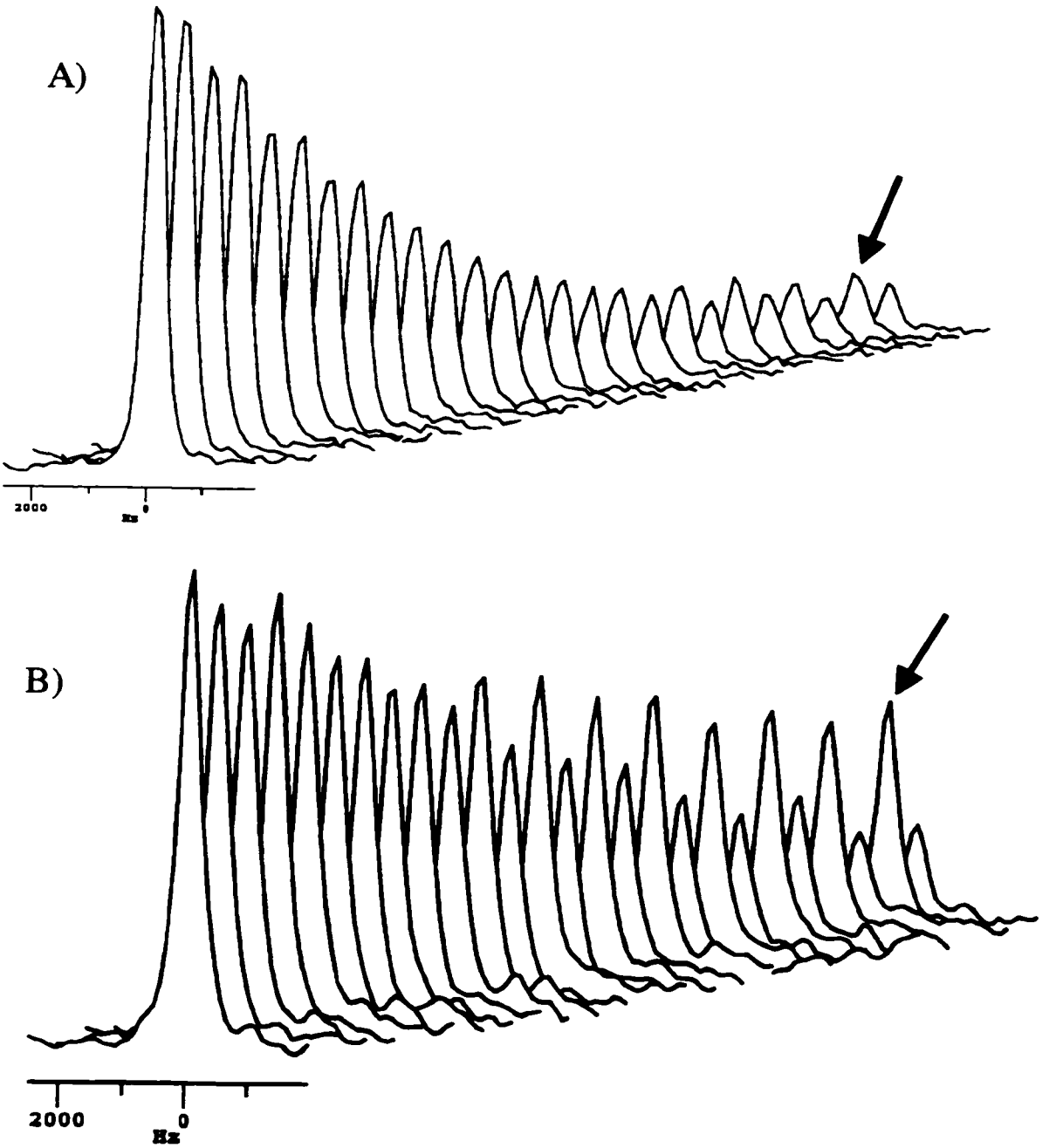

Figure 3.7. Experimental REDOR So and S spectra (alternating) for: A) a doubly carbonyl labeled, singly ^{15}N labeled peptide (SN15-$F_7L_8\underline{G}_{12}$) and B) the corresponding singly carbonyl labeled peptide (SN15-$L_8\underline{G}_{12}$). Notice particularly the drop in the So curve for the doubly carbonyl labeled peptide, while the singly labeled peptide maintains intensity (indicated with arrows).

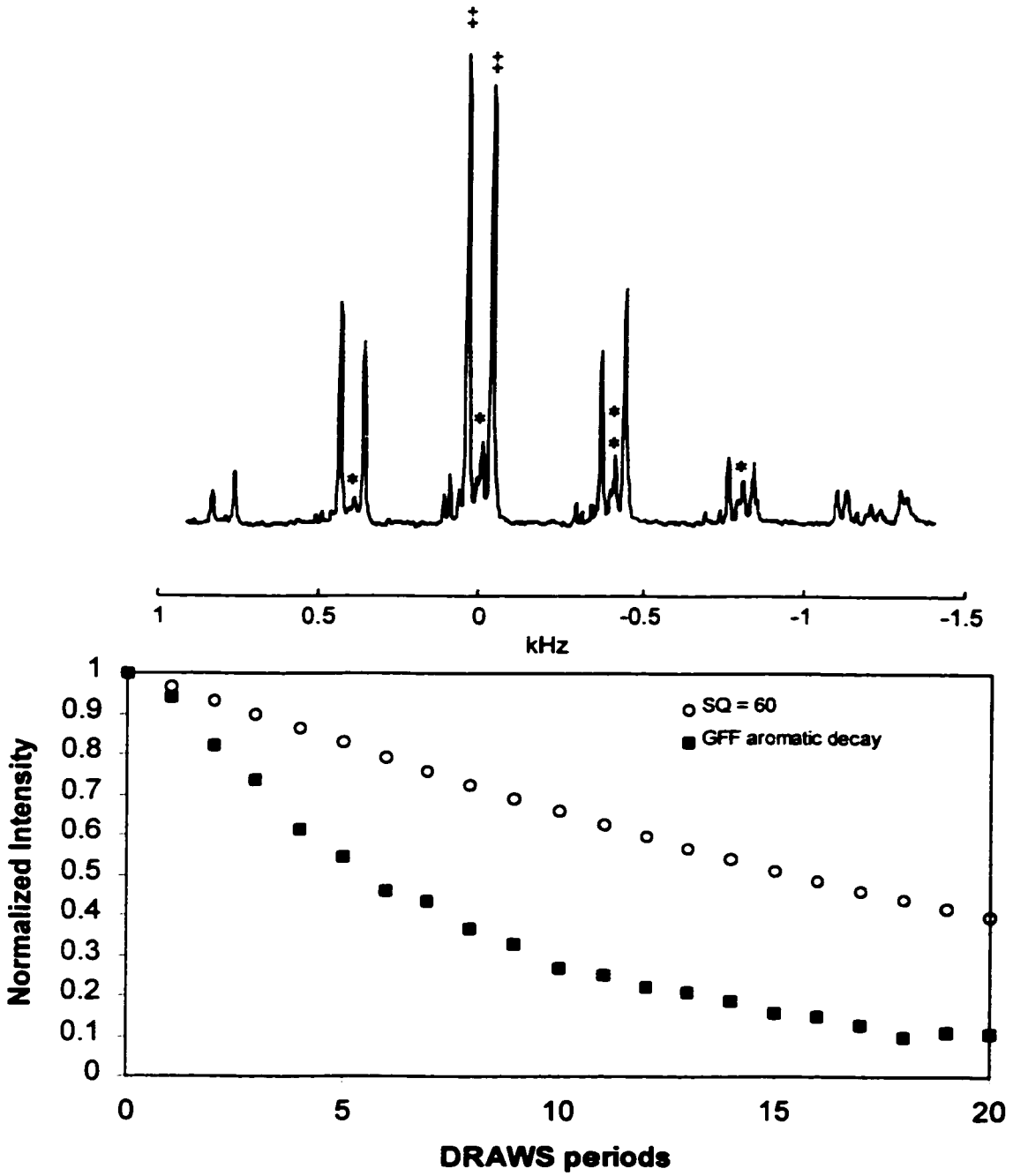

Figure 3.8. A spectrum of *GFF* is shown at a spinning speed of 4 kHz, where the aromatic peaks are indicated with *, and the isotropic aromatic peak is marked with a double *. The isotropic peaks for the carbonyl labels are indicated with ‡'s. The natural abundance decay of the aromatic region in GFF is shown, along with a single quantum decay of 60 Hz for comparison. Natural abundance subtractions took this decay into account for statherin DRAWS curves.

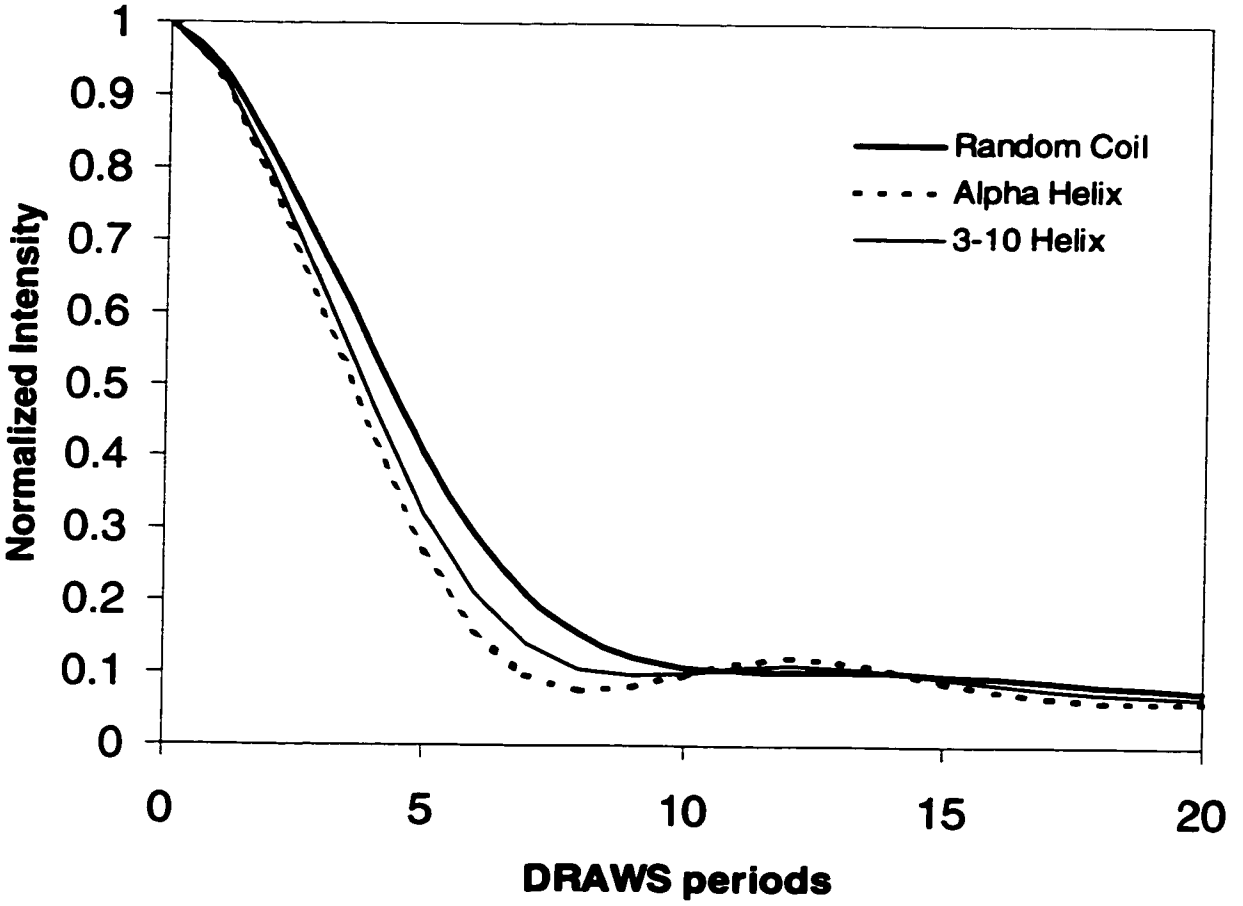

Figure 3.9. Distributions generated based on the relative contributions to α-helix, 3_{10}-helix and β-sheet secondary structures as determined from crystallographic data.[9] The three secondary structures are easily distinguishable from one another and allow the fitting of DRAWS dephasing curves that may contain conformational distributions.

CHAPTER 4:

SN15 STRUCTURE

The helical structure observed in the N-terminus of statherin in solution has been implicated in its prevention of secondary precipitation. To explore this, the N-terminal peptide SN15 (DpSpSEEKFLRRIGRFG) was prepared, with isotopic labels incorporated into 3 sites, indicated in bold italics, for DRAWS analysis, shown pictorially in Figure 1.

SN15-pSpS D***pSpS***EEKFLRRIGRFG

SN15-FL DpSpSEEK***FL***RRIGRFG

SN15-IG DpSpSEEKFLRR***IG***RFG

These measurements directly determine the torsion angle φ, allowing correlation to secondary structure and were made for peptides lyophilized from buffer as well as peptides adsorbed to HAP, to determine any conformational changes occurring upon binding.

One SN15 sample was prepared to measure the presence of global helical structure by measuring the heteronuclear coupling between the backbone carbonyl and the backbone nitrogen involved in the hydrogen bond in an α-helix. For SN15, one REDOR measurement was made from L_8 to G_{12}, where L_8 is a ^{13}C carbonyl label, and G_{12} is an ^{15}N label.

SN15-LG DpSpSEEKF***L***RRI***G***RFG

All of the above samples, along with two other singly carbonyl labeled samples were used to measure relaxation parameters and to determine conformational heterogeneity.

SN15-pS_3 DpS***pS***EEKFLRRIGRFG

SN15-G_{12} DpSpSEEKFLRRI***G***RFG

4.1 Results

4.1.1 Peptide Characterization.

Peptides were purified to homogeneity using reverse-phase HPLC. MALDI mass spectrometry analysis of the purified peptide yielded molecular weights of 1959.2 (SN15-pSpS), 1959.8 (SN15-FL), 1959.6 (SN15-IG), 1959.9 (SN15-pS_3), 1958.7 (SN15-L_8), and 1959.0 (SN15-G_{12}) daltons (theoretical mw: 1959.8 daltons). Figure 4.2 shows a representative MALDI mass spectrum of purified SN15.

4.1.2 Chemical Shift Characterization.

The CPMAS spectra of lyophilized and adsorbed peptides are shown in Figure 4.3. The isotropic chemical shift values and linewidths (measured with 100 Hz line broadening) for each of the singly and doubly-labeled SN15 peptides on and off the HAP crystal surface are given in Table 4.1. SN15-pSpS displays two overlapping peaks convoluted into one broad resonance both on and off the surface (total linewidth 7.16 ppm and 5.18 ppm, respectively). SN15-FL off the surface displays two overlapping resonances (combined peak width 5.06 ppm) in the CPMAS spectrum. Preparation by the quick-freezing method did not significantly reduce the linewidth. When adsorbed to the surface, a combined linewidth of 7.07 ppm is observed. SN15-IG displays two unresolved resonances (total linewidth 5.4 ppm) off the surface, which remain unresolved when adsorbed to the surface (total peak width 7.05 ppm). Singly labeled peptides have

linewidths off the surface of 4.2 ppm (SN15-pS_2), 3.3 ppm (SN15-pS_3), 3.9 ppm (SN15-F_7), 3.4 ppm (SN15-L_8), 3.6 ppm (SN15-I_{11}) and 5.3 ppm (SN15-G_{12}). On the surface, the linewidths are 7.3 ppm (SN15-pS_2), 6.0 ppm (SN15-pS_3), 6.6 ppm (SN15-F_7), 6.6 ppm (SN15-L_8), 6.9 ppm (SN15-I_{11}) and 6.8 ppm (SN15-G_{12}).

4.1.3 Fluorometry Measurements

The following peptide adsorptions were followed using fluorometry: SN15-FL, SN15-pSpS, SN15-LG and SN15-G. The peptide bound before and after washes is presented in Table 4.2. The range of peptide bound per 100 mg is 3-10.5 mg (0.39-1.36 mg/m^2), and reduces to 1.1-7.5 mg after washing with phosphate buffer. It should be stressed that this was not done for every binding but for a select few to approximately determine how much peptide was being bound.

4.1.4 DRAWS Measurements

To test the ability of DRAWS data to identify structural dispersions, DRAWS data were obtained for the crystalline tripeptide ***AG***G, and for the lyophilized peptide, ***FL***R. Figure 4.3a shows the experimental DRAWS dephasing curve of ***AG***G, a doubly carbonyl labeled crystalline peptide, along with simulations for φ = -73°, -83°, and -93°. Additionally, a simulation (dotted line) for an average φ of -83° with Gaussian distribution of conformations (σ = 30°) is shown. Inspection of Figure 4.4a shows that the φ = -83° simulation fits the data better than φ = -73° or φ = -93°. Table 4.4 compares the change in χ^2 observed when comparing the first 6 points of the two curves versus comparing all 21 points. For the crystalline peptide (***AG***G) the change in χ^2 comparing

the single conformation to a distribution for the first 6 points is very small (2.96×10^{4}) in comparison to the relative probability observed when the entire curve is taken into consideration (5.08×10^{49}). For the lyophilized, non-crystalline ***FL***R tripeptide (Figure 4.3b), the early timepoints are best fit using $\varphi = -103°$. A Gaussian distribution of structures ($\sigma = 30°$) fits the data with a higher relative probability (9.18×10^{-6}) than a single conformation (Table 4.4) (the large negative rather than positive exponent resulting from the definition of P_1/P_2—see Chapter 3.16).

The DRAWS dephasing curves were fit with a $T_2^{SQ} = 80$ and a T_2^{DQ} of 128, except for N15-pSpS off HAP, and N15-FL on HAP which were fit with a $T_2^{SQ} = 100$ and a $T_2^{DQ} = 200$. The dephasing curves for SN15-pSpS on and off HAP are shown in Figure 4.5, and. The bars represent the standard deviation in multiple distance measurements made on the same sample. The average distances obtained from the first 7-10 points in the dephasing curve are shown in Table 4.3 and the relative fits of distributions are summarized in Table 4.5. SN15-pSpS on the surface of HAP displayed an average $\varphi = -85°$ (3.18 Å), and a confidence level (based on χ_ν^2, and taken from standard tables[1]) of 95-98%. The accuracy of DRAWS at these distances is generally within 0.1 Å ($\varphi \pm 10°$) when using two-spin simulations.[2] Statistical analysis of the longer time points indicates that for the pSpS region of SN15 on the surface, the DRAWS data is best fit with a random coil distribution of φ with a relative probability = 1.41×10^{-7} (see equation 3). DRAWS dephasing curves of SN15-pSpS off the surface fit an average φ of –85° (3.18 Å) with a confidence level of 90-95%. The longer data points for SN15-pSpS off the

surface are modeled most accurately by applying a ± 20° Gaussian distribution of conformations (relative probability = 0.091).

SN15-FL on the surface yields a shorter distance of 2.98 Å, corresponding to a φ of -60°, at a confidence level of 85-90%. For the peptide on the surface, models of a single conformation or small distributions of ≤ 20° fit the long time points equally well. SN15-FL displayed an average distance of 3.09 Å off the surface corresponding to φ = -73° at the 99% confidence limit (Figure 4.6). The longer time points are modeled well with a distribution of ± 20°, or by a weighted distribution of angles observed for 3_{10} helices.[3]

The average distance of SN15-IG adsorbed to HAP is 3.08 Å (φ = -73°, confidence level 95-98%) with the later data points indicating a larger Gaussian distribution of ± 30° to ± 50° or a random coil distribution (Figure 4.7).[3] The average distance of SN15-IG measured off the surface was 3.14 Å, corresponding to a φ torsion angle of -80° degrees (confidence level 95-98%), with a distribution being best described by a single conformation or by Gaussian distributions of ± 10° or ± 20°.

4.1.5 REDOR Measurements.

S/S_0 REDOR curves are shown in Figure 4.8, where the bars on the experimental data indicate the standard deviation of multiple measurements on the same sample. Simulations of 4.0, 4.4 and 4.8 Å are also shown. The measured distance of SN15-LG off the surface was found to be 4.4 ± 0.5 Å. The peptide adsorbed to HAP had a slightly longer distance of 4.8 ± 0.5 Å.

4.2 Discussion

Protein structure and biomineral recognition are closely tied, and thus the determination of protein structure on crystal surfaces is an important fundamental goal. SSNMR techniques provide a unique route to determining molecular structure at the protein/inorganic solid interface. In this study, the DRAWS technique was utilized to measure distances between adjacent backbone carbonyl carbons in N-terminal peptides of the salivary protein statherin. The distance measurement from DRAWS is independent of the angle ψ, resulting in a direct and unambiguous measurement of φ at the selected backbone positions. Three labeling schemes were used to independently probe the conformation of the 15mer: near the N-terminus, in the middle of the peptide, and near the C-terminus. For a peptide with classical ideal α-helical structure (φ = -57), a distance of 2.95 Å is expected between adjacent backbone carbonyl carbons. The distance expected for a fully extended secondary structure (φ = -180) would be 3.7 Å, and for a β sheet structure (φ = -119) would be 3.5 Å. A more recent study based on the high resolution crystal structure of 85 proteins suggests less rigid definitions, with the α-helical structure having an average $\varphi = -65° \pm 13°$ and β sheet $\varphi = -113° \pm 41°$.[3]

4.2.1 Conformational Distributions

The observed dephasing in the first 5-8 msec of the DRAWS experiment is determined by the average dipolar coupling or distance and is largely independent of conformational dispersion, while the long timepoints in the dephasing curve contain

information on conformational dispersion.[2] The question of conformational distribution is an important aspect of these structural determinations, and while the signal to noise levels at the longer time points in these DRAWS experiments are relatively low, we have conducted a statistical analysis of the data in order to determine the statistical significance of simulations that include conformational dispersion, that is summarized in Table 4.5. The ability of DRAWS to distinguish conformational distributions is demonstrated in the experimental DRAWS dephasing curves of crystalline ***AG***G and lyophilized ***FL***R, where the improved fit to DRAWS data for ***FL***R obtained with a φ distribution of $\pm$ 30° is shown in Table 4.4 to be statistically significant. There are experimental parameters such as insufficient decoupling or phase transients that can result in dephasing behavior similar to that produced by a distribution.[2] Although this is an important consideration, attempts are made to remove these experimental contributions, the success of which is demonstrated in the model peptide data (Figure 4.4). It should be noted that the reduced χ^2 for AGG shown in Table 4.4 is large compared to the reduced χ^2 values for SN15 peptides (Table 4.3). This demonstrates that χ^2 values themselves must be interpreted with some degree of caution. The reduced χ^2 given by equation 3.3 is frequently interpreted as measuring the agreement between data and a model, but only does so within the uncertainties associated with the data.[1] Therefore, data with small experimental uncertainties can yield a large χ^2 because the inadequacies of the model become evident.

4.2.2 Secondary structure

The average φ (–60°) at the FL position in the SN15 peptide falls in classical α-helical conformational space, indicating there is substantial secondary structure in the central region of SN15 when adsorbed to HAP. REDOR experiments confirm the helical structure in the middle portion of the peptide, yielding a distance of 4.8 Å, compared to the expected distance of 4.22 Å, as calculated with Insight II. The N-terminal binding site (pSpS) displays the largest φ (–85°) and the longer time points in the dephasing curve are best fit by a random coil distribution model (see Chapter 3). This is consistent with a disordered N-terminus, which may allow the negatively charged side-chains and phosphates at the serine positions to interact maximally with the positively charged calcium ions on the HAP surface. The IG position exhibits an average φ of -73° on the surface, which is at the upper end of α-helical space. The broad conformational dispersion observed suggests that the C-terminus exists with some distribution between α-helix and more extended structures. The large dispersion at the C terminus could be related to the lack of a hydrogen bond donor available for the glycine position due to its proximity to the C-terminus. The REDOR result is consistent with this finding in that the adsorbed peptide has a slightly longer distance across the hydrogen bond, still suggestive of significant helical content, but indicative of a dispersion of conformations. The confidence limits shown in Table 4.3 demonstrate that there is a high confidence in the average distances measured for these peptides regardless of any conformational heterogeneity which may be present. Similar φ values on and off the surface for all

regions of the peptide suggest that the peptide does not exhibit a large change in structure upon binding to HAP. There is a small but significant shortening at the FL position upon adsorption that suggests binding energy might be used to stabilize α-helical structure in the middle region of the peptide. Figure 4.9 summarizes the DRAWS data, demonstrating the best distribution model for each peptide as a function of the torsion angle φ, both off and on the surface.

4.2.3 Chemical Shifts and Linewidths

The chemical shifts and linewidths potentially contain complementary information to the DRAWS data, as chemical shifts have traditionally been used to qualitatively distinguish between various secondary structures.[4-8] The carbonyl labeling scheme utilized here to obtain high resolution distance measurements limits the interpretation of the absolute chemical shift, as it has been shown in detail in the literature that the susceptibility of carbonyls to hydrogen bond within the protein and with the solvent makes secondary structure prediction impossible.[4,5,7,9] Multiple resonances and linewidths of the carbonyl resonances can be a qualitative indicator of conformational heterogeneity, however. Figure 4.10 shows a well ordered model compound, designed to have 3_{10}-helical structure. The two unique resonances observed, with 2.4 ppm linewidths, are representative of helical and random coil secondary structure as proven with further experiments.[10] The observed linewidths for the singly labeled SN15-pS_2, SN15-pS_3, SN15-F_7, SN15-L_8, and SN15-I_{11} (3-4 ppm) off the surface are typical of lyophilized, ordered peptides, which have linewidths of 2-4 ppm.[11] The linewidth of

SN15-G_{12} is greater than 5 ppm, reflecting structural heterogeneity at the C-terminus of the free peptide. The quick-freezing protocol outlined in the methods section has been used to maintain a single conformation of a soluble peptide upon lyophilization[12] that may become disordered during the relatively slow freezing that liquid nitrogen provides. Using this technique for the SN15 peptide did not produce a narrowed linewidth, indicating that there is some structural heterogeneity, or possibly something else is contributing to the linewidths.

All SN15 carbonyl linewidths increase 1.5-2 times upon adsorption to the surface. This increased breadth could be due to conformational heterogeneity, relaxation processes, and/or the anisotropic magnetic susceptibilities of the HAP crystals.[13-15] The measured T_2^{SQ} value of 12.5 msec indicates that relaxation processes are not contributing greatly to the linewidths. Further studies involving hydrating the surface adsorbed peptides[16] further support the interpretation that motion is not a significant narrowing mechanism. When the surface adsorbed peptide is hydrated, the singly labeled linewidth is reduced from 6.0 ppm to 3.4 ppm in the case of SN15-pS_3. The chemical shift anisotropy is narrowed only slightly (approximately 10 ppm). To be discussed in more depth in Chapter 5, the volume magnetic susceptibilities of crystalline phosphate salts are large, typically ranging from –150 to –200 ppm cm^3/mol and are not completely removed by MAS.[17] One interpretation of the above observations is that wetting the surface fills the spaces between the HAP crystals with buffer, partially matching the isotropic and anisotropic susceptibility of the HAP particles, resulting in narrowed lines. A similar

effect was reported by Elbayed et al.[15] Conformational dispersion is another factor contributing to broadened linewidths, and some conformational dispersion is certainly expected for this small peptide. Hydrated linewidths on the order of 3-4 ppm suggest that regardless of narrowing mechanism, some conformational dispersion is contributing to the linewidth as well. The chemical shifts are thus consistent with a relatively narrow but real distribution of conformations. However, given the possibility of susceptibility contributions it is difficult to use chemical shift spectra alone to assess structural heterogeneity. In contrast, DRAWS decay curves are obtained by integration of the CPMAS spectrum observed following DRAWS irradiation. Therefore DRAWS data are not perturbed by magnetic susceptibility broadening and may provide a more straightforward basis for estimating the structural dispersion of peptides adsorbed to HAP crystals.

4.3 Conclusions

Previously it was determined that the N-terminal N6 statherin peptide was disordered on HAP at the pSpS residues.[18] The data presented here are in agreement with that finding and show that the corresponding residues remain largely unstructured in the longer SN15 peptide. The middle and C-terminal portion of the peptide on the surface exhibit conformations consistent with torsion angles expected for α–helices and a mixture of α–helices and extended structure, respectively, with REDOR data supporting a helical structure from the middle to the C-terminus. Electrostatic interaction theory has been implicated in the literature as a model for the interactions of peptides with the

overall charge of a crystal.[19-21] The lack of a specific secondary structure observed at the pSpS position allows multiple side-chain electrostatic interactions with the surface, consistent with the fact that the phosphoserines have been shown to play a key role in binding affinity.[22] The α-helix motif has been considered to be a lattice matching conformation for side chain interactions with specific calcium ions in the HAP crystal.[23] The presence of some α-helical content in the middle and at the C-terminus of SN15 on the HAP surface is consistent with this model.

4.4 Notes to Chapter 4

1. Bevington, P. R. & Robinson, D. K. *Data Reduction and Error Analysis for the Physical Sciences* (WCB/McGraw-Hill, Boston, 1992).

2. Mehta, M. A. *et al.* Distance Measurements in Nucleic Acids Using Windowless Dipolar Recoupling Solid State NMR. *Solid State Nuclear Magnetic Resonance* **7**, 211-228 (1996).

3. Smith, L. J. *et al.* Analysis of Main Chain Torsion Angles in Proteins: Prediction of NMR Coupling Constants for Native and Random Coil Conformations. *Journal of Molecular Biology* **255**, 494-506 (1996).

4. Asakawa, N. *et al.* Hydrogen-Bonding Effect on ^{13}C NMR Chemical Shifts of L-alanine Residue Carbonyl Carbons of Peptides in the Solid State. *Journal of the American Chemical Society* **114**, 3261 (1992).

5. Asakawa, N., Kurosu, H. & Ando, I. Structural Study of Peptides Containing L-alanine Residues by *ab initio* Chemical Shielding Calculation. *Journal of Molecular Structure* **323**, 279 (1994).

6. Fuijisawa, R. & Kuboki, Y. Conformation of Dentin Phophophoryn Adsorbed on Hydroxyapatite Crystals. *European Journal or Oral Sciences* **106**, 249-253 (1998).

7. Wishart, D. S. & Sykes, B. D. The ^{13}C Chemical-Shift Index: A Simple Method for the Identification of Protein Secondary Structure Using ^{13}C Chemical-Shift Data. *Journal of Biomolecular NMR* **4**, 171 (1994).

8. Spera & Bax, A. Emperical Correlation Between Protein Backbone Conformation and C_α and C_β ^{13}C Nuclear Magnetic Resonance Chemical Shifts. *Journal of the American Chemical Society* **113**, 5490 (1991).

9. Saito, H. Conformation-Dependent ^{13}C Chemical Shifts: A New Means of Conformational Characterization as Obtained by High-Resolution Solid-State ^{13}C NMR. *Magnetic Resonance in Chemistry* **24**, 835-852 (1986).

10. Unpublished Results.

11. Long, H. W. & Tycko, R. Biopolymer Conformational Distributions From Solid State NMR: α-Helix and 3_{10}-Helix Contents of a Helical Peptide. *Journal of the American Chemical Society* **120**, 7039 (1998).

12. Christensen, A. M. & Schaefer, J. Solid-State NMR Determination of Intra- and Intermolecular 31P-13C Distances for Shikimate 3-Phosphate and [1-13C]Glyphosate Bound to Enolpyruvylshikimate-3-phosphate Synthase. *Biochemistry* **32**, 2868-2873 (1993).

13. VanderHart, D. L., Earl, W. L. & Garroway, A. N. Resolution in 13C NMR of Organic Solids Using High-Power Proton Decoupling and Magic-Angle Sample Spinning. *Journal of Magentic Resonance* **44**, 361-401 (1981).

14. Stoll, M. E. & Majors, T. J. Reduction of Magnetic Susceptibility Broadening in NMR by Susceptibility Matching. *Journal of Magnetic Resonance* **46**, 283-288 (1982).

15. Elbayed, K. *et al.* Origin of the Residual NMR Linewidth of a Peptide Bound to a Resin under Magic Angle Spinning. *Journal of Magnetic Resonance* **136**, 127-129 (1999).

16. Shaw, W. J., Long, J. R., Campbell, A. A., Stayton, P. S. & Drobny, G. P. *Journal of the American Chemical Society* (In Press).

17. Weast, R. C. (ed.) *Handbook of Chemistry and Physics* (CRC Press, Boca Raton, 1982).

18. Long, J. R. *et al.* A Peptide That Inhibits Hydroxyapatite Growth is in an Extended Conformation on the Crystal Surface. *Proceedings of the National Academy of Science* **95**, 12083-12087 (1998).

19. Raj, P. A., Johnsson, M., Levine, M. J. & Nancollas, G. H. Dependence on Sequence, Charge, Hydrogen Bonding Potency, and Helical Conformation for Adsorption to Hydroxyapatite and Inhibition of Mineralization. *Journal Biological Chemistry* **267**, 5968-5976 (1992).

20. DeOliviera, D. B., Laursen, R. A. & . Control of Calcite Crystal Morphology by a Peptide Designed to Bind to a Specific Surface. *Journal of the American Chemical Society* **119**, 10627- 10631 (1997).

21. Johnsson, M., Levine, M. J. & Nancollas, G. H. Hydroxyapatite Binding Domains in Salivary Proteins. *Critical Reviews In Oral Biology and Medicine* **4**, 371-8 (1993).

22. Schlesinger, D. H. & Hay, D. I. Complete Covalent Structure of Statherin, a Tyrosine-rich Acidic Peptide Which Inhibits Calcium Phosphate Precipitation from Human Parotid Saliva. *Journal of Biological Chemistry* **252**, 1689-1695 (1977).

23. Hauschka, P. V. & Carr, S. A. Calcium-Dependent α-Helical Structure in Osteocalcin. *Biochemistry* **21**, 2538-2547 (1982).

Table 4.1. Chemical shift values and linewidths of SN15 as a lyophilized free peptide and adsorbed on the surface of HAP.

	Chemical Shift Off/On Surface (ppm)	**Double labels Linewidth** Off/On surface (ppm)	**Single labels-Linewidth** Off surface (ppm)	**Single labels-Linewidth** On surface (ppm)
SN15-pSpS	173.0 / 172.4	5.2, 7.2	4.2, 3.3	7.3, 6.0
SN15-FL	175.6 / 174.5	5.1, 7.1	3.9, 3.4	6.6, 6.6
SN15-IG	175.1 / 175.0	5.4, 7.1	4.2, 5.3	7.0, 6.8

Table 4.2. Adsorbed protein in mg per 100 mg HAP (expected 23.5 mg).

	mg protein adsorbed	mg left on surface after washing
SN15-pSpS	3.5 mg	1.1 mg
SN15-FL (1)	9.8 mg	5.9 mg
SN15-FL (2)	8.8 mg	7.1 mg
SN15-LG	2.9 mg	1.7 mg
SN15-G	10.6 mg	7.5 mg

Table 4.3. φ determined at the three labeled sites in SN15 and the χ_v^2 of the first 7-10 points in the DRAWS dephasing curve. The probabilities obtained from standard tables[1] are shown as percentages in parentheses.

	Average φ	χ_v^2 (confidence level)
SN15-pSpS off HAP	-85°	0.348 (90-95%)
SN15-pSpS on HAP	-85°	0.271 (95-98%)
SN15-FL off HAP	-73°	0.215 (99%)
SN15-FL on HAP	-60°	0.391 (85-90%)
SN15-IG off HAP	-80°	0.183 (99%)
SN15-IG on HAP	-73°	0.218 (95-98%)

Table 4.4. Simulations of short model peptides demonstrating the ability of DRAWS to simulate a distribution without significantly effecting the average distance.

	Simulation	χ_v^2 for average distance	χ_v^2 for entire curve	Relative Probability (first 7-10 points / entire curve)
AGG-crystalline	-83 degrees	0.7511	0.9	
	-83 +/- 30	4	12.4	4.07e5/5.08e49
FLR-lyophilized	-103 degrees	0.323	2.15	
	-103 +/- 30	0.505	1	0.44 / 9.18e-6

Table 4.5. This table shows the relative probability of simulations of DRAWS dephasing curves with and without distributions giving rise to the experimental data. A χ^2 ratio less than one indicates a better fit, a χ^2 ratio greater than one is a worse fit. If the relative probability falls between 0.51 to 1.95 (within a standard deviation) the two simulations are statistically the same. The numbers in bold are the best fit. The calculations used are shown in the Chapter 3.

	Simulation	χ^2	**Relative Probability based on χ^2**
N15-SS off HAP	-85 degrees	19.0	1.0
	-85 +/- 10	16.6	0.29
	-85 +/- 20	**14.2**	**9.1e-2**
	-85 +/- 30	16.2	0.25
	-85 +/- 50	17.5	0.47
	Random Coil	15.72	0.19
N15-SS on HAP	-85 degrees	42.6	1.0
	-85 +/- 10	38.9	0.15
	-85 +/- 20	29.2	1.21e-3
	-85 +/- 30	**20.2**	**1.38e-5**
	-85 +/- 50	20.8	1.83e-5
	Random Coil	**11.07**	**1.41e-7**
N15-FL off HAP	-73 degrees	55.9	1.0
	-73 +/- 10	44.8	3.85e-3
	-73 +/- 20	**36.0**	**4.66e-5**
	-73 +/- 30	49.3	3.71e-2
	-73 +/- 50	44.9	4.09e-3
	3-10 helix	**33.1**	**1.13e-5**
N15-FL on HAP	-60 degrees	23.1	1.0
	-60 +/- 10	**22.6**	**0.81**
	-60 +/- 20	23.1	1.01
	-60 +/- 30	26.2	4.93
	-60 +/- 50	25.8	3.98
	α-helix	24.2	1.75
N15-IG off HAP	**-80 degrees**	**3.7**	**1.0**
	-80 +/- 10	4.2	1.28
	-80 +/- 20	5.7	2.72
	-80 +/- 30	13.9	164.0

	-80 +/- 50	111.2	2.23e23
	Random coil	23.7	2.15e4
N15-IG on HAP	-72 degrees	64.0	1.0
	-72 +/- 10	57.7	4.17e-2
	-72 +/- 20	47.6	2.76e-4
	-72 +/- 30	43.4	3.33e-5
	-72 +/- 50	**42.8**	**2.43e-5**
	3-10 helix	**40.9**	**9.69e-6**

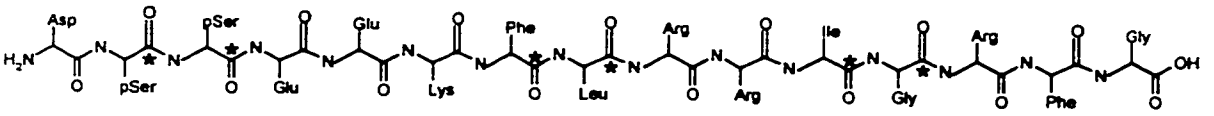

Figure 4.1 SN15 peptide showing the labeling scheme incorporated into three separate peptides across the N-terminal domain for DRAWS studies.

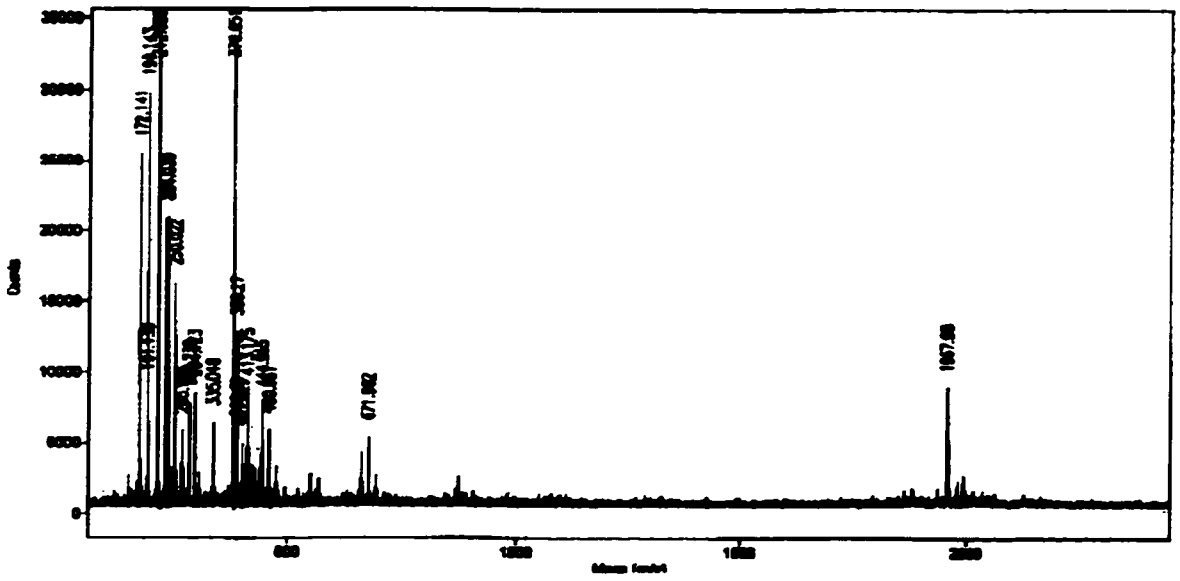

Figure 4.2 MALDI mass spectrum of purified SN15.

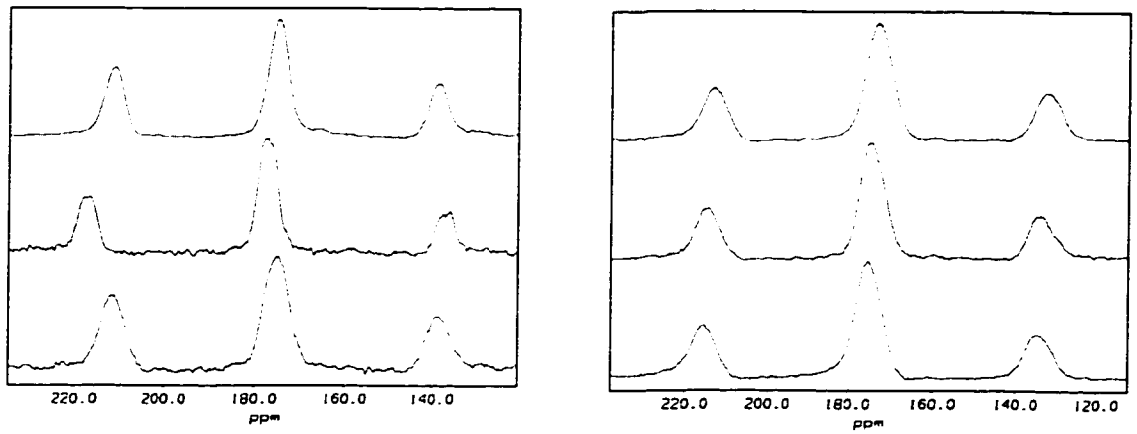

Figure 4.3 ^{13}C CPMAS spectra of peptide lyophilized (left) and adsorbed to hydroxyapatite (right). From top to bottom: SN15-pSpS, SN15-FL and SN15-IG.

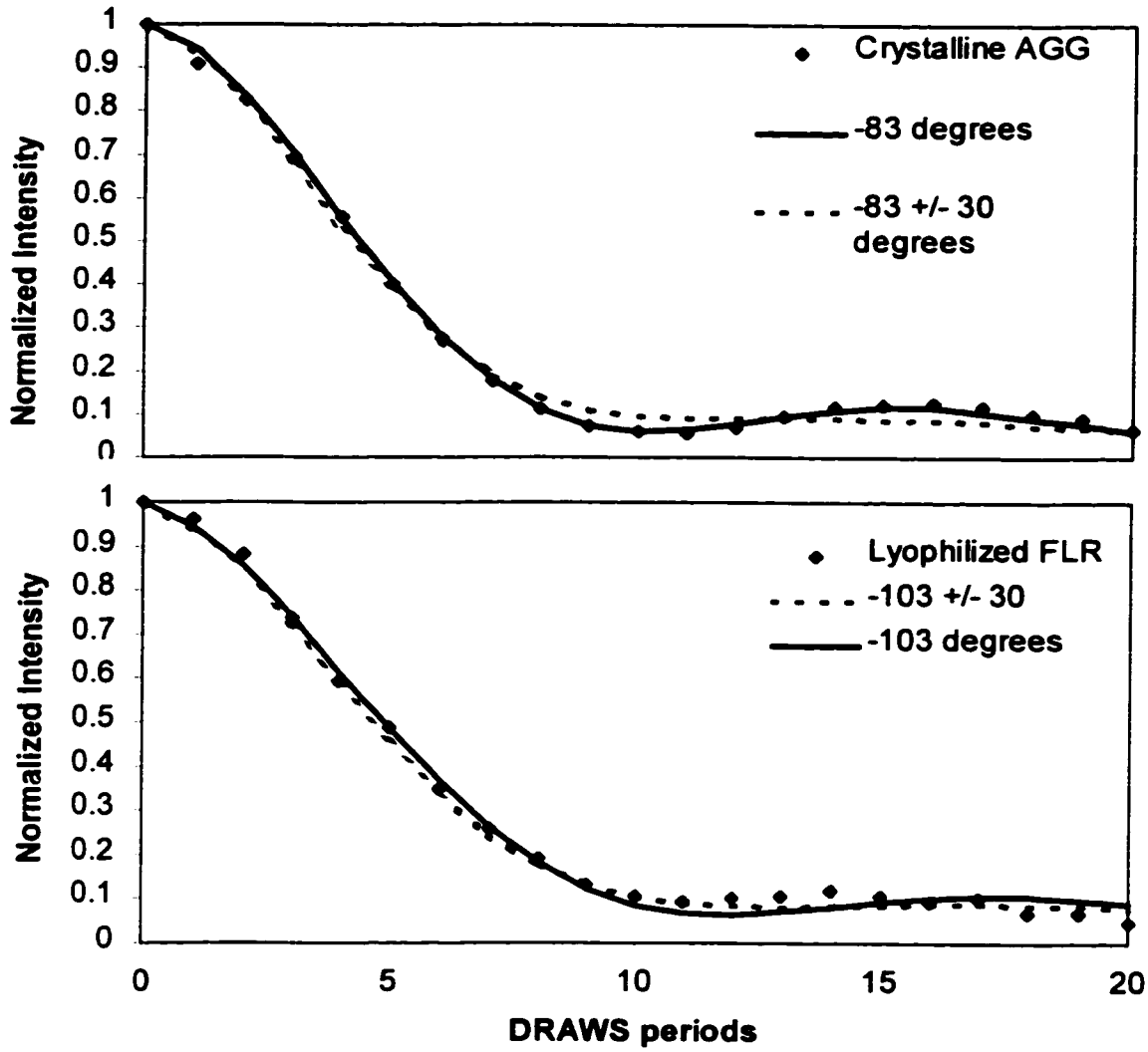

Figure 4.4. These two peptides illustrate the ability of DRAWS to indicate structural heterogeneity. The upper graph is for an ordered, crystalline tripeptide, *AGG*. The experimental data is represented by diamonds, and the simulation for the crystallographic torsion angle φ of –83° is a solid line. The dashed line is a simulation using an average φ angle -83° with a Gaussian distribution of ± 30°. Visually, the single conformation is a much better simulation of the experimental data. This is also supported statistically in Table 4.3, where the single conformation has a 5.08 x 10^{49} higher relative probability based on χ^2 to fit the data then the Gaussian distribution. The lower graph shows data and simulations for a disordered tripeptide, *FLR*. The solid line represents a single conformation of –103°; the dashed line a Gaussian distribution of –103° ± 30°. In Table 4.3, it is shown that the distribution fits the data with a 9.18 x 10^{-6} higher relative probability than the single conformation. In both cases it is important to note that applying a distribution only marginally changes the average distance.

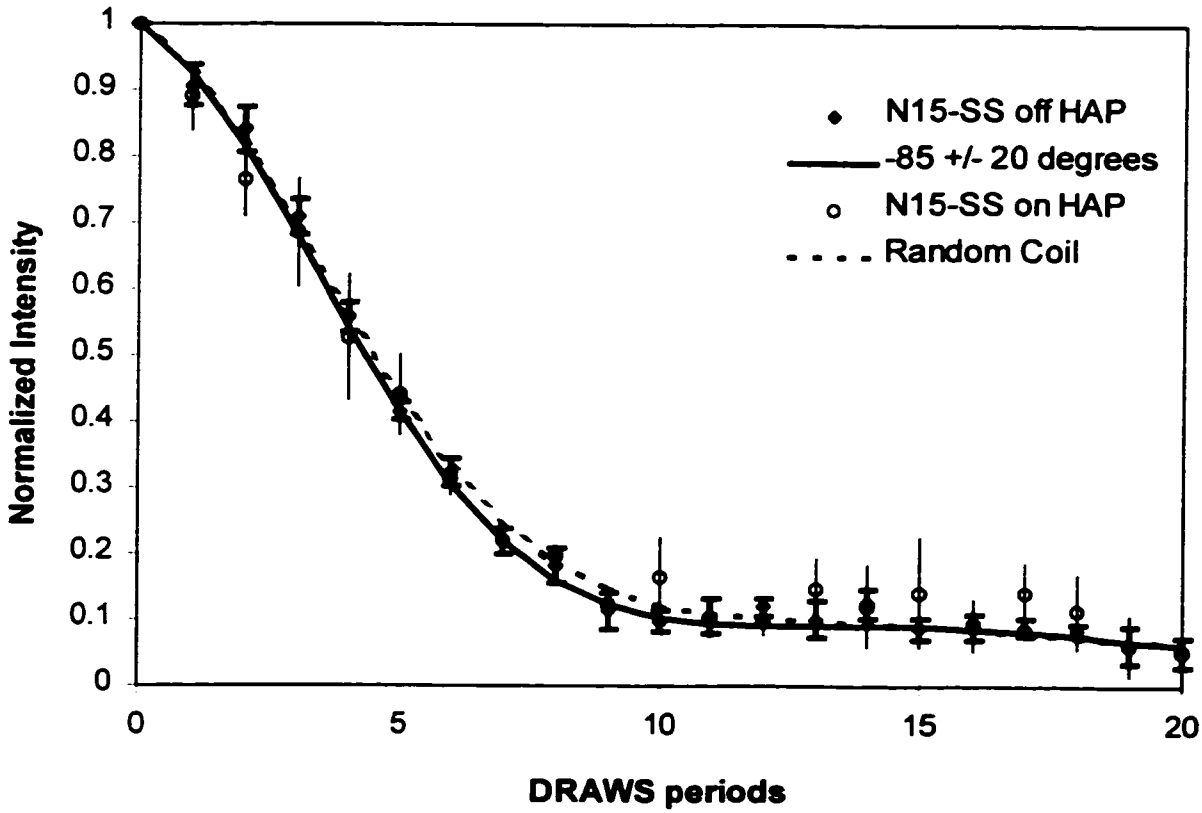

Figure 4.5. Experimental DRAWS dephasing curve of SN15-pSpS on HAP (open circles) and off HAP (diamonds). The average distance for SN15-pSpS on HAP is fit most accurately (solid line) by $\varphi = -85°$ (3.18 Å). The longer time points are more closely fit by a Gaussian distribution of $\sigma = 30°$ around –85° (dashed line), or by a distribution commonly observed in proteins to be random coil, indicating that the peptide has little structure at the N-terminus. SN15-pSpS off of the HAP surface has similar secondary structure with slightly less conformational heterogeneity, where the best fit is $\varphi = -85°$ with a Gaussian distribution of $\pm$ 20°.

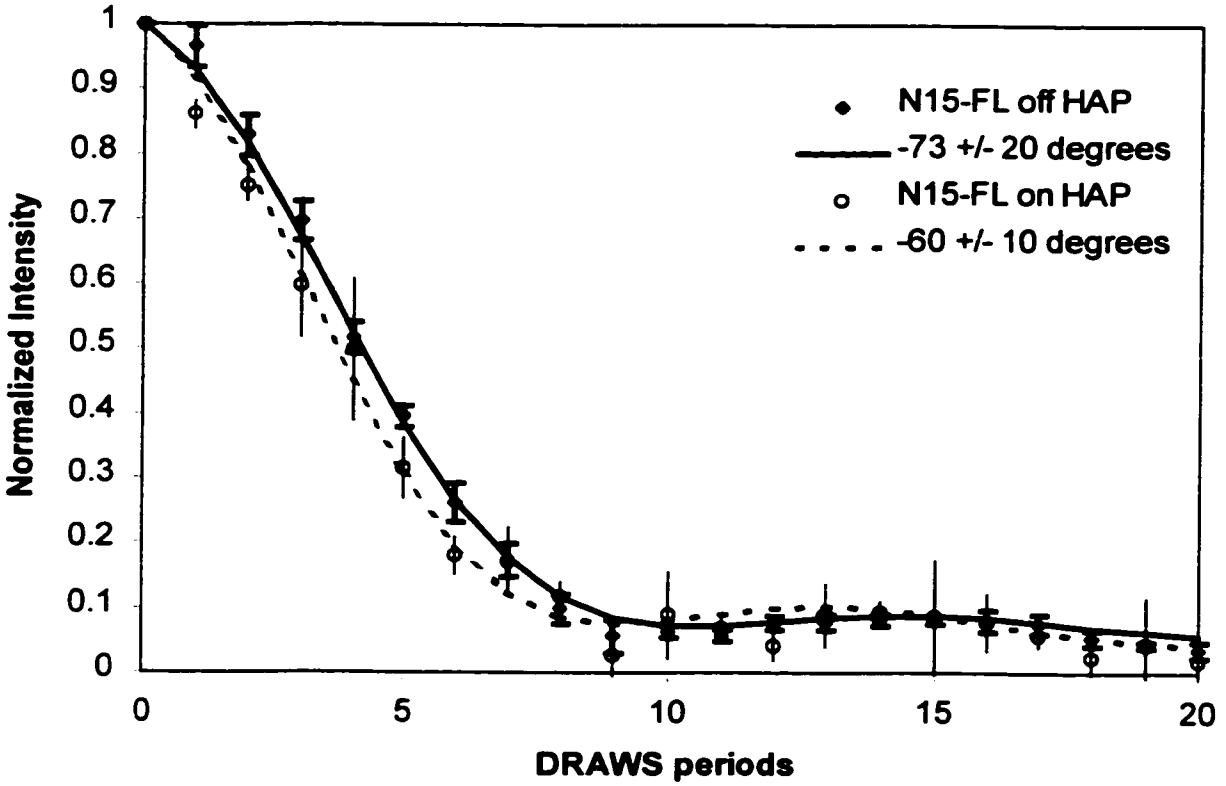

Figure 4.6. Experimental DRAWS dephasing curves of SN15-FL off HAP (diamonds) and SN15-FL on HAP (open circles). The simulated fit for SN15-FL off HAP (solid line) is 3.09 Å, corresponding to an average φ angle of –73°. At longer times, applying a distribution of ± 20° fits the data more accurately, as well as a distribution of angles seen for 3-10 helices. The fit for SN15-FL on HAP (dashed line) is 3.0 Å, which corresponds to a φ of –60°. The data is fit within a standard deviation by a single conformation, a Gaussian distribution of ± 10° and a Gaussian distribution of ± 20°. The average torsion angles correspond to angles commonly observed for helices.

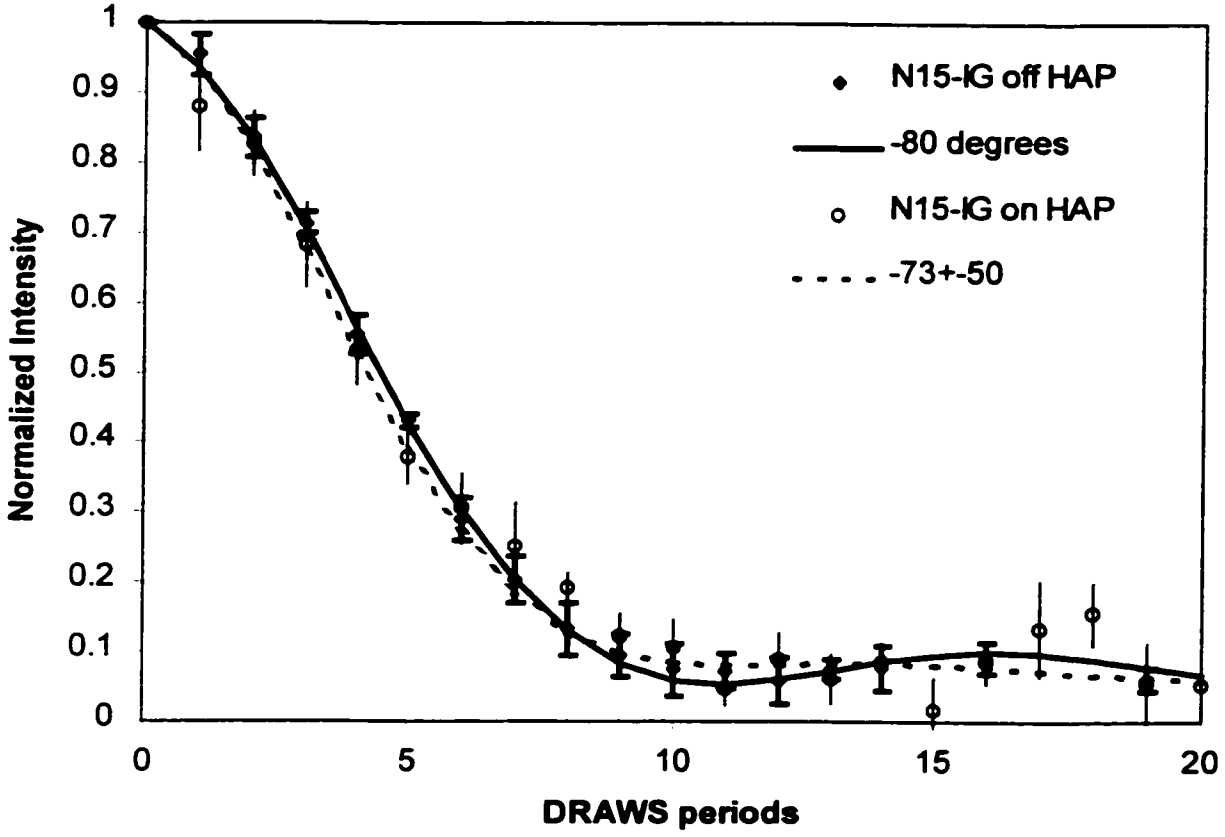

Figure 4.7. Experimental DRAWS dephasing curves of SN15-IG off HAP (diamonds) and SN15-IG on HAP (open circles). The simulated fit to the experimental data for SN15-IG on HAP is $\varphi = -72°$ (3.08 Å). Long time points are best fit by an average distribution of $\pm$ 50° around –72°, or by a distribution of angles observed for 3-10 helices. SN15-IG off HAP fits an average distance of 3.15 Å, corresponding to a $\varphi = -80°$. This data is fit equally well by a single conformation, or by a distribution of conformations with σ =10° or 20°.

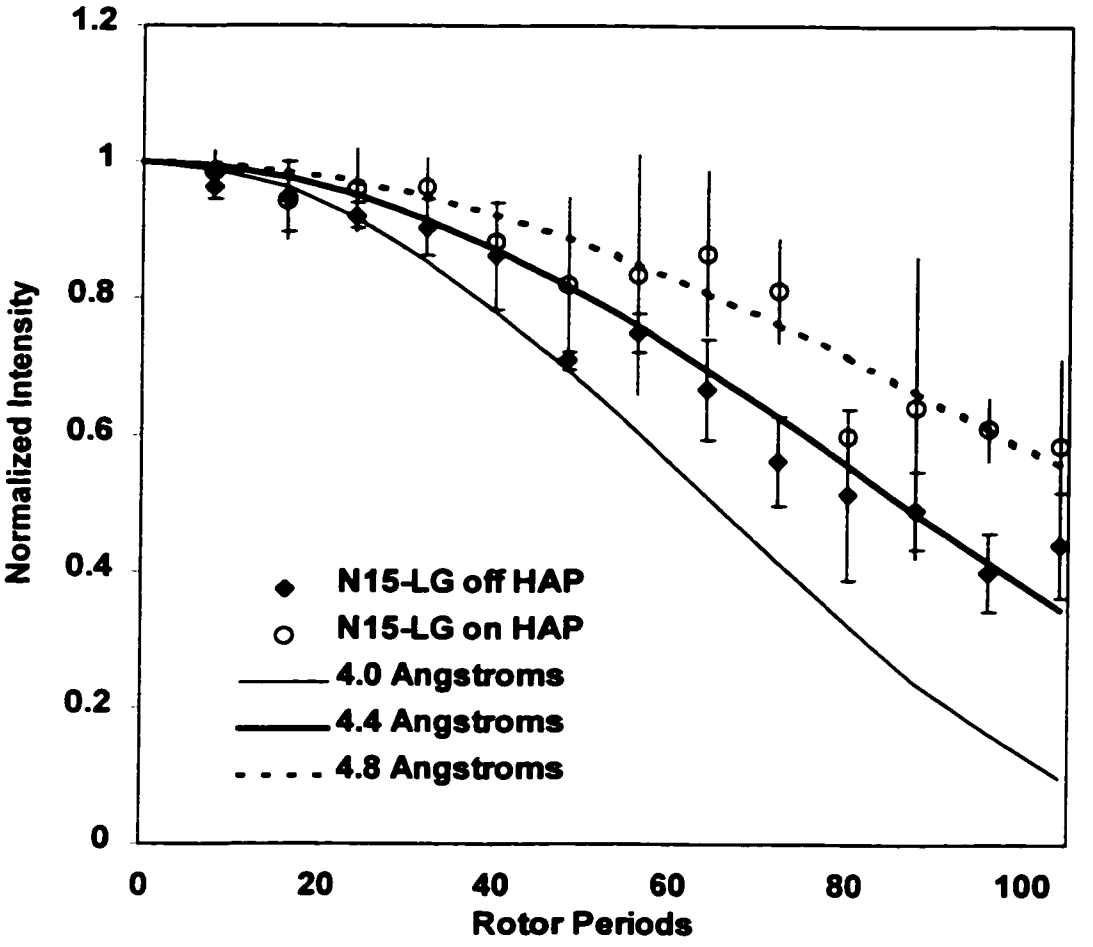

Figure 4.8. Experimental REDOR data of SN15-LG both on (open circles) and off (dark diamonds) HAP. The off the surface data fits best to a distance of 4.4 Å and the on the surface data fits to 4.8 Å most accurately. The expected distance for a classical alpha helix is 4.2 Å, clearly indicating a significant portion of helical content both on and off the surface. Simulations shown are of 4.0, 4.4 and 4.8 Å as indicated.

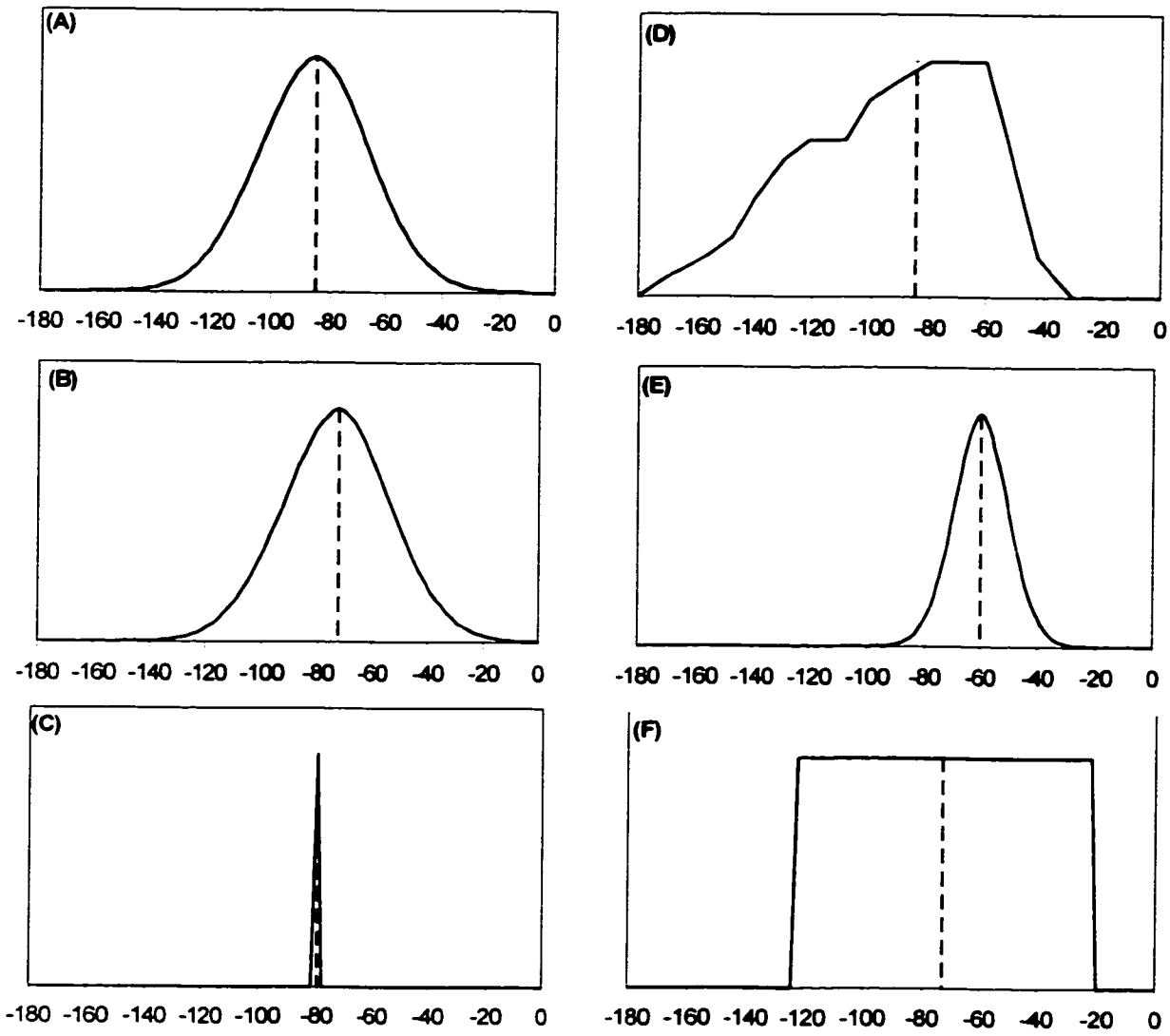

Figure 4.9. The distribution most closely simulating the experimental DRAWS dephasing curves are shown for each sample on and off the surface. A) SN15-SS off HAP ($\varphi = -85 \pm 20°$), B) SN15-FL off HAP ($\varphi = -73 \pm 20°$), C) SN15-IG off HAP ($\varphi = -80$) D) SN15-SS on HAP ($\varphi = -85$, with a random coil distribution), E) SN15-FL on HAP ($\varphi = -60 \pm 20°$), and F) SN15-IG on HAP ($\varphi = -73 \pm 50°$).

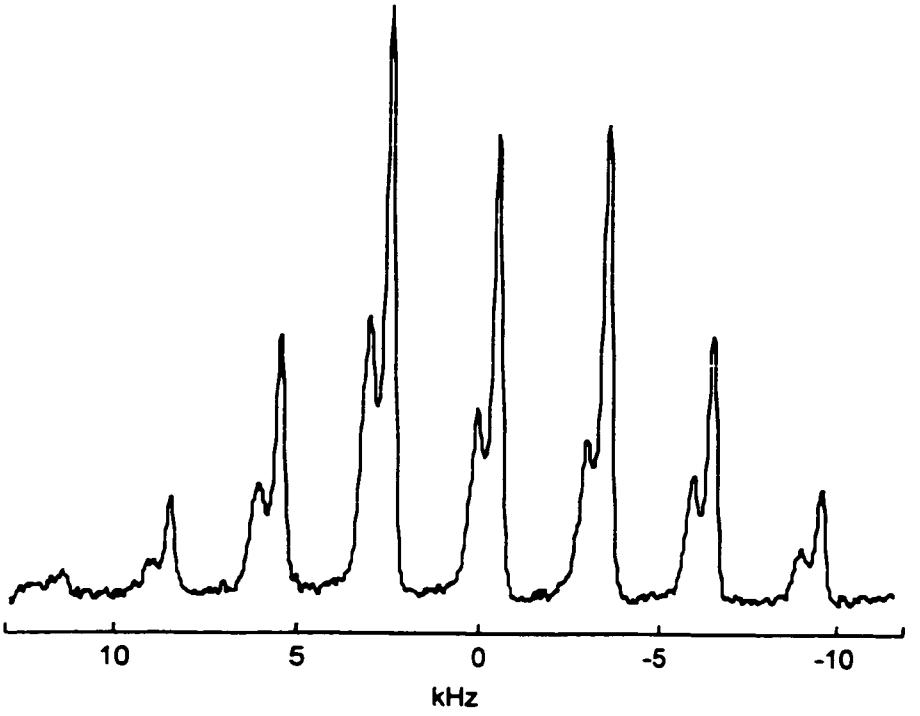

Figure 4.10. A CPMAS spectrum of LK-3_{10} taken by Dr. Joanna Long at a spinning speed of 3 kHz on a 500 MHz magnet. The unique resonances are representative of 2 secondary structures. Notice the difference in the CSA of the two contributing species, with an η=0.60 for the less abundant peak and an η=0.85 for the more abundant species, determined by other experiments to be representative of α-helical and random coil secondary structures, respectively.

CHAPTER 5:

DYNAMICS OF SN15

Dynamics and structure are often implicated as being directly related to each other and the function of a given biopolymer. Dynamics of surface adsorbed samples can be particularly revealing, giving an indication of how strongly the protein is interacting with the surface. SSNMR is particularly insightful where site specific labels allow correlation of motion with residue position.

In this Chapter, the dynamics of the SN15 peptide adsorbed onto hydroxyapatite and studied under hydrated conditions will be discussed. Solid state NMR was used to extract site specific mobility by examining peptides isotopically labeled at six unique backbone carbonyl carbon positions in the SN15 peptide of salivary statherin. The doubly labeled backbone carbonyl samples made for DRAWS measurements were utilized here, and for clarity in the discussion, are referred to as:

SN15-*pS$_2$pS$_3$* D***pSpS***EEKFLRRIGRFG

SN15-*F$_7$L$_8$* DpSpSEEK***FL***RRIGRFG

SN15-*I$_{11}$G$_{12}$* DpSpSEEKFLRR***IG***RFG

The three peptides containing single backbone carbonyl isotopic labels incorporated at the corresponding three positions were also utilized, and here are called:

SN15-*pS$_3$* DpS***pS***EEKFLRRIGRFG

SN15-*L$_8$* DpSpSEEKF***L***RRIGRFG

SN15-G_{12} DpSpSEEKFLRRI*G*RFG

MAS line shape analysis performed on each of the six positions allowed determination of the chemical shift tensor values. Relaxation measurements were also made on each of the doubly labeled samples to further characterize motional modes. Finally a simple model and its applicability are discussed.

5.1 Chemical Shift Anisotropy (CSA) results

Dynamic information was obtained from cross polarization magic angle spinning (CPMAS) spectra by determining chemical shift anisotropy (CSA) tensor values, listed in Table 1. CSA tensor values were obtained for each sample under 3 conditions: the lyophilized peptide off the surface, the peptide adsorbed to the surface, hydrated and the peptide adsorbed to the surface, lyophilized. Also shown in Table 1 are the span and η, indicating the breadth of the anisotropy and the deviation from axial symmetry, respectively. Figure 1 shows the CPMAS spectra (unnormalized) at each of the 6 positions along the SN15 peptide under hydrated conditions (a) and lyophilized conditions (b). Figure 1a shows CPMAS spectra of the hydrated samples. Motional averaging on the timescale of the chemical shift anisotropy is clearly increasing as the probe site is moved away from the N-terminus and toward the C-terminus, based on the extreme narrowing of the CSA, particularly evident in the I_{11} and G_{12} spectra. Figure 1b displays the spectra for the identical sample after lyophilization and collected with the same instrumental parameters. Typical CSA values for rigid carbonyl carbons in a peptide bond are observed, i.e. an anisotropy approaching 150 ppm and an η of almost

0.8-0.9 (shown in Table 5.2), indicating that the observed motion is not inherent in the protein, but is unique to the bound, hydrated protein.[1]

The results for both lyophilized and hydrated surface adsorbed samples, along with results for the peptide lyophilized from buffered solution are summarized in Figure 2. Under hydrated conditions, there is little change in the backbone carbonyl carbon CSA at the phosphoserine positions, with δ's narrowing by only 6 and 8 ppm, respectively. Slightly more change is observed at the phenylalanine and leucine positions where the $|\sigma_{11} - \sigma_{33}|$ narrow by 10 ppm and 28 ppm, respectively. The most remarkable motional averaging is observed at the isoleucine ($\Delta|\sigma_{11} - \sigma_{33}| = 75$ ppm) and glycine ($\Delta|\sigma_{11} - \sigma_{33}| = 91$ ppm) positions. The comparison here clearly shows the presence of large amplitude motion at the I_{11} and G_{12} positions, less motion at the F_7 and L_8 positions and virtually no motion (on the scale of the CSA interaction) at the pS_2 and pS_3 positions. The anisotropy of the peptides off the surface are nearly identical to the lyophilized peptide adsorbed to the surface (as shown in Table 5.1), indicating that there is no motion in either the surface bound or unbound peptide in the lyophilized state.

Another interesting feature obtained from the tensor value analysis is the decrease in η in the hydrated samples. Particularly for the pS_2, pS_3, F_7 and L_8 positions (the η at the I_{11} and G_{12} positions should be interpreted carefully, due to the high degree of averaging), η reduces to ~0.6, which is indicative of a secondary structural change.[1,2] Based on work done by J.R. Long[3], an η of 0.6 is indicative of helical secondary structures, while 0.8-0.9 is more consistent with random coil structures. Also interesting

to note is that the off the surface samples have a similar value of η (ie 0.6). While the chemical shift anisotropy has been shown to provide secondary structural information[1], the motion present in the hydrated samples could also cause the observed change in η and makes any statement of structure or structural change based on CSA very difficult. The contribution from the hydroxyapatite is also unclear, however frozen hydrated surface adsorbed samples might allow further structural information through the CSA as a function of hydration. In this case, the dipolar recoupling measurements already made are highly quantitative and interpretational ambiguities have been accounted for in simulations. This being the case, correlating changes in the CSA to the known structure may provide insight into the ongoing discussion of the accuracy of the chemical shift and chemical shift parameters in determining secondary structure.

5.2 $T_{1\rho}$ Results

To further investigate the dynamics, ^{1}H and ^{13}C $T_{1\rho}$ measurements were obtained for the I_{11}-G_{12} region[4]. The ^{13}C $T_{1\rho}$ is a site-specific probe, sensitive to the specific carbon being observed. The ^{13}C $T_{1\rho}$ were measured for each doubly labeled sample under all three conditions and are summarized in Table 5.2. SN15-pS_2pS_3 had $T_{1\rho}$ values of 36, 26 and 36 msec for free, lyophilized and hydrated samples. The ^{13}C $T_{1\rho}$ for SN15-F_7L_8 were 30 msec off, 21 msec on and 11.7 msec hydrated, indicating an increase in motion in this region of the protein. SN15-$I_{11}G_{12}$ have $T_{1\rho}$ values of 41 msec off the surface, 110 msec on the surface and 3 msec hydrated on the surface. These results are shown in Figure 5.3 A-C, respectively. It can be seen in these figures that values above

approximately 20-25 msec are nearly indistinguishable, suggesting that numbers above these values should be interpreted as generally rigid. To distinguish between these curves, experimental data would need to be taken out to much longer times. These results are consistent with the motion observed in the Herzfeld-Berger analysis, showing no motion at the pS_2pS_3 region, slightly more mobility at the F_7L_8 region and a large increase at the $I_{11}G_{12}$ C-terminal portion. Other contributions to the $T_{1\rho}$ relaxation include the dipolar coupling and CSA. The dipolar coupling should be similar for the samples under each of the three conditions since each of them should experience very similar coupling. This is also true for the CSA, which remains fairly constant in all cases except in the IG region. The CSA could be contributing to relaxation in this region, however, the CSA narrows by a factor of 2.5, whereas the $T_{1\rho}$ decreases by a factor of 10-30, which is significantly larger than the CSA narrowing. Also, the agreement of the CSA results with the Herzfeld-Berger results supports the interpretation of large amplitude motion on a timescale faster than 1×10^{-5} seconds.

The mobility of the IG region is also observed in the loss of signal in the hydrated sample. While the spectra in Figure 5.1 are not normalized, the decrease in signal to noise in the I_{11} and G_{12} spectra as compared to the pS samples is substantial, particularly when considering the significantly narrowed CSA. The F_7 and L_8 samples cannot be compared this way since the L_8 sample had fewer scans taken for the hydrated sample (this was the only case that this happened), resulting in different signal to noise.

^1H $T_{1\rho}$ is sensitive to the motion of the proton bath, giving information on the mobility of the entire system being studied. The ^1H $T_{1\rho}$ was measured only for SN15-

$I_{11}G_{12}$ under all three sample conditions and were found to be nearly identical for each condition. In this case, the contribution of protons in the peptide that do not experience motion, as well as the proton contribution from HAP makes extracting the peptide mobility information very difficult. The site specificity of the ^{13}C $T_{1\rho}$ measurement is far superior for the peptide/HAP system and remained the main focus of relaxation measurements.

5.3 Linewidth Results

Also of significance in comparing the lyophilized and hydrated adsorbed peptides is the remarkable decrease in linewidth of the hydrated samples. In the pS_2pS_3 region, the linewidths narrow from 7.3 ppm to 4.3 ppm for pS_2 and 6.1 to 3.5 ppm for pS_3, comparing lyophilized and hydrated samples, respectively. The middle portion of the peptide displays even greater narrowing where F_7 narrows from 6.6 ppm to 3.3 ppm and L_8 narrows from 6.6 ppm to 3.0 ppm. At the C-terminus, I_{11} has a linewidth of 7.0 ppm in the lyophilized state and 2.3 ppm in the hydrated state. Similarly, G_{12} reduces in linewidth from 6.8 ppm to 2.3 ppm.

There are many contributions to line narrowing, including motion, conformational heterogeneity and magnetic susceptibility. In Chapter 4, the large magnetic susceptibility of dry hydroxyapatite was postulated to contribute to the peptide linewidth. Magnetic susceptibility contributes to linewidth in the following way. Magnetic susceptibility is a tensorial component that contains isotropic and anisotropic components. Van der Hart[5] explained how the isotropic bulk magnetic susceptibility (IBMS) could be thought of as dividing up a randomly shaped sample into many small spheres, each containing a dipole.

The field inside each sphere is uniform, and a single spherical shaped particle with isotropic magnetic susceptibility would experience no susceptibility broadening. The interaction of a single sphere with other spheres in the sample causes different fields to be experienced at different places in the sample, causing line broadening. Since the field inside a sphere can be thought of as a dipole, there is a $(3\cos^2\theta - 1)$ dependence and broadening effects can thus be removed by MAS. This is more clearly pictured in Figure 5.4. The anisotropic bulk magnetic susceptibility (ABMS) creates dipolar fields that are orientation dependent, and depend on the orientation of the magnetic susceptibility tensor with the field. This can be thought of in a way similar to ring current effects and are not removed during magic angle spinning. Broadening effects due to ABMS are observed as has been reported often for polymer and paramagnetic systems.[5-9] Surrounding a single crystal having ABMS with a particle having similar isotropic susceptibility will help to reduce the line broadening by matching the susceptibility. The broadening will never be completely removed by dilution in a medium with IBMS since shape effects will persist.

HAP has a bulk magnetic susceptibility of 150 ppm $cm^3/mole$[10], or 20 kHz at 500 MHz proton frequency. The observed narrowing of the carbonyl linewidths of 1.5-2 times when calcium phosphate buffer is added supports the idea of susceptibility matching. While MAS may partially remove isotropic contributions, the magnitude of the magnetic susceptibility makes it is very conceivable that it has not been completely removed by MAS, and as stated above the ABMS broadening is not removed by MAS.

By filling in the spaces surrounding each crystal with a highly ionic calcium phosphate buffer, either or both the IBMS and the ABMS could be matched, allowing each peptide to experience a more uniform environment and thus narrowing the lines. Associated with this, the effect of magnetic susceptibility as a function of distance from the surface could contribute to linewidth. If the labeled regions of the peptide are different distances from the surface, magnetic susceptibility effects may not be the same for all regions of the peptide, resulting in varying degrees of line narrowing upon susceptibility matching. The extent that this would contribute is unknown, as this effect has heretofore been unexamined in the literature.

Motion may still contribute as a narrowing mechanism. The timescale of the motion being measured here is in the kilohertz region (10^3 to 10^5). Motions slower than this could be contributing to narrowed linewidths. The I_{11} and G_{12} regions, where large amplitude and timescale motions are observed, would also be a potential candidate for motional narrowing. The observation that lines for I_{11} and G_{12} narrow significantly more than the other labeled regions under hydrated conditions and the additional observation that there is more motion in this region of the peptide suggests motional narrowing at the C-terminus as a reasonable possibility.

Conformational heterogeneity could also contribute to broad linewidths, suggesting that the narrower linewidths observed for the hydrated samples could be a result of water molecules stabilizing a more narrow range of conformations. The exact mechanism for line narrowing is unclear but is likely a combination of several or all of the above factors.

5.4 Discussion

The N-terminal 6 residues of statherin have been shown to play a key role in the binding of salivary statherin to hydroxyapatite, with the phosphoserines directly implicated in the recognition mechanism.[11] It was demonstrated in Chapter 4 that the phosphoserines in the adsorbed peptide most likely exist in a random coil secondary structure, which may facilitate maximal electrostatic interactions with HAP. The apparent rigidity in this portion of the surface-adsorbed peptide directly supports the hypothesis that these phosphoserines function as direct HAP binding contacts.

The F_7 and L_8 positions displayed slightly more motional freedom. The proximity to the phosphoserine (and potentially the glutamic acid) binding contacts is likely restricting motion at this portion of the peptide. Other potential restrictions to large motion are the helical structure of the peptide in this region and electrostatic interactions between surface phosphate groups and the arginine and lysine sidechains which follow the F_7L_8 position.

The I_{11} and G_{12} positions clearly experience a great deal of motional averaging, though it is currently unclear whether it is a single large amplitude motion or a result of many small amplitude fluctuations along the peptide backbone. These two residues are flanked on both sides by arginine residues, which have the potential to interact with phosphates on the HAP surface. The dynamics results suggest that these arginine residues do not interact strongly with the surface. The measured secondary structure at the I_{11}-G_{12} position for the lyophilized surface adsorbed peptide is also consistent with large motional averaging in that it was seen to have a broad distribution of conformations.

5.5 Motional Model

A peptide-HAP interaction model that is consistent with the current dynamic studies and previous structural studies is shown in Figure 5.5. This model suggests that the random coil conformation at the N-terminus allows strong interactions between HAP and the phosphoserine and glutamic acid side-chains. The α-helical middle region of the peptide is still interacting with the surface but is less rigidly attached, while the C-terminal end of the peptide has very little interaction with the surface. The averaging of the motion at the I_{11} and G_{12} positions is most consistent with a multiaxial, rather than uniaxial motion. Two reasonable interpretations would be that of large frequency and large amplitude dynamics, or large frequency dynamics with small amplitude contributions from many different positions along the peptide backbone. A simple model analysis of the dynamic results was performed using diffusion of a rigid rod on a cone[12] to describe the motion of the four observed carbonyl carbons in the helical portion of the peptide (F_7, L_8, I_{11}, G_{12}), and is discussed in more detail in Appendix II. The simulations did not provide results consistent with experimentally determined averaging for the four carbonyls. The failure can be explained by inspection of Figure 1.4. Since the carbonyl groups are all pointed in approximately the same direction, their tensors would be averaged similarly, or least, F_7 and I_{11} would experience similar averaging and L_8 and G_{12} would be similar. That is not what is observed and is enough to discard this simple model. A more accurate model would include internal torsional motions in the simulated model, and a more appropriate model may be one that represents the peptide as a flexible rod that is bound to the surface at the N-terminus, with three torsional degrees of freedom

being added per residue as distance is increased from the immobilized end. Another model may involve two rigid rods with a hinge site allow the $I_{11}G_{12}$ region to experience much different averaging then the FL region. The experiments performed here also do not address the orientation of the helix to the surface, and thus the current results do not uniquely determine a detailed dynamic motional model. In order to more specifically constrain and determine the motional modes, interactions with the surface are necessary, as well as additional relaxation measurements, such as T_1 as a function of B_0 field or $T_{1\rho}$ as a function of B_1 field.

5.6 Notes to Chapter 5.

1. Gu, Z. & McDermott, A. Chemical Shielding Anisotropy of Protonated and Deprotonated Carboxylates in Amino-Acids. *Journal of the American Chemical Society* **115**, 4282-4285 (1993).

2. Ando, S. *et al.* Confromational Characterization of Glycine Residues Incorporated into Some Homoppolypeptides by Solid-State ^{13}C NMR Spectroscopy. *Journal of the American Chemical Society* **107**, 7648-7652 (1985).

3. Unpublished Results.

4. Schaefer, J., Stejskal, E. O. & Buchdahl, R. Magic-Angle 13C NMR Analysis of Motion in Solid Glassy Polymers. *Macromolecules* **10**, 384-405 (1977).

5. VanderHart, D. L., Earl, W. L. & Garroway, A. N. Resolution in 13C NMR of Organic Solids Using High-Power Proton Decoupling and Magic-Angle Sample Spinning. *Journal of Magentic Resonance* **44**, 361-401 (1981).

6. Burum, D. P. & Rhim, W. K. Analysis of Multiple Pulse NMR in Solids. III. *Journal of Chemical Physics* **71**, 944-956 (1979).

7. Alla, M. & Lippmaa, E. Resolution Limits in Magic-Angle Rotation NMR Spectra of Polycrystalline Solids. *Chemical Physics Letters* **87**, 30-33 (1982).

8. Elbayed, K. *et al.* Origin of the Residual NMR Linewidth of a Peptide Bound to a Resin under Magic Angle Spinning. *Journal of Magnetic Resonance* **136**, 127-129 (1999).

9. Stoll, M. E. & Majors, T. J. Reduction of Magnetic Susceptibility Broadening in NMR by Susceptibility Matching. *Journal of Magnetic Resonance* **46**, 283-288 (1982).

10. Weast, R. C. (ed.) *Handbook of Chemistry and Physics* (CRC Press, Boca Raton, 1982).

11. Raj, P. A., Johnsson, M., Levine, M. J. & Nancollas, G. H. Dependence on Sequence, Charge, Hydrogen Bonding Potency, and Helical Conformation for Adsorption to Hydroxyapatite and Inhibition of Mineralization. *Journal Biological Chemistry* **267**, 5968-5976 (1992).

12. Wittebort, R. J., Olejnicxak, E. T. & Griffen, R. G. Analysis of Deuterium Nuclear Magnetic Resonance Line Shapes in Anisotropic Media. *Journal of Chemical Physics* **86**, 5411-5430 (1987).

Table 5.1. Summary of chemical shift and CSA data.

	Sample Prep	Linewidth	Chemical Shift	σ_{11}	σ_{22}	σ_{33}	η	Ω
pS_2	Off	4.85	173.2	-65.5	-16.0	81.5	0.61	146
	Bound, lyophilized	7.33	173.0	-68.8	-5.6	74.7	0.85	145
	Bound, Hydrated	4.25	174.2	-59.0	-18.4	77.5	0.53	137
pS_3	Off	3.26	172.6	-65.2	-14.1	79.3	0.65	148
	Bound, lyophilized	6.10	171.8	-71.9	-5.7	76.6	0.88	148
	Bound, hydrated	3.53	179	-64.8	-11.5	76.3	0.62	141
F_7	Off	3.9	174.2	--	--	--	--	147
	Bound, lyophilized	6.64	173.8	-68.0	-5.8	73.8	0.84	144
	Bound, hydrated	3.31	175.2	-62.7	-10.8	73.5	0.70	134
L_8	Off	3.43	177.1	-67.6	-15.6	83.2	0.62	150
	Bound, lyophilized	6.56	175.2	-65.9	-12.8	78.7	0.67	144
	Bound, hydrated	3.04	177.0	-55.1	-17.3	72.4	0.52	116
I_{11}	Off	4.17	172.2	-60.1	-21.2	81.3	0.48	141
	Bound, lyophilized	6.96	173.0	-68.1	-8.0	76.0	0.79	144
	Bound, hydrated	2.27	174.8	-28.1	-16.1	44.2	0.97*	70
G_{12}	Off	5.23	172.6	-69.8	-9.3	79.0	0.77	148
	Bound, lyophilized	6.81	171.9	-71.5	-6.9	78.4	0.82	148
	Bound, hydrated	2.26	171.8	-25.7	4.0	37.4	1.0*	57

*These values should be interpreted carefully as the large extent of averaging made fitting tensor values more difficult.

Table 5.2. Summary of $T_{1\rho}$ data, in msec.

	Off	Bound, lyophilized	Bound, hydrated
pS_2pS_3	36	26	36
F_7L_8	30.4	21.3	11.7
$I_{11}G_{12}$	41.00	110.00	3.30

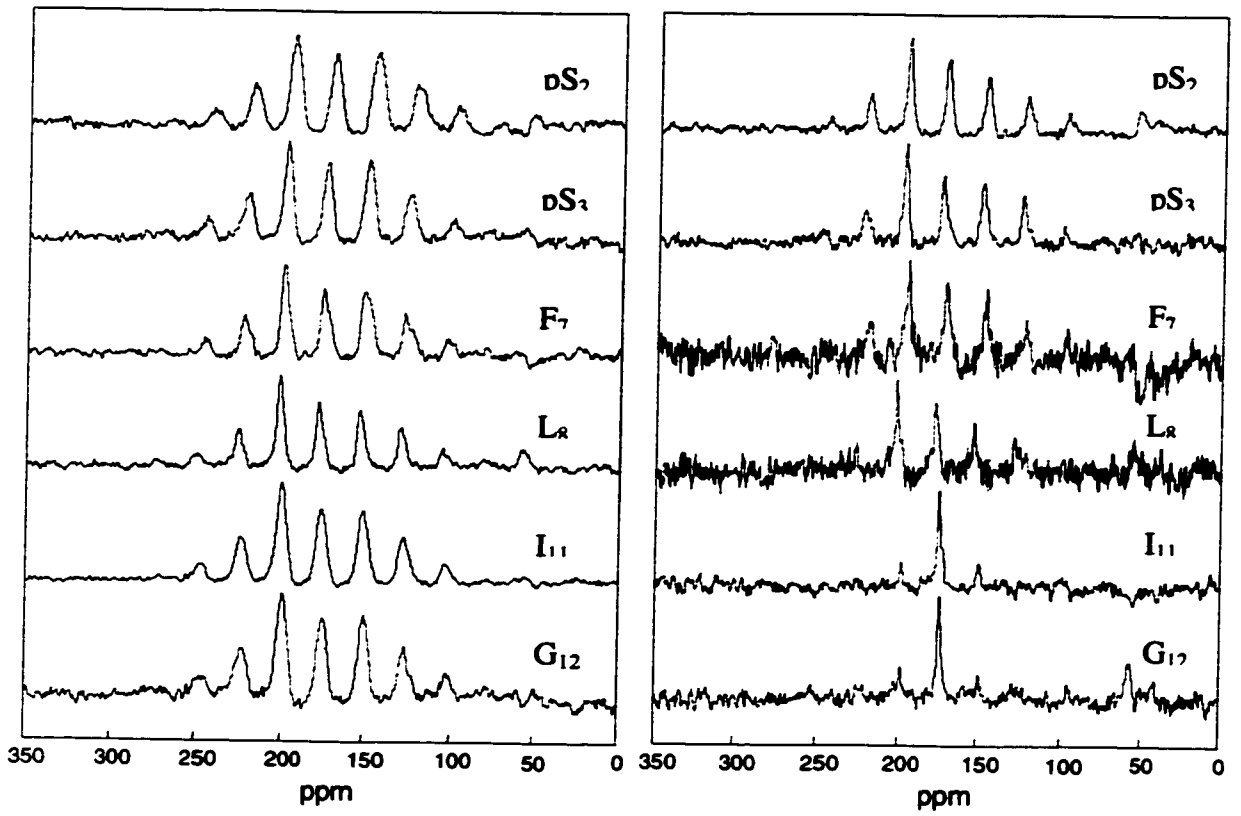

Figure 5.1. CPMAS spectra of SN15 samples adsorbed to HAP (* indicates isotropic): a) lyophilized b) hydrated. From top to bottom: SN15-pS_2, SN15-pS_3, SN15-F_7, SN15-L_8, SN15-I_{11} and SN15-G_{12}. Subtracting the single isotopically labeled spectra from the doubly labeled spectra resulted in the 3 spectra for SN15-S_2, SN15-F_7 and SN15-I_{11}, and each sample was corrected for natural abundance signal. The lyophilized samples all fit approximately the same tensor values. The tensor values extracted from the hydrated spectra change very little for the labeled sites at the N-terminus (pS_2pS_3), more significantly for the middle of the peptide (F_7L_8) and very noticeably at the C-terminus ($I_{11}G_{12}$), suggesting there is increasing motion toward the C-terminus when bulk water is present. The lower apparent signal to noise for the F_7 and L_8 positions is a result of fewer scans taken for the L_8 hydrated sample (this sample only), resulting in lower signal to noise for the SN15-L_8 spectrum, and upon subtraction from SN15-F_7L_8, lower S/N for the SN15-F_7 spectrum. The lower S/N for the I_{11} and G_{12} regions is real.

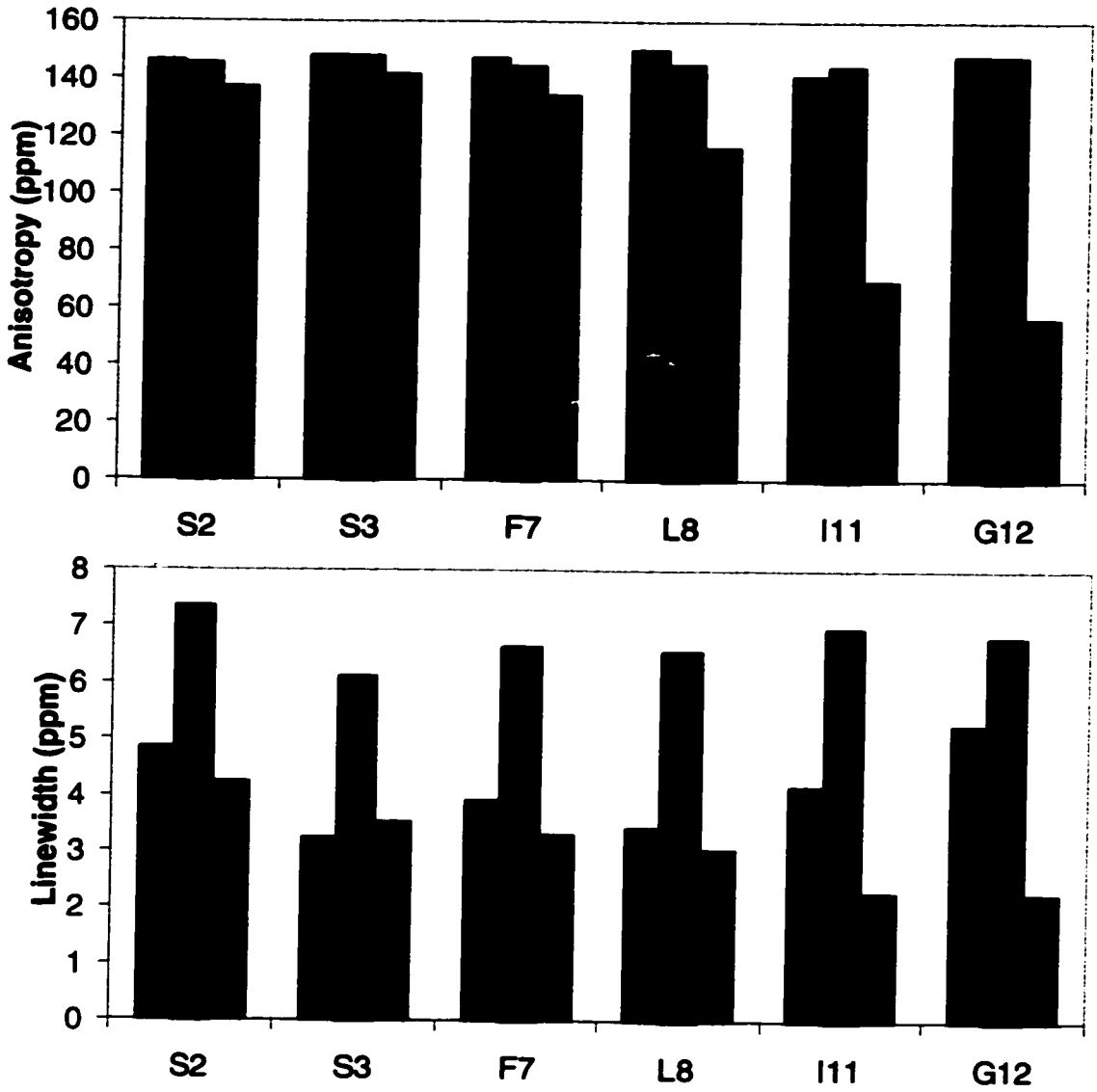

Figure 5.2. Top. $|\sigma_{11}-\sigma_{33}|$ values as a function of sample preparation (dots = off the surface, horizontal lines = lyophilized on the surface and diagonal lines = hydrated on surface). The lyophilized samples all have very similar CSA patterns and thus anisotropy values (140-150 ppm). Upon hydration, the change in anisotropy for F_7, L_8, I_{11} and G_{12} (10, 28, 75 and 90 ppm, respectively) is significant, suggesting the presence of motion at these sites.

Bottom. The linewidth as a function of sample preparation is shown. The lyophilized peptides off the surface have linewidths on the order of 3-4 ppm. Upon adsorption to the surface, the lyophilized samples have a linewidth of 6-7 ppm. Hydrated, the adsorbed peptides have linewidths of only 2-4 ppm. As discussed in the text, the observed linewidths could be a function of the bulk magnetic susceptibility of HAP, conformational heterogeneity, or motional averaging.

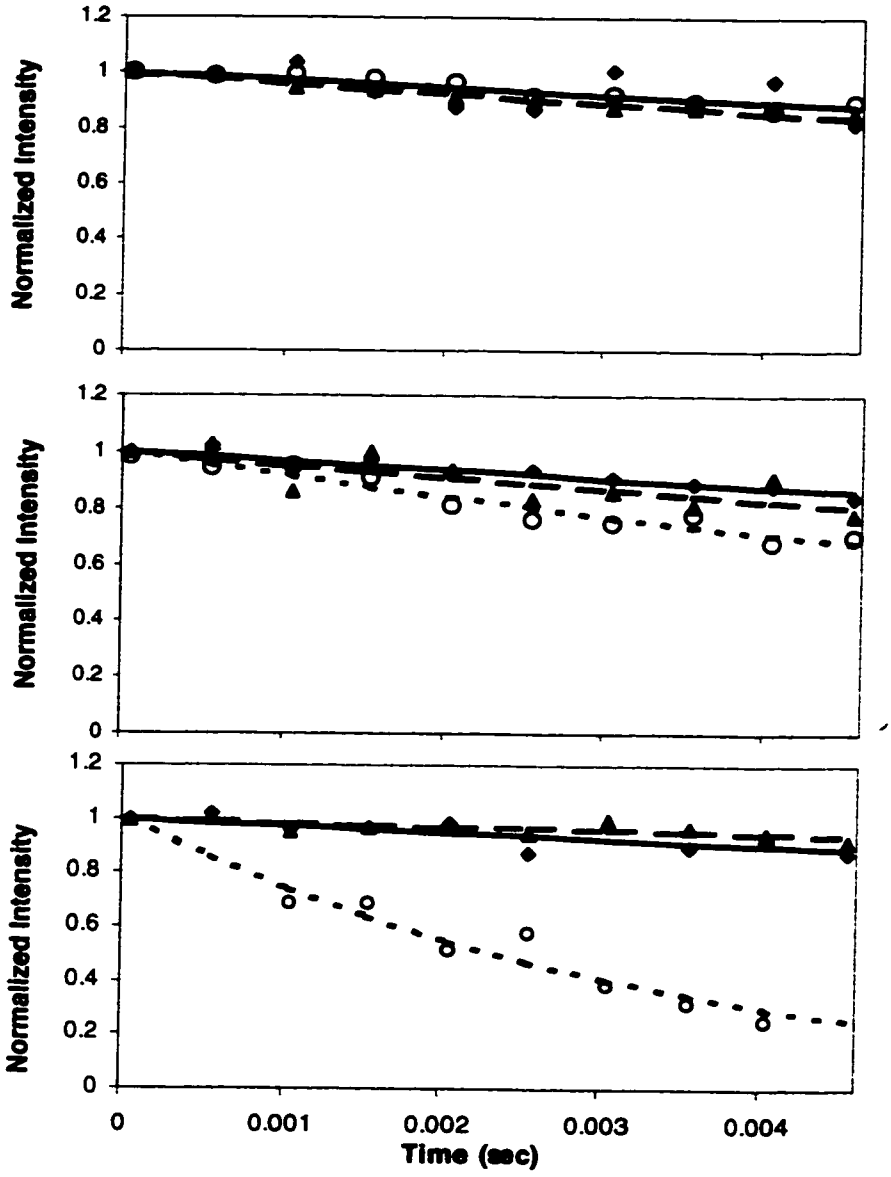

Figure 5.3. ^{13}C $T_{1\rho}$ relaxation data for A) SN15-pS_2pS_3, B) SN15-F_7L_8 and C) SN15-$I_{11}G_{12}$. Experimental data are shown for off the surface (♦), adsorbed to HAP, lyophilized, (▲) and adsorbed to HAP, hydrated, (O). The off the surface and on the surface, lyophilized samples all have very similar $T_{1\rho}$ (above 20 msec). The hydrated SN15-pS_2pS_3 has a long correlation time (36 msec), suggesting little motion on the timescale of the experiment. A slightly faster correlation time is seen at F_7L_8 (11.7 msec) and a significantly faster correlation time is observed at $I_{11}G_{12}$ (3.3 msec), indicating mobility on a timescale between 10^3-10^5 Hz.

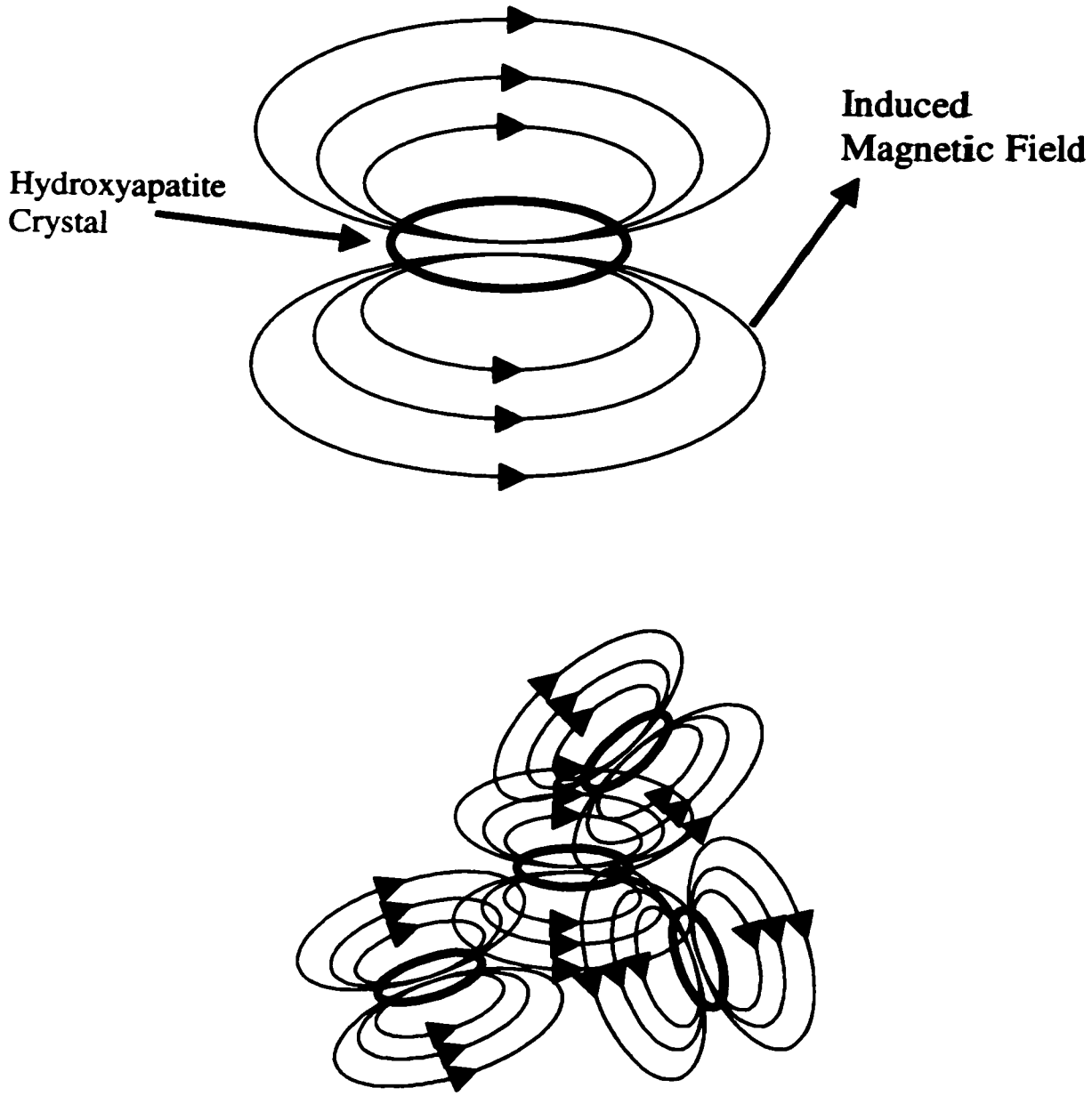

Figure 5.4. Top. A single ellipsoid hydroxyapatite particle, showing the lines of force radiating from it, creating a uniform field within the particle. Bottom. Many hydroxyapatite particles together experience their neighbors magnetic fields, causing magnetic susceptibility. In the non-ideal case where the hydroxyapatite particles have random shapes, the field inhomogeneity effects are even more pronounced.

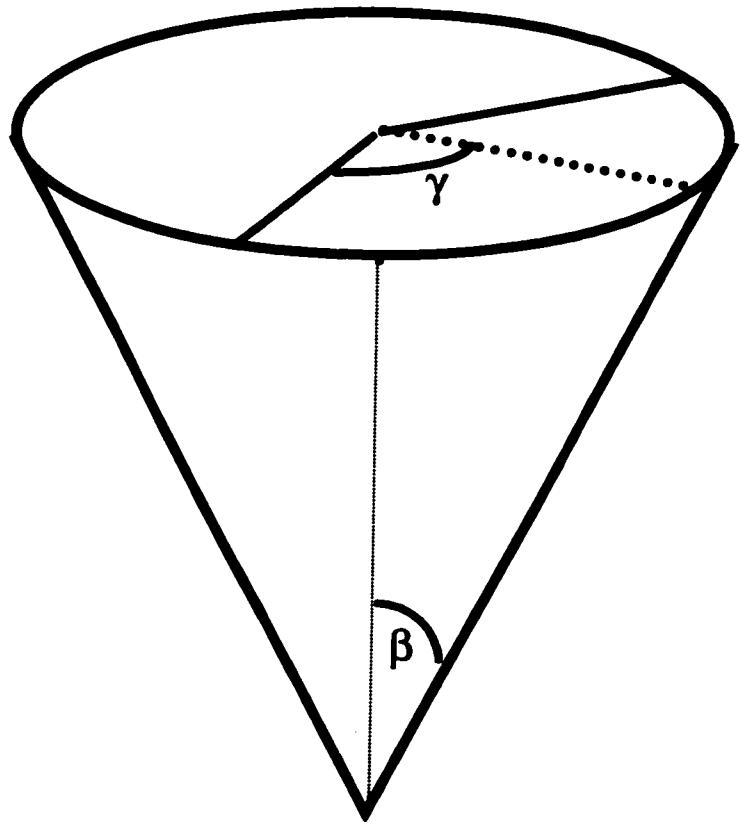

Figure 5.5. Motional model used for a simple dynamics calculation, where β and γ are defined as the cone ½ angle and the rotation ½ amplitude, respectively. Refer to Appendix II for more discussion.

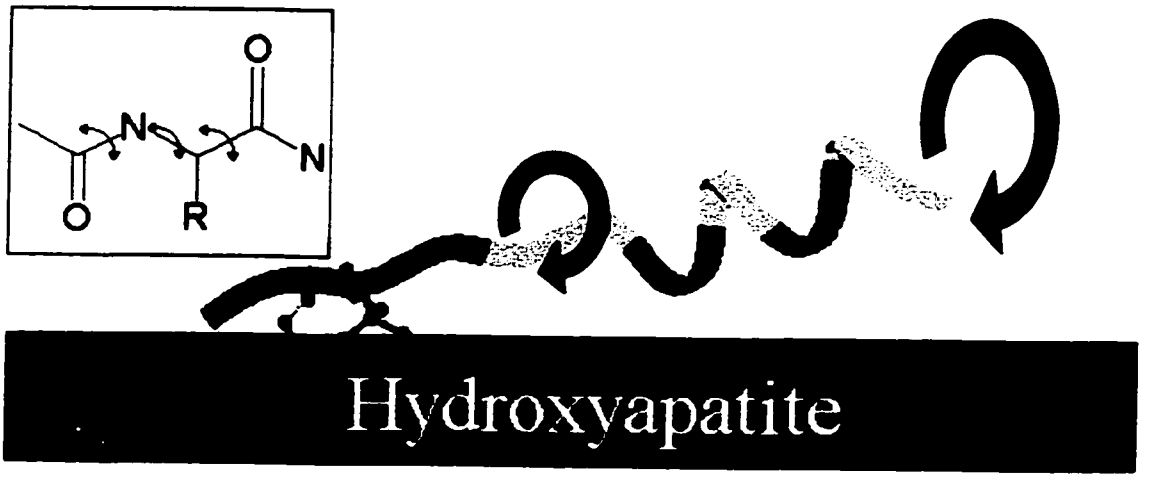

Figure 5.6. A cartoon of the proposed interaction with the surface is shown (darkened regions correspond to charged residues), with arrows indicating one possible collective motion, and the subset indicating the possible torsional contributions. The number of degrees of freedom available to the C-terminal residues supports a multiaxial, large frequency and amplitude motion. The data are most consistent with the subset, indicating increased motion, rather than a collective motion as the distance from the N-terminus is increased.

CHAPTER 6:
STRUCTURE AND DYNAMICS OF STATHERIN

In this chapter, the structure and dynamics of the full protein statherin bound to the surface under hydrated and lyophilized conditions will be presented and discussed and a comparison will be made with the N-terminal peptide.

This study focused on the structure of the N-terminal interaction region of statherin. To facilitate comparisons to the SN15 peptide, samples were prepared with labels corresponding to the same positions as were labeled in the SN15 peptide. The three labeling schemes utilized for DRAWS measurements are shown below, with backbone carbonyl labels indicated in bold italics.

Stath-pS_2pS_3 D***pSpS***EEKFLRRIGRFGYGYGPYQPVPEQPLYPQPYQPQYQQYTF

Stath-F_7L_8 DpSpSEEK***FL***RRIGRFGYGYGPYQPVPEQPLYPQPYQPQYQQYTF

Stath-$I_{11}G_{12}$ DpSpSEEKFLRR***IG***RFGYGYGPYQPVPEQPLYPQPYQPQYQQYTF

3 samples were prepared for REDOR measurements, extending across the entire N-terminus, where the bold, italics refer to backbone carbonyl labels and the underline differentiates the ^{15}N backbone labeled amide:

Stath-pS_3F_7 DpS***pS***EEK***F***LRRIGRFGYGYGPYQPVPEQPLYPQPYQPQYQQYTF

Stath-L_8G_{12} DpSpSEEKF***L***RRI***G***RFGYGYGPYQPVPEQPLYPQPYQPQYQQYTF

Each of the above samples was also used for dynamics measurements. An additional sample was prepared to probe the effects of the only charged residue in the C-terminus, E_{26}. Backbone carbonyl carbons were incorporated into the $I_{11}G_{12}$ positions and the Glu was replaced with a Gln (unlabeled), as indicated in bold, to observe any differences in the dynamics at the N-terminus when the C-terminus is completely hydrophobic.

Stath-Q DpSpSEEKFLRR***IG***RFGYGYGPYQPVP***Q***QPLYPQPYQPQYQQYTF

Lastly, a doubly labeled ^{15}N sample was prepared to determine the torsion angle, ψ. This sample also served as a natural abundance carbon sample.

15N-Stath-FL DpSpSEEK***FL***RRIGRFGYGYGPYQPVPEQPLYPQPYQPQYQQYTF

6.1 Results

6.1.1 Characterization

Proteins were characterized with matrix assisted laser desorption ionization (MALDI) and preferentially, with electrospray mass spectrometry. A representative spectrum is shown in Figure 6.1 and molecular weights in Daltons were as follows: Stath-pS_2pS_3 (5380.0), Stath-pS_3F_7 (5383.0), Stath-F_7L_8 (5381.9), Stath-L_8G_{12} (5382.0), Stath-$I_{11}G_{12}$ (5384.2), Stath-Q (5382) and 15N-Stath-FL (5385.0).

6.1.2 Chemical Shift

Chemical shift spectra are shown in Figure 6.2 and 6.3. The chemical shift values of the hydrated, surface adsorbed samples were determined by external reference to hexamethyl benzene, 17.35 and 132 ppm from TMS. Stath- pS_2pS_3 had a chemical shift of 174.1 ppm, with the individual labels having chemical shifts of 174.1 ppm for Stath-

pS_2 and 173.9 ppm for Stath-pS_3. Stath- F_7L_8 had a chemical shift of 174.9 ppm with subtractions yielding chemical shift values of 174.9 for Stath-F_7 and 178.2 ppm for Statherin-L_8. The chemical shift of the doubly labeled Stath- $I_{11}G_{12}$ was found to be 177.1 ppm.

6.1.3 Linewidth

The linewidths of each of the statherin samples were determined using 150 Hz line broadening. The lyophilized linewidth of Stath-pS_2pS_3 (6.48 ppm) narrows to 4.9 ppm upon hydration. In comparison, the off the surface sample has a linewidth of 4.7 ppm. Stath-F_7L_8 had linewidths of 6.3 ppm for the hydrated surface bound protein, 7.2 ppm for the lyophilized bound protein and 5.7 ppm for the off the surface protein. At the C-terminal end of the pentadecyl domain, Stath-$I_{11}G_{12}$ had linewidths of 9.18 ppm hydrated, on the surface, 6.66 ppm lyophilized, on the surface, and 7.17 ppm off the surface. At higher decoupling (>100 kHz) and faster spinning (5 kHz), the Stath-$I_{11}G_{12}$ sample has a linewidth of 7.5 ppm (all other samples remained the same under these conditions).

The corresponding singly labeled proteins were measured for the hydrated and lyophilized surface bound samples. The linewidths for the hydrated samples were 4.4 ppm for Stath-pS_3F_7 and 4.97 ppm for Stath-L_7G_8, and the corresponding linewidths for the lyophilized samples were 5.9 ppm and 7.2 ppm, respectively. Subtractions of the singly labeled spectrum from the corresponding doubly labeled spectrum resulted in the pS_2 and F_7 spectra. The linewidths for these labels were 5.1 ppm for Stath-pS_2 and 3.1

ppm for Stath-F_7 under hydrated conditions and 5.4 ppm and 6.4 ppm for the lyophilized samples, respectively.

6.1.4 Distance Measurements

Structural determinations were made using DRAWS and REDOR, under lyophilized and hydrated conditions and are summarized in Table 6.1. Under hydrated conditions, at –25° C, Stath-pS_3F_7 gave a measured distance of 4.2 Å (37 Hz) using REDOR. The experimental data is shown in Figure 6.4 as circles, and the 4.2 Å distance as a solid line. REDOR measurements at this distance typically have an associated error of ±0.5 Å, and the error bars indicate that to be an appropriate approximation for these experiments. After lyophilization, the distance between pS_3 and F_7 lengthened to 5.2 Å (22 Hz), shown in Figure 6.4 as diamonds, with the simulation at 5.2 Å represented by a line of long dashes and a 4.5 Å simulation shown as short dashes. The dephasing curve for Stath- L_7G_8 for the hydrated, surface bound sample at –25° C is shown in Figure 6.5 (circles) and is simulated well between 4.8 Å (28 Hz—short dashes). The distance was essentially the same for Stath-L_7G_8, lyophilized, within the scatter of the data (diamonds), fitting to 4.6 Å. Also shown are simulations for 4.0 Å and 5.5 Å, as indicated.

DRAWS data were fit with an experimentally determined T_2^{SQ} of 50 Hz and T_2^{DQ} of 110 Hz, and the experimental data and simulations are shown in Figures 6.6, 6.7, 6.8 and 6.9. DRAWS measurements for lyophilized, Stath-pS_2pS_3 bound to the surface (Figure 6.6--diamonds) yielded a φ torsion angle of -83°-88° (3.18-3.21 Å). Preliminary results for hydrated Stath- pS_2pS_3 bound to the surface (Figure 6.7, circles) taken at

ambient temperatures were best simulated by a torsion angle φ and distribution of –58° (light solid line) or -58° +/- 30° (heavy solid line). Also shown are the corresponding singly labeled samples under lyophilized (diamonds) and hydrated (triangles) conditions, without any background correction. The lyophilized, surface bound Stath-F_7L_8 (Figure 6.8—diamonds) fit well to an average distance of –68°, shown as a solid line. The lyophilized, surface bound sample labeled at the $I_{11}G_{12}$ region (Stath- $I_{11}G_{12}$) fit an average distance and distribution of –78° (3.12 Å), shown in Figure 6.9 as diamonds (experimental) and a solid line (simulation).

6.1.5 CSA tensor values

The CSA tensor values are summarized in Table 6.2. The doubly labeled lyophilized samples all have very similar chemical shift tensor values with an η around 0.75-0.85, and a Ω of roughly 150 ppm. The tensor values for the hydrated Stath-pS_2 sample were found to be –61.5, -12.4 and 74.0 ppm for σ_{11}, σ_{22} and σ_{33}, respectively with a span of 136 ppm, and an η of 0.66. The Stath-pS_3 region was very similar, giving tensor values of –62.5, -15.1 and –77.6 ppm, with a span of 140 ppm, and an η of 0.61. The F_7 and L_8 regions had slightly more averaged tensor values with spans of 135 ppm and 127 ppm and η's of 0.51 and 0.52, respectively, with the difference explained by a small change in tensor values, -58.4, -18.6 and 77 for F_7 and –54.9, -17.8 and 72.7 ppm for L_8. The doubly labeled $I_{11}G_{12}$ region was fit without the aid of a single label subtraction. The combined span was 111 ppm, with an η of 0.69, and tensor values of –50.9, -9.4 and 60.3 ppm.

6.1.6 *$T_{1\rho}$ measurements*

The ^{13}C $T_{1\rho}$ values for all statherin samples were measured at B_1 fields of 35 and 42 kHz and are summarized in Table 6.1. The measured values for the lyophilized samples at 35 kHz are: Stath-pS_2pS_3 11.7 msec, Stath-F_7L_8 13.0 msec and Stath-$I_{11}G_{12}$ is 11.5 msec. The hydrated samples have $T_{1\rho}$ values of 11.2 msec, 3.5 msec and 2.5 msec for the pSpS, F_7L_8 and $I_{11}G_{12}$ regions, respectively. $T_{1\rho}$ measurements were also made for two of the doubly labeled lyophilized, unbound protein samples, and gave values of 17.5 msec for Stath- F_7L_8 and 9.4 msec for Stath- $I_{11}G_{12}$. The single labeled samples had $T_{1\rho}$ values of 9.5 and 9.1 msec for lyophilized and hydrated samples carbonyl labeled at pS_3 and for the carbonyl label at L_8, gave 7.9 and 4.3 msec for lyophilized and hydrated, respectively. The $T_{1\rho}$ measurement for Stath-Q was determined to be 2.9 msec at this larmor frequency and B_1 field.

Each of the bound samples was run again at a proton Larmor frequency of 300 MHz and a B_1 field of 42 kHz to allow direct comparisons to be made with the SN15 data. These values are also summarized in Table 6.1 and are, lyophilized and hydrated, respectively: 26.3 msec and 18.2 msec for Stath-pS_2pS_3, 57.8 msec and 7.5 msec for Stath-F_7L_8, 32.7 msec and 3.5 msec for Stath- $I_{11}G_{12}$.

6.2 Discussion

6.2.1 Secondary structure

The secondary structure of the hydrated surface adsorbed protein represents some of the first high-resolution measurements made of a biomineralization protein on the

relevant biomineral surface under biologically relevant conditions. The data taken under hydrated conditions indicate a well-defined helix at the N-terminal binding region. REDOR data of the hydrated surface bound sample are simulated well by a distance of 4.2 Å from pS_3 to F_7, which is consistent with the distance expected for an ideal α-helix. These data were taken at –25° C to freeze out any motions occurring on the timescale of the REDOR experiment. Preliminary DRAWS data taken under hydrated conditions measuring φ at the pS_2pS_3 region agree with the REDOR data. The hydrated, surface bound protein is simulated with torsion angles corresponding to a very well defined α-helix (φ = -58°). These are preliminary results in that the DRAWS data were taken at ambient temperature. The single label control under hydrated conditions decays much more quickly than the lyophilized counterpart (Figure 6.7), indicating mobility of this protein on the NMR timescale (10^3 Hz), so repeating this experiment at reduced temperature is necessary to confirm this result.

The lyophilized surface bound protein also had a significant portion of helical content as measured across the pS_3 F_7 hydrogen bond, but was found to be more extended than the hydrated sample. The REDOR measurement gave a distance of 5.2 Å, which is more consistent with a 3_{10} helix or a conformational distribution. The experimental DRAWS data for the lyophilized, surface bound protein simulated a distance consistent with a random coil (φ = –83° to –88°). This could be in agreement with the REDOR data, if the change in the measured REDOR distance correlates to an extension of the helix at the pS_3 end (rather than the F_7 end) during lyophilization. The

REDOR measurement is from pS_3-F_7, however, and the torsion angle determined by the DRAWS measurement (between pS_2 and pS_3) is not encompassed by that measurement, so the results are possibly independent of one another. The low temperature hydrated pS_2pS_3 DRAWS measurement would help to correlate the REDOR and DRAWS data and indicate if the two regions are changing in concert or independently of one another as a result of lyophilization. The structure determined with REDOR does indicate a change in secondary structure from an ideal helix during lyophilization and suggests a stabilizing mechanism when the biomineral system is hydrated.

In the central region of the N-terminal pentadecyl domain (Stath-L_8G_{12}), the hydrated, surface bound protein secondary structure was determined to be significantly helical according to low temperature REDOR measurements which yield a distance of 4.8 Å. This distance remains approximately the same for the lyophilized protein (4.6 Å), within the scatter of the data. The simulated fit is indicative of a slightly extended conformation, or of multiple conformations possibly containing some 3_{10}-helix, as the distance is slightly longer than expected for an ideal α-helix. DRAWS data of the lyophilized sample are in agreement with REDOR measurements, simulating the average φ for Stath-F_7L_8 as –68°, falling within the region of φ angles seen for helical structures, but longer than the distance expected for a classic α-helix.

Stath-$I_{11}G_{12}$ was found to have a φ angle of –78°, still within, but towards the edge of the distribution of torsion angles observed for α-helices, and is probably indicative of some helical structure combined with some extended structures. This would

be consistent with the REDOR distance determined for Stath-L_8G_{12}, which is due at least partially to an extended secondary structure, or multiple conformations.

From these data, the N-terminus of the protein statherin is determined to be helical from residue 3 to residue 12. This is consistent with a recognition mechanism between the sidechains of the helix and the calcium ions in HAP[1,2] as the N-terminus has been found to be integral in the binding of statherin to HAP and the α-helix has been suggested as a structural framework for protein binding, where the sidechains in an α-helix are spaced at a distance similar to the Ca^{2+} ion spacing in the 001 face of hydroxyapatite (5.4 Å).[3] This result could also be consistent with an electrostatic binding mechanism, and the experiments performed here do not uniquely determine the binding mode. The helical structure that is observed from pS_3 to F_7 in both the lyophilized and hydrated full protein cannot be directly compared to the shorter peptide (since the REDOR measurement for the SN15 peptide was not measured), but does suggest a stabilized secondary structure. This could be consistent with the full protein tertiary structure stabilizing the N-terminal domain structure through the hydrophobic face of the amphipathic N-terminal helix.[4]

6.2.2 *Dynamics*

To more fully understand the function of the surface bound protein, the dynamics of the singly and doubly labeled proteins were studied with relaxation measurements, along with chemical shift tensor analysis (summarized in Table 6.2, and Figure 6.2, 6.3 and 6.10). Loss in CP efficiency was also used as an indicator of motion at unique sites

in the surface adsorbed protein.[5] Figure 6.2 shows each of the doubly labeled samples under hydrated conditions, normalized to the natural abundance methyl region to account for any differences in protein bound. Also shown is a representative spectrum of a lyophilized, surface bound protein (Stath-pS_2pS_3) for comparison. The substantial loss in signal in the carbonyl region at the F_7L_8 and $I_{11}G_{12}$ positions indicates a loss in cross-polarization efficiency, clearly indicating motion. Figure 6.3 shows spectra of the singly labeled, hydrated, surface bound proteins, obtained from direct measurement and subtraction from doubly labeled spectra. The chemical shift tensor values were calculated for each labeled region after natural abundance subtraction and subtraction of the corresponding singly labeled protein.

The hydrated, surface bound pS_2pS_3 domain was found to be largely immobile on the time scale of the CSA as evidenced by the nearly unchanged sideband pattern for both pS_2 and pS_3 (Figure 6.3 and Table 6.2), with an Ω of 135 and 140 ppm, respectively, as compared to the rigid protein Ω of 146 ppm. To further support a very rigid segment on this timescale, there was little, if any loss in signal intensity for the hydrated, surface bound protein as compared to the lyophilized, surface bound protein as seen in Figure 6.2. The ^{13}C $T_{1\rho}$ data (at both 35 and 42 kHz B_1 fields) for this region are also indicative of very little mobility, with the lyophilized and hydrated surface bound samples having nearly unchanging $T_{1\rho}$ values, as summarized in Table 6.1. All of these data consistently indicate that this portion of the peptide is experiencing very little mobility and is interacting very strongly with the surface charges. The single labeled DRAWS control

experiment indicated that there is motion on a slower timescale (on the order of 10^3 Hz) at this position, most likely representing very small amplitude torsional librations.

It is noticeable in Table 6.1 that the magnitude of the $T_{1\rho}$ values at the two B_1 fields are very different, even though the trend in the $T_{1\rho}$ as a function of sample conditions is the same. Although $T_{1\rho}$ itself is dependent on the effective field and not the static field, the CSA, which also contributes to the $T_{1\rho}$ relaxation process, is dependent on field. The 35 kHz data was taken on a 500 MHz proton frequency magnet, while the 42 kHz data was taken at 300 MHz magnet, so contributions from the CSA, whose breadth changes by 40% at these two fields, are likely incorporated into the $T_{1\rho}$ relaxation. Thus, the data at the two fields should not be compared to each other, but can be compared to data taken at the same field and trends at each field are consistent and can be compared.

The significant loss in CP efficiency at the F_7L_8 and $I_{11}G_{12}$ positions with hydration is characteristic of mobile sites.[5,6] The F_7L_8 region had very little narrowing of the CSA, with Ω values of 135 and 128 ppm, respectively, putting an upper limit on the frequency of the observed motion at about 20 kHz, the frequency of the CSA. The $T_{1\rho}$ measurements also indicate motion, with relaxation measurements for Stath-F_7L_8 of 7.5 msec and 39.0 msec for the hydrated and lyophilized protein at 42 kHz. These data bracket the timescale of the motion to 10^{-3} to 10^{-5} sec.

The CSA at the $I_{11}G_{12}$ region was the only portion of the studied segments of the protein to show any significant narrowing, reducing in span to 111 ppm. This alone indicates a higher frequency or amplitude motion than that observed in other regions.

The $T_{1\rho}$ measurements are in agreement with the cross polarization experiments, fitting the hydrated Stath-$I_{11}G_{12}$ $T_{1\rho}$ to 3.5 msec, as compared to the lyophilized measurement of 32.7 msec at 42 kHz.

These data support a very rigid protein in the binding region and a more mobile protein segment from F_7 to G_{12}, although there is a noticeable change in the motional modes in comparing L_8 and $I_{11}G_{12}$. The presence of a highly mobile protein segment could explain observations made by others in the field. Moreno et al[8] found that statherin inhibited secondary crystal growth at a higher level than that expected based on coverage size, assuming a globular protein. The mobility of statherin could allow it to effectively block more sites than a completely rigid protein. The uniquely different dynamic regions of statherin may also play a significant role in the lubricating properties of the protein. The rigidly attached portion serving to anchor the protein to the surface, while the mobile portion of the protein protects the tooth during mastication.

6.2.3 Chemical shift and linewidths

As discussed in Chapter 4, the absolute chemical shift for backbone carbonyl carbons is not quantitative with respect to determining a secondary structure, but the chemical shift anisotropy, as well as measurable changes in the chemical shift, broad linewidths or multiple resonances can provide additional insight into structural determination. Figure 4.10 shows an example of an ordered peptide (LK-3_{10}) where unique secondary structures can be observed. As mentioned in Chapter 4, this peptide was designed to be 3_{10}-helical, but when lyophilized from low solution concentrations, it is only partially helical, with the remaining portion being random coil. In this model

peptide, the difference in the two secondary structures is easily seen as two narrow, unique resonances. The absence of multiple unique resonances in statherin, along with broad linewidths suggests some dispersion of secondary structures, thus for this protein, the CSA and linewidth provide further insight.

As observed for the SN15 peptide, the assymetry parameter of the full protien samples are observed to change from ~0.85 (lyophilized) to ~0.6 (hydrated). Separating the effects of motion and the contributions of the hydroxyapatite surface from that of secondary structure contributions in the assymetry parameter is very difficult and, as for the SN15 samples, the distance measurements are much more quantitative precluding the necessity of further study. The qualitative comparison is interesting, however and may be important for initial observation when studying surface bound proteins.

Ordered peptides are known to have linewidths in the lyophilized state of 2-4 ppm as stated by Long and Tycko[9], and as evidenced in Figure 4.10 (2.4 ppm). In Chapter 4, the linewidths of surface bound SN15 were observed to narrow significantly upon hydration, so that most of the peptide fell into the domain of a highly ordered structure. As seen in Table 6.2, the doubly labeled linewidths for full length statherin are between 6 and 7 ppm for all three samples for the lyophilized surface bound samples and do not narrow significantly in the hydrated state. The doubly labeled samples decrease in linewidth in the hydrated state to roughly 5 and 6 ppm for the pS_2pS_3 and F_7L_8 regions, but for the IG region, is seen to increase to 9.2 ppm. Singly labeled linewidths of the hydrated, surface bound protein are 5.6, 4.4, 3.1 and 5.0 ppm for pS_2, pS_3, F_7 and L_8, as compared to the lyophilized linewidths of 5.9 ppm at pS_3 and 7.2 ppm at L_8. The

linewidths are broader than those seen for the hydrated SN15 peptide in all cases but F_7, suggesting a contribution to line broadening that was unseen for the SN15 peptide. Line broadening and narrowing contributions discussed in Chapters 4 and 5 are still considered here. A higher degree of conformational heterogeneity is a distinct possibility, particularly in the case of the $I_{11}G_{12}$ region, where mobility is seen to increase, along with the linewidth. However, in the $I_{11}G_{12}$ region, data taken at a higher spinning speed and decoupling field narrow the resonance to 7.5 ppm. As none of the other samples show a change in linewidth due to these conditions, the increased spinning rate is likely not the cause of the narrowed line. It is most likely due to the increased decoupling strength, and is consistent with the inverse of the decoupling field approaching the motional rate, as has been seen previously.[10] A slow motional process, on a timescale of the acquisition, could cause a decrease in T_2, broadening the observed lines. Magnetic susceptibility effects could also be contributing to the linewidth. For the SN15 peptide, the calcium phosphate solution was thought to match the magnetic susceptibility, thus reducing susceptibility broadening. The statherin linewidths would appear to dispute this claim, or at least suggest that for statherin, there is a significant contribution to the linewidth other than the magnetic susceptibility broadening. Possibly broadening due to magnetic susceptibility as a function of distance from the surface is occurring, if statherin is more closely associated with the surface than SN15 based on the observed reduction in mobility. A hole burning experiment[5] may serve to differentiate between possible contributions, causing a "hole" in the resonance if the broadening is inhomogeneous, as in the case of conformational heterogeneity or magnetic susceptibility broadening, and no

hole if the broadening is homogeneous, as would be observed for motional processes contributing to linewidth or T_2 relaxation. Although this experiment would not uniquely define the broadening mechanism, it would narrow the possible contributions to the linewidth and help answer the question of the presence of conformational distributions.

6.3 Comparison to SN15

The secondary structure of SN15 and statherin are very similar within the regions measured. In SN15[11], as well as in SN6[12], the binding region was seen to have a random coil secondary structure, thought to maximize electrostatic interactions with the highly charged surface. While the DRAWS pS_2pS_3 measurement for full length statherin under lyophilized conditions is consistent with that seen for the shorter N-terminal peptides, the remainder of the binding region in statherin is found to be a well defined helix under hydrated conditions, and remaining significantly helical under lyophilized conditions. These results could be interpreted in two ways. First, the pS_2pS_3 region could be acting independently of the pS_3-F_7 region, allowing the two regions to have different secondary structure. A second interpretation is that the waters of hydration are providing stabilization for the surface-helix interaction, which is lost upon lyophilization. The effect of any possible stabilization in this region is unique to the binding region, as the L_8G_{12} region did not show a significant change in secondary structure under hydrated conditions. The F_7L_8 and $I_{11}G_{12}$, as well the L_8G_{12} measurements made on the full protein under lyophilized conditions are nearly identical with those made for SN15 under the same conditions. These measurements suggest that under lyophilized conditions, the full protein has similar secondary structure as the shorter peptide fragments. To further

confirm the consistency of the structure between the shorter peptide and full protein, either the pS_2pS_3 low temperature DRAWS measurement, or a low temperature REDOR measurement from D_1 to E_5 is needed.

The general trend in the dynamics of the full protein and the SN15 peptide are similar, with the pS_2pS_3 region showing very little mobility with more mobility at the F_7L_8 and $I_{11}G_{12}$ regions. Noticeable differences were found in the F_7L_8 and $I_{11}G_{12}$ regions. While both the protein and the peptide experience motional freedom, the C-terminal end of the pentadecyl region of the peptide appears to be less well anchored then the full protein. This is observed in the CSA, which narrows by more than ½ of the original breadth at the $I_{11}G_{12}$ postion in the SN15 peptide[7]. In comparison, statherin ($I_{11}G_{12}$) narrows by less than half that observed for the peptide. The $T_{1\rho}$ values remain approximately the same for both the N-terminal peptide and the full protein, while the noticeable change in mobility is observed in the changes in lineshape. Since $T_{1\rho}$ is most sensitive to frequency of motion, and lineshape is sensitive to both frequency and amplitude of motion, the changes in dynamics between the shorter peptide and the full protein are likely due to a change in amplitude of motion rather than the frequency of motion.

The increased mobility at the C-terminus in the peptide is reasonable given that the SN15 peptide is unconstrained at the C-terminal end and the change in backbone mobility could be due to one of several factors, including motional limitations due to the larger size of the protein, or possibly protein interactions with the surface in the C-terminus. To explore the later possibility, the only charged residue in the C-terminus was

replaced with its uncharged counterpart (Glu_{26}-->Gln_{26}) and backbone carbonyl carbons were incorporated at I_{11} and G_{12}, where the largest amplitude and/or frequency motion was observed in the full unmodified protein. The $T_{1\rho}$ and CSA of the mutant protein were nearly identical with the unmodified protein, with a $T_{1\rho}$ value at $I_{11}G_{12}$ of 2.9 msec, identical to the $T_{1\rho}$ value at the same positions of the unmodified protein (2.5 msec) within error (taken at 500 MHz proton frequency). This indicates that Glu_{26} is not providing sufficient interaction to prevent high amplitude motions in the N-terminal region, and the simplest explanation is that the size of the protein is preventing large amplitude motion. Other possible explanations that could prevent large amplitude motions would include: 1) tertiary folding, 2) hydrogen bonding of polar, uncharged residues in the C-terminal end of the protein with the surface, or 3) increased interactions between arginine and lysine sidechains and the phosphate groups in the surface of the protein due to secondary or tertiary structure.

Figure 6.11 shows the secondary structure determined in this study, indicating the helical N-terminal binding region of the hydrated, surface bound protein, statherin. The strong interaction of statherin through the phosphoserines and the other highly charged residues in the pentapeptide interaction region is indicated, and the more weakly interacting, higher mobility C-terminus is also shown. The model proposed in Chapter 5, namely, viewing the more weakly interacting residues in this domain as a flexible rod, with torsional motions increasing with increasing distance from the highly immobile portion, is still an appropriate model, but to adequately model the observed motions, the surface bound tertiary structure and experimental evidence orienting the protein to the

surface is required to constrain motional modes. SSNMR is capable of providing this information and future direction will likely continue with these goals in mind.

6.4 Relevance to Other Biomineralization Proteins

While these results can't directly determine the structure and dynamics of other biomineralization proteins, some general trends and predictions can be made. The rigidity that was observed in the pSpS region indicates that this region is very important in interacting with HAP. The sequence "pSpSEE" is seen frequently in acidic biomineralization proteins such as osteonectin, bone sialoprotein and bone acidic glycoprotein.[13] Potentially this sequence would be an immobile region in these other proteins as well, and studying these other systems could yield insight into the general importance of this sequence.

The structure of statherin would suggest that either a lattice matching or electrostatic mechanism is responsible for the binding of statherin to HAP. Comparison of the secondary structure of other surface bound proteins containing this binding segment may provide valuable insight into the necessity of the pSpSEE binding sequence, and any specific structure correlation. The frequency of this sequence in acidic biomineralization proteins as well as its clear affinity for HAP warrant further study to provide insight into any secondary structure preservation which may be correlated to the binding mechanism, as well as investigating the dynamics which yield direct evidence into the binding affinity.

6.5 Notes to Chapter 6

1. Gururaja, T. L. & Levine, M. J. Solid-Phase Synthesis and Characterization of Human Salivary Statherin: A Tyrosine-Rich Phosphoprotein Inhibitor of Calcium Phosphate Precipitation. *Peptide Research* **9**, 283-289 (1996).

2. Raj, P. A., Johnsson, M., Levine, M. J. & Nancollas, G. H. Dependence on Sequence, Charge, Hydrogen Bonding Potency, and Helical Conformation for Adsorption to Hydroxyapatite and Inhibition of Mineralization. *Journal Biological Chemistry* **267**, 5968-5976 (1992).

3. Hauska, P. V. & Frank H. Wians, J. Osteocalcin-Hydroxyapatite Interaction in the Extracellular Organic Matrix of Bone. *The Anatomical Record* **224**, 180-188 (1989).

4. Ramasubbu, N., Thomas, L. M., Bhandary, K. K. & Levine, M. J. Structural Characteristics of Human Salivary Statherin: A Model for Boundary Lubrication at the Enamel Surface. *Critical Reviews in Oral Biology and Medicine* **4**, 363-370 (1993).

5. Mehring, M. *Principles of High Resolution NMR in Solids* (Springer-Verlag, New York, 1983).

6. Wemmer, D. E. in *Lawrence Livermore Berkeley, Laboratory Materials and Molecular Research Division* 288 (University of California, Berkeley, Berkeley, 1978).

7. Shaw, W. J., Long, J. R., Campbell, A. A., Stayton, P. S. & Drobny, G. P. *Journal of the American Chemical Society* (In Press).

8. Moreno, E. C., Varughese, K. & Hay, D. I. Effect of Human Salivary Proteins on the Precipitation Kinetics of Calcium Phosphate. *Calcified Tissue International* **28**, 7-16 (1979).

9. Long, H. W. & Tycko, R. Biopolymer Conformational Distributions From Solid State NMR: α-Helix and 3_{10}-Helix Contents of a Helical Peptide. *Journal of the American Chemical Society* **120**, 7039 (1998).

10. Long, J. R., Sun, B. Q., Bowen, A. & Griffin, R. Molecular Dynamics and Magic Angle Spinning NMR. *Journal of the American Chemical Society* **116**, 11950-11956 (1994).

11. Shaw, W. J. *et al.* Determination of Statherin N-Terminal Peptide Conformation on Hydroxyapatite Crystals. *Journal of the American Chemical Society* **122**, 1709-1716 (2000).

12. Long, J. R. *et al.* A Peptide That Inhibits Hydroxyapatite Growth is in an Extended Conformation on the Crystal Surface. *Proceedings of the National Academy of Science* **95**, 12083-12087 (1998).

13. Gorski, J.P. Acidic Phosphoproteins From Bone Matrix: A Structural Rationalization of Their role in Biomineralization. *Calcified Tissue International* **50**, 391-396 (1992).

Table 6.1. Summary of structure results for surface bound statherin, hydrated and lyophilized.

Name	^{13}C $T_{1\rho}$ (35 kHz B_1) 500 MHz B_0 Hydrated Lyophilized (msec)	^{13}C $T_{1\rho}$ (42 kHz B_1) 300 MHz B_0 Hydrated Lyophilized (msec)	Secondary structure Hydrated Lyophilized
Stath-pS_2pS_3	11.2 11.7	18.2 26.3	-58° -83°
Stath-F_7L_8	3.5 13	7.5 57.8	------ -68°
Stath-$I_{11}G_{12}$	2.5 11.5	3.5 32.7	----- -78°
Stath-pS_3F_7	9.1 9.5	-- 22.9	4.2 Å 5.2 Å
Stath-L_8G_{12}	4.3 7.9	-- 44.6	4.8 Å 4.6 Å
Stath-Q	----- 2.9	-- --	-- --

Table 6.2 Summary of the chemical shift parameters for surface bound samples of statherin.

Hydrated:

	Linewidth (ppm)	Chemical Shift (ppm)	σ_{11} (ppm)	σ_{22} (ppm)	σ_{33} (ppm)	Ω (ppm)	η
Stath-pS_2pS_3	4.9	174.2	-55.7	-18.0	73.7	129.4	0.51
Stath-pS_2	5.1	174.1	-61.5	-12.4	74.0	135.5	0.66
Stath-pS_3	4.4	173.9	-62.5	-15.1	77.6	140.2	0.61
Stath-F_7L_8	6.3	175.2	-60.3	-14.6	74.9	135.2	0.61
Stath-F_7	3.1	174.9	-58.4	-18.6	77.0	135.4	0.52
Stath-L_8	5.0	178.2	-54.9	-17.8	72.7	127.6	0.51
Stath-$I_{11}G_{12}$	9.2	177.1	-50.9	-9.4	60.3	111.2	0.69
			Lyophilized:				
Stath-pS_2pS_3	6.5	--	-67.3	-12.8	80.1	147.4	0.68
Stath-pS_2	5.4	--	-71.1	-11.4	82.5	153.7	0.72
Stath-pS_3	5.9	--	-65.5	-8.6	74.1	139.6	0.92
Stath-F_7L_8	7.2	--	-68.7	-9.0	77.6	146.3	0.77
Stath-F_7	6.4	--	-78.3	-6.2	84.5	162.8	0.85
Stath-L_8	7.2	--	-65.4	-9.8	75.1	140.5	0.74
Stath-$I_{11}G_{12}$	6.7	--	-69.8	-5.2	75.1	144.9	0.86

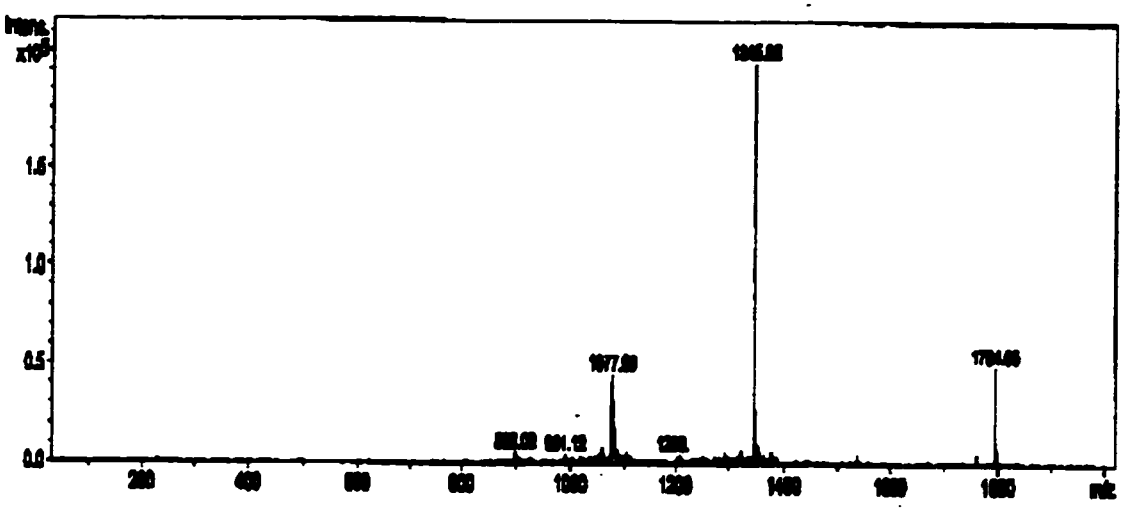

Figure 6.1. Electrospray mass spectrum of a purified statherin peptide. The molecular weight of the doubly labeled protein is 5382. The electrospray technique shows only the charged species, where the 1795 peak is triply charged, the 1347 is the quadruply charged and the 1078 peak is pentuply charged species.

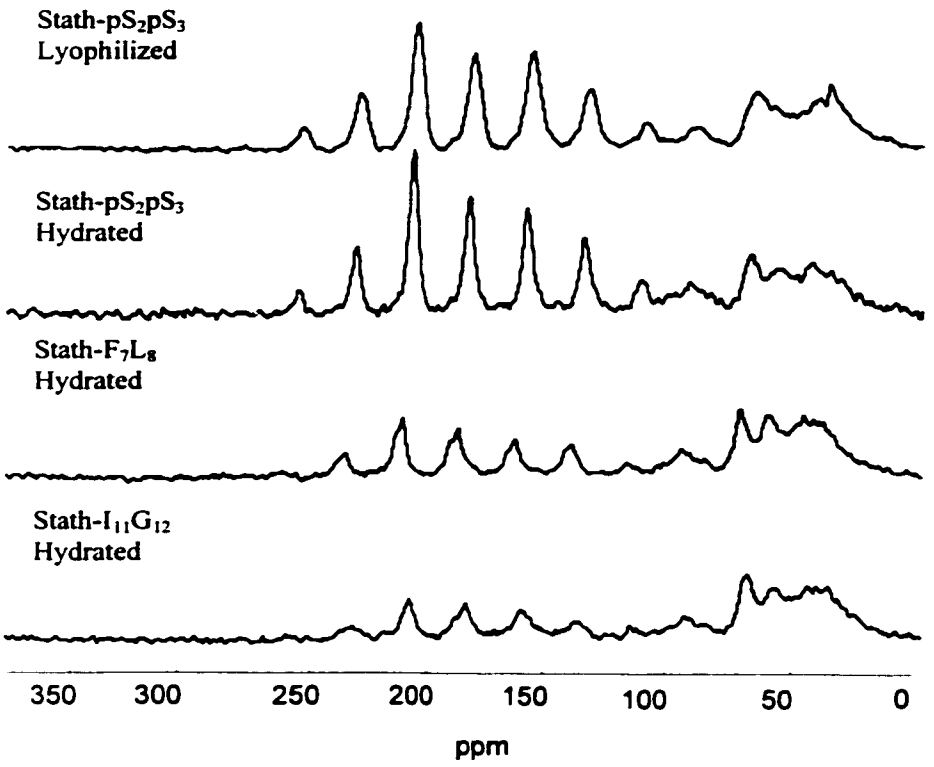

Figure 6.2 Spectra of doubly labeled statherin samples on hydroxyapatite. The lyophilized spectrum is shown on top for comparison. The hydrated samples below go in order from the N to C terminus, pS_2pS_3, F_7L_8 and $I_{11}G_{12}$. The significant loss in CP efficiency is evidenced by comparison to the normalized natural abundance region, indicating significant mobility at the F_7L_8 and $I_{11}G_{12}$ regions.

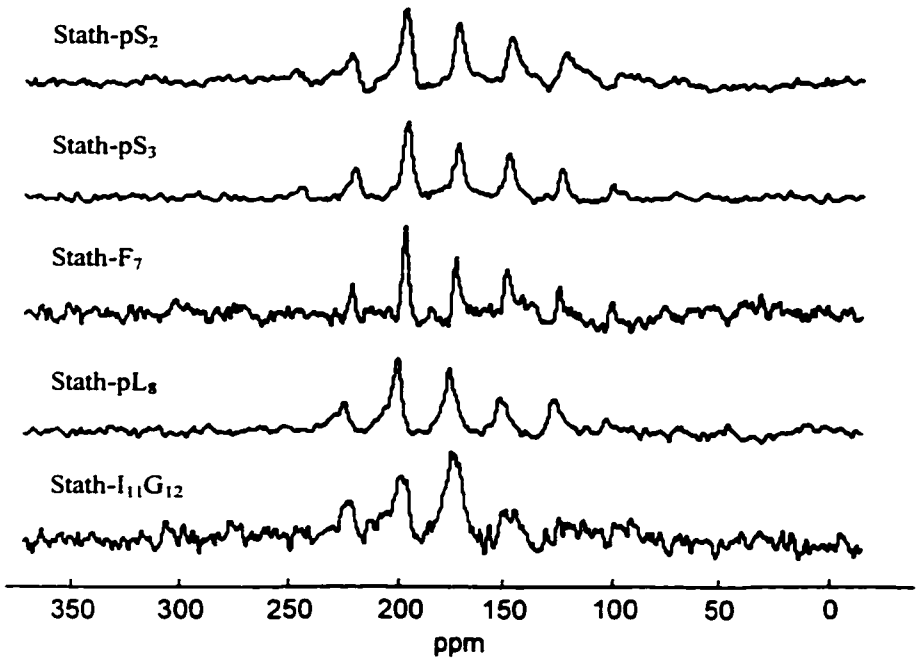

Figure 6.3. Natural abundance and single label subtractions yielded the CSA tensors of the hydrated statherin samples adsorbed to hydroxyapatite. From top to bottom, pS_2, pS_3, F_7, L_8, and $I_{11}G_{12}$ (natural abundance subtraction but no single label subtraction for the last sample). The span of the powder pattern changes very little in most cases, as is tabulated in Table 6.1, indicating that any mobility is slower than the timescale of the CSA. The $I_{11}G_{12}$ region is the only region that loses a significant breadth in the anisotropy, indicating the presence of motion faster than the CSA (2×10^4 Hz) in this region of the protein. The assymetry parameter (η) changes from that typically seen for a rigid carbonyl (η=0.8-0.9) as seen in Figure 6.1 (top), to an η of 0.5-0.6 for the top 4 spectra, which could result from conformational changes or motional averaging.

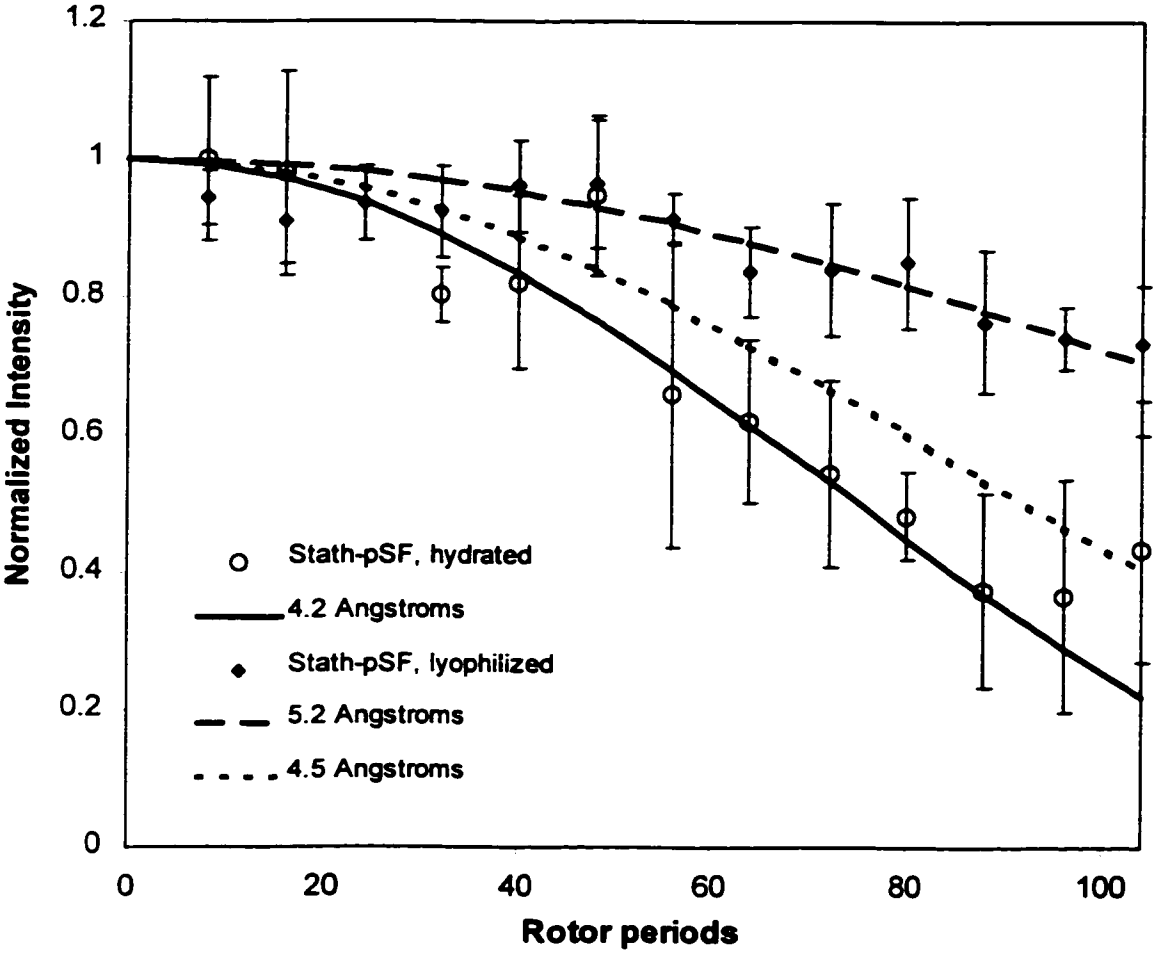

Figure 6.4. REDOR dephasing curves of Stath-pS_2F_7 on HAP, hydrated ( ) and lyophilized ( ), with simulations as indicated. A distance of 4.2 Å was simulated for the hydrated data, fitting a distance observed for an ideal helix. Lyophilized, the distance is longer, fitting to 5.2 Å, indicating a change in structure upon lyophilization. The lyophilized distance could be indicating a more extended or random coil structure, but is also observed for 3_{10} helices.

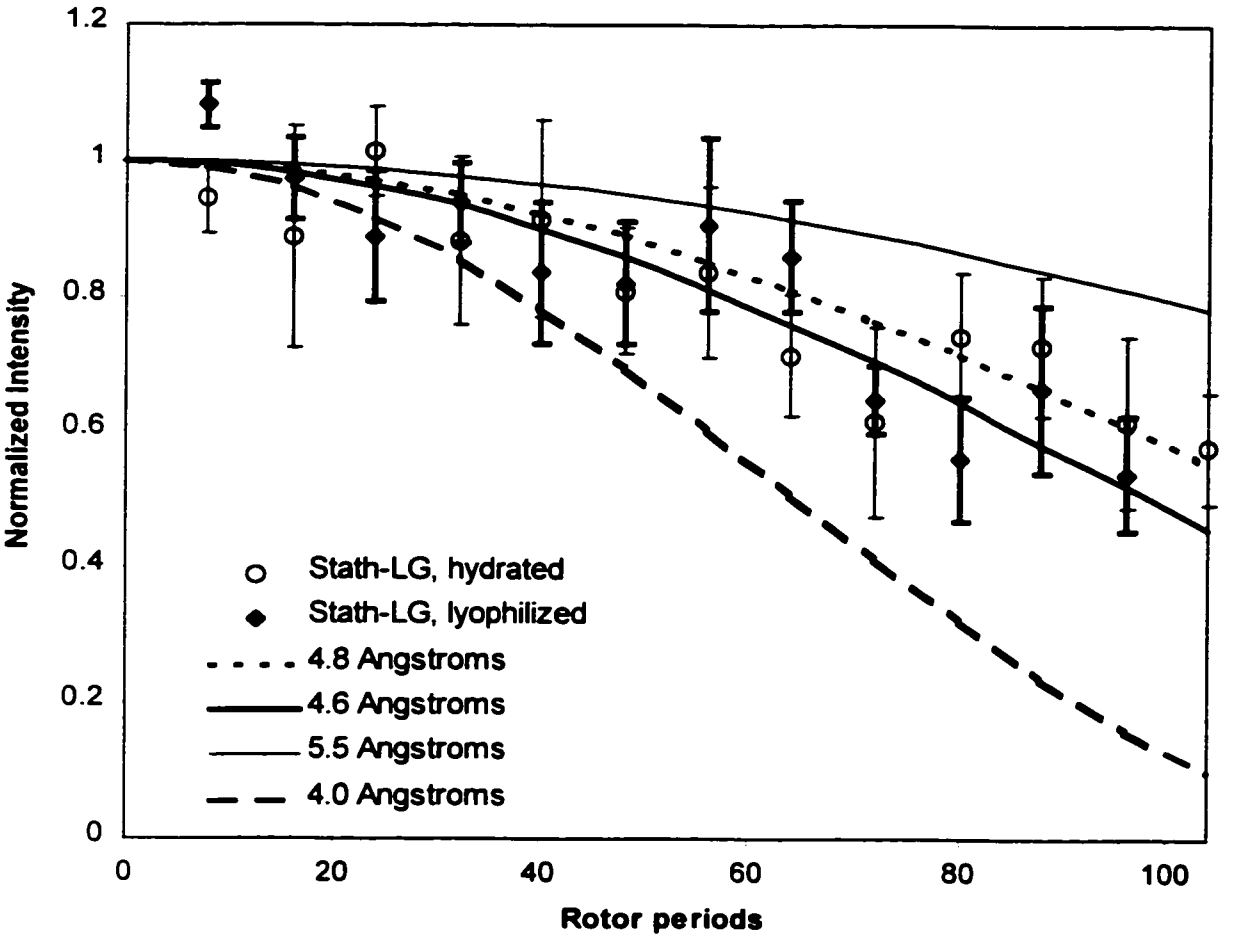

Figure 6.5. REDOR dephasing curves of Stath-L_8G_{12}, hydrated ( ) and lyophilized ( ), with simulations as indicated. The hydrated dephasing curve is simulated well by a distance of 4.8 Å, and the lyophilized curve is essentially the same at 4.6 Å, indicating significant helical content, with either a slightly extended structure or multiple conformations contributing to the longer than expected distance.

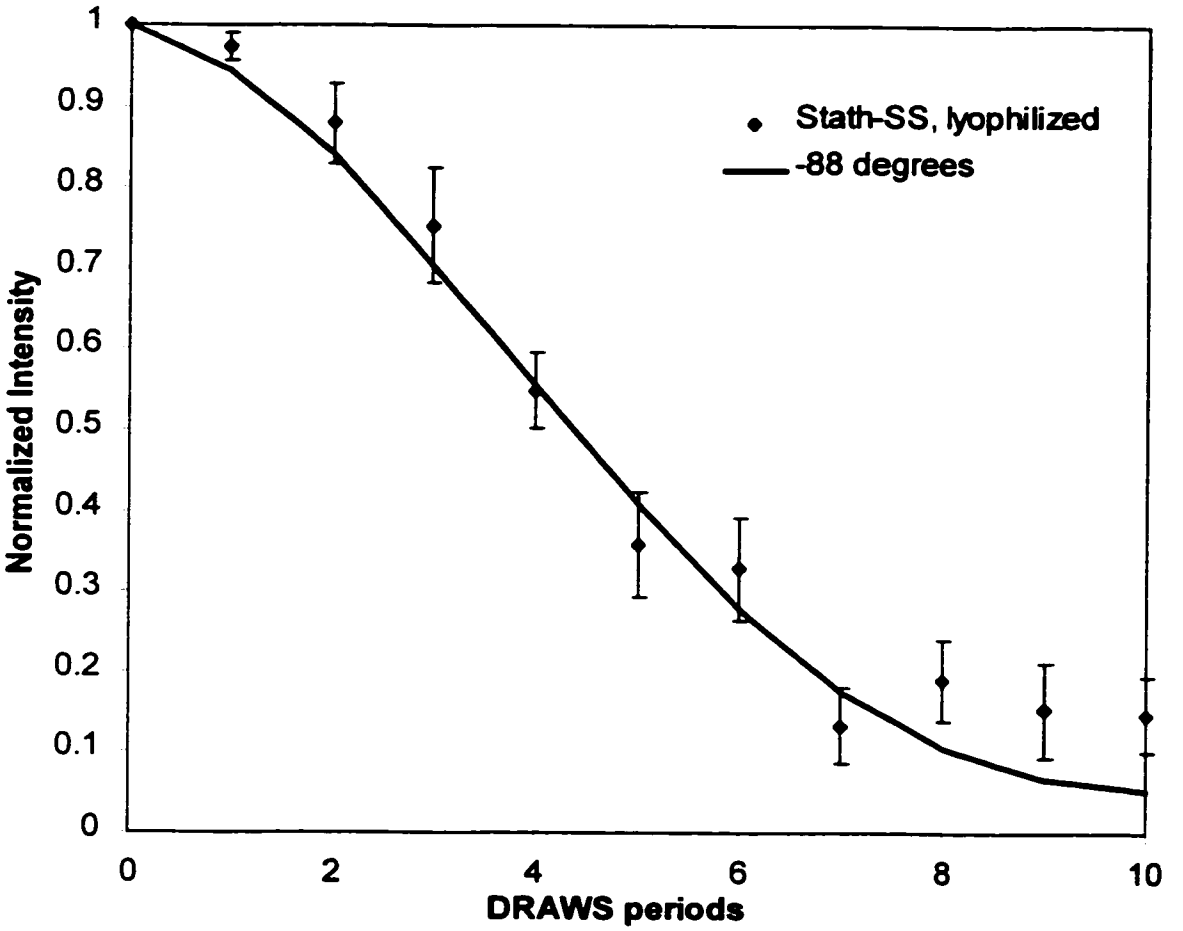

Figure 6.6. DRAWS data for Statherin pS_2pS_3 on HAP, lyophilized. Diamonds show lyophilized data that fit equally well to an average φ of –83° or –88°. This is consistent with a random coil secondary structure from pS_2 to pS_3.

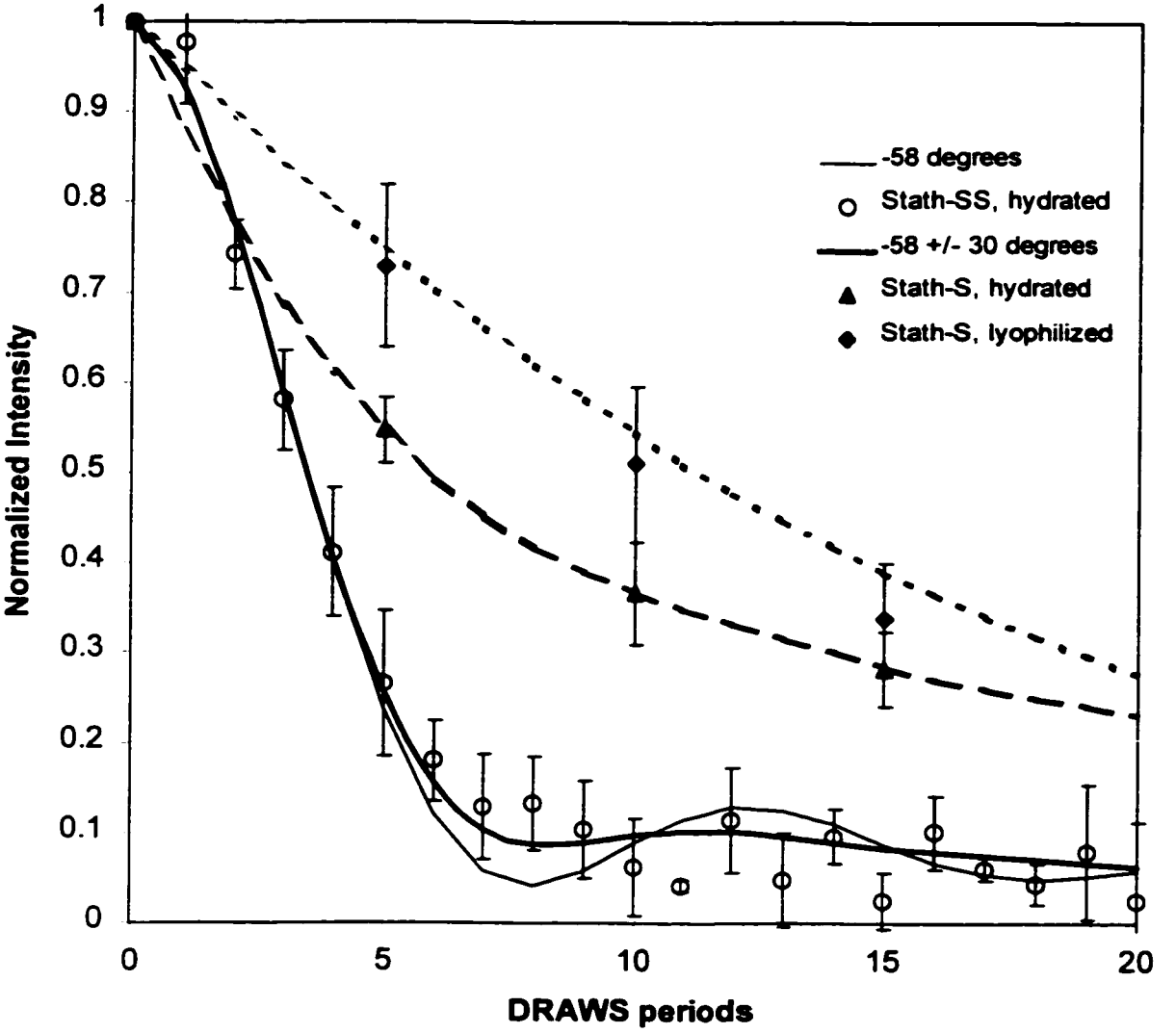

Figure 6.7. DRAWS dephasing curve for Stath-pS_2pS_3 on HAP, hydrated. Simulations best fit an average torsion angle of −58° consistent with an ideal α-helix. The single label control indicated motion on the timescale of the DRAWS experiment however, so the measurement would need confirmed at low temperature.

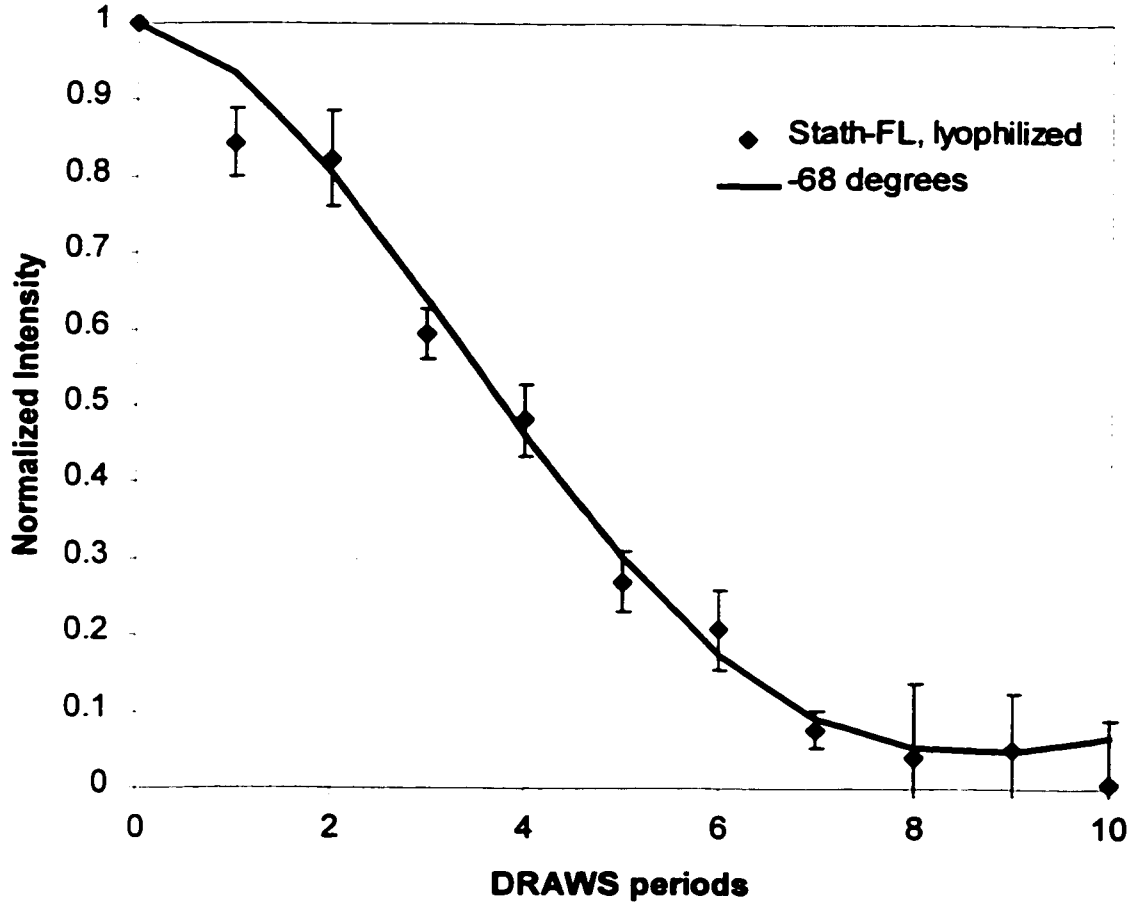

Figure 6.8. DRAWS dephasing curve for Stath-F_7L_8 on HAP, lyophilized. Simulations best fit an average torsion angle of –68°. This distance is consistent with α-helical structure in that it falls within the region of torsion angles observed for α-helices.

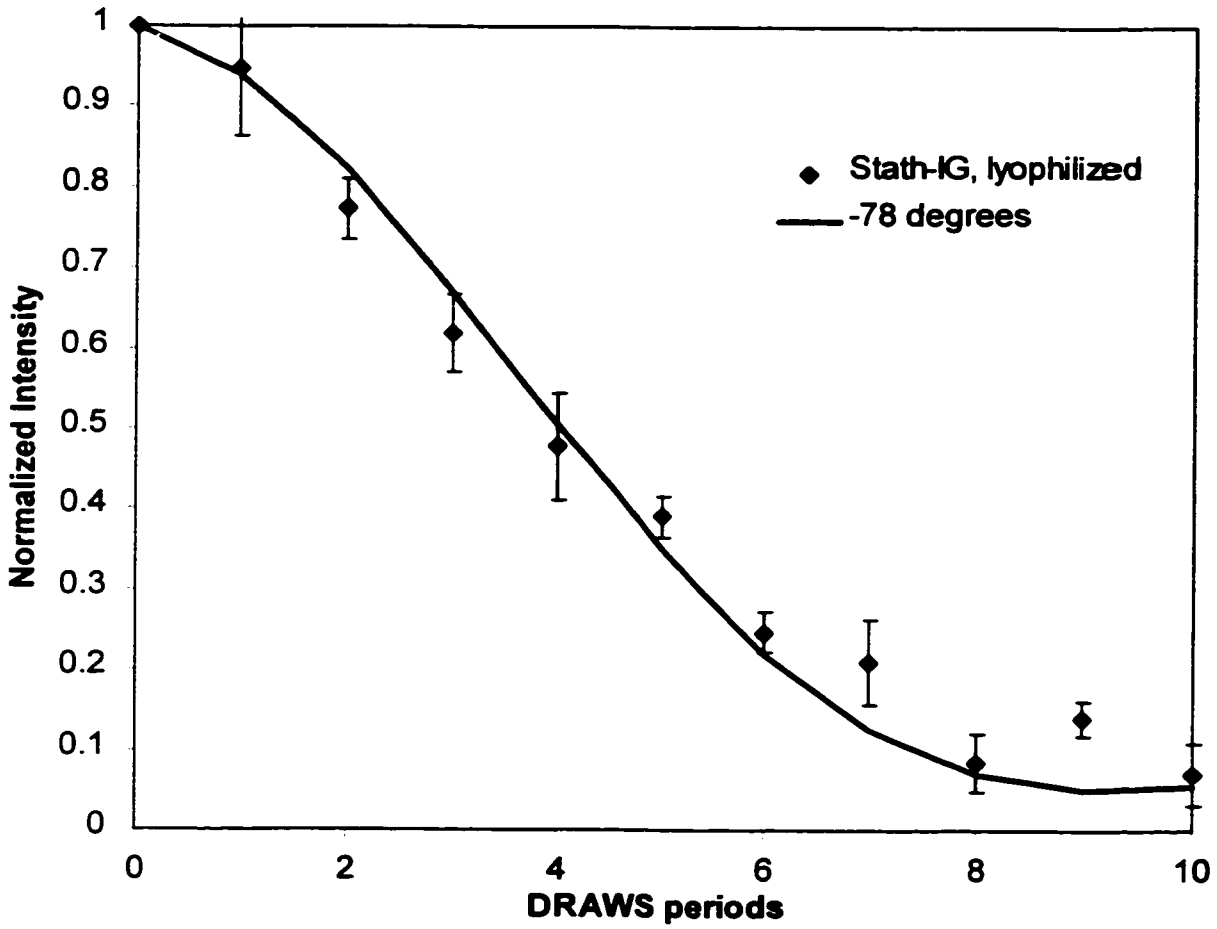

Figure 6.9. Stath-$I_{11}G_{12}$ on HAP, lyophilized has DRAWS curves best simulated by φ = –78°, falling at the edge of the α-helical region and probably indicating a combination of some helix and some extended structures. The experimental data is shown in diamonds and the simulation is represented by a solid line.

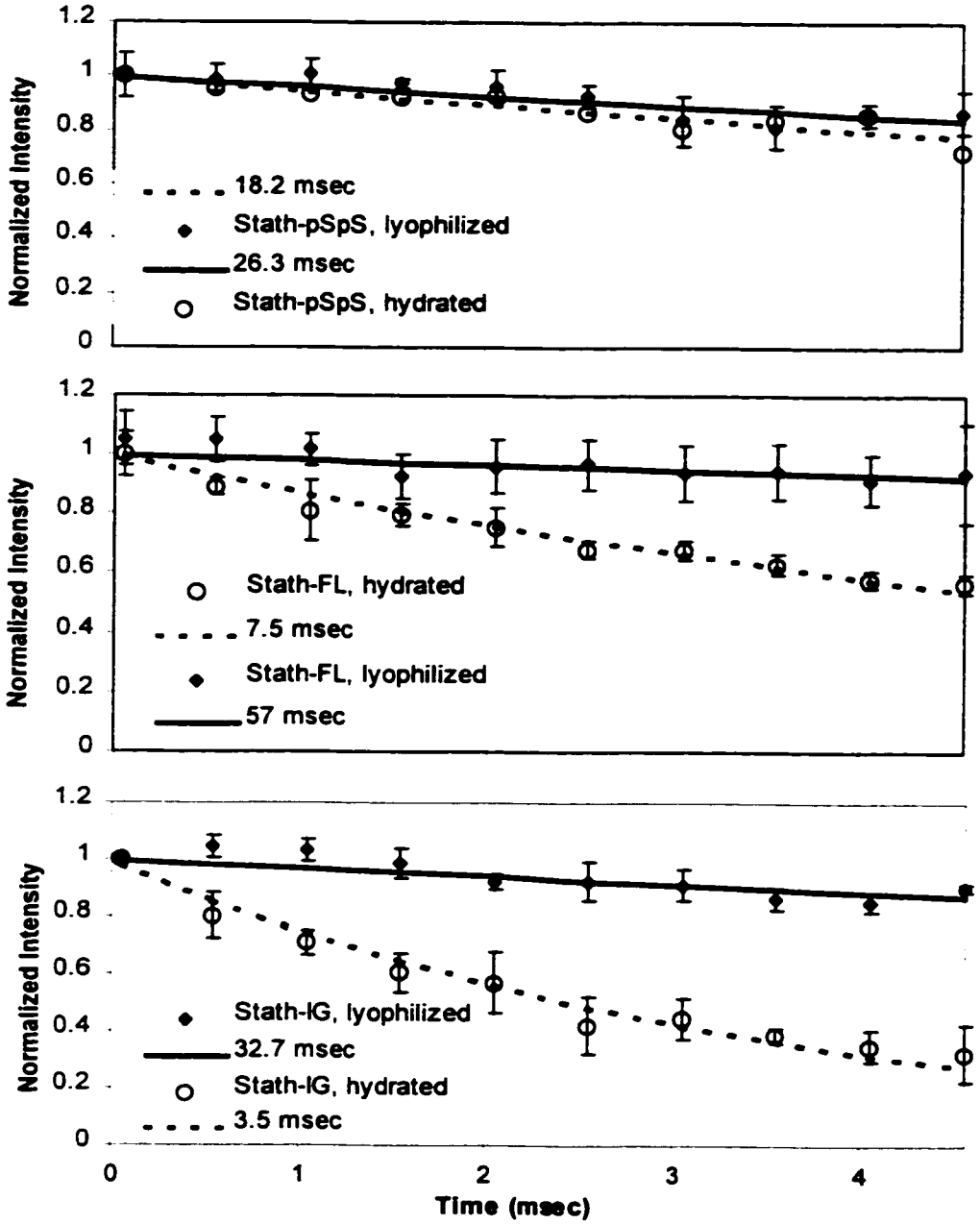

Figure 6.10. $T_{1\rho}$ plots for the doubly labeled statherin samples, pS_2pS_3, F_7L_8 and $I_{11}G_{12}$ from top to bottom, both lyophilized and hydrated, bound to hydroxyapatite. Relaxation values for the lyophilized and hydrated samples respectively, indicated on each graph, are 26 and 18.2 msec for Stath- pS_2pS_3, 57 and 7.5 msec for Stath- F_7L_8 and 32.7 and 3.5 msec for Stath- $I_{11}G_{12}$.

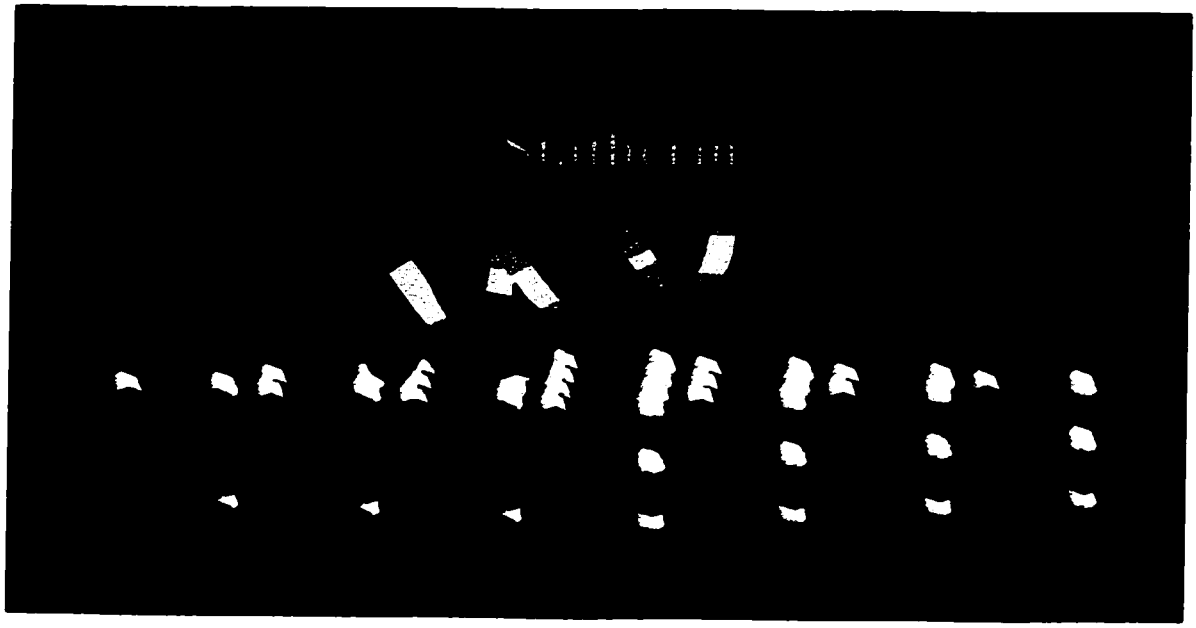

Figure 6.11. Cartoon of statherin on the 001 face of HAP, with the backbone shown in yellow, the $^{13}C{=}O$ shown in red, and the ^{15}N labels shown in blue. The hydrogen bonds are shown in white and indicate the helical structure observed throughout the N-terminus. The dynamic information is indicated in the strongly interacting phosphoserine groups, shown in purple, and the less strongly interacting C-terminal region of the pentadecyl domain. The C-terminus of statherin is left as a shapeless entity and is an area of future study to understand the secondary and tertiary structure of the remainder of the protein.

BIBLIOGRAPHY

1. *433A Peptide Synthesizer User's Manual* (Applied Biosystems Inc, 1993).

2. Abragam, A. *Principles of Nulcear Magnetism* (Oxford University Press, New York, 1961).

3. Addadi, L. & Weiner, S. Interactions Between Acidic Proteins and Crystals: Sterochemical Requirements in Biomineralization. *Proceedings of the National Academy of Science* **82**, 4110-4114 (1985).

4. Aizenberg, J., Hanson, J., Koetzle, T. F., Weiner, S. & Addadi, L. Control of Macromolecule Distribution within Synthetic and Biogenic Single Calcite Crystals. *Journal Of The American Chemical Society* **119**, 881-886 (1997).

5. Alla, M. & Lippmaa, E. Resolution Limits in Magic-Angle Rotation NMR Spectra of Polycrystalline Solids. *Chemical Physics Letters* **87**, 30-33 (1982).

6. Amano, A., Kataoka, K., Raj, P. A., Genco, R. J. & Shizukuishi, S. Binding Sites of Salivary Statherin for *porphyromonas gingivalis* Recombinant Fimbrillan. *Infection and Immunity* **64**, 4249-4254 (1996).

7. Ando, S. *et al.* Confromational Characterization of Glycine Residues Incorporated into Some Homoppolypeptides by Solid-State ^{13}C NMR Spectroscopy. *Journal of the American Chemical Society* **107**, 7648-7652 (1985).

8. Ando, S., Ando, I., Shoji, A. & Ozaki, T. Intermolecular Hydrogen-Bonding Effect on ^{13}C NMR Chemical Shifts of Glycine Residue Carbonyl Carbons of Peptides in the Solid State. *Journal of the American Chemical Society* **110**, 3380-3386 (1988).

9. Andrew, E. R. & Eades, R. G. *Proceedings of the Royal Society of London* **A216**, 398 (1953).

10. Asakawa, N. *et al.* Hydrogen-Bonding Effect on ^{13}C NMR Chemical Shifts of L-alanine Residue Carbonyl Carbons of Peptides in the Solid State. *Journal of the American Chemical Society* **114**, 3261 (1992).

11. Asakawa, N., Kurosu, H. & Ando, I. Structural Study of Peptides Containing L-alanine Residues by *ab initio* Chemical Shielding Calculation. *Journal of Molecular Structure* **323**, 279 (1994).

12. Asakura, T. & et al. . NMR Study of Silk I Structure of *Bombyx mori* Silk Fibroin with ^{15}N-and ^{13}C-NMR Chemical Shift Contour Plots. *Biopolymers* **41**, 193-203 (1997).

13. Baldus, M., Geurts, D. G. & Meier, B. H. Broadband Dipolar Recoupling in Rotating Solids: A Numerical Comparison of some Pulse Schemes. *Solid State Nuclear Magnetic Resonance* **11**, 157-168 (1998).

14. Barker, W. W., Welch, S. A. & Banfield, J. F. Experimental Observations on the Effects of Microorganisms on Silicate Weathering. *American Mineralogist* **83**, 1551-1563 (1998).

15. Belcher, A. M. *et al.* Control of Crystal Phase Switching and Orientation by Soluble Mollusc-Shell Proteins. *Nature* **381**, 56-58 (1996).

16. Bennett, A. E., Ok, J. H., Griffin, R. G. & Vega, S. Chemical Shift Correlation Spectroscopy in Rotating Solids: Radio Frequency-Driven Dipolar Recoupling and Longitudinal Exchange. *Journal of Chemical Physics* **96**, 8624-8627 (1992).

17. Bennett, A. E., Weliky, D. P. & Tycko, R. Quantitative Conformational Measurements in Solid State NMR by Constant-Time Homonuclear Dipolar Recoupling. *Journal of the American Chemical Society* **120**, 4897-4898 (1998).

18. Berman, A., Addadi, L. & Weiner, S. Interactions of Sea-Urchin Skeleton Macromolecules with Growing Calcite Crystals--a Study of Intracrystalline Proteins. *Nature* **331**, 546-548 (1988).

19. Berman, A. *et al.* Biological Control of Crystal Texture: A Widespread Strategy for Adapting Crystal Properties to Function. *Science* **259**, 776-779 (1993).

20. Bevington, P. R. & Robinson, D. K. *Data Reduction and Error Analysis for the Physical Sciences* (WCB/McGraw-Hill, Boston, 1992).

21. Boncheva, M. & Vogel, H. Formation of Stable Polypeptide Monolayers at Interfaces: Controlling Molecular Conformation and Orientation. *Biophysical Journal* **73**, 1056-1072 (1997).

22. Bower, P. V. *et al.* Determination of Torsion Angles in Proteins and Peptides Using Solid State NMR, Journal of the American Chemical Society. *Journal of the American Chemical Society* **121**, 8373-8375 (1999).

23. Burum, D. P. & Rhim, W. K. Analysis of Multiple Pulse NMR in Solids. III. *Journal of Chemical Physics* **71**, 944-956 (1979).

24. Burum, D. P., Linder, M. & Ernst, R. R. A New "Tune-Up" NMR Pulse Cyclo for Minimizing and Characterizing Phase Transients. *Journal of Magnetic Resonance* **43**, 463-471 (1981).

25. Carpino, L. A. & Han, G. Y. The 9-Fluorenylmethoxy carbonyl Amino-Protecting Group. *Journal of Organic Chemistry* **37**, 3404-3409 (1972).

26. Chakrabartty, A., Yang, D. S. C. & Hew, C. L. Structure-Function Relationship in a Winter Flounder Antifreeze Polypeptide I. *The Journal of Biological Chemistry* **264**, 11307-11312 (1989).

27. Chakrabartty, A., Yang, D. S. C. & Hew, C. L. Structure-Function Relationship in a Winter Flounder Antifreeze Polypeptide II. *The Journal of Biological Chemistry* **264**, 11313-11316 (1989).

28. Chittur, K. K. FTIR/ATR for protein Adsorption to Biomaterial Surfaces. *Biomaterials* **19**, 357-369 (1998).

29. Christensen, A. M. & Schaefer, J. Solid-State NMR Determination of Intra- and Intermolecular 31P-13C Distances for Shikimate 3-Phosphate and [1-13C]Glyphosate Bound to Enolpyruvylshikimate-3-phosphate Synthase. *Biochemistry* **32**, 2868-2873 (1993).

30. Creighton, T. E. *Proteins, Structures and Molecular Properties,* (W.H. Freeman and Company, New York, 1993).

30. Davies, J. E. In Vitro Modeling of the Bone/Implant Interface. *The Anatomical Record* **245**, 426-445 (1996).

31. DeGrado, W. F. & Lear, J. D. Induction of Peptide Conformation at Apolar/Water Interfaces. 1. A study with Model Peptides of Defined Hydrophobic Periodicity. *Journal of the American Chemical Society* **107**, 7684-7689 (1985).

32. DeOliviera, D. B., Laursen, R. A. & . Control of Calcite Crystal Morphology by a Peptide Designed to Bind to a Specific Surface. *Journal of the American Chemical Society* **119**, 10627- 10631 (1997).

33. Diekwisch, T. G. H., Berman, B. J., Gentner, S. & Slavkin, H. C. Initial Enamel Crystals are not Spatially Associated with Mineralized Dentine. *Cell and Tissue Research* **279**, 149-167 (1995).

34. Douglas, W. H. & et al. Statherin: A Major Boundary Lubricant of Human Saliva. *Biochemical and Biophysical Research Communications* **180**, 91-97 (1991).

35. Dumais, J. J. in *Chemistry Department* 199 (University of Washington, Seattle, WA).

36. Duncan, T. M. *Principal Components of Chemical Shift Tensors: A Compilation; 2nd Ed.* (The Farragut Press, Madison, 1997).

37. Elbayed, K. *et al.* Origin of the Residual NMR Linewidth of a Peptide Bound to a Resin under Magic Angle Spinning. *Journal of Magnetic Resonance* **136**, 127-129 (1999).

38. Elgavish, G. A., Hay, D. I. & Schlesinger, D. H. ^{1}H and ^{31}P Nuclear Magnetic Resonance Studies of Human Salivary Statherin. *International Journal of Peptide and Protein Research* **23**, 230-234 (1984).

39. Falini, G., Albeck, S., Weiner, S. & Addadi, L. Control of Aragonite or Calcite Polymorphism by Mollusk Shell Macromolecules. *Science* **271**, 67-69 (1996).

40. Farrrar, T. C. & Harriman, J. E. *Density Matrix Theory and Its Applications in NMR Spectroscopy* (The Farragut Press, Madison, WI, 1998).

41. Fernandez, V. L., Reimer, J. A. & Denn, M. M. Magnetic Resonance Studies of Polypeptides Adsorbed on Silica and Hydroxyapatite Surfaces. *Journal of the American Chemical Society* **114**, 9634-9642 (1992).

42. Fields, C. G., Lloyd, D. H., Macdonald, R. L., Ottesen, K. M. & Noble, R. L. *Peptide Research* **4**, 95-101 (1990).

43. Fincham, A. G., Moradian-Oldak, J. & Simmer, J. P. The Structural Biology of the Developing Dental Enamel Matrix. *Journal of Strucutral Biology* **136**, 270-299 (1999).

44. Fuijisawa, R. & Kuboki, Y. Conformation of Dentin Phophophoryn Adsorbed on Hydroxyapatite Crystals. *European Journal or Oral Sciences* **106**, 249-253 (1998).

45. Fujisawa, R., Wada, Y., Nodasaka, Y. & Kuboki, Y. Acidic Amino Acid-Rich Sequences as Binding Sites of Osteonectin to Hydroxyapatite Crystals. *Biochimica Et Biophysica Acta* **1292**, 53-60 (1996).

46. Garcia-Ramos, J. V., Carmona, P. & Hidalgo, A. The Adsorption of Acidic Amino Acids and Homopolypeptides on Hydroxyapatite. *Journal of Colloid and Interface Science* **83**, 479-484 (1981).

47. Gebe, J. A., Allison, S. A., Clendenning, J. B. & Schurr, J. M. Monte Carlo Simulations of Supercoiling Free Energies for Unknotted and Trefoil Knotted DNAs. *Biophysical Journal* **68**, 619-633 (1995).

48. Geheagin, K., Meints, G. A., Hatcher, M. E. & Drobny, G. P. The Dynamic Impact of CpG Methylation in DNA. *Biochemistry* (2000).

49. George, A., Sabsay, B., Simonian, P. A. & Veis, A. Charcterization of a Novel Dentin Matrix Acidic Phosphoprotein--Implications for Induction of Biomineralization. *Journal Of Biological Chemistry* **268**, 12624-12630 (1993).

50. Goldberg, H. A., Warner, K. J., Stillman, M. J. & Hunter, G. K. Determination of the Hydroxypatite Nucleating Region of Bone Sialoprotein. *Connective Tissue Research* **35**, 439-446 (1996).

51. Gorski, J. P. Acidic Phophoproteins from Bone Matrix: A Structural Rationalization of Their Role in Biomineralization. *Calcified Tissue International* **50**, 391-396 (1992).

52. Gregory, D. M. *et al.* Windowless Dipolar Recoupling: The Detection of Weak Dipolar Couplings Between Spin 1/2 Nuclei With Large Chemical Shift Anisotropies. *Chemical Physics Letters* **246**, 654-663 (1995).

53. Gregory, D. M., Wolfe, G. M., Jarvie, T. P., Sheils, J. C. & Drobny, G. P. Double-Quantum Filtering in Magic-Angle-Spinning NMR Spectroscopy Applied to DNA Oligomers. *Molecular Physics* **89**, 1835-1849 (1996).

54. Gregory, D. M., Mehta, M. A., Shiels, J. C. & Drobny, G. P. Determination of Local Structure in Solid Nucleic Acids Using Double Quantum Nuclear Magnetic Resonance Spectroscopy. *Journal of Chemical Physics* **107**, 28 (1997).

55. Gregory, D. M. *et al.* Dipolar Recoupling NMR of Biomolecular Self-Assemblies: Determining Inter- and Intrastrand Distances in Fibrilized Alzheimer's β-Amyloid Peptide. *Solid State Magnetic Resonance* **13**, 149-166 (1998).

56. Gu, Z. & McDermott, A. Chemical Shielding Anisotropy of Protonated and Deprotonated Carboxylates in Amino-Acids. *Journal of the American Chemical Society* **115**, 4282-4285 (1993).

57. Gullion, T. & Schaefer, J. Rotational-Echo Double-Resonance NMR. *Advances in Magnetic Resonance* **13**, 57 (1989).

58. Gullion, T. & Vega, S. A Simple Magic Angle Spinning NMR Experiment for the Dephasing of Rotational Echoes of Dipolar Coupled Homonuclear Spin Pairs. *Chemical Physics Letters* **194**, 423 (1992).

59. Gururaja, T. L. & Levine, M. J. Solid-Phase Synthesis and Characterization of Human Salivary Statherin: A Tyrosine-Rich Phosphoprotein Inhibitor of Calcium Phosphate Precipitation. *Peptide Research* **9**, 283-289 (1996).

60. Haeberlen, U. *High Resolution NMR in Solids Selective Averaging* (ed. Waugh, J. S.) (Academic Press, New York, 1976).

61. Hanein, D., Geiger, B. & Addadi, L. Differential Adhesion of Cells to Enantiomorphous Crystal Surfaces. *Science* **263**, 1413-6 (1994).

62. Hartmann, S. R. & Hahn, E. L. Nuclear Double Resonance in the Rotating Frame. *Physical Review* **128**, 2042-2053 (1962).

63. Hatcher, M. E., Mattiello, D. L., Meints, G. A., Orban, J. & Drobny, G. P. A Solid-State Deuterium NMR study of the Localized Dynamics at the C9pG10 Step in the DNA Dodecamer [d(CGCGAATTCGCG)]2. *Journal of the American Chemical Society* **120**, 9850-9862 (1998).

64. Hauschka, P. V. & Carr, S. A. Calcium-Dependent α-Helical Structure in Osteocalcin. *Biochemistry* **21**, 2538-2547 (1982).

65. Hauska, P. V. & Frank H. Wians, J. Osteocalcin-Hydroxyapatite Interaction in the Extracellular Organic Matrix of Bone. *The Anatomical Record* **224**, 180-188 (1989).

66. Hay, D. I., Smith, D. J., Schluckebier, S. K. & Moreno, E. C. Relationship Between Concentration of Human Salivary Statherin and Inhibition of Calcium Phosphate Precipitation in Stimulated Human Parotid Saliva. *Journal of Dental Research* **63**, 857-863 (1984).

67. Heller, J. *et al.* Solid-State NMR Studies of the Prion Protein H1 Fragment. *Protein Science* **5**, 1655-1661 (1996).

68. Herzfeld, J. & Berger, A. E. Sideband Intesities in NMR Spectra of Samples Spinning at the Magic Angle. *Journal of Physical Chemistry* **73**, 6021-6030 (1980).

69. Hunter, G. K. & Goldberg, H. A. Modulation of Crystal Formation by Bone Phosphoproteins: Role of Glutamic Acid-Rich Seuqences in the Nucleation of Hydroxyapatite by Bone Sialoprotein. *Biochemical Journal* **302**, 175-9 (1994).

70. Hunter, G. K., Hauschka, P. V., Poole, A. R., Rosenberg, L. C. & Goldberg, H. A. Nucleation and Inhibition of Hydroxyapatite Formation by Mineralized Tissue Proteins. *Biochemical Journal* **317**, 59-64 (1996).

71. Hunter, G. K. Interfacial Aspects of Biomineralization. *Current Opinion in Solid State and Materials Science* **1**, 430-435 (1996).

72. Jarvie, T. P. & Went, G. T. Simultaneous Multiple Distance Measurements in Peptides via Solid-State NMR. *Journal of the American Chemical Society* **118**, 5330-5331 (1996).

73. Johnsson, M., Levine, M. J. & Nancollas, G. H. Hydroxyapatite Binding Domains in Salivary Proteins. *Critical Reviews In Oral Biology and Medicine* **4**, 371-8 (1993).

74. Kestell, M. F. & et al. A Calcium-binding Protein in Bile and Gallstones. *Hepatology* **16**, 1315-1321 (1992).

75. Kim, H. S., Hartgerink, J. D. & Ghadiri, M. R. Oriented Self-Assembly of Cyclic Peptide Nanotubes in Lipid Membranes. *Journal of the American Chemical Society* **120**, 4417-4424 (1998).

76. Klug, C. A., Burzio, L. A., Waite, J. H. & Schaefer, J. *In Situ* Analysis of Peptidyl DOPA in Mussel Byssus Using Rotational-Echo Double-Resonance NMR. *Archives Of Biochemistry And Biophysics* **333**, 221-224 (1996).

77. Knight, C. A., Cheng, C. C. & DeVries, A. L. Adsorption of α-Helical Antifreeze Peptides on Specific Ice Crystal Surface Planes. *Biophysical Journal* **59**, 409-418 (1991).

78. Kresak, M., Moreno, E. C., Zahradnik, R. T. & Hay, D. I. Adsorption of Amino Acids onto Hydroxyapatite. *Journal of Colloid and Interface Science* **59**, 283-292 (1977).

79. Lalitha, V., Subramanian, E. & Bordner, J. Structure and Conformation of Linear Peptides.4. Crystal Structure of L-alanyl-glycyl-glycine Monohydrate. *Indian Journal of Pure and Applied Physics* **23**, 506 (1985).

80. Lamkin, M. S. & Oppenheim, F. G. Structural Features of Salivary Function. *Critical Reviews in Oral Biology and Medicine* **4**, 251-259 (1993).

81. Lansbury, P. T. & et al. Structural Model for the β-Amyloid Fibril Based on Interstrand Alignment of an Antiparallel-Sheet Comprising a C-terminal Peptide. *Nature Structural Biology* **2**, 990-998 (1995).

82. Lee, Y. K. *et al.* Efficient Dipolar Recoupling in the NMR of Rotating Solids. A Sevenfold Symmetric Radiofrequency Pulse Sequence. *Chemical Physics Letters* **242**, 304-309 (1995).

83. Lee, T.-H., Thompson, P. E., Hearn, M. T. W. & Aguilar, M.-I. Conformational Stability of a Type II' β-turn Motif in Human Growth Hormone [6-13] Peptide Analogues at Hydrophobic Surfaces. *Journal Peptide Research* **49** (1997).

84. Levitt, M. H., Raleigh, D. P., Creuzet, F. & Griffin, R. G. Theory and Simulations of Homonuclear Spin Pair Systems in Rotating Solids. *Journal of Chemical Physics* **92**, 6347 (1990).

85. Lingbeck, J. *et al.* Effect of Adenine Methylation on the Structure and Dynamics of TpA Steps in DNA: NMR Structure Determination of {d(CGAGGTTTAAACCTCG)]2 and Its A9-Methylated Derivative at 750 MHz. *Biochemistry* **35**, 719-734 (1996).

86. Long, J. R., Sun, B. Q., Bowen, A. & Griffin, R. Molecular Dynamics and Magic Angle Spinning NMR. *Journal of the American Chemical Society* **116**, 11950-11956 (1994).

87. Long, J. R. *et al.* A Peptide That Inhibits Hydroxyapatite Growth is in an Extended Conformation on the Crystal Surface. *Proceedings of the National Academy of Science* **95**, 12083-12087 (1998).

88. Long, H. W. & Tycko, R. Biopolymer Conformational Distributions From Solid State NMR: α-Helix and 3_{10}-Helix Contents of a Helical Peptide. *Journal of the American Chemical Society* **120**, 7039 (1998).

89. Lowe, I. J. Free-Induction Decays in Solids. *Physics Review Letters* **2**, 285-287 (1959).

90. Lowenstam, H. A. & Weiner, S. *On Biomineralization* (Oxford University Press, New York, 1989).

91. Marshall, G. R. *et al.* Determination of Precise Interatomic Distance in a Helical Peptide by REDOR NMR. *Journal of the American Chemical Society* **112**, 963 (1990).

92. Mehring, M. *Principles of High Resolution NMR in Solids* (Springer-Verlag, New York, 1983).

93. Mehta, M. A. *et al.* Distance Measurements in Nucleic Acids Using Windowless Dipolar Recoupling Solid State NMR. *Solid State Nuclear Magnetic Resonance* **7**, 211-228 (1996).

94. Merritt, M. E., Christensen, A. M., Kramer, K. J., Hopkins, T. L. & Schaefer, J. Detection of Intercatechol Cross-Links in Insect Cuticle by Solid-State Carbon-13 and Nitrogen-15 NMR. *Journal Of the American Chemical Society* **118**, 11278-11282 (1996).

95. Moradian-Oldak, J., Leung, W. & Fincham, A. G. Temperature and pH-Dependent Supramolecular Self-Assembly of Amelogenin Molecules: A Dynamic Light-Scattering Analysis. *Journal of Structural Biology* **122**, 320-327 (1998).

96. Moreno, E. C., Kresak, M. & Hay, D. I. Adsorption of Two Human Parotid Salivary Macromolecules on Hydroxy-,Fluorhydroxy- and Fluorapatites. *Archives of Oral Biology* **23**, 525-533 (1978).

97. Moreno, E. C., Varughese, K. & Hay, D. I. Effect of Human Salivary Proteins on the Precipitation Kinetics of Calcium Phosphate. *Calcified Tissue International* **28**, 7-16 (1979).

98. Moreno, E. C., Kresak, M. & Hay, D. I. Adsorption Thermodynamics of Acidic Proline-Rich Human Salivary Proteins onto Calcium Apatites. *The Journal of Biological Chemistry* **257**, 2981-2989 (1982).

99. Moreno, E. C., Kresak, M. & Hay, D. I. Adsorption of Molecules of Biological Interest onto Hydroxyapatite. *Calcified Tissue International* **36**, 48-59 (1984).

100. Naganagowda, G. A., Gururaja, T. L. & Levine, M. J. Delineation of Conformational Preferences in Human Salivary Statherin by ^{1}H- ^{31}P- NMR and CD Studies: Sequential Assignment and Structure-Function Correlations. *Biomolecular Structure & Dynamics* **16**, 91-107 (1998).

101. Narita, M., Tomotake, Y., Isokawa, S., Matsuzawa, T. & Miyauchi, T. Syntheses and Properties of Resin-Bound Oligopeptides. 2. Infrared Spectroscopic

Conformational Analysis of Cross-Linked Polystrene Resin Bound Oligoleucines in the Swollen State. *Macromolecules* **17**, 1903-1906 (1984).

102. Nielsen, N. C., Bildsoe, H., Jakobsen, H. J. & Levitt, M. H. Double-Quantum Homonuclear Rotary Resonance--Efficient Dipolar Recovery in Magic-Angle Spinning Nuclear-Magnetic-Resonance. *Journal of Chemical Physics* **101**, 1805-1812 (1994).

103. Pauling, L. et al The Structure of Proteins: Two Hydrogen-bonded Helical Configurations of the Polypeptide Chain. *Proceedings of the National Acadamy of Science USA* **37**, 205-211 (1951).

104. Peersen, O. B., Groesbeek, M., Aimoto, S. & Smith, S. O. Analysis of Rotational Resonance Magnetization Exchange Curves from Crystalline Peptides. *Journal of the American Chemical Society* **117**, 7228-7237 (1995).

105. Pines, A., Gibby, M. G. & Waugh, J. S. Proton-Enhanced NMR of Dilute Spins in Solids. *Journal of Chemical Physics* **59**, 569-590 (1973).

106. Raj, P. A., Johnsson, M., Levine, M. J. & Nancollas, G. H. Dependence on Sequence, Charge, Hydrogen Bonding Potency, and Helical Conformation for Adsorption to Hydroxyapatite and Inhibition of Mineralization. *Journal Biological Chemistry* **267**, 5968-5976 (1992).

107. Ramasubbu, N., Thomas, L. M., Bhandary, K. K. & Levine, M. J. Structural Characteristics of Human Salivary Statherin: A Model for Boundary Lubrication at the Enamel Surface. *Critical Reviews in Oral Biology and Medicine* **4**, 363-370 (1993).

108. Ratner, B. D., Horbett, T. A., Shuttleworth, D. & Thomas, H. R. Analysis of the Organization of Protein Films on solid Surfaces by ESCA. *Journal Of Colloid and Interface Science* **83** (1981).

109. Ruocco, J. J., Siminovitch, D. J., Long, J. R., Das Gupta, S. K. & Griffen, R. G. ^{2}H and ^{13}C Nuclear Magnetic Resonance Study of N-Palmitoylgalactosylsphingosine (Cerebroside)/Cholesterol Bilayers. *Biophysical Journal* **71**, 1776-1788 (1996).

110. Saito, H. Conformation-Dependent ^{13}C Chemical Shifts: A New Means of Conformational Characterization as Obtained by High-Resolution Solid-State ^{13}C NMR. *Magnetic Resonance in Chemistry* **24**, 835-852 (1986).

111. Schaefer, J. & Stejskal, E. O. Carbon-13 Nuclear Magnetic Resonance of Polymers Spinning at the Magic Angle. *Journal of the American Chemical Society* **98**, 1031 (1976).

112. Schaefer, J., Stejskal, E. O. & Buchdahl, R. Magic-Angle 13C NMR Analysis of Motion in Solid Glassy Polymers. *Macromolecules* **10**, 384-405 (1977).

113. Schlesinger, D. H. & Hay, D. I. Complete Covalent Structure of Statherin, a Tyrosine-rich Acidic Peptide Which Inhibits Calcium Phosphate Precipitation from Human Parotid Saliva. *Journal of Biological Chemistry* **252**, 1689-1695 (1977).

114. Schwartz, S. S., Hay, D. I. & Schluckebier, S. K. Inhibition of Calcium Phosphate Precipitation by Human Salivary Statherin: Structure-Activiy Relationships. *Calcified Tissue International* **50**, 511-517 (1992).

115. Shaw, W. J. *et al.* Determination of Statherin N-Terminal Peptide Conformation on Hydroxyapatite Crystals. *Journal of the American Chemical Society* **122**, 1709-1716 (2000).

116. Shaw, W. J., Long, J. R., Campbell, A. A., Stayton, P. S. & Drobny, G. P. *Journal of the American Chemical Society* (In Press).

117. Sicheri, f. & Yang, D. S. C. Ice-binding Structure and Mechanism of an Antifreeze Protein from Winter Flounder. *Nature* **375**, 427-431 (1995).

118. Simmons, A. H., Michal, C. A. & Jelinski, L. W. Molecular Orientation and Two-Component Nature of the Crystalline Fraction of Spider Dragline Silk. *Science* **271** (1996).

119. Slichter, C. P. *Principles of Magnetic Resonance* (ed. Fulde, P.) (Springer-Verlag, Berlin, 1990).

120. Smith, L. J. *et al.* Analysis of Main Chain Torsion Angles in Proteins: Prediction of NMR Coupling Constants for Native and Random Coil Conformations. *Journal of Molecular Biology* **255**, 494-506 (1996).

121. Spera & Bax, A. Emperical Correlation Between Protein Backbone Conformation and C_α and C_β ^{13}C Nuclear Magnetic Resonance Chemical Shifts. *Journal of the American Chemical Society* **113**, 5490 (1991).

122. Spiess, H. W. *Rotation of Molecules and Nuclear Spin Relaxation* (eds. Diehl, P. & Kosfeld, E. F. R.) (Springer, Berlin, 1978).

123. Steer, D. L., Thompson, P. E., Blondelle, S. E., Houghten, R. A. & Aguilar, M.-I. Comparison of the Binding of α-helical and β-sheet Peptides to a Hydrophobic Surface. *Journal of Peptide Research* **51**, 401-412 (1998).

124. Stejskal, E. O., Schaefer, J. & Waugh, J. S. Magic-Angle Spinning and Polarization Transfer in Proton-Enhanced NMR. *Journal of Magnetic Resonance* **28**, 105-112 (1977).

125. Stejskal, E. O. & Memory, J. D. *High Resolution NMR in the Solid State* (Oxford University Press, New York, 1994).

126. Stoll, M. E. & Majors, T. J. Reduction of Magnetic Susceptibility Broadening in NMR by Susceptibility Matching. *Journal of Magnetic Resonance* **46**, 283-288 (1982).

127. Stringer, J. in *Chemistry Department* (University of Washington, Seattle, 1998).

128. Strong, A. E. & Moore, B. D. Self-assembling Chiral Monolayers of Helical Peptides Bound to Gold via Side-chain Thioethers. *Chemical Communications*, 473-474 (1998).

129. Stupp, S. I. & Braun, P. V. Molecular Manipulation of Microstructures: Biomaterials, Ceramics, and Semiconductors. *Science* **277**, 1242-1248 (1997).

130. Sun, B. Q., Costa, P. R., Kocisko, D., Lansbury, P. T. & Griffen, R. G. Internuclear Distance measurements in Solid State Nuclear Magnetic Resonance: Dipolar Recoupling via Rotor Synchronized Spin Locking. *Journal of Chemical Physics* **102**, 702-707 (1995).

131. Tycko, R. & Dabbagh, G. Measurement of Nuclear Magnetic Dipole-Dipole Coupling in Magic Angle Spinning NMR. *Chemical Physics Letters* **173**, 461-465 (1990).

132. van den Berg, L. & Rose, D. Effect of Freezing on the pH and Composition of Sodium and Potassium Phosphate Solutions: the Reciprocal System KH2PO4-Na2HPO4-H2O. *Archives of Biochemistry. and Biophysics* **81**, 349 (1959).

133. VanderHart, D. L., Earl, W. L. & Garroway, A. N. Resolution in 13C NMR of Organic Solids Using High-Power Proton Decoupling and Magic-Angle Sample Spinning. *Journal of Magentic Resonance* **44**, 361-401 (1981).

134. Walters, D. A. *et al.* Modification of Calcite Crystal Growth by Abalone Shell Proteins: An Atomic Force Microscope Study. *Biophysical Journal* **72**, 1425-1433 (1997).

135. Wang, A. C., Kennedy, M. A., Reid, B. R. & Drobny, G. P. A Solid-State 2H NMR Investigation of Purine Motion in a 12 Base Pair RNA Duplex. *Journal of Magnetic Resonance, Series B* **105**, 1-10 (1994).

136. Weast, R. C. (ed.) *Handbook of Chemistry and Physics* (CRC Press, Boca Raton, 1982).

137. Weiner, S. & Addadi, L. Design Strategies in Mineralized Biological Materials. *Journal of Materials Chemistry* **7**, 689-702 (1997).

138. Wemmer, D. E. in *Lawrence Livermore Berkeley, Laboratory Materials and Molecular Research Division* 288 (University of California, Berkeley, Berkeley, 1978).

139. Wen, D. & Laursen, R. A. Structure-Function Relationships in an Antifreeze Polypeptide. *The Journal of Biological Chemistry* **267**, 14102-14108 (1992).

140. Wierzbicki, A., Sikes, C. S., Madura, J. D. & Drake, B. Atomic Force Microscopy and Molecular Modeling of Proetin and peptide Binding to Calcite. *Calcified Tissue International* **54**, 133-141 (1994).

141. Wikiel, K., Burke, E. M., Perich, J. W., Reynolds, E. C. & Nancollas, G. H. Hydroxyapaptite Mineralization and Demineralization in the Presence of Synthetic Phosphorylated Pentapeptides. *Archives Of Oral Biology* **39**, 715-21 (1994).

142. Wishart, D. S. & Sykes, B. D. The ^{13}C Chemical-Shift Index: A Simple Method for the Identification of Protein Secondary Structure Using ^{13}C Chemical-Shift Data. *Journal of Biomolecular NMR* **4**, 171 (1994).

144. Wittebort, R. J., Olejnicxak, E. T. & Griffen, R. G. Analysis of Deuterium Nuclear Magnetic Resonance Line Shapes in Anisotropic Media. *Journal of Chemical Physics* **86**, 5411-5430 (1987).

APPENDIX I:

TRIPLE RESONANCE PROBE

The probe design used (electrical design by John Stringer[Stringer, 1998 #114] incorporated both lumped elements and transmission lines as shown in Figure A.1 and was designed to maximize efficiency. A full description of the electrical circuit is described in Dr. John Stringers thesis. The transmission lines were primarily used for isolation, while the tuning was controlled in the capacitors and inductors. Isolation was achieved between the proton channel and lower frequency channels by incorporating an 1/8 λ-proton transmission line (T1) in series with a capacitor (C_{T1}) to provide a low impedance path to ground for the proton channel. Another 1/8 λ-proton transmission line (T2) was placed on the opposite side of the coil to ground the lower frequency channels and prevent carbon leak-through into the proton circuitry. The two lower frequency channels were isolated with a standard lumped element trap.

The carbon channel is the only channel that met the calculated efficiency. Both ^{31}P and ^{1}H were much lower than expected. This observation has not been reproducible with calculations, so the exact source of the loss is unknown. The physical layout of the probe required T1 to be located above the coil, rather than below it. While it is not evident how this may have effected the efficiencies, it is the only difference between that and similar probes built, and thus may have a contribution to loss in efficiency. Even with the lower efficiency, the performance of the probe meets or exceeds many commercially available probe specifications.

The efficiencies of each channel and the isolation of the channels from each other are shown in Tables A.I.1 and A.I.2. Figure A.I.1 is a schematic of the circuit design and Table A.I.3 lists the values of the components used in the probe.

Table A.I.1. Efficiencies of the HCP probe, along with experimentally measured 90 times and input powers needed to generate the respective fields.

Nucleus	Predicted	Actual	90 time (sec)	Voltage	Power (W)	Power Handling
^{13}C	33%	29.4%	5.0	217	118	300W
^{31}P	16%	3.5%	7.6	352	309	400W
^{1}H	18%	5.0%	2.4	400	400	600W

Table A.I.2. Isolation measured between each channel for the HCP probe.

In/Out	Isolation
1H/13C	18.3 dB
13C/1H	20.9 dB
31P/1H*	15 dB
13C/31P	23.4 dB
1H/31P*	>30 dB
31P/13C	26.1 dB

*The ^{1}H to ^{31}P isolation and vice versa is isolated via an external trap placed on the ^{1}H input.

Table A.I.3. Actual component values used for the HCP probe.

Component	Value
C_S low tune	4.68 pF
C_P low tune	4.35 pF
C_S high tune	5.03 pF
C_P high tune	33.3 pF
C_S proton tune	2.00 pF
C_P proton tune	10.71 pF
C_{TI}	3.3 pF
C-low node	12 pF
C_P-trap	16.5 pF
Sample Coil	30.1 nH
I_S-trap	24 nH
I_P-trap	24 nH

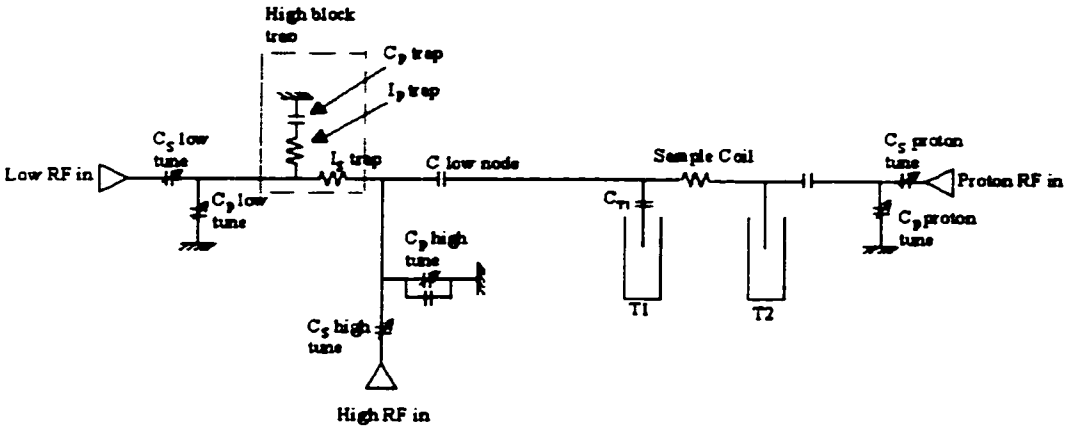

Figure A.1. The circuit diagram used in the HCP probe.

Appendix II:

Dynamics Simulation Code

Diffusion on a cone.

The model described in Chapter 5 was based on diffusion on a cone, as described by Wittebort et al. The theoretical model used makes several assumptions: 1) The motion is in the fast limit regime. Under such conditions, the following equation can be utilized:

$$\bar{\sigma}_{ij} = \int d\Omega P(\Omega)\sigma_{ij}(\Omega) \qquad [A.1]$$

where σ_{ij} is the rigid chemical shift tensor, $\bar{\sigma}_{ij}$ is the motionally averaged chemical shift tensor and $P(\Omega)$ is the equilibrium distribution of molecular orientations. $\sigma_{ij}(\Omega)$ is obtained by first rotating σ^{PAS} into the helix axis, so all motionally averaged tensors are calculated in the helix reference frame. This can be done using the rotation matrix shown in Chapter 2 according to the following equation:

$$\sigma(helix) = r^{+}\sigma^{PAS}r(helix) \qquad [A.2]$$

$\sigma_{ij}(\Omega)$ is then calculated by rotating σ^{helix} into the motionally averaged reference frame:

$$\sigma(\Omega) = r^{+}\sigma^{helix}r(\Omega) \qquad [A.3]$$

2) An equiprobable distribution can be assumed ($P(\gamma) = \frac{1}{2}\gamma_o, for -\gamma_0 \le \gamma \le \gamma_o$), meaning all orientations are equally likely and no activation barrier is present, such as a barrierless cone. The cone is defined by two angles, β and γ, shown in Figure 5.5. A third angle, α, is carried through each of the equations. This angle is used to orient to an

arbitrary axis, but in this case, the rotation was performed independently to orient the PAS values to the helix axis, so $\alpha = 0$ for the system describe here.

The steps required to calculate these the motionally averaged tensors are shown below:

1) Rotate the PAS tensor values into the helix axis (already predetermined to be helical)
2) Calculate $\sigma_{ij}(\Omega)$ by rotating around the motionally averaged angles, α, β and γ.
3) Insert these values into equation A.1, calculate $\bar{\sigma}_{ij}$ and diaganolize to get the motionally averaged CS tensor values in the PAS.
4) Sort the resulting values by finding the best fit to the observed, motionally averaged tensor values.

The results for several of these steps are shown in the following text and in Table A.II.1-A.II.3. The results for step 3), $\bar{\sigma}_{ij}$ matrix values, are shown for the general case, where $c_x = \cos x$, $s_x = \sin x$, $s_+ = \frac{1}{2}(1 + \frac{\sin 2\gamma_0}{\gamma_0})$, $s_- = \frac{1}{2}(1 - \frac{\sin 2\gamma_o}{\gamma_o})$ and $s_a = \frac{\sin 2\gamma_0}{\gamma_o}$

$$\begin{aligned}\bar{\sigma}_{11} = [&(c_a^2 c_b^2 s_+ + s_a^2 s_-)\sigma_{11} + (c_a s_a c_b^2 s_+ - s_a c_a s_-)\sigma_{12} - c_a c_b s_b s_+ \sigma_{13} \\ &+ (c_a s_a c_b^2 s_+ - c_a s_a s_-)\sigma_{21} + (s_a^2 c_b^2 s_+ + c_a^2 s_-)\sigma_{22} - s_a c_b s_b s_+ \sigma_{23} \\ &- c_a c_b s_b s_+ \sigma_{31} + s_a s_b c_b s_+ \sigma_{32} - s_b^2 s_+ \sigma_{33}]\end{aligned}$$

$$\begin{aligned}\bar{\sigma}_{12} = [&(-c_a s_a c_b s_+ + c_a s_a c_b s_-)\sigma_{11} + (-s_a^2 c_b s_+ - c_b c_a^2 s_-)\sigma_{12} - s_a s_b s_+ \sigma_{13} \\ &+ (c_a^2 c_b s_+ + c_b s_a^2 s_-)\sigma_{21} + (c_a s_a c_b s_+ - s_a c_a c_b s_-)\sigma_{22} - c_a s_b s_+ \sigma_{23} \\ &- s_a s_b s_- \sigma_{31} + c_a s_b s_- \sigma_{32}]\end{aligned}$$

$$\begin{aligned}\bar{\sigma}_{13} = [&c_a^2 s_b c_b s_o \sigma_{11} + c_a c_b s_a s_b s_o \sigma_{12} - c_a s_b^2 s_o \sigma_{13} \\ &+ c_a s_a c_b s_b s_o \sigma_{21} + s_a^2 c_b s_b s_o \sigma_{22} - s_a s_b^2 s_o \sigma_{23} \\ &- c_a c_b^2 s_o \sigma_{31} + s_a c_b^2 s_o \sigma_{32} - c_b s_b s_o \sigma_{33}]\end{aligned}$$

$$\begin{aligned}\bar{\sigma}_{21} = [&(-c_a s_a c_b s_+ + c_a s_a c_b s_-)\sigma_{11} + (s_a^2 c_b s_- + c_b c_a^2 s_+)\sigma_{12} - s_a s_b s_- \sigma_{13} \\ &+ (-c_a^2 c_b s_- + c_b s_a^2 s_+)\sigma_{21} + (-c_a s_a c_b s_- + s_a c_a c_b s_+)\sigma_{22} + c_a c_b s_- \sigma_{23} \\ &- s_a s_b s_+ \sigma_{31} + c_a s_b s_+ \sigma_{32}]\end{aligned}$$

$$\begin{aligned}\bar{\sigma}_{22} = [&(c_a^2 c_b^2 s_- + s_a^2 s_+)\sigma_{11} + (c_a s_a c_b^2 s_- - s_a c_a s_+)\sigma_{12} - c_a c_b s_b s_- \sigma_{13} \\ &+ (c_a s_a c_b^2 s_- - c_a s_a s_+)\sigma_{21} + (s_a^2 c_b^2 s_- + c_a^2 s_+)\sigma_{22} \\ &- c_a c_b s_b s_- \sigma_{31} - s_a s_b c_b s_- \sigma_{32} + s_b^2 s_- \sigma_{33}]\end{aligned}$$

$$\begin{aligned}\bar{\sigma}_{23} = [&-c_a s_a s_b s_0 \sigma_{11} + c_a^2 s_b s_o \sigma_{12} \\ &- s_b s_a^2 s_0 \sigma_{21} + c_a s_a s_b s_o \sigma_{22} \\ &- s_a c_b s_o \sigma_{31} + c_a c_b s_0 \sigma_{32}]\end{aligned}$$

$$\begin{aligned}\bar{\sigma}_{31} = [&c_a^2 s_b c_b s_o \sigma_{11} + c_a c_b s_a s_b s_o \sigma_{12} + c_a c_b^2 s_o \sigma_{13} \\ &+ c_a s_a c_b s_b s_o \sigma_{21} + s_a^2 c_b s_b s_o \sigma_{22} + s_a c_b^2 s_o \sigma_{23} \\ &- c_a c_b^2 s_o \sigma_{31} + s_a s_b^2 s_o \sigma_{32} + c_b s_b s_o \sigma_{33}]\end{aligned}$$

$$\begin{aligned}\bar{\sigma}_{32} = [&-c_a s_a s_b s_0 \sigma_{11} - s_a^2 s_b s_o \sigma_{12} - s_a c_b s_o \sigma_{13} \\ &- s_b c_{ab}^2 s_o \sigma_{21} + c_a s_a s_b s_o \sigma_{22} + c_a c_b s_0 \sigma_{32}]\end{aligned}$$

$$\begin{aligned}\bar{\sigma}_{33} = [&c_a^2 s_b^2 s \sigma_{11} + c_a s_a s_b^2 \sigma_{12} - c_a c_b s_b \sigma_{13} \\ &+ c_a s_a c_b^2 \sigma_{21} + s_a^2 s_b^2 \sigma_{22} + c_b s_a s_b \sigma_{23} \\ &+ c_a c_b s_b \sigma_{31} + s_a s_b c_b \sigma_{32} + c_b^2 \sigma_{33}]\end{aligned}$$

Table A.II.1 Helical coordinates generated using Insight II

Atom	X	Y	Z
N1	0.162	-0.202	0.00
CA1	1.612	-0.031	0.00
C1	1.985	1.432	0.00
O1	1.137	2.319	0.00
N2	3.277	1.700	0.000
CA2	3.784	3.070	0.000
C2	3.412	3.784	-1.278
O2	3.055	4.958	-1.286
N3	3.495	3.070	-2.385
CA3	3.167	3.629	-3.693
C3	1.703	3.991	-3.775
O3	1.316	5.014	-4.331
N4	0.865	3.140	-3.213
CA4	-0.578	3.361	-3.216
C4	-0.940	4.587	-2.412
O4	-1.808	5.373	-2.780
N5	-0.267	4.764	-1.291
CA5	-0.510	5.905	-0.414
C5	-0.140	7.201	-1.097
O5	-0.821	8.215	-0.979
N6	0.958	7.177	-1.828
CA6	1.437	8.355	-2.545
C6	0.464	8.763	-3.625
O6	0.203	9.940	-3.855
N7	-0.089	7.778	-4.308
CA7	-1.047	8.023	-5.382
C7	-2.311	8.653	-4.846
O7	-2.897	9.548	-5.447

Table A.II.2. Angles calculated to rotate from the experimental PAS to the helix axis:

Amino acid residue	α	β	γ
F	174.4062	96.5847	163.1292
L	289.7926	149.7880	278.4699
R	333.7623	60.2075	322.5272
R	91.7086	60.1428	248.7900
I	188.4300	131.3498	177.1625
G	319.9445	118.9594	308.6724

Table A.II.3. Results for diffusion on a cone model for the individual mobile sites in SN15.

	F_7	L_8	I_{11}	G_{12}
β	60-70	170	50	165
γ	125-150	135-155	100-170	30-40

WENDY J. SHAW

Education

Ph.D. in Physical/Biophysical Chemistry (May 2000)
University of Washington, Seattle, WA
Dissertation Title:
"Determination of the structure and dynamics of salivary statherin and N-terminal fragments bound to hydroxyapatite using solid state NMR."
Research Supervisor: Gary P. Drobny

Bachelor of Arts: Chemistry (1993)
Minor: Environmental Science.
Whitman College, Walla Walla, WA
Senior Thesis Title:
"The Chemical Study of the Environmentally Related Human Impacts on Langdon Lake."
Research Advisor: Professor Charles Templeton

Employment History

Research Assistant. (1996-2000)
University of Washington, Seattle, WA

Teaching Assistant. (1996-1997)
University of Washington, Seattle, WA

Technical Specialist II (1993-1996)
Battelle, Richland, WA

Lab Technician (1992-1993)
Whitman College, Walla Walla, WA

Undergraduate Internship (1993)
Battelle, Richland, WA

Undergraduate Internship (1992)
Whitman College, Walla Walla, WA

Awards and Affiliations

Recipient of Graduate Fellowship, Associated Western Universities (1996-2000).
Tank Waste Remediation Science Team Award, Battelle (1995).
Undergraduate Award in Analytical Chemistry, Whitman College (1993).
Recipient of NORCUS Undergraduate Fellowship (1993).
American Chemical Society, member (1991-2000)

Publications

"Structure and Dynamics of Hydrated Statherin on Hydroxyapatite via Solid State NMR." Shaw, W.J.; Long, J.R.; Stayton P.; Drobny G.P.;, In Preparation.

"A Solid State NMR Study of Dynamics in a Hydrated Salivary Peptide Adsorbed to Hydroxyapatite." Shaw, W.J.; Long, J.R.; Campbell, A.A.; Stayton P.; Drobny G.P.; *Journal of the American Chemical Society*, **2000**, In Press.

"Chimeric Peptides of Statherin and Osteopontin that Bind Hydroxyapatite and Mediate Cell Adhesion." Gilbert, M.; Shaw, W.; Long, J.; Nelson, K.; Drobny, G.; Giachelli, C.; Stayton, P. *Journal of Biological Chemistry*, **2000**

"Determination of Statherin N-Terminal Peptide Conformation on Hydroxyapatite Crystals." Shaw, W.J.; Long, J.R.; Dindot, J.L.; Campbell, A.A.; Stayton P.; Drobny G.P.; *Journal of the American Chemical Society*, **2000**, *122*, 1709-1716.

Janata, J.; Linehan, J.C.;Shaw, W.J.; Hallen, R.T.; Lafermina, J.P.;Peden, C.H.F.; Daschbach, J.L.; Heller, A. *Interface*, **1995**, *4*, 149.

"Identification of 4-(N,N-Dipropylamino)Benzaldehyde as a Potent, Reversible Inhibitor of Mouse and Human Class I Aldehyde Dehydrogenase." Russo, J.; Chung, S.; Contreras, K.; Lian, B.; Lorenz, J.' Stevens, D.; Trousdell (Shaw), W. *Biochemical Pharmacology*, **1995**, *50*, 3, 399.

Presentations

W.J. Shaw*, J.R.Long, P. Stayton, G. Drobny, "Structure and Dynamics of Statherin on the Biomineral Surface via Solid State NMR." ENC, Asilomar, CA. April, 2000.

W.J. Shaw*, J.R.Long, A.A. Campbell, P. Stayton, G. Drobny, "Determination of Statherin N-Terminal Peptide Conformation on Hydroxyapatite Crystals." AVS, Seattle, WA. October, 1999.

W.J. Shaw*, J.R.Long, J.L.Dindot, A.A. Campbell, P. Stayton, G. Drobny, "Solid State Nuclear Magnetic Resonance Studies of Salivary Statherin Adsorbed on Hydroxyapatite." ENC, Asilomar, CA. March, 1998.

W.J. Shaw*, J.R.Long, J.L.Dindot, A.A. Campbell, P. Stayton, G. Drobny, "Solid State NMR Studies of Salivary Statherin Adsorbed to Hydroxyapatite." NORM '98, Pasco, WA, June, 1998.

W.J. Shaw*, D.M. Camaioni, S.T. Autrey, J.A. Franz. "Molecular Orbital Calculation and Direct Kinetic Measurement of Ketyl-Ketone Hydrogen Transfer Reactions." NORM '96, Corvallis, OR. June, 1996.

J. Lorenz*, D. Stevens, W. Trousdell (Shaw)*, L. Wade, J. Russo. "Kinetic Analysis of the Inhibition of Mouse Class 1 Aldehyde Dehydrogenase By a Series of 4-Diethylamino Benzaldehyde Analogs." Presented at the Denver National ACS meeting, March 1993.